Eindhoven University of Technology

MASTER

Laser-single cluster interaction
modelling and understanding laser-single cluster interaction for cluster fusion

Verhaegh, K.H.A.

Award date:
2014

Technische Universiteit
Eindhoven
University of Technology

Department of Applied Physics
Coherence Quantum Technology & Science and Technology of Nuclear Fusion

Laser-single cluster interaction

Modelling and understanding laser-single cluster interaction for cluster fusion

Kevin Verhaegh, BSc.

Supervisors:

Dr. Ir. Seth Brussaard
Prof. Dr. Niek Lopes Cardozo

Additional committee members:

Prof. Dr. Ir. Jom Luiten
Dr. Ir. Leon Kamp
Prof. Dr. Anton Tijhuis

Final Version

Eindhoven, July 2014

Abstract

When an ultrashort, intense laser pulse interacts with a nano-cluster (radius $\sim$ nm, solid-state density), high ion energies and high ion charges are obtained in a very short amount of time. These high ion energies can be used to induce fusion reactions: cluster fusion. In current cluster fusion experiments sub nanosecond neutron pulses of $10^4 - 10^6$ neutrons per pulse with Q-values of $10^{-8} - 10^{-7}$ are obtained. We have devised a simplified process-based laser-single cluster interaction model for ascertaining the theoretical feasibility of single cluster fusion (fusion within one exploding nano-cluster upon laser irradiation) and for ascertaining the possibility of generating mono-energetic ion energy spectra from a single cluster for enhancing fusion yields in current cluster fusion schemes.

Laser-cluster interaction has been dissected in three processes: inner field ionisation, electron ejection and cluster expansion. In low-Z laser-cluster interaction, these processes occur sequentially. Field ionisation rapidly ionises the cluster, creating a nano-plasma. The resulting electron cloud is subjective to a driving force by the laser field and a retaining force by the ion cloud, resulting in a forced oscillator model for the electron cloud motion during the laser pulse irradiation, which is used for determining the portion of ejected electrons from the cluster. After electron ejection, the cluster obtains an ion charge excess causing the cluster to expand under its self-generated potential, accelerating the cluster ions to high energies when all electrons are ejected. In the case of high-Z laser-cluster interaction we have shown that the electron cloud oscillation and field ionisation processes occur simultaneously and have a synergistic effect on each other, which explains why extraordinarily high charge states can be obtained by laser-single cluster interaction.

We used our process-based model to show that it is theoretically possible to obtain nuclear fusion for deuterium-deuterium, deuterium-tritium and proton-boron fuel mixes from a single exploding nano-cluster by using peaked density cluster profiles and/or by combining ion species with a different mass/charge ratio. Single cluster fusion results in a sub picosecond neutron (deuterium-deuterium, deuterium-tritium fusion) / α radiation (proton-boron fusion) pulse, which can potentially lead to very high instantaneous (pulsed) neutron fluxes of up to $10^{22} - 10^{24}$ neutrons/s m^2. Additionally, we have shown that it is theoretically possible to obtain mono-energetic ion energy spectra from cluster fusion by controlling the density profile in a double pulse set-up, which can enhance the fusion yield in current cluster fusion schemes by up to a factor 4.

Preface

This project would not have been possible without the support of my supervisors, group members and colleagues (both CQT and Fusion), which I'd like to thank gratefully.

First of all, I would like to thank my direct supervisors Seth Brussaard and Niek Lopes Cardozo for their kind support during this project. Even though of their busy work schedules, they were still able to offer plenty of time and their advice, enthusiasm and motivation are greatly appreciated. I would like to thank Seth specifically for his devotion and for proof-reading this work during his holidays. I would like to thank Niek specifically for his out-of-the-box thoughts on the project and for his crystal-clear advice. My gratitude to Maarten de Bock, my previous supervisor who is now working at ITER, should also not go unnoticed. Additionally I would like to thank the additional committee members for sacrificing their precious time to read this work.

Furthermore, Jom Luiten's and Edgar Vredenbregt's insightful feedback and advice during the Tuesday morning meetings in the beginning of the project are gratefully acknowledged. Also Bas van de Geer is kindly acknowledged for providing the GPT simulation package and for his excellent programming support in the beginning of this project, which has been indispensable for this work. Additionally, Koen van der Straaten's introduction to GPT and his help during my first GPT simulations is greatly acknowledged. I would like to thank Peter Smorenburg for initialising this extremely interesting project of extreme physics with ultra-short; ultra-intense laser pulses acting on nano-clusters leading to extremely high ion energies and extremely high ion charge states. Also his expert analytical insight in the subject matter has helped me to kick-start my thesis work. Roger Jasper's kind advice during the proof reading a portion of this work is greatly appreciated and has helped me to significantly improve my work. I would also like to thank Luis O. Silva of the IST in Lisbon for his insightful discussions on cluster fusion during the PlasmaSurf summer school in Lisbon.

I would like to thank the staff members of both the Coherence Quantum Technology (CQT) group and the Science and Technology of Nuclear Fusion group at Eindhoven University of Technology for their insightful discussions; pleasant work environment; fascinating Science Lunches presentations and cosy group outings. Naturally, I would like to thank my colleagues (both current and ex-) from both the CQT group and Fusion group, which are too plentiful to mention in person. The lunch breaks, coffee breaks, fun discussions and Thursday drinks have been greatly appreciated.

Last but not least, I would like to thank my friends and family for their kind motivation and immense support during my studies.

Tenslotte wil ik graag mijn vrienden en familie bedanken voor hun motivatie en geweldige steun gedurende mijn studie.

Contents

List of Figures

Chapter 1

Introduction

The interaction of an ultra-short, intense laser pulse with a jet of nano-clusters, causes the nano-clusters to explode, from which high ion energies are produced in a very short amount of time. The high energy ions from neighbouring clusters collide, which can be used to induce fusion reactions: *cluster fusion*. In cluster fusion experiments $10^6 - 10^7$ neutrons are obtained per laser pulse [5, 6, 7, 8] with a neutron pulse duration of less than a nano-second [9] and a Q-factor of $10^{-8} - 10^{-6}$ [7, 8, 1, 10]. This indicates that, although cluster fusion is not likely a viable option as a power source, it is promising as a relatively inexpensive, table-top neutron source with the unique property that very short, intense neutron pulses can be generated.

In this work, we study the fundamental characteristics of the laser-cluster interaction process of a *single* cluster, for which we derive a simplified laser-single cluster interaction model. The purpose of this model is to understand the fundamental characteristics of laser-single cluster interaction; to predict the outcome of a laser-single cluster experiment and to control the cluster expansion process. Using this model we investigate whether it is possible to create conditions and to optimise conditions in which fusion occurs during the expansion of a *single* cluster by applying density gradients on the cluster and by optimising the cluster composition: *single cluster fusion.* Single cluster fusion is potentially interesting, because it is expected that even shorter neutron pulses can be obtained. Additionally we study whether it is possible, by using this model, to tune and optimise the ion energy spectrum of a single cluster for current cluster fusion schemes.

1.1 Background

In order to unlock the electrostatic energy of a cluster, first the atoms have to be ionised rapidly, which involves breaking the Coulomb barrier with a laser pulse. This requires intense light pulses of an intensity of $10^{20} W/\mathrm{m}^2$, which corresponds to TW laser powers in the waist of the laser beam, which seems very unrealistic - considering the average world power consumption is roughly 16 TW.

However, this has been realised since the late 1980s with the birth of ultrashort laser pulses, which have a duration of 10-100 femtoseconds ($1fs = 10^{-15}$s). This timescale is comparable to the vibration period of molecules and the characteristic time at which chemical reactions take place on a molecular level. When such a laser pulse has an energy of $\sim$ mJ, the power of the laser pulse is $\sim$ TW: therefore by generating such short laser pulses it is possible to obtain intensities high enough to break the Coulomb potential and rapidly ionise atoms: *field ionisation.* Laser induced field ionisation in gasses and solids leads to the generation of a plasma: an excited state in which the electrons can obtain keV energies during the laser pulse while the ions remain cold: conditions which are unattainable through other means.

When a small jet of nano-clusters is irradiated, the plasma conditions can become more extreme. A nano cluster is a small sphere $r \sim$ nm of solid-state density $10^{27} - 10^{29}$ m^{-3} containing 10^{2-8} atoms/molecules, and forms a bridge between atomic and macroscopic matter [11]. This

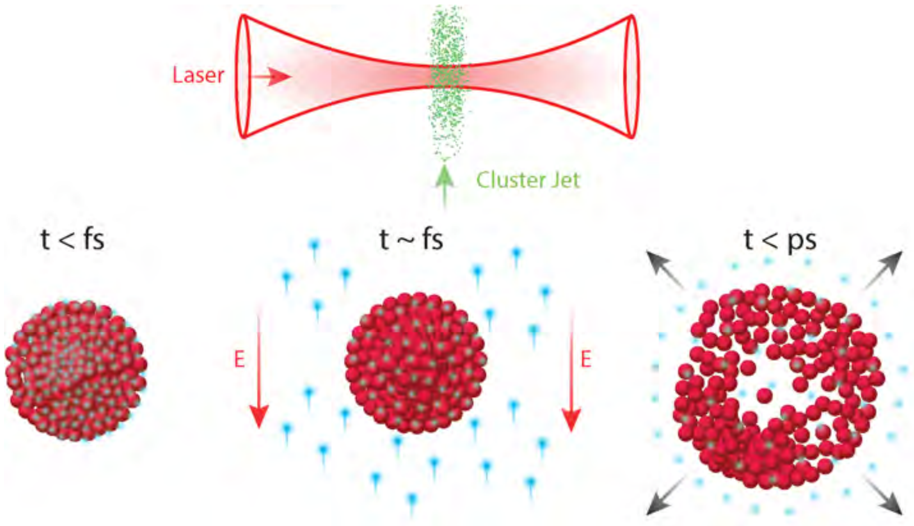

Figure 1.1: A schematic overview of the processes evolved in laser cluster interaction.

interest in clusters started the investigation of the interaction between an intense, femtosecond laser pulse and a jet of nano-clusters as shown in figure 1.1. Surprisingly, it was found that laser-cluster interaction is profoundly different than laser gas or laser solid interaction yielding extremely energetic (∼ MeV) and highly charged ions (Xe^{36+} [1, 12]). [13, 12, 14, 15, 16]. The high energies and charge-states in laser-cluster interaction are unique properties that can be used for several purposes, as indicated in figure 1.2 [1, 17, 18, 5, 19].

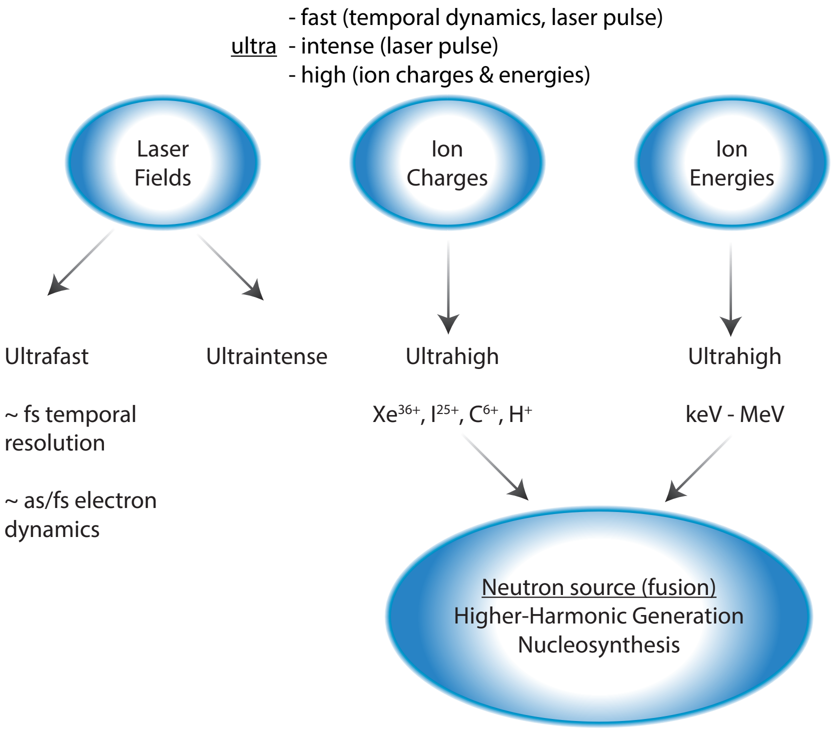

Figure 1.2: In this figure the various characteristics of cluster fusion are schematically related to their applications. [1]

Why does laser-cluster interaction yield much higher ion energies and ion charges than laser-atom/molecule and laser-solid interaction? Similar to laser-atom and laser-molecule interaction, the atoms inside the cluster get promptly ionized by field ionization, after which a nano-plasma is formed. The prompt ionisation occurs at the beginning of the laser pulse and eventually the laser force becomes strong enough to eject a portion of the electrons from the cluster [14, 15, 20, 21]. This leads to a charge separation and hence a build-up of ion charges. In the case of heavy cluster elements, this build-up of charges effectively amplifies the electric field of the laser, increasing the ionisation probability - hence ions can obtain extraordinary high charge states during laser-cluster interaction. Recombination of electrons with the highly ionised ions can be used to obtain intense x-ray radiation: *Higher-Harmonic Generation.* The build-up of ion charges, which repel each other, leads to cluster expansion, accelerating cluster ions to high energies. Ions from the neighbouring clusters can collide against each other and induce fusion reactions: *Cluster Fusion.*

Fusion for Energy and Neutrons Fusion is the natural process that powers the stars. The high pressure inside a star causes collisions between light ions in the star. Such a collision can cause these two particles to fuse together - releasing large amounts of energy in the form of a nuclear particle (for most "standard" fusion reactions a neutron). Fusion is a hot research topic for power generation. Nevertheless, up to this date, net energy production from fusion has not been achieved. The fusion fuel has to be heated for fusion collisions to occur and in order to obtain net energy from this process, the kinetic energy of the fusion fuel has to be confined for a sufficiently long time for fusion reactions to occur. Currently there are two main approaches to confining the fusion fuel: by using magnetic fields or by using the fusion fuel's inertia, which are both being investigated using large scale, multi-billion dollar facilities.

Fusion also releases nuclear particles (for the common fusion mixes - neutrons), which are consistently released at the same energy. Hence, fusion can be used to obtain a mono-energetic neutron source. Neutron sources are often used in medical applications, neutron imaging (which uses neutrons to create "x-ray like" images - where the neutrons are not stopped by dense materials [22]) and neutron diffraction (to study the atomic and/or magnetic structure of materials [22]). Ultra-short, mono-energetic neutron pulses can be used to achieve neutron diffraction in a pump-probe experiment, which could be used to study fundamental material studies in time-resolved measurements [9]. There are many different types of neutron sources available, but none of them are ultra-short. The largest high energy neutron flux (14.1 MeV neutrons) is predicted for the International Fusion Materials Irradiation Facility, IFMIF: 10^{18}n/m^{2}s. IFMIF is expected to be operational around 2025 and is being built to test wall materials for future fusion reactors.

Cluster Fusion As explained previously, the Q-value (power out divided by power in) of current cluster fusion experiments is too low for cluster fusion to be viable as an energy source. However, cluster fusion as a neutron source distinguishes itself from other neutron sources because of its potential to generate short, intense neutron pulses. In current cluster fusion experiments, fusion occurs due to the ions of neighbouring clusters (*multi-cluster fusion*), the neutron pulse has a duration of 100 - 1000 ps [9], which is mainly caused due to the distance the accelerated ions have to travel before they can interact. For the analysis of multi-cluster fusion, only cluster expansion has to be taken into account and the other fundamental laser-cluster interaction processes can be ignored [23, 5, 24, 25, 9, 6]. It is assumed that a large portion ($\approx 80-95\%$) of the laser energy is transferred to the electrons, ejecting the electrons from the cluster. The ejected electrons interact with each other, forming a thermal electron gas which serves as a background for the fully stripped nano-clusters. These nano-clusters explode - leading to multi-cluster fusion, without taking the laser-cluster interaction process into account. These assumptions can be made because the fusion reactions occur at a slower timescale than the laser-cluster interaction.

1.2 Research focus

In contrast to multi-cluster fusion, it might be possible to achieve fusion during the expansion of a single cluster: *single cluster fusion*, by creating conditions in which the ions of the *same* cluster collide against each other at fusion relevant velocities.

Single cluster fusion literature The possibility of single cluster fusion has been analysed previously in literature [26, 27, 28, 29]. One benefit of single cluster fusion is the high, solid-state density of the cluster - which could lead to higher neutron yields. Furthermore, when single cluster fusion occurs, the ions do not have to travel a large distance in order to fuse, drastically lowering the neutron pulse duration [26]. In addition, the ion energy in laser-cluster interaction can be tuned up to MeVs - which increases the range of feasible fusion mixes. By using a-neutronic fusion mixes a mono-energetic short pulse of α or γ pulses can be obtained, which might lead to future applications [27, 30, 28, 10, 7, 8, 1, 19, 26]. When investigating single cluster fusion the timescales of the fusion reactions and the laser-cluster interaction become similar and it is necessary to take all the fundamental processes of laser-cluster interaction into account. Although single cluster fusion has not been achieved experimentally yet, it has been shown that single cluster fusion is theoretically feasible by using a double pulse irradiation scheme [26, 29]; by using clusters with inhomogeneous density profiles [31, 32] and by using clusters with multiple ion species combined [19, 28, 27]. Recently, the first single cluster experiment has been performed [33], which have indicated that shock shells (when the inner ions collide against the outer ions) can indeed occur and mono-energetic ion energy spectra can be obtained by the double pulse irradiation of a single cluster. Previously, it has been predicted that mono-energetic ion energy spectra can be obtained using heterogeneous clusters [34, 3]. Apart of the experiment by [33], in all other experiments a multi-cluster jet is irradiated. The parameters measured in such an experiment are ”polluted” by multi-cluster effects - and in practice not much data of the laser-single cluster interaction can be extracted from the measurements from measurements.

Laser-single cluster interaction theory in literature The interaction of a single cluster with a laser pulse has been studied in literature previously, most often using extensive simulation techniques [26, 4, 29, 27, 16, 35, 19, 23]. The problem of such simulations is that they often do not hold in the case of laser-single cluster interaction - which will be explained in more detail in chapter 2.

In most literature sources it has been identified the total laser-cluster interaction process can be dissected in three separate processes: the *field ionisation* process - in which the neutral atoms of the cluster are ionised and a nano-plasma sphere is created; the *electron ejection* process - in which a portion of the electrons is removed from the cluster by the laser field and the *cluster expansion* process - in which the charge excess of ions leads to the expansion of the cluster due to repelling Coulomb forces between the ions [14, 1, 36]. There are many different theoretical models for each process in literature. However, these models often use different assumptions; are valid in different parameter regimes and hence often do not agree with each other. In addition, when simulations are not performed, these models are treated separately in literature, whereas a combination of these models is required for describing the total laser-cluster interaction process.

Field ionisation literature Field ionisation is an increasingly important topic in literature, as it is the first process of high power laser matter interaction [37, 38, 39, 40, 41]. Nevertheless, there is still much debate about field ionisation theory [42, 43, 44, 45, 46]. In the field of laser-cluster interaction, mostly a very rudimentary model of field ionisation (barrier suppression ionisation - which is a deterministic, classical ionisation model) is applied in combination with collisional ionisation [35, 16, 19]. However, recent laser atom interaction experiments [47, 48] indicate that ionisation is a probabilistic process and quantum mechanical tunnelling ionisation should be taken into account.

Electron ejection literature In literature, the electron ejection process is mostly referred to as outer ionisation [49, 50, 16, 20]. There are several outer ionisation models available [14] which lead to different scalings and different predictions. Hence it is uncertain which analytical approach should be used. In some cases [16, 35, 31] anomalous constants have to be determined using extensive simulations and a fully analytical approach is not applicable. Therefore it is uncertain whether a fully analytical approach is even possible.

Cluster expansion literature There are two main approaches in literature to cluster expansion: either it is assumed all electrons are removed from the cluster, which results in a Coulomb explosion [51, 52, 32, 31]; or it is assumed no electrons are removed from the cluster, leading to ambipolar-like expansion (which is referred to as hydrodynamic expansion in literature) [4, 2]. Recent investigations by [4, 2, 3] have lead to a general theory for the cluster's expansion for an arbitrary fraction of electrons ejected from the cluster. Current Coulomb models are designed for single cluster specie [53, 32] and are mostly used for homogeneous cluster densities [51, 52].

1.3 Global research objective and specific research questions

Although there are various attempts in literature to study the separate laser-cluster interaction process, the models in literature often do not correspond with each other and are mostly studied separately. In addition, extensive simulation schemes have been performed in literature to study laser-cluster interaction, which often use potentially problematic assumptions. Hence, the first aim of this work is to provide a theoretical framework for studying the fundamental characteristics of laser-single cluster interaction. Our process-based laser-cluster interaction model is general enough to take clusters with cluster gradients and multiple ion species into account. Secondly, we use our process-based model to investigate under which conditions single cluster fusion can occur and what fusion yields and their duration can be obtained from single cluster fusion in an optimized case. Additionally it is investigated how our understanding of laser-single cluster interaction can be used to optimize the resulting ion energy distribution of a single cluster for current cluster fusion schemes.

Studying the fundamental characteristics of laser-single cluster interaction More specifically investigating laser-cluster interaction implies the following research questions:

- What is the physics behind laser-single cluster interaction ? (subdivision in processes: chapter 2, detailed overview per process: chapter 3 to 5)
- What are the output parameters of a single cluster (ion energies, ion charges, electron energies) after laser-cluster interaction given the input parameters (laser parameters, cluster parameters) ? (chapter 3 to 5)
- How can the cluster expansion dynamics be controlled? More specifically, what are the cluster expansion dynamics of a certain cluster and what can be done to control this ? (chapter 5)

We will use two methods for investigating laser-single cluster interaction: numerical particle tracer simulations and a simplified process-based laser-cluster interaction model. The advantage of particle tracer models compared to current simulation techniques is that assumptions of such a model are not violated by laser-cluster interaction process - in contrast to other modelling techniques (explained in chapter 2). In particle tracer simulations, the ions and electrons are approximated as point charges and the interaction of every point charge with every other point charge is taken into account fully relativistically, resulting in a computational cost that scales with the number of particles squared. Given our current computing power limits, this scaling limits our particle tracer simulations to 1500 atoms, whereas we are investigating clusters of 10^7 atoms when discussing cluster fusion.

Therefore, a simplified process based model has been introduced, where laser-cluster interaction is separated in field ionisation 3; electron ejection 4 and cluster expansion 5. For each process a model is used, which provides a more intuitive physical understanding of the fundamental processes in laser-single cluster interaction. Additionally, this model is not limited by computational costs and scaling problems are not an issue. However, the disadvantage of such a system is that each model, describing each process requires a set of assumptions and a careful approach is required to prevent the violation of these assumptions. Each process is validated separately using particle tracer simulations in chapters 3 to 5.

Single cluster fusion Using this theoretical understanding, the possibility of single cluster fusion is investigated by using the ion expansion dynamics in our laser cluster interaction model. Additionally, it is investigated whether obtaining mono-energetic ion energy spectra from tuning the expansion of a single cluster can benefit current cluster fusion schemes. Single cluster fusion and mono-energetic ion energy spectra can both be obtained by applying a density gradient on the cluster, by changing the cluster's composition and by using layered clusters. More specifically investigating the possibility of using intra-nuclear cluster fusion involves the following research questions, which will be answered in chapter 6:

- Which parameters play a role in single cluster fusion? What should these parameters be for single cluster fusion to occur and can these parameters be optimised for single cluster fusion?
- Which parameters play a role in tweaking the ion-energy spectrum? What should these parameters be for obtaining mono-energetic ion energy spectra?
- Controlling the expansion dynamics can be performed by using density gradients. Hence, how can the density profile of a cluster obtain such gradients? More specifically, how can the cluster density profile be controlled?
- Can obtaining mono-energetic ion energy spectra benefit current cluster fusion schemes and is this feasible?
- What laser intensity would be required to fully strip single cluster fusion relevant clusters and would such a field by feasible?
- What are the fusion yield, pulse duration and Q-factor of single cluster fusion for a single cluster? How is this related to multi-cluster fusion and can this single cluster fusion be distinguished from a multi-cluster fusion experimentally?
- Is it possible to combine single cluster fusion with an a-neutronic fusion mix for the generation of short α pulses?

Chapter 2

The ”simple” laser-single cluster interaction model

One goal of this thesis is to create a general laser-single cluster interaction model. This model should support four goals:

- The model should be general enough to support multiple different scenarios for realising single cluster fusion
- It should provide a physical unintuitive picture of the laser-single cluster interaction process ?
- What are the output parameters of a single cluster (ion energies, ion charge states) after laser-cluster interaction given the input parameters (laser parameters, cluster parameters) ?
- How can the cluster expansion dynamics be controlled? More specifically, what are the cluster expansion dynamics of a certain cluster and what can be done to control this ?

In this chapter we will discuss a simplified picture of a homogeneous deuterium cluster being irradiated by a laser. This qualitative understanding of laser-single cluster irradiation leads to a laser-single cluster irradiation model containing three different processes, which can be separated because they work on three different timescales. The three different, sequential, processes, which are also indicated in literature [14, 1], are illustrated in figure 2.1. The aim of this chapter is to highlight the dissection of the laser-cluster interaction process in three sub-processes and to provide a physically intuitive picture of laser-cluster interaction in its simplest form, before going into detail of the three separate processes (which is explained in chapters 3 to 5).

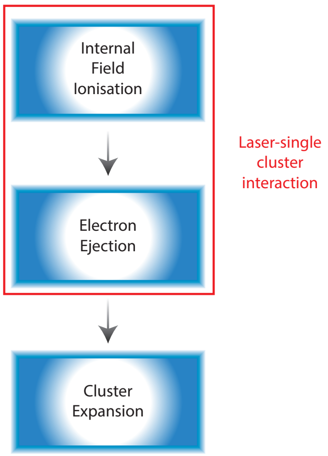

Figure 2.1: A schematic overview of the laser-cluster interaction model.

First, the laser ionises the atoms inside the cluster by **field ionisation**. Field ionisation in a cluster will be referred to as the **internal field ionisation** process. It is assumed the cluster consists of deuterium atoms, which can only be single charged. Therefore, the deuterium atoms are fully ionised rapidly in the beginning of the laser pulse, after which the internal field ionisation process is completed. The ionisation leads to a spherical collection of ions and electrons: a nano-plasma sphere, which is small enough to be fully penetrated by the laser light, since the cluster radius is much smaller than the laser wavelength [23, 8, 35, 7, 24].

Secondly, the light electrons are displaced by the laser field, whereas the much heavier ions remain approximately static in the laser field on the laser-action timescale (femtoseconds). This is referred to as the **electron ejection** process, which takes only place during the laser pulse interaction. Removing the electrons from the cluster leads to a charge build-up in the cluster, which eventually - at a sub-picosecond timescale - leads to the cluster expansion. Hence, the process of the electrons leaving the cluster generates a charge build-up and drives the cluster's expansion.

Thirdly, the positive ions in this charge build-up repel each other. Hence the cluster expands under its self-generated potential, leading to the *cluster expansion* process after the electrons have been removed from the cluster. In the cluster expansion process, the ions can be accelerated to high energies.

In order to understand the physics of laser-single cluster interaction, simulations of laser-single cluster interaction are performed. The simulation method is performed using particle tracer simulations, which is discussed in section 2.1. The simulation results are visualised by presenting a plot of all x, y, z, v_x, v_y, v_z (positions and velocities) of all electrons and ions as a function of time. The simulations performed in section 2.2 are Coulomb case simulations, which is the intuitive simplest case of laser-cluster interaction and is thoroughly studied in literature [51, 54, 55, 24]. In the Coulomb case, the laser pulse ejects all electrons from the cluster, leaving a cluster which consists of only ions. When this occurs, the inner field ionisation and electron ejection processes have no effect on the ion sphere expansion (the effect of these processes is covered in the statement all electrons are ejected). Hence, in this case, it does not matter whether the laser intensity is just high enough to eject all electrons or whether it is twice the required laser intensity for electron ejection: the cluster expansion dynamics stay the same.

However, as is explained in section 2.3, whether all electrons are ejected from the cluster will depend on the electron dynamics inside the cluster: the electron ejection process. The electron ejection process depends on how the nano-plasma is created, which is determined by the internal field ionisation. If not all electrons are ejected, complications arise in the calculation of the ion cloud expansion, which becomes dependent on the portion of electrons ejected. Additionally, when the remaining electrons in the cluster is larger than 30 % (which will be explained in 5), the electron and ion cloud dynamics start depending on each other, and the system has to be solved self-consistently. Therefore, in a general case - non-Coulomb explosion case, the internal field ionisation and the electron ejection have an effect on the ion expansion dynamics. This implies that the simple qualitative pictures provided here of the internal field ionisation and the electron ejection have to be generalised and quantified in order to determine the ion cloud expansion. Discussing and studying these processes extensively forms a large portion of the report and involves chapters 3-5.

2.1 Particle Tracer Simulations

One important tool for developing an understanding of laser-single cluster interaction and for validating and verifying our process-based laser-cluster interaction model is particle tracer simulations. These particle tracer simulations are performed by using the General Particle Tracer code (GPT) by Pulsar Physics. More information can be found at [56, 57]. This section contains an overview of the GPT code and a summary of the most important remarks of the implementation of laser-cluster interaction in GPT. For more information about the implementation of laser-cluster interaction in GPT, see appendix B.

Particle tracer simulations are initialised by providing a set of charged particles (electrons/ions) and an applied - external - electromagnetic field. The temporal dynamics of this system are determined by integrating the relativistic equations of motion numerically (using Runge-Kutta integration methods) and tracing the trajectory of every charged particle. The interaction of each particle with every other particle is taken into account by taking the electric and magnetic field generated by each particle into account, leading to an $\mathcal{O}(N^2)$ system. The GPT code can only handle the evolution of a system of charged particles classically: field ionisation, collisional

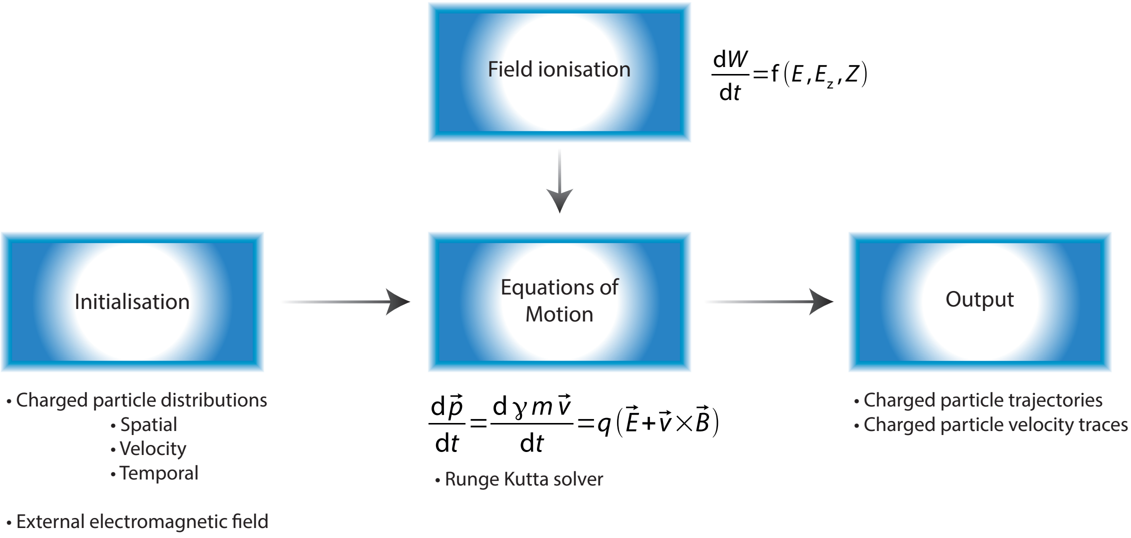

Figure 2.2: General schematic overview of GPT.

ionisation and quantum effects are not taken into account. For more information about the numerical schemes used, see [56] and appendix B. A schematic overview of the general GPT simulation strategy is shown in figure 2.2.

Implementation of laser-single cluster interaction in GPT The cluster is represented in GPT by a sphere with a certain density function and radius. Since the particle tracer tracks all particles, there is always a finite number of particles in the cluster, which varies between 10^2 and 10^4. The positions of the atoms are determined using Monte-Carlo methods. A surface representing the density function is created in a box. By generating random points in the box and checking whether these points are below this surface, a random distribution of charged particles obeying the density function is generated. GPT calculates the classical electromagnetic interaction between point charges and does not take ionisation into account. Therefore, we have developed an additional field ionisation model for GPT, which can be generally applied for solving high field physics questions. A similar method has been developed for OSIRIS, which is a particle-in-cell code [58, 59, 60, 61] - although, in contrast to our implementation, the tunnelling ionisation in OSIRIS does not take the limitations of tunnelling ionisation into account.

Field ionisation routines in GPT The ionisation routines work by calculating the electric field vector at the position of every "ionisable element" (atom or not-fully ionised ion). Using this electric field vector, the field ionisation routine calculates the ionisation probability using a tunnelling ionisation model for every "ionisable" element. Tunnelling ionisation models are analytic models for field ionisation based on the quasi-static electric approximation (it is assumed the oscillation of the laser field is slow compared to the oscillation of the bound electron and it is assumed magnetic field effects can be neglected), which will be discussed in chapter 3 and appendix B, C.1. The result of these theories is an analytical function determining the tunnel ionisation probability per unit of time times as a function of electric field strength and atomic parameters. Using Monte Carlo methods, it is determined whether ionisation occurs. When ionisation occurs, the charge of the "ionisable element" is increased and an additional electron is created in the simulation. The position and momentum of the created electron is determined using the theory in chapter 3. Care should be taken when using field ionisation, because quasi-static electric field approximations are only valid in a restricted regime and tunnelling ionisation models are often used in literature at too high field intensities [60, 59].

Laser pulse The laser is modelled by a plane wave linearly polarized electromagnetic field convoluted by an envelope, which is provided by the equations 2.1. Here the electric field is $\vec{E}$, the magnetic field is $\vec{B}$, the maximum value of the electric field in the laser pulse is E_0, the phase of the laser field is $\eta = \omega_L(t - \frac{z}{c})$, in which ω_L is the laser frequency, t is the time, c is the speed of light and x, y, z represents Carthesian coordinates. The parameter $f(\eta)$ represents the "envelope function", which describes the shape of the laser pulse - usually assumed to be Gaussian: $f(\eta) = \exp(-\frac{1}{2\tau^2}\eta^2)$. The parameter τ represents the width/time duration of the Gaussian laser pulse; e.q, which is related to the Full Width Half Maximum (FWHM) duration by $t_{\mathrm{FWHM}} = 2\sqrt{2\ln 2}\tau$.

$$\begin{aligned}
\vec{E} &= E_0 f(\eta)\sin\eta\vec{e}_x \\
\vec{B} &= \frac{E_0}{c} f(\eta)\sin\eta\vec{e}_y \\
\eta &= \omega_L(t - \frac{z}{c})
\end{aligned} \tag{2.1}$$

Particle tracing versus Particle-In-Cell simulations. As stated in the introduction, Particle-In-Cell (PIC) models and non-relativistic molecular dynamics models are often used in literature for studying laser-cluster interaction. In PIC models, the charge density is smoothed over a 3D grid and the point-like nature of charges is ignored. In addition, in PIC models the stochastic heating [56] of the charged particles, due to interactions with each other in a cell, is neglected. This implies that the electrons/ions repelling each other is neglected when a cell contains only electrons/ions for a sufficiently long time. In laser-single cluster interaction, stochastic heating is of paramount importance, especially in the Coulomb case. Therefore, PIC models are expected to lead to inaccurate results in the Coulomb case, [35, 3], which makes simulating laser-cluster interaction complicated. Nevertheless, PIC simulations have been used in literature previously for the investigation of laser-cluster interaction [26, 23, 31]. The problem with (scaled) molecular dynamics models is that often relativistic effects, magnetic field effects and ionisation effects are not taken into account, although there are some exceptions, which use scaling techniques [35]. In contrast, the particle tracer simulations performed in this work take the interactions of all particles fully relativistically taken into account. This provides a more accurate simulation strategy, than existing simulation PIC strategies for laser-cluster interaction. However, taking all interactions into account severely increases the computational cost. The computational cost scales with the number of particles in the system squared: $\mathcal{O}(N^2)$, instead of $\mathcal{O}(N)$ in the case of PIC simulations. This limits the cluster size to a few thousand particles in the case of particle tracer simulations.

Assumptions. The assumptions in particle tracer simulations can be classified in two categories: one category are the assumptions used to implement the cluster-laser interaction in GPT (e.g.: assuming spherical clusters with a homogeneous density, assuming a Gaussian laser profile, etc.). A detailed overview of these assumptions can be found in the appendix B.1. The second category of assumptions are general assumptions which are intrinsic in GPT. A short overview of these assumptions is listed below, more details can be found in appendix B.

- The charged particles in the GPT code span a Coulomb electric field in the rest frame, which is only valid in the assumption that the electromagnetic interaction between two charged particles is instantaneous. In certain relativistic cases this might be erroneous, because the medium of interaction is intermediated by a photon, travelling at the speed of light, leading to retardation effects. Furthermore, an accelerated charged particle emits Larmor radiation and loses energy, which is not taken into account in the Coulomb electric field. In order to incorporate retardation and radiation effects, the Coulomb field has to be replaced by the field generated by the Lienard-Wiechelt potentials, which would require much more computation time. For each simulation, it is carefully checked whether retardation and radiation effects could alter the charged particle trajectories. By using the GPT trajectories as a priori trajectories, the force on a particle is calculated and compared for the Coulomb field potential and for the Lienard-Wiechelt potentials. If these two forces do not deviate, radiation and retardation effects can be neglected. For more information, see appendix B.

- As mentioned before, the GPT code only takes classical EM interaction into account. Quantum effects and ionisation effects are not taken into account (although, as explained previously, a field ionisation model has been implemented in GPT). More specifically this implies that collisional ionisation (electrons that are swept through an ion/atom/molecule can induce ionisation) and recombination (an electron swept through an ion can recombine with the ion) are neglected. The effect and magnitude of these processes are estimated and discussed in appendix B.

- One problem with the interaction of point particles using the Coulomb interactions is that the Coulomb field goes to infinity when the limit of the distance between the particles goes to zero, which produces a numerical singularity. Therefore, a cut-off distance has to be introduced, which gives the point charges a certain "size". When two point charges are close together, closer than the cut-off distance, the Coulomb fields of the charged particles are evaluated at the cut-off distance. Therefore, the Coulomb field evaluated at this distance is the maximum Coulomb field a charged particle can experience from another charged particle (discrete effect). For more information see appendix B.

2.2 Coulomb case laser-single cluster simulations

For convenience each simulation result is tagged with a green tag, for example: [COUL1]. A list of all simulations and tags is given in appendix D.1. In some cases plots of this simulation are provided in appendix D.1.1.

In this section, we will evaluate five different laser-single cluster interaction simulations. Each of these simulation contains different parameters, listed below. In all simulations, the cluster consists of 100 deuterium atoms with a homogeneous density distribution. Furthermore, all simulations here use a plane wave laser field with a Gaussian envelope, as discussed previously, with a wavelength of $\lambda = 800$ nm.

In each case the laser displaces (almost) all electrons from the cluster - Coulomb case. When all electrons are removed, the ion expansion dynamics and resulting ion energies solely depends on the cluster parameters (radius, density, ion specie). Hence it is expected that the ion dynamics are not affected by the laser parameters when all electrons are ejected, which is confirmed by our simulations. Coulomb case simulations of a homogeneous Z=1 cluster are the intuitively relatively simple to understand and provides a starting case for our laser-cluster interaction model, which is developed in chapters 3 (inner field ionisation process), 4 (electron ejection process) and 5 (cluster expansion process).

1. $E_{\max} = 2\times10^{12}\,\frac{\mathrm{V}}{\mathrm{m}}$, $n = 1\times10^{27}$ m^{-3}, $t_{\mathrm{FWHM}} = 75$ fs, [COUL1].
2. $E_{\max} = 5\times10^{11}\,\frac{\mathrm{V}}{\mathrm{m}}$, $n = 1\times10^{27}$ m^{-3}, $t_{\mathrm{FWHM}} = 75$ fs, [COUL2].
3. $E_{\max} = 1\times10^{11}\,\frac{\mathrm{V}}{\mathrm{m}}$, $n = 1\times10^{27}$ m^{-3}, $t_{\mathrm{FWHM}} = 75$ fs, [COUL3].
4. $E_{\max} = 5\times10^{11}\,\frac{\mathrm{V}}{\mathrm{m}}$, $n = 1\times10^{27}$ m^{-3}, $t_{\mathrm{FWHM}} = 25$ fs, [COUL4].
5. $E_{\max} = 2\times10^{12}\,\frac{\mathrm{V}}{\mathrm{m}}$, $n = 5\times10^{27}$ m^{-3}, $t_{\mathrm{FWHM}} = 75$ fs, [COUL5].

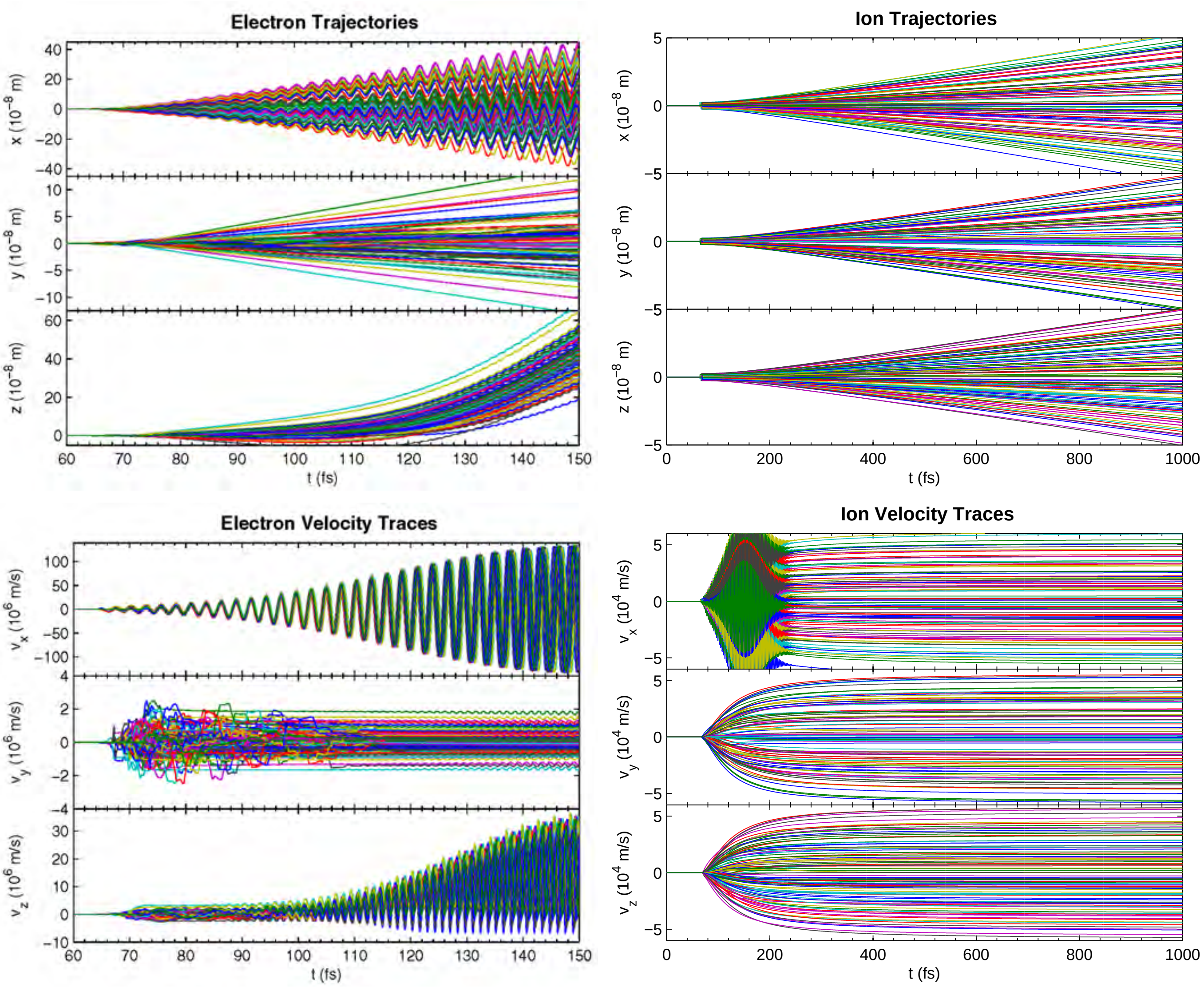

Figure 2.3: "Simple" model case 1: electron/ion trajectories and velocity traces [COUL1TRAJ]

2.2.1 Trajectory plots

In order to give a full picture of the laser-single cluster dynamics, for the first case the $x(t), y(t), z(t)$ trajectories of the electrons and ions are plot and the $v_x(t), v_y(t), v_z(t)$ velocity traces of the electrons and ions are plot in figure 2.3 - referred to as a *trajectory plot*. Each line represents the trajectory/velocity trace of an electron/ion in the simulation as a function of time. The lines are coloured in order to distinguish the lines from each other. The electron data is plot in a different time axis than the ion data, because the electron dynamics take place during the laser interaction $\sim$ fs, whereas the ion dynamics take place on a slower timescale $\sim 10^2$fs. Therefore, it is possible to separate the electron ejection process and the cluster expansion process. When a single atom in the deuterium cluster is tracked, this atom is ionised at some time (t_{ion}), where it is transformed in the simulation from a neutral atom to a singly charged ion and an electron. In the simulation this implies that the electron and ion start appearing for $t > t_{\text{ion}}$. The maximum of the laser pulse is located at $t = 150$ fs, which is in the beginning of the ion trajectory/velocity plots and at the end of the electron trajectory/velocity plots.

2.2.2 Internal field ionisation

In figure 2.3 electrons and ion start appearing at $t = 66$ fs, meaning that ionisation has not taken place until $t = 66$. In between $t = 66 - 72$ fs the atoms are ionised and transformed into electrons and ions, after $t = 72$ fs the ionisation process is completed.

2.2.3 Electron ejection

From our simulations, we can determine that the electron velocity traces (which govern the electron trajectory traces) are a diagnostic for understanding electron ejection. Electron ejection is an important laser-cluster interaction process, which determines whether/when/why electron ejection takes place and it determines whether an ejected electron returns to the cluster (for Coulomb explosion to occur, the ejected electrons have to stay ejected from the cluster). When an electron moves inside the cluster, it collides with cluster ions (discrete effects). During these collisions a force works shortly on the electron, leading to a sudden change of velocity, which leads to chaotic, irregular behaviour in velocity space - as seen in the beginning of the y and z velocity traces. The dynamics of the system can be simplified by grouping the electrons together as one electron cloud, on which two forces work. A force due to the laser field acts to displace the electron cloud from the ion cloud centre. A second force works on the electron cloud by the ion cloud collective space charge, attracting the electron cloud - which effectively acts as a retaining force. The laser field force increases in time until the laser pulse has reached its maximum amplitude at $t = 150$ fs. At some point the laser field force becomes much larger than the retaining force. In this case, the laser force is also much larger than the forces due to discrete effects and the electron's trajectory is determined mainly by the laser force - which leads to a regular behaviour in the electron velocity plot. Therefore, the electron velocity trace changes from chaotic behaviour to regular behaviour at the point when the laser force overpowers the retaining force by the ion cluster. This transition occurs differently for each direction, which is caused by the fact that the laser force is different in each direction. In the y direction there is no laser force. The electron is swept through the ion cluster, causing collisions changing the y velocity - leading to irregular behaviour in the y velocity timetrace. When this irregular behaviour stops, the electron is no longer swept through the cluster and the electron's momentum remains constant (the small oscillations in v_y near the laser pulse maximum are caused by relativistic effects due to the large v_x, v_y, increasing the electron's mass).

An electron in a laser pulse ($\vec{E} = E\vec{e}_x, \vec{B} = B\vec{e}_y, \vec{k} = k\vec{e}_z$) quivers on the oscillating field, leading to the oscillation shown in v_x. Since the laser pulse maximum is at $t = 150$ fs, the oscillation is maximum at the end of the trajectory plot. After the laser pulse maximum, the laser amplitude is decreased and the oscillation amplitude becomes smaller, eventually leading to a constant velocity. Additionally, the magnetic field of the laser pulse, in combination with the particle's quivering motion in the x direction, leads to a net velocity in the z direction (and hence a net displacement), which is a $\frac{v}{c}$ effect. The velocity in the z direction is maximum at the laser pulse maximum. Eventually after the laser pulse maximum, the v_z is lowered and leads to a set of constant velocities after the laser pulse. Therefore, even after the laser pulse, the ejected electrons obtain a net momentum in the x, y, z directions. In chapter 4, this will be studied in detail and it will be shown that this net momentum is a result from the sudden transition between chaotic (discrete effects dominated behaviour) and regular (laser dominated behaviour) behaviour. For convenience, we will refer to this transition time (which is different per direction and per electron) as $t^{x,y,z}_{\text{transition}}$. Electron ejection occurs when this transition has occurred in all three directions. Because the electric field effects have an earlier onset than magnetic field effects, the transition occurs first in the x direction, secondly in the z direction and thirdly in the y direction: $t^{x}_{\text{transition}} < t^{z}_{\text{transition}} < t^{y}_{\text{transition}}$. When transition in the x direction occurs, the electron quivers on the laser electric field oscillation in the x direction. Because these transitions occur in a time interval, the instant at which the transition occurs is differs per electron, leading to a difference in net momentum. This net momentum, in combination with the displacement due to the magnetic field, are the reasons why ejected electrons generally stay ejected, which is why the cluster expansion after the laser pulse is possible.

2.2.4 Cluster expansion

Just after the electron ejection, the cluster consists out of a spherical collection of ions. The ions repel each other, increasing the distance between the ions. Therefore, the acceleration of the ions is the highest just after electron ejection, after which the acceleration (due to cluster expansion) decreases, eventually leading to constant velocities and a linear expansion of the cluster radius, as indicated in figure 2.3. The cluster expansion is expected to be radial. Nevertheless, the simulation results indicate that the ions are affected by the laser light at high laser intensities, which is evident by the rapid oscillations in v_x trace of the ion velocity between 100-200 fs. This disturbance leads to a 10 % deviation between v_x and v_y, v_z. Therefore, this effect can be neglected and it can be assumed the dynamics is radial. In this analysis, we separated the electron ejection and cluster expansion. However, shortly after a few electrons have been ejected the cluster starts expanding. Nevertheless, the mass of the ions is relatively high compared to the mass of the electrons. Hence ion dynamics is expected to occur at a slower timescale, which agrees with the simulation results of figure 2.3, where it takes 300 fs before the cluster expansion leads to a relatively constant ion velocity.

A homogeneous ion cluster corresponds to a charged sphere in a fluid approximation. Such a cluster is a storage of electric potential energy and when the cluster explodes due to its Coulomb forces - Coulomb explosion - this potential energy is converted to electric energy, which is studied in literature [51, 55, 52]. In section 5.1.1 the Coulomb explosion dynamics of a homogeneous density single specie ion cluster is derived. As explained in chapter 5, the Mie time $\tau_{\text{Mie}} = \sqrt{\frac{\rho Z e^2}{3\epsilon_0 m_i}}$ (inverse of the Mie frequency) serves as a measure for the characteristic time of the Coulomb explosion and the acceleration of the ions is completed in 3-5 times the Mie time resulting in a constant ion velocity and a linear cluster radius expansion [32, 12, 14, 23]. During the Coulomb explosion, the ions near the core of the cluster obtain the lowest velocities, whereas the ions near the outer edge f the cluster obtain the highest velocities. The maximum obtainable ion velocity of a Coulomb explosion is calculated to be 4.8×10^4 m/s, using section 5.1.1, which corresponds within 15 % of the simulated result.

Therefore, in a preliminary view, the simulation results agrees with the results provided by the analytic theory in the case of a Coulomb explosion of a homogeneous, single specie cluster. However, when a portion of the electrons remain inside the cluster, complications arise in the expansion dynamics, as discussed in chapter 5. Additionally, when the cluster has a density gradient or consists out of multiple ion species, a generalised Coulomb model has to be applied, which will be shown in section 5.1.

2.2.5 Differences in the other cases

After having discussed the simulations of case 1 ([COUL1]) in detail, in order to gain more insight in laser-cluster interaction in the Coulomb case, we will discuss what happens when the laser/cluster parameters are changed. For this purpose, we discuss the differences of the simulation results of cases 2-5 ([COUL2] - [COUL5]) compared to case 1 ([COUL1]). Trajectory plots for cases 2-5 are provided in the appendix, figures: D.2 to D.5.

Changing the laser intensity In case 2 and 3 ([COUL2, COUL3]) only the laser intensity is decreased with respect to case 1 ([COUL1]). Because the laser intensity is lower, it is expected that it takes longer for the field ionisation to occur and it is expected that field ionisation occurs closer to the laser pulse maxima. This is confirmed in figure D.2 and D.3: in case 2 the inner field ionisation lasts from $t = 76$ fs to $t = 92$ fs and in case 3 the inner field ionisation lasts from $t = 97$ fs to $t = 118$ fs, in contrast to case 1 where the inner field ionisation lasts from $t = 66$ fs to $t = 72$ fs.

Since the laser intensity is lower, we expect that also $t^{x,y,z}_{\text{transition}}$ occurs at a later time, closer to the laser pulse maxima. This change in transition time affects the net momenta of the electrons. Additionally, changing the laser pulse intensity has a strong effect on the motion of the electrons in the z direction, because magnetic effects depend on $\frac{v}{c}$. Therefore, the displacement effect by the laser is expected to greatly decrease for lower laser intensities. A change in net momenta and electron displacement change the portion of ejected electrons being reabsorbed by the cluster after laser irradiation, which can affect cluster expansion. Furthermore, the effect of the laser might, in some cases, not be strong enough to eject all the electron from the cluster. These expectations are confirmed in the simulation results portrayed in figures D.2 and D.3, where the magnetic field effects become non-existent in case 3.

In case 2 10 % of the electrons stay inside the cluster and in case 3 20 % of the electrons stay inside the cluster. For now, we will assume these electrons spread homogeneously through the cluster and actively shield the cluster charge, which is valid when 30 % or less of the electrons remain in the cluster - as will be shown in section 5.1. According to the analytical Coulomb model, the decrease in net charge of the cluster is expected to lower the maximum ion velocity in case 2 by 5 % and in case 3 by 10 % as compared to case 1. From a preliminary investigation this is confirmed by the simulations, which show a maximum ion velocity decrease of respectively 4 % and 8 % compared to case 1.

Hence, although the laser intensity is varied by a factor 20, the maximum obtainable ion velocity is only changed by 8 %. This illustrates the statement made in the beginning of the chapter that the cluster expansion is independent on the laser intensity *if* (almost) all electrons are removed from the cluster. Naturally, if the laser intensity is decreased even further, more electrons will remain in the cluster (as explained in chapter 4) and the simplified Coulomb picture no longer holds, as explained in chapter 5.

Changing the laser pulse duration In case 4 [COUL4], the same parameters have been used as in case 2 but with a factor 3 decrease in laser pulse duration. The maximum of the laser pulse is still at $t = 150$ fs. Therefore we expect that the inner field ionisation takes place closer to the maximum of the laser pulse. In addition, we expect that the interval in which the inner field ionisation takes place decrease, because for shorter laser pulses the gradient of the laser intensity is steeper near the ionisation threshold. This corresponds to the simulation result shown in figure D.4, where the inner field ionisation occurs at $t = 128 - 131$ fs, which is a much shorter interval than compared to case 2 where inner field ionisation occurs at $t = 78 - 92$ fs.

Similar to field ionisation, in the case of shorter laser pulses, we expect $t^{x,y,z}_{\text{transition}}$ is closer to the laser pulse maximum and the ejected electrons have less time to obtain the displacement required to prevent re-absorption by the cluster after the laser pulse maximum. Additionally, we expect that the interval of $t^{x,y,z}_{\text{transition}}$ is made smaller due to the steep pulse gradient, which results in a smaller electron momenta spread. These expectations are confirmed by the particle tracer simulation result in figure D.4: in the x direction the displacement is less at $t = 150$ fs in case 4 than in case 2 (because the time between the ejection and laser pulse maxima is smaller). However, the drift momentum of the electrons is higher in case 4 than in case 2 (the slope of the electron x trajectory is larger in case 4 than in case 2), which can be explained by the stronger envelope gradient and by the smaller momenta spread.

After the laser pulse around 10 % of the electrons stay inside the cluster in case 4, which is the same as in case 2. This indicates that the amount of reabsorbed electrons is the same in case 2 and 4, which indicates that the effect of the higher electron momenta and the effect of the smaller time interval between the ejection and laser pulse maxima balance each other when comparing case 2 and 4. As a result, also the ion expansion dynamics are comparable for the short pulse and the long pulse and the simulations only indicate a 1 % difference in ion velocities between case 2 and case 4.

Changing the cluster density In case 5 [COUL5] a similar laser pulse is used as in case 1, with a 5 times higher density cluster, which still contains 100 atoms, and has a corresponding factor $(1/5)^{1/3} = 0.58$ decrease in radius. At a higher density, the field ionisation process is not expected to change. Furthermore, the laser interaction with individual electrons is also not expected to change. The retaining force working on a single electron by the ion cloud is expected to increase, because the ions are closer together. However, the electron also has to travel less distance in order to escape the cluster higher density leads to more charges pulling the electron to the centre of the cloud). Because the increased density is a collective volume effect, we expect that the increased retaining force has a stronger effect than the decrease in distance required for the electron to be ejected from the cluster. Therefore a stronger laser field is required for electron ejection in case 5 than in case 1, leading to an increase in $t^x_{\text{transition}}$. This cannot be confirmed by the simulation results as $t^x_{\text{transition}}$ occurs almost instantly after field ionisation both in case 1 and 5, due to the high field strength. After the $t^x_{\text{transition}}$ the electrons are free to quiver on the laser field. This implies that as soon as $x(t) > R$, the electron no longer experiences collisions inside the cluster, leading to $t^y_{\text{transition}}$ - which leads to the electron's ejection. Because the radius is smaller in case 5 than in case 1, we expect that in this case, electron ejection occurs occurs earlier in case 5 than in case 1, which is confirmed by the simulation results in figure D.5. In addition, v_y of the electrons is determined by space charge effects (when the ions are closer together, collisions of an electron swept through the ion cluster occur more frequently and result in higher velocities), it is expected that v_y of the electrons will increase in case 5 compared to case 1, which is indeed confirmed in D.5.

The higher density leads to higher ion energies, because the smaller distance between the ions leads to a stronger expansion. By using section 5.1.1, we expect that the higher density of case 5 results in a 30 % increase in maximum ion velocity in case 5 compared to case 1. This corresponds to our simulation results, which indicate a 33 % increase in maximum ion velocity due to the higher density. Due to the higher density, the ion repulsion is stronger, resulting in a faster ion expansion dynamics. Hence, the Mie time is expected to decrease by a factor of $\sqrt{5}$ to 32 fs, which implies that it is expected that the cluster ions are fully accelerated within 90-160 fs as is confirmed in figure D.5. The general dynamics of a Coulomb explosion (rapid acceleration of the ions until a constant velocity is reached, resulting in a linear expansion of the cluster) is the same for case 1 and 5.

2.3 Conclusion and outlook

From this chapter we can conclude that the laser-cluster interaction can be divided in three sequential processes: internal field ionisation (the field perturbs the Coulomb potential, allowing the bound electron to escape), electron ejection (freed electrons are ejected from the cluster - and stay ejected from the cluster) and cluster expansion (because a portion of the electrons is freed from the cluster, a charge builds up in the cluster leading to a cluster expansion and acceleration of the ions). When almost all electrons are ejected from the cluster, only the Coulomb explosion of the cluster has to be taken into account to predict the ion cloud expansion dynamics: the precise interaction of the laser with the cluster affects the ion expansion dynamics negligibly in this case.

However, this is not sufficient for a general laser-cluster interaction case, where all three processes have to be taken into account. Whether all electrons are ejected from the cluster depends on the electron ejection process. This involves understanding and quantifying the interplay of the retaining force by the ion cloud on the electron cloud and the ejecting laser force on the electron cloud and understanding charged particle trajectories in a plane wave laser field, which is studied in chapter 4. The inner field ionisation process might affect the electron ejection process. Therefore, the time and time interval in which ionisation occurs has to be predicted, which involves understanding and quantifying field ionisation - which is discussed in chapter 3. The Coulomb expansion model works well for fully stripped, homogeneous, one specie clusters. For general clusters with multiple ion species, density gradients a generalisation of the standard Coulomb expansion is required. Additionally, when a significant amount of electrons is still inside the cluster, the electron and ion expansion dynamics have to be taken into account self-consistently and a different type of expansion model is required. These two expansion models will be discussed in chapter 5. This chapter and the detailed study of the separate processes in chapters 3 to 5 conclude our process-based laser-cluster interaction model.

Chapter 3

Internal field ionisation

Please note that in this section atomic units are used. In atomic units the electron mass m_e, electron charge e, reduced plank's constant $\hbar$ and the Coulomb constant $\frac{1}{4\pi\epsilon_0}$ are defined as 1 (dimensionless): $m_e = e = \hbar = \frac{1}{4\pi\epsilon_0} = 1$. Making the units of the atomic constant dimensionless, has a large impact on the physical meaning of units. Using atomic units in atomic physics is common practice and a conversion table to SI units is provided in appendix A.4.

Internal field ionisation is the process in laser-cluster interaction where the laser field perturbs the Coulomb potential and frees the bound electron from an atom/ion in the cluster, transforming the atomic cluster into a nano-plasma. Hence, field ionisation sets the initial conditions of the electromagnetic interaction between the laser, the electrons and the ions. Therefore, in order to understand laser-single cluster interaction, it is important to understand why, how and when the bound electron is freed by the laser field.

In order to understand the effect of field ionisation in laser-cluster interaction, the field ionisation of a single atom has to be investigated. An overview of the theory of field ionisation is provided in section 3.1, where it is explained that field ionisation (when the laser pulse is approximated as a quasi-static electric field) can be treated classically - leading to a deterministic theory (Barrier Suppression Ionisation - BSI) and quantum-mechanically - leading to a probabilistic theory (Ammosov - Delone - Krainov (ADK) tunnelling theory). The difference between these two approaches for the ionisation of hydrogen and deuterium is discussed in , where it is explained how ADK is implemented in particle tracer simulations and where it is shown under which circumstances probabilistic ionisation has to be taken into account.

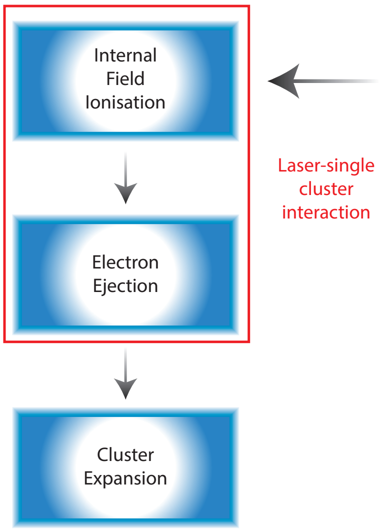

Figure 3.1: A schematic overview of the laser-cluster interaction model.

Applying this information on clusters, it is investigated how ionisation can affect the total laser-cluster interaction process in section 3.3. Here it is shown that the clusters can be divided in two categories: low-Z clusters, whose atoms are fully ionised by the laser pulse and high-Z clusters, whose atoms are not fully ionised by the laser pulse. In the case of low-Z clusters field ionisation does not influence the subsequent stages of laser-cluster interaction. Whereas, in the case of high-Z clusters, it will be shown that higher charge states are obtained by field ionisation than can be expected from the laser field alone, which implies that the electric field generated by the space charges amplifies the laser field - leading to higher ionisation stages. The field generated by the space charges depends on the electron dynamics in the cluster during the laser pulse irradiation - which is governed by the electron ejection process (see chapter 4): therefore the electron ejection process and the field ionisation process operate synergistically.

3.1 Field ionisation theory

In this section we will explain the basics of field ionisation theory adopted from: [41, 40, 38, 39, 47, 62, 63, 64, 65, 44, 45, 43, 42, 43, 66, 58].

Field ionisation theory is an active field of research. There is much debate about the applicability of the available theories. The goal of this section is to provide a background on field ionisation theory: which main approaches there are; the physics of these approaches and their limits.

Field ionisation generally can be divided in two mechanisms: quasi-static ionisation and multi-photon ionisation. In ultrashort, intense laser pulses, the electron movement is fast compared to the laser oscillation due to the strong electric field. In that case, the electric *field* of the laser can be approximated as a *quasi-static electric field* (QSE) (neglecting magnetic field effects). In this case, the laser pulse field perturbs the Coulomb potential, causing ionisation. Quasi-static ionisation is distinctly different from multi-photon ionisation, where ionisation takes place due to the high energy *photons*.

3.1.1 Barrier Suppression Ionisation

The simplest model for QSE field ionisation is the Barrier Suppression Ionisation model (BSI). In the BSI model the perturbation of the Coulomb potential, as indicated in figure 3.2, is treated classically. The perturbation is assumed to only affect the Coulomb potential in the polarization direction of the electric field - leading to a 1D model. In this classical model, ionisation occurs instantly when the perturbation is large enough to bend the potential barrier below the ionisation energy as indicated in figure 3.2, where BSI occurs at an electric field of $2E$. The critical electric field strength for BSI is presented in equation 3.1, in which E_z is the ionisation energy and Z is the atom/ion charge.

$$E_{\min} = \frac{E_z^2}{4(Z+1)} \tag{3.1}$$

In laser-gas irradiation experiments, BSI has been proven to give an accurate, practical and simple prediction of the resulting charge states for [67, 38]. In the case of hydrogen, it is argued that the 1D BSI model has to be adapted [38], because field perturbation affects the Coulomb potential in the perpendicular direction as well - due to the symmetry of the hydrogen wavefunction (which is broken in many-electron systems), resulting in an adopted BSI of: $E^H_{\min} = (\sqrt{2}-1)E_z^{3/2}$ for hydrogen, which is an increase of the prediction of equation 3.1.

3.1.2 Tunnelling ionisation

BSI theory is a *deterministic* field ionisation theory: field ionisation occurs instantly after the critical field strength is reached. In contrast, the field ionisation problem can also be treated quantum mechanically: in that case there is a *probability* $\frac{dW}{dt}$ the electron can escape the potential barrier by tunnelling through the red sketched area in figure 3.2. This probabilistic, *tunnelling ionisation (TI)* behaviour is confirmed experimentally [62, 47]. In this case, ionisation can occur before the BSI intensity is reached. However, the ionisation probability becomes exponentially larger when the distance to tunnel becomes smaller [68, 69, 64] - and the ionisation probability is much larger close to the BSI threshold.

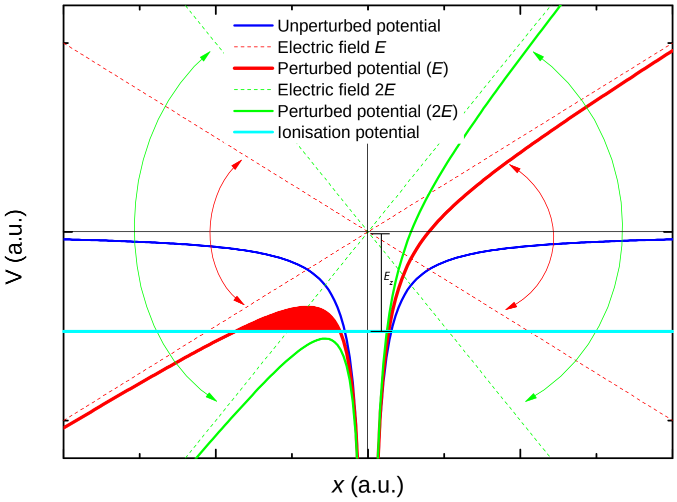

Figure 3.2: Visualisation of the perturbation of the potential in the quasi-static domain.

Landau tunnelling model One of the first tunnelling ionisation models was derived by Landau [64] for hydrogen atoms in static (instead of quasi-static) electric fields (derivation in appendix C.1.5). The Landau rate is derived by approximating the perturbed wavefunction of the hydrogen atom by using the Wentzel - Kramers - Brillouin (WKB) approximation, which assumes that the wavefunction is slowly changing. This results in a probability current, which is integrated to obtain the tunnelling probability per time, resulting in equation 3.2. The exponential behaviour in equation 3.2, is the same for all tunnelling ionisation models (and only pre-factor changes).

$$\frac{dW}{dt} = \frac{4}{E}\exp(-\frac{2(2E_z)^{3/2}}{3E}) \tag{3.2}$$

Perelomov, Popov and Terent'ev (PPT) generalised [65] the Landau model for multiple-electron atoms and time-varying electric (but QSE) fields. The derivation of this model is provided in appendix C.1. The PPT model can be used to investigate general ionisation stages for time-varying electric fields because the time-dependent interaction of the electron with the ionic core is taken into account as a correction term. Additionally, a generalised wavefunction for the electron is used, which requires the determination of an asymptotic atomic constant, which are only limitedly available [70, 44] (see appendix C.1).

Ammosov, Delone, Krainov (ADK) tunnelling model The Ammosov, Delone, Krainov (ADK) [63] tunnelling model (the most popular tunnelling ionisation model [59, 58, 71, 44]) uses Hartree's method [72] in order to determine these constants and create a more generally applicable form of PPT, which is explained in appendix C.1 and results in equation 3.3. The exponential behaviour of ADK is the same as the Landau tunnelling model - but with a different pre-factor. The term $(\frac{2\kappa^3}{E})^{2(Z-1)/\kappa-1}$ arises from taking the interaction of the electron with the ionic core into account and the rest of the pre-factor results from using Hartree's method to approximate the electron wavefunction.

$$\begin{aligned} \frac{dW}{dt} &= \frac{\kappa^2}{\sqrt{36\pi n^\star}}(\frac{2e}{n^\star})^{n^\star}(\frac{2\kappa^3}{E})^{2Q/\kappa-1}\exp(-2\kappa^3/3E) \\ \kappa &= \sqrt{2E_z} \\ n^\star &= \frac{Z}{\kappa} \end{aligned} \tag{3.3}$$

We have extended the particle tracer simulations with ADK tunnelling ionisation routines. Equation 3.3 is investigated for each atom or not-fully ionised ion for each time step using a

Monte-Carlo approach. When ionisation takes place, the charge of the ion is increased by one and an electron is created in the numerical model. The electron's position is determined by using the outer end of the tunnelling distance of figure 3.2 and the electron's velocity is determined by using the theory of [73]. When ADK is applied in the particle tracer simulations, the limitations of tunnelling ionisation are checked, which is important - as these limits are often violated in literature. ADK ionisation theories have been implemented in particle-in-cell codes previously [58, 59], however, they are applied in regimes where the limitations of tunnelling ionisation theories are violated [59, 60, 61]. For more information about the implementation of ADK in the numerical particle tracer simulations, see appendix C.1.

Limitations of tunnelling ionisation theories Tunnelling ionisation theories assume a quasi-static electric field - which implies two assumptions. The first assumption is that only an electric field has been assumed, whereas a laser pulse is a plane wave field - which contains a magnetic field component. In [42, 46, 43], the magnetic field effect on the ionisation is approximated by assuming that the bound electron moves in a figure-8 motion in its binding potential due to the plane wave laser field. When the movement of the electron becomes larger than the Bohr radius in a figure-8 motion, it is assumed that magnetic field effects can have an impact on ionisation - and hence tunnelling ionisation theories no longer hold. This sets a limit on the maximum applicable laser field, as indicated in equation 3.4.

The second assumption is that the oscillation of the electric field is assumed to be quasi-static and hence ionisation takes place due to the field nature of the laser pulse. In that case, many photons are required for ionisation and the photon energy should be smaller than the ionisation potential, which sets a limit on the maximum laser frequency, indicated in equation 3.4.

$$\begin{aligned} \omega_L &< E_z \\ E_0 &< \sqrt{8c\omega_L^3} \end{aligned} \tag{3.4}$$

The previous part is based on literature work of: [41, 40, 38, 39, 47, 62, 63, 64, 65, 44, 45, 43, 42, 43, 66, 58].

3.2 When does tunnelling ionisation have to be applied?

Due to the sharp dependence of the tunnelling probability on the electric field evolution, it is expected that TI occurs almost instantly near the BSI threshold when the electric field rapidly rises in intensity and exceeds the BSI critical electric field. For a Gaussian pulse envelope, the relative slope of the envelope (in time) is larger at the edge of the laser pulse than in the centre of the laser pulse. Hence it is expected that BSI and TI have a similar behaviour when ionisation occurs at the edges of the laser pulse. However, when BSI occurs near the laser pulse centre or when the laser pulse intensity does not reach the critical BSI level, it is expected that TI and BSI obtain different results.

This qualitative description is confirmed in figure 3.3, where calculations have been performed on the ionisation of a single hydrogen/deuterium atom for four different laser pulses (Gaussian pulse envelope, $\lambda = 700$ nm) (top graph). The cumulative ionisation probability ($p(t) = \int \frac{dW}{d\tau} d\tau$) for BSI (hydrogen-corrected and "standard" hydrogen), Landau (hydrogen) and ADK (deuterium and hydrogen) are compared for these four laser pulses in the middle graph. For each laser case, 25 separate particle tracer simulations with ADK theory implemented have been performed and the time at which ionisation occurs in each simulation is presented in the lowest graph, representing the cumulative ionisation probability of the ADK ionisation implementation in the particle tracer simulations. The analytical ADK calculations of the middle graph corresponds well with the Monte-Carlo implementation of ADK in the particle tracer simulations of the lower graph. This indicates that ADK ionisation has been correctly implemented in the particle tracer simulations.

As an indication, most of the laser pulses for laser-cluster interaction have an intensity of at least 10^{20} W/m^{2}s.

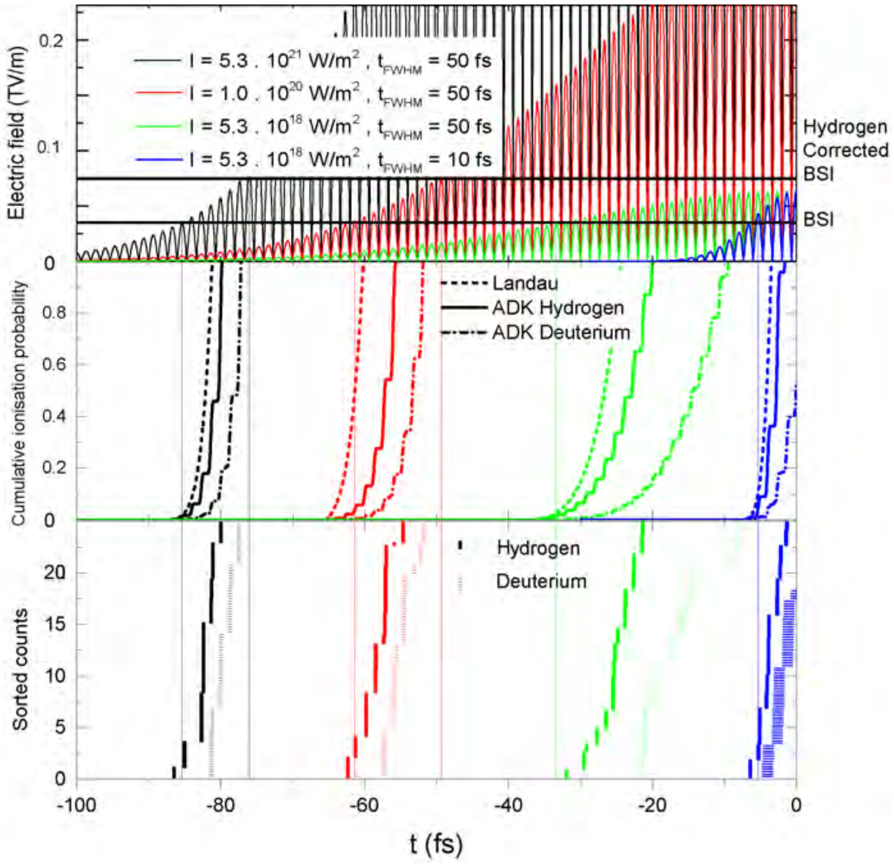

Figure 3.3: An illustration of the analytical and numerical ionisation rates of deuterium and hydrogen for various laser pulses.

As predicted, the various ionisation models converge when ionisation occurs in the edge of the laser pulse due to a higher relative slope of the pulse envelope, which results in a very short, almost instant, tunnelling time interval. When the laser pulse intensity is decreased, while the pulse duration remains the same (from black to green), ionisation occurs closer to the laser pulse maximum and the relative slope of the envelope at which ionisation occurs is flattened. This causes the various model predictions to diverge and the time interval in which tunnelling occurs is increased - showing more probabilistic behaviour. When the laser pulse duration is decreased (from green to blue), the slope at which BSI occurs of the field envelope is increased, which results in less deviation between the ionisation theories and a much shorter tunnelling time interval.

Therefore, BSI and TI predict a similar behaviour when BSI occurs at a relatively large envelope slope, whereas TI and BSI obtain different results when the laser pulse intensity is too low for BSI to occur and when the laser pulse envelope slope at which ionisation occurs is relatively small. In this case probabilistic TI, such as ADK, has to be used to obtain an accurate prediction for the laser-field interaction process.

3.3 The effect of field ionisation in laser-cluster interaction

With this knowledge of BSI and TI, we will investigate whether field ionisation can have an effect on the subsequent processes of laser-cluster interaction. If field ionisation would have an effect on laser-cluster interaction, it would affect the amount of electrons ejected from the cluster. Therefore, by studying the sensitivity of the electron ejection fraction in particle tracer simulations on the ionisation, we can determine how accurately ionisation should be taken into account in our simplified laser-cluster interaction model.

We will assume that the ionisation process starts at the critical (hydrogen-corrected) BSI intensity (defined as $t = 0$) and lasts a time τ, throughout which the ionisation probability is constant. By studying the effect of τ on the electron ejection fraction, we can determine how ionisation can affect the laser-cluster interaction process. In figure 3.4 we have plotted the number of electrons in the cluster as a function of time for different τ, for a cluster with: 800 hydrogen atoms, density of 5×10^{27} m^{-3}, laser wavelength $\lambda = 700$ nm, laser pulse duration $t_{\mathrm{FWHM}} = 70$ fs (Gaussian envelope) and peak electric field $E_0^{\max} = 1 \times 10^{10}$ V/m (which is close to the BSI critical value).

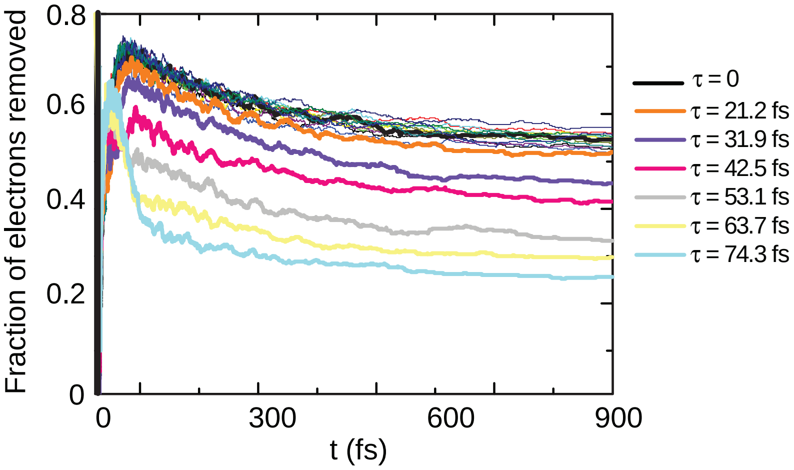

Figure 3.4: A time trace of the fraction of electrons removed for different "ionisation durations".

The electron ejection fraction rises in time until the maximum of the laser pulse has been reached at $t = 30$ fs, at which the electron ejection fraction is the highest. Afterwards some of the ejected electrons are re-absorbed by the cluster - leading to a decrease in electron ejection fraction (see chapter 4). When the tunnelling duration is up to 21.2 fs, the deviation in electron ejection fraction is negligible compared to the 5-10 % inaccuracy in the electron ejection fraction, which is indicated by the thick black, thick orange and thinner coloured lines (for which τ is in between 0 and 21.2 fs) in figure 3.4. For $\tau > 31.9$ fs onwards, the ionisation duration impacts the electron ejection fraction and therefore has an effect on the laser-cluster interaction. Therefore, we can conclude that ionisation has an effect on the sequential processes of laser-cluster interaction when ionisation is still taking place in the decaying edge of the laser pulse.

When all ionisation is completed in the leading edge of the laser pulse, field ionisation does not have an effect on electron ejection and it can be assumed that ionisation occurs instantly: which is the case when the atom is fully ionised by BSI when taking the laser field into account. This will be defined as *low-Z laser-cluster interaction*. When the cluster atoms are not full ionised according to BSI, tunnelling ionisation can still occur throughout the laser pulse and ionisation has to be taken into account accurately.

3.3.1 Ionisation in high-Z clusters

Experiments have been performed investigating the charge states of obtained by high-Z laser-cluster interaction [36, 14, 15, 1, 12, 16]. These experiments indicate that charge states of Xe^{26+} can be obtained in laser cluster interaction - whereas ionisation states of Xe^{18+} were obtained in laser gas interaction - using the same laser pulse ($I = 10^{18} W/\mathrm{cm}^2$) [16]. This indicates that when high-Z clusters interact with an ultra-short, intense laser pulse - a unique interaction occurs, resulting in extremely high charge states.

In this work, we have analysed the dynamics of high-Z clusters qualitatively using our process based model and numerically using particle tracer simulations, due to three reasons. First, obtaining high charge states from high-Z laser-cluster interaction is a unique aspect for laser-cluster interaction - and understanding the fundamental physical characteristics of laser-cluster interaction also hence also involves understanding why high charge states are obtained. Secondly, high charge states in laser-cluster interaction are caused by single cluster effects measurable in experiments. Hence high-Z cluster predictions can be directly related to experimental data. Thirdly, using a combination of high and low-Z species in clusters provides an extra degree of freedom for tuning the expansion dynamics of a single cluster.

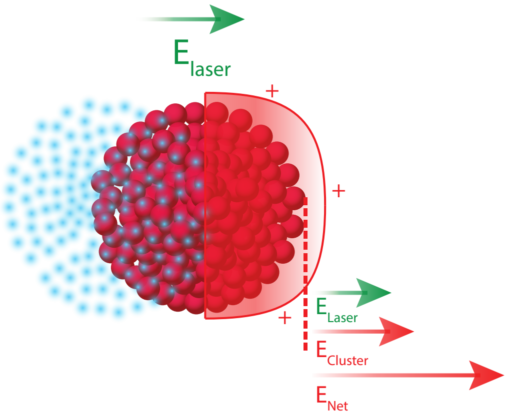

Figure 3.5: Illustration of the ignition ionisation model.

By taking only the electric field of the laser into account, it would be expected that the charge states in laser-cluster interaction are the same as those in laser-gas interaction (collisional ionisation is neglected, see appendix B). Therefore, the applied electric field on the cluster *has* to be higher than the electric field of the laser, which can only be caused by the cluster's space charge. Therefore, the laser field is enhanced by the cluster space charge. To illustrate this effect, a schematic representation is given in figure 3.5, which corresponds to the ignition model developed by [14, 15] to explain this phenomenon qualitatively. Here the cluster (a nano-plasma after the first ionisation) is represented by a rigid, static ion cloud and a rigid electron cloud, oscillating on the laser frequency through the ion cloud. When both clouds are displaced, a dipole is formed, where the electric field is amplified locally. When the charge of the cluster is sufficient, this results in a strong enhancement of the laser field, which leads to a higher ionisation probability. When ionisation occurs, the space charge of the cluster is increased and the enhancement of the laser field is even stronger, resulting in a synergistic relation between the ionisation and the space charge of the cluster - which is determined by the electron cloud's motion. In chapter 4, we will derive a more accurate model for the electron cloud's motion than provided by the ignition model, which we combine with tunnelling ionisation to create a model for high-Z clusters in section 4.2.5.

Why is it necessary to take ADK ionisation into account for high-Z clusters? Particle tracer simulations have been performed on a cluster with 500 Xenon atoms with a cluster density of 10^{27} m^{-3} with a laser pulse of $\lambda = 700$ nm, $E_0^{\text{max}} = 3.5 \times 10^{11}$ V/m and Gaussian envelope with $t_{\text{FWHM}} = 70$ fs. In the simulation, the xenon cluster obtains charge states of up to 19+ when ADK ionisation (top graph) is used, whereas charge states of 9+ are obtained when BSI is used (middle graph). In the bottom graph the laser pulse envelope is indicated and the horizontal lines indicate at which electric field ionisation is expected to occur - which would predict charge states of up to 8+.

In the ADK ionisation simulation, the amount of particles of the first line goes down and

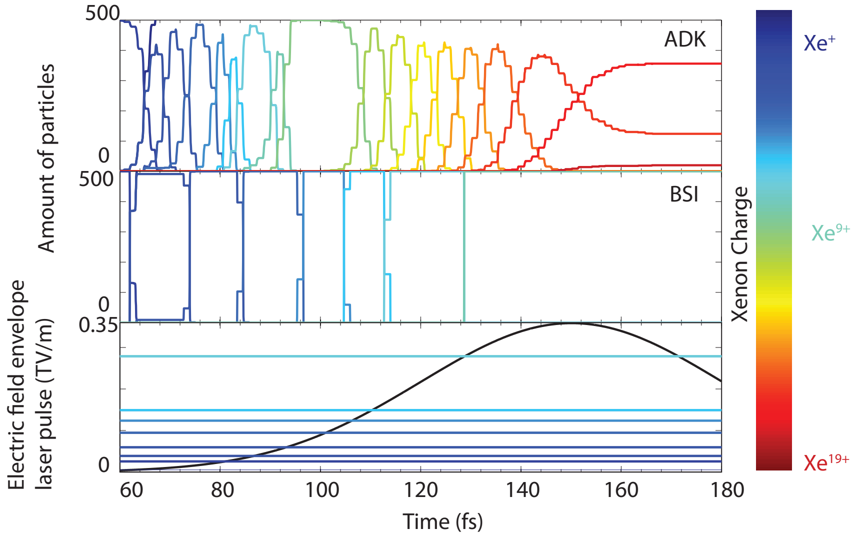

Figure 3.6: A timetrace of the amount of Xe^{A+} in particle tracer simulations of a Xenon cluster by using ADK and BSI.

the amount of particles by the second line goes up: this is where ionisation occurs: the cluster atoms are transformed from neutral (amount of neutral particles goes down) to 1+ (amount of 1+ particles goes up). This occurs sequentially until just after the laser pulse maximum, where the cluster consists out of xenon 17+, 18+ and 19+. The colour represents the charge states of the various lines, starting with dark blue for xenon atoms, to dark red for xenon 19+. A similar trend occurs in the BSI case where the transitions upon ionisation are almost instant. However, although the laser field is also enhanced by the cluster space charge in the BSI case, the ionisation in the BSI simulation in this case mostly coincides with the ionisation expected by the laser field, which results in remarkably lower charge states than in ADK simulations. The enhancement of the field strength due to the space charge depends on the cluster parameters: when a cluster is larger/more dense (contains more particles), the effect of the space charge enhancement is larger. In this case, the effect is sufficient for ADK, but insufficient for BSI, to result in a strong enhancement. As discussed previously, differences between BSI and ADK are expected to occur when ionisation does not take place fully according to BSI, which occurs (by definition of high-Z cluster) for some time during the laser cluster interaction. For these simulation parameters, this difference leads to a very large ionisation difference between ADK and BSI. Therefore, it is vital to take probabilistic tunnelling ionisation into account when analysing high-Z clusters.

3.4 Conclusion

From this study we can conclude that field ionisation for laser-cluster interaction can be separated in field ionisation in low-Z clusters (laser electric field is sufficient for full BSI of the atoms) and field ionisation in high-Z clusters. In the case of low-Z laser-cluster interaction, the effect of the field ionisation on electron ejection is negligible and therefore does not have to be taken into account. In the case of high-Z laser-cluster interaction, the cluster space charge amplifies the laser field in order to obtain very high charge states, for which it is necessary to take probabilistic tunnelling ionisation into account.

Chapter 4

Electron ejection model

The electron ejection process is the process in which the freed electrons are displaced and ejected from the cluster. For clarity we will refer to *electron ejection* as the electron being freed from the cluster, whereas we will refer to *displacement* as the distance an electron is displaced from the centre of the cluster. When ionisation occurs, a collection of ions and electrons: a nano-plasma is generated. Since the electrons are much lighter than the ions, the electrons are partly displaced by the laser field. This leads to a build-up of charges, which leads to the cluster expansion, leading to high energy ions. For now we will assume that the electron ejection process and cluster expansion process occur sequentially, which will be discussed in further detail in chapters 5.

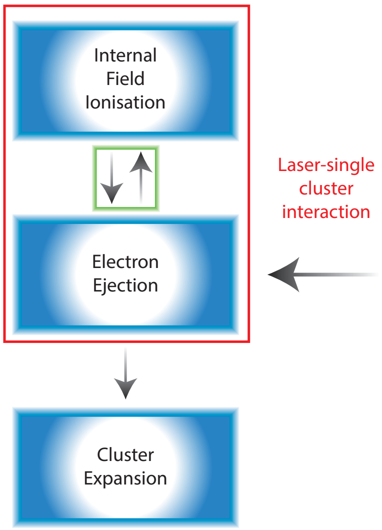

Figure 4.1: A schematic overview of the laser-cluster interaction model.

As explained in the previous chapter, for low Z clusters the field ionisation process can be assumed to occur instantaneously and the field ionisation process and electron ejection process occur sequentially. To predict the cluster expansion, the number of electrons remaining inside the cluster is required, hence obtaining the fraction of ejected electrons *after* the laser pulse is a requirement of the cluster expansion model. In contrast for high Z clusters, the field ionisation process and electron ejection process occur simultaneously - as explained in the previous chapter. Hence, also the dynamics of the electron cloud *during* the electron ejection phase should be predicted by the electron ejection model.

Although in literature it is assumed that electrons can be ejected from the cluster [74, 14, 15, 20, 75, 16], it is not trivial that a single electron can obtain a net displacement or a net acceleration by a laser field. To get more insight in how the electrons can be ejected from the cluster, the laser-charged particle interaction, which was briefly discussed in chapter 2, is studied in detail in section 4.1.1. Here it is shown that the magnetic field of the laser can lead to a net displacement of a charged particle in a laser field at sufficient laser intensities. In addition, it is shown that a charged particle can obtain a net momentum in a laser field which remains even after the laser pulse, when the electron is "injected" in the laser field under a certain laser phase. In section 4.1.1 we show that hence electrons obtain a net drift during laser-atom interaction, which is used experimentally for studying field ionisation on an atto-second timescale [47, 48, 62].

Similarly, electrons are ejected (and generally remain ejected) from a cluster, when they are displaced from the cluster - which we will show in chapter 4.2. An electron in a cluster is subjective to two forces during laser-cluster interaction: a force due to the laser action, displacing the electron from the centre and a restoring force in the opposite direction, pushing the electron to the centre due to the ion cloud space charge. When the laser electric field is sufficient, the displacement of the electron is so large that it is displaced from the cluster, leading to the electron ejection, which was discussed previously in chapter 2. In section 4.2 we create a model electron ejection based on the motion of a forced oscillator - the forced oscillator model (FOM) - which can be used to predict the number of electrons in the cluster after laser irradiation and which can be used to predict the electron dynamics during the laser irradiation. This model will be compared with numerical particle tracer simulations and models used in literature [74, 14, 15, 20, 75, 16, 53]. The FOM is more generally applicable than other models in literature and does not require the determination of anomalous constants by simulation. Therefore, the FOM is predicted to be more robust to scaling than other models (our particle tracer simulations are limited to 1500 particles, whereas in chapter 6, we will investigate clusters with 10^6 particles).

4.1 Laser-charged particle interaction

When an electron interacts with a plane wave laser field, the electron will quiver on the oscillating electric field with no net momentum gain and no net displacement. This behaviour changes when the quivering electron's motion becomes relativistic, which we indicate by using the laser strength parameter: $a = \frac{eE}{m_e \omega c}$. When the electron's motion is mildly relativistic $a = 1$, the electron is affected by the magnetic field of the laser pulse, accelerating the electron in the propagation direction of the laser; displacing the electron. In the case of super-intense laser pulses $a > 10$, this effect is strong enough to accelerate the electron to relativistically in the propagation direction. Because the laser pulse travels in the propagation direction, the electron obtains a Doppler shift, which effectively increases its oscillation period. Therefore, in the super-intense regime, the electron is displaced a relatively large distance by the laser pulse. The velocity of an electron as a function of time in the polarization (v_x) and propagation direction (x) is shown in figure 4.2a for sub-relativistic ($a = 0.1$), mildly relativistic ($a = 1$) and super-relativistic ($a = 10$) laser-electron interaction. These velocity traces have been calculated analytically by using a self derived model presented in appendix C.2. This analytical model, which does not take radiation effects into account, corresponds within 1 % of the results of particle tracer simulations: which indicates that the charged particle trajectories under an intense laser field (while neglecting radiation effects) are correctly determined by the charged particle simulations. Laser-cluster interaction studied in this thesis usually occurs at relatively high laser intensities of $I = [10^{22}...10^{25}]$ W/m^2, which corresponds to $a = [0.6...19]$. Under these conditions, the displacement of the electron due to magnetic field effects is one of the effects causing the electron ejection.

"Injection" phase effects Although magnetic field effects of the laser pulse play a role in ejecting electrons from cluster, the electron will not obtain a net momentum due to this effect. A laser-cluster interaction experiment is usually performed on a cluster jet. Therefore, when an electron is displaced from the cluster - but obtains no momentum by the laser interaction, it can be re-absorbed by another charged cluster after the laser-pulse irradiation. The Lawson-Woodward criterion states that an electron can only obtain a net momentum when one of these conditions are violated [76, 77, 78, 79]: the laser field is in vacuum with no walls or boundaries present; no static electric or magnetic fields are present; the region of interaction is infinite.

When an electron is "injected", with zero velocity ($\dot{x}(0) = 0$), in a laser field at a certain laser phase ϕ_0, the electron can obtain a drift momentum. To illustrate this, only the electric field of the laser pulse is taken into account and the spatial dependence of the laser field is neglected. In that case, the equation of motion of the electron is: $\ddot{x} = -\frac{eE_0}{m_e} \sin(\omega t + \phi_0)$, in which x is the polarization direction of the laser, E_0 is the electric field strength, m_e is the electron mass, e is the electron charge and ω_L is the frequency of the laser pulse. The velocity of the electron is: $\dot{x} = \frac{eE_0}{\omega m_e} \cos(\omega t + \phi) + v_{\text{drift}}$, in which $v_{\text{drift}} = -\frac{eE_0}{\omega m_e} \cos(\phi)$ is the drift velocity of the electron. Therefore, an electron can indeed obtain a drift velocity if it is suddenly "injected" in a laser field. Using the analytical theory in appendix C.2, the momentum (in the polarization direction) of an electron as function of time in a laser pulse with a duration of 120 fs and a Gaussian envelope is shown in figure 4.2b for three cases: injection at t=-60 fs, injection at $\phi_0 = \frac{1}{2}\pi$ (near $t \approx 0$)

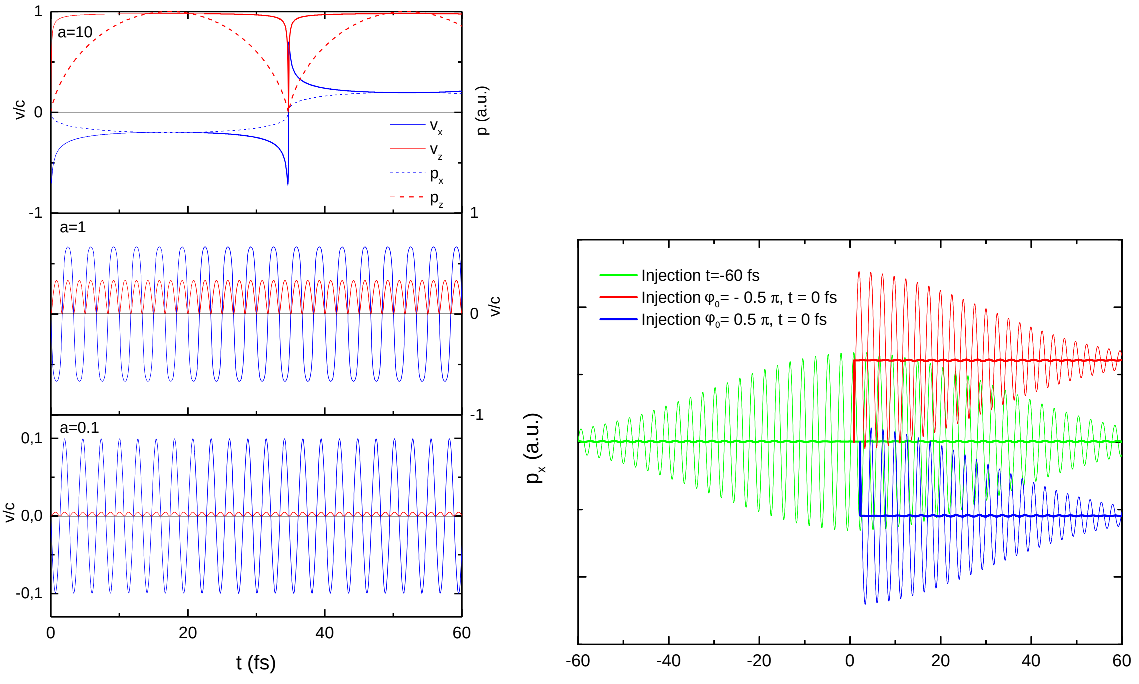

(a) The velocity of an electron in a plane wave field in the propagation direction and in the polarization direction.

(b) The momentum in the polarization direction in the case of phase injection near t=0.

Figure 4.2: Electron trajectories under laser interaction calculated by our charged particle-laser interaction model derived in section C.2.3

and injection at $\phi_0 = -\frac{1}{2}\pi$ (near $t \approx 0$). Here, the electron obtains a drift momentum when it is injected at a non-zero phase, which depends on the intensity and phase of the laser pulse at the time of injection. The reason the Lawson-Woodward theorem is violated in this case is that injecting the electron at a certain laser phase makes the region of interaction finite. In section 4.2 it will be explained that this phenomenon plays a role in the electron ejection in laser-cluster interaction.

4.1.1 Laser-atom interaction

Using the charged particle laser interaction model in combination with field ionisation theory makes it possible to study laser-atom interaction. This will prove to be an insightful model for understanding why electrons that are displaced from the cluster generally stay ejected from the cluster. In addition, our laser-atom interaction model can qualitatively explain how this effect can be used to perform measurements on field ionisation, performed in [47, 62, 48] to prove experimentally that field ionisation is a probabilistic process.

From chapter 3, it is expected that an atom in an intense laser field will at some point become ionised. At ionisation, we assume the neutral atom is transformed into a charged ion and an electron, which behave classically. Two forces work on the electron: an attracting force pulling the electron towards the positively charged ion and an expelling force due to the laser interaction. Electric field effects occur at lower velocities than magnetic field effects. Since ionisation occurs at $a << 1$ field strengths and the displacements around the ion are small, the magnetic field and spatial dependence of the field are neglected. The equation of motion (1D) of the electron is shown in equation 4.1, where the ion is assumed static and is positioned in the origin.

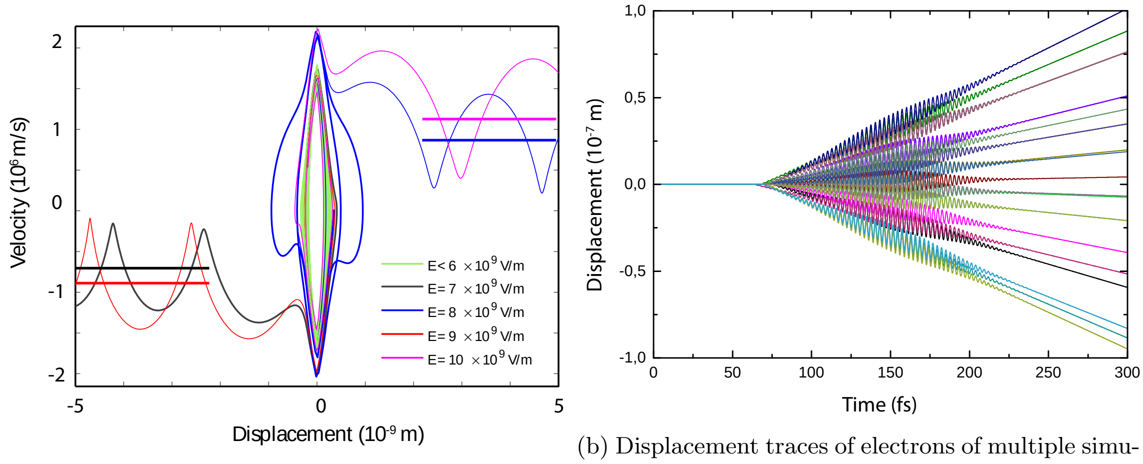

(a) Phase space trajectory plot indicating critical behaviour for $E \geq 7 \times 10^9$ V/m.

(b) Displacement traces of electrons of multiple simulations of laser-atom interaction. Each line represents a different simulation with the same parameters

Figure 4.3: Phase space trajectories and particle tracer simulation results for laser-atom interaction

$$\begin{aligned} \frac{d^2x}{dt^2} &= \frac{eE_0}{m_e} f(\omega t)\sin(\omega t) - F_{\text{Coulomb}} \\ F_{\text{Coulomb}} &= \begin{cases} \frac{1}{4\pi\epsilon_0 m_e}\frac{Ze^2}{x^2}\text{sgn}(x), & |x| > x_{\text{CutOff}} \\ \frac{1}{4\pi\epsilon_0 m_e}\frac{Ze^2}{x^2_{\text{CutOff}}}\text{sgn}(x), & |x| < x_{\text{CutOff}} \end{cases} \end{aligned} \tag{4.1}$$

The envelope of the electric field is slowly varying compared to the oscillatory behaviour of the field. Therefore, we assume the field amplitude is quasi-static $E_0 f(\omega t)\sin(\omega t) \to E_0 f(\tau)\sin(\omega t)$. In this case, equation 4.1 is that of a forced oscillator with a non-linear restoring force $F_{\text{res}} \propto \frac{1}{x^2}$ (outside the cut-off range). In order to prevent the numerical problems resulting from the singularity of the Coulomb force in the origin, a cut-off parameter has been introduced similarly to the cut-off parameter introduced in the particle tracer simulations 2.1.

The phase space map in figure 4.3a studies the trajectory of the solutions of equation 4.1 (in a displacement $(x(t))$, velocity $(x'(t)$ plane) for $\lambda = 700$ nm for various E. The initial position of the electron is comparable to the position predicted by BSI in chapter 3 with $Z = 1$. The trajectory makes a nearly closed curve for low E, which implies that the electron oscillates in the Coulomb potential. Beyond a critical E, this limit cycle becomes unstable, diverges and leads to outgoing asymptotes. At this instability, the electron is displaced far away from the Coulomb potential, hence the Coulomb restoring force becomes negligible and the electron behaves as a free particle with a drift velocity indicated by the horizontal asymptotes in figure 4.3a. Physically, this occurs because the restoring force (i.e. the Coulomb force) in equation 4.1 scales with x^{-2} and becomes weaker when the distance increases, which enhances the displacement - leading to unstable behaviour, which occurs almost instantly when the electron is displaced beyond the cut-off length. The critical electric field required for electron ejection is: $E \leq 7 \times 10^9$ V/m, which is smaller than the required field for field ionisation ($E = 2.5 \times 10^{10}$ V/m). Therefore, the electron is freed from the Coulomb potential of the ion directly after ionisation. We expect the drift velocity (indicated by the horizontal asymptotes in figure 4.3a) is obtained because the electron is "injected" in the laser field upon electron ejection, which is confirmed when we compare the drift velocity obtained in equation 4.1 with the laser-charged particle interaction model of the previous chapter by using the electron ejection moment as an "injection phase" (both models correspond within 5 %). Therefore, the drift momentum an electron obtains in laser-atom interaction is determined by the electron ejection, which is determined by the field ionisation (because the critical field required for electron ejection is lower than the field required for ionisation).

Particle tracer simulation results By using our particle tracer simulation code, which has ADK ionisation theory incorporated, we have performed 25 simulations of the laser-atom interaction with the same parameters using a laser pulse of $E_{\max} = 2 \times 10^{12} \frac{\mathrm{W}}{\mathrm{m}^2}$, $t_{\mathrm{FWHM}} = 75$ fs, $\lambda = 800$ nm. The result of these simulations is shown in figure 4.3b, where the displacement of an electron in the x direction is shown for each simulation and each separate line/colour represents a separate simulation. Since ionisation is a probabilistic process (ADK model), ionisation takes place at a slightly different time for each simulation, which leads to a spread in drift momenta. In one laser oscillation a particle can obtain a large range of drifts, but by performing statistics on this range, information from the ionisation process can be distilled. When a circular/elliptical polarized laser pulse is used, this is easier to perform, because the momentum vector by the electron corresponds to the hands of a clock operating at the laser frequency: an "attoclock". This principle has been used to measure laser-atom processes on an attosecond temporal resolution, which show that field ionisation is a probabilistic process [47, 80, 62, 48]. A similar experimental technique might be applicable to perform measurements on the electron ejection dynamics of a single cluster.

4.2 Forced oscillator model

In this section we use our understanding of the laser-atom interaction process to present a self-derived fully analytical model for the electron ejection process: the forced oscillator model (FOM). First we investigate the dynamics of a single electron in an ion cluster sphere. The ion cluster is approximated as a homogeneously charged sphere with a continuous charge distribution, neglecting discrete effects. Similarly to laser-atom interaction, two forces work on an electron in the cluster: the laser force, driving the electron and a restoring force, which is provided by the ion cloud space charge. The electric field of a homogeneously charged sphere is shown in equation 4.2, in which R is the cluster radius and ρ is the cluster charge density. This electric field leads to a linear restoring force $\propto x$ inside the cluster and a non-linear restoring force $\propto x^{-2}$ outside the cluster (similar to laser-atom interaction). The 1D dynamics of an electron under influence of these two forces leads to the model of a driven harmonic oscillator, presented in equation 4.2, in which $\omega_{\mathrm{Mie}} = \sqrt{\frac{\rho e^2}{3\epsilon_0 m_e}} = \frac{\omega_p}{\sqrt{3}}$ is the so-called Mie frequency: the "plasma frequency" [14, 15, 74, 21] of a sphere - which corresponds to the standard plasma frequency divided by $\sqrt{3}$.

$$
\begin{aligned}
E_{\mathrm{Cluster}} &= \begin{cases} \frac{\rho e^2 x}{3\epsilon_0}, & |x| < R \\ \frac{\rho R^3}{3x^2\epsilon_0}\mathrm{sgn}(x), & |x| > R \end{cases} \\
\frac{d^2x}{dt^2} &= \begin{cases} \frac{eE_0}{m_e} f(\omega t)\sin(\omega t) - \omega_{\mathrm{Mie}}^2 x & |x| < R \\ \frac{\rho R^3}{3x^2\epsilon_0}\mathrm{sgn}(x), & |x| > R \end{cases}
\end{aligned}
\tag{4.2}
$$

When an electron is displaced from the cluster, it is subjective to the r^{-2} non-linear restoring force of the ion cluster: which is the same as in the laser-atom model. This leads to unstable behaviour, resulting in the electron's ejection. This transient behaviour occurs when the electron is displaced from the cluster, indicating that the electron is ejected and obtains a drift at the moment it is displaced from the cluster. This behaviour agrees with the explanation of the simulated electron trajectories in section 2.2, where it was shown that a transition occurs from collision dominated behaviour to field dominated behaviour - leading to a net velocity. The electron drift momentum is the main reason, especially for non super-intense laser fields, why electrons that are ejected from the cluster generally stay ejected from the cluster.

The FOM and electron trajectory plots The difference between the FOM and the explanation of the electron trajectory plots in section 2.2 is that the FOM only takes the displacement in the polarization direction (x direction) into account - therefore when the electron is displaced from the cluster in the FOM model, this immediately leads to ejection. This is in contrast to the simulation results, where separate transitions in each direction are seen. First the transition occurs in the x direction of the laser, after which the electron's movement is determined by the laser field in the x direction and the electron obtains a net momentum ("injection" phase effect) in the x direction. When the *net* displacement of the electron due to this momentum is large enough to be displaced from the cluster in the x direction *throughout a laser oscillation*, it is ejected from the cluster. Hence there is essentially a delay between the instantaneous displacement of the electron from the cluster *during* a laser pulse oscillation and the ejection of the electron from the cluster, which is not taken into account in the FOM.

4.2.1 Quantitative forced oscillator model

As explained in the beginning of this chapter, we require a model for the electron ejection that can:

1. Predict the *amount* of electrons in the cluster *after* the cluster irradiation (required for determining the cluster's expansion).
2. The electron ejection model should be general enough to be scalable to large clusters (our particle tracer simulations are limited to 1500 particles, whereas in chapter 6, we will investigate clusters with 10^6 particles). In addition it should be fully analytical.
3. Predict the *dynamics of the electron cloud* (required for integrating the field ionisation and electron ejection models for high-Z laser-cluster interaction). Ionisation in high-Z clusters will be discussed in section 4.2.5.

Assumptions When the cluster is ionised, a nano-plasma of static ions and light, mobile electrons is created. The movement of a single electron in the ion cloud is described by a driven oscillator in equation 4.2. We will use this model to describe the motion of the electron cloud in the cluster. Once an electron of the electron cloud is displaced from the cluster - we will assume it remains ejected from the cluster. However, our simulations show that some electrons can be re-absorbed by the cluster after ejection when the laser pulse intensity decreases after the laser pulse maximum in time. Hence, this model is expected to over-estimate the electron ejection fraction. Additionally we will assume:

- The electron and ion cloud can be described by a continuous, homogeneous, spherical charge distribution - neglecting the fact that electrons and ions are point charges
- The ion cloud remains rigid and static. The electron cloud remains rigid and undergoes the same behaviour as a single electron in the cluster starting at the cluster's center. A similar approach has been adopted in literature for the ignition field model [15, 14] and for the collective model [20, 14]. This can be assumed, because the electrons adapt to the ion distribution - spreading through the cluster in order to minimise their energy
- Because the electron cloud is assumed to remain static the thermal evaporation of electrons from the cluster is neglected. When the electrons and ions are initialised - effectively a system is formed which has an electrostatic energy, which is - in time - converted to a thermal distribution of the electrons. The electron temperature of the nano-sphere plasma leads to the evaporation of electrons from the surface (thermionic emission). This effect becomes important when "cold" emission of the electrons due to the electric field is smaller than 20 %. In that case the electron cloud is no longer rigid and around 10-20 % of the electrons will evaporate from the cluster. [21, 14]
- The magnetic field effect of the laser is neglected, because it is assumed that the velocity of the electrons in the electron cloud is sub-relativistic.
- The charge distribution is homogeneous, therefore the model of a harmonic forced oscillator is valid for an electron in the ion cluster.

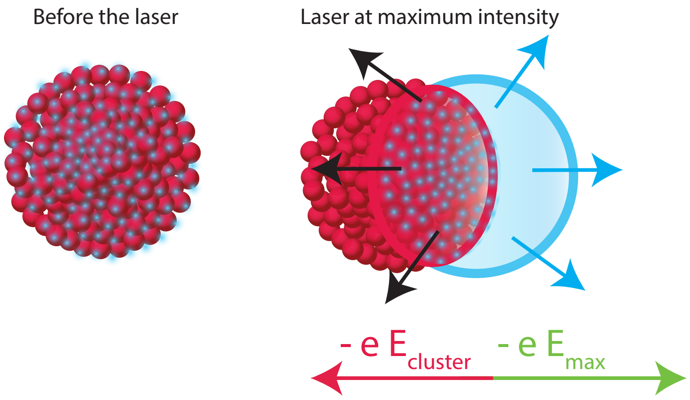

Figure 4.4: Schematic overview of the forced oscillator model for determining how many electrons are ejected from a cluster after laser-cluster interaction.

Deriving the FOM The equation of motion of the centre of the electron cloud is the same as the equation of motion of a single electron (equation 4.2) for $|x| < R$: the restoring force by the cluster is linear, resulting in the equation of a harmonic forced oscillator. The solution of a forced harmonic oscillator results in a periodic motion at the driving frequency with amplitude A [81]. When the rigid electron cloud oscillates through the immobile ion cloud, at some point a portion of the electron sphere does not overlap with the ion sphere - as indicated in figure 4.4. We assume that the electrons in this part of the electron sphere are ejected from the cluster (because they are displaced from the cluster). Therefore, the amount of electrons ejected from the cluster can be calculated by determining the part of the electron sphere which no longer overlaps with the cluster, which is essentially the volume of a sphere-sphere intersection, which is shown in figure 4.4.

The volume of the overlap of two spheres (with radius R), which are a distance d apart is $V = \frac{4\pi R^3}{3}\pi(1 + \frac{1}{4}\frac{d}{R})(1 - \frac{1}{2}\frac{d}{R})^2$. For simplicity, we will define $\xi = \frac{d}{R}$. The overlap between the clusters will be less when ξ is larger. When $\xi = 0$, the electron and ion cloud overlap perfectly and when $\xi > 2R$ there will be no overlap. By using the amplitude of electron sphere oscillation as the displacement of the electron sphere ($A = d$), the fraction of overlap between the electron and ion sphere can be determined, which corresponds to the fraction of electrons that *remain* in the cluster f. Because the amount of electrons *ejected* becomes larger for a higher electric field strength, we will use the *electron ejection fraction*: $\eta = 1 - f$.

When the laser is at its peak amplitude E_0 the displacement of the electron cloud is the largest and the largest electron ejection fraction is achieved. Since we assume ejected electrons remain ejected, η evaluated at the laser's peak intensity corresponds to the electron ejection fraction *after* the laser pulse irradiation, which depends on laser parameters (E_0 and ω_L) and cluster parameters (ρ and R). The cluster is fully stripped when $d = 2R$, which corresponds to a laser electric field of E_0^{ejection} in equation 4.3.

$$\begin{aligned} \xi(R, \rho, E_0, \omega_L) &= \frac{eE_0}{Rm_e}\frac{1}{|\omega_{\text{Mie}}^2 - \omega_L^2|} \\ \eta(\xi) &= 1 - (1 + \frac{1}{4}\xi)(1 - \frac{1}{2}\xi)^2 \\ E_0^{\text{ejection}} &= \frac{2m_e}{e}R|\frac{\rho e^2}{3\epsilon_0 m_E} - \omega_L^2| \end{aligned} \tag{4.3}$$

Validation and verification In order to verify the forced oscillator model, we will study special cases of the forced oscillator model in section 4.2.3 and compare these with literature. We will show the FOM prediction corresponds to literature predictions in several special cases, which indicates the FOM is more generally applicable than most theoretical models (which are limited to one special case). In section 4.2.4 we have compared the FOM electron ejection predictions with particle tracer simulation results, which indicate that the FOM is applicable in a large regime of laser-cluster interaction parameters and can be used as an upper limit estimation for the electron ejection fraction (up to 15 % overestimation).

In summary, the FOM can predict the amount of electrons inside a cluster after the laser pulse and describe the dynamics of the electron cloud in the cluster during the laser pulse. It treats the electron cloud, under action of an oscillating force from the laser and an attracting force from the ion cloud, as an harmonic oscillator. When an electron is displaced from the cluster during this oscillation, it is ejected from the cluster. At the maximum electron cloud displacement, this results in the electron ejection fraction.

4.2.2 Forced oscillator model and peaked density clusters

We have argued that our simplified model for laser-cluster interaction should be general enough to take clusters with density gradients into account, whereas in the FOM it has been assumed that each cluster has a homogeneous density. We will show in chapter 6 that single cluster fusion can be obtained by deuterium clusters with a peaked density in the centre of the cluster. In order to determine the electron ejection process in such a cluster, we will describe these peaked density clusters as a cluster with a high homogeneous density in the centre and an edge with a decaying density. In this decaying edge, the restoring force by the ion cluster is less than linear - representing a softening spring [81]. Hence an oscillator model is formed with a linear restoring force in the center (represented by the FOM) and an oscillator with a softening spring in the decaying edge. The forced oscillation of a softening spring is unstable [81], which means that an electron would experience a restoring force by a "decreasing spring constant" upon displacement in the decaying edge, therefore leading to the electron's ejection. This is similar to the $\propto r^{-2}$ force an electron experiences outside the cluster, which leads to the electron's ejection. Hence, in a crude approximation, a peaked density cluster can be approximated (concerning the electron ejection), by treating the high density core as a homogeneous density cluster and applying the FOM only to the core.

4.2.3 Special cases of the forced oscillator model

Quasi-static approximation When the density of the cluster is high, the Mie frequency can be much higher than the laser frequency $\omega_L << \omega_{\text{Mie}}$ and the amplitude of the displacement of the electron cloud is the same as in the case of a static electric field. In this case: $\xi = \frac{3\epsilon_0}{e}\frac{E_0}{\rho R} \rightarrow \eta \propto \frac{E}{\rho R}$. This implies that: when the electric field is larger, the electron cloud experiences a stronger force and obtains a larger amplitude, leading to more ejected electrons; when the charge density of the cluster becomes higher, the retaining force becomes larger, lowering the electron amplitude and leading to less ejected electrons; when the radius of the cluster becomes larger, the electrons have to be expelled a larger distance in order to escape, which leads to less electrons ejected.

This $\eta \propto \frac{E}{\rho R}$ behaviour is also predicted by the CBSI model [16] and single-particle model [14], where the laser field is treated as a quasi-static distortion on the potential barrier formed by the electrons (similarly to the classic BSI model for field ionisation in chapter 3). These models state: $\eta = \alpha\frac{E}{\rho R}$, where α is often an anomalous constant obtained using simulations [16, 26] or is only valid in a limited regime [14]. When the laser frequency is larger than or approaches the Mie frequency, these models start to fail, because the field oscillation is not taken into account, which is confirmed by using particle tracer simulations in the next section.

Resonance effects In the case $\omega_{\text{Mie}} \approx \omega_L$, the laser field is driving the electron cloud at resonance and the excursion of the electron cloud becomes very large ($A \rightarrow \infty$), which occurs at a cluster density of: $\omega_L = \omega_{\text{Mie}} \rightarrow \rho = \frac{3\epsilon_0 m_e}{e^2}\omega_L^2$. In this limit case, the energy transmission of the laser to the electron cloud is enhanced and the forced oscillator model predicts that the electron

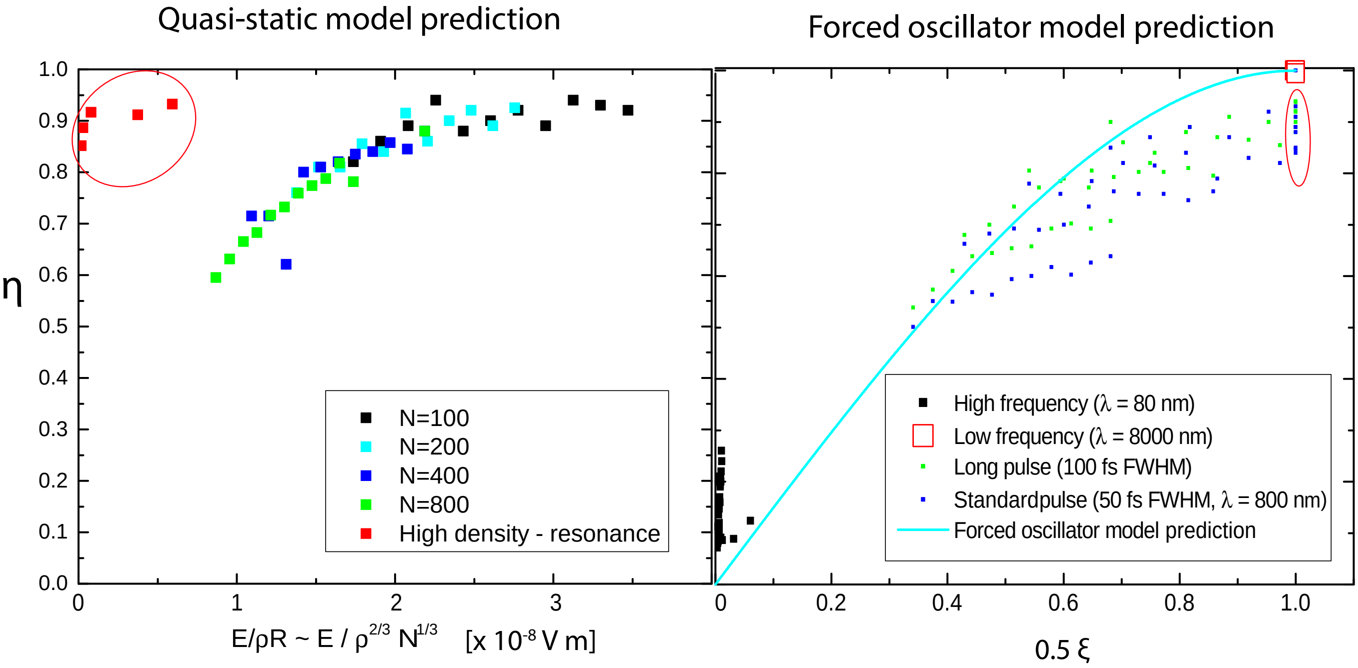

Figure 4.5: Fraction of electrons removed predicted by the quasi-static model and forced oscillator model compared to numerical particle tracer results.

cloud is instantly displaced from the cluster, which is also predicted in [20] and an increase in η is confirmed by particle tracer simulations in this case in the next section. Electron ejection is a gradual process (not all electrons are ejected at once, in contrast to theoretical predictions by [20, 12]) and the cluster starts expansion when the first electrons are ejected, lowing the cluster density - which leads to a decrease in Mie frequency. Therefore, when the initial Mie frequency is just larger than the laser frequency, resonance can still occur, which was confirmed using hydrodynamics simulations in [33]. In our process-based model, we have assumed electron ejection and cluster expansion are sequential and hence we do not take these effects into account. Nevertheless, it is possible in future work, as will be described in chapter 5 and discussed in the discussion, to integrate the electron ejection and cluster expansion in our process-based model, which would allow us to take such effects into account.

4.2.4 Comparisons of the forced oscillator model with particle tracer simulations

As part of the validation of the forced oscillator model, we compare the predictions by the FOM with particle tracer simulations. have been compared with particle tracer simulation results. At the moment, there is no experimental data on electron ejection fractions and hence a comparison with experiments is impossible. In these simulations, the full laser-cluster interaction process is taken into account by starting with a spherical cluster where atoms are randomly initialised. ADK ionisation theory is used for the field ionisation. The particle tracer simulation technique is described in section 2.1.

Quasi-static model The fraction of ejected electrons predicted by the quasi-static model for laser parameters ($\lambda = 800$ nm,$t_{\mathrm{FWHM}} = 50$ fs) has been compared with particle tracer simulations in the left figure of 4.5. The density, radius and amount of particles in the simulations are related and we choose to vary the density and amount of particles in the simulations. In this study, the $\eta = \alpha\frac{E}{\rho R}$ scaling holds when the density of the clusters is not changed drastically. According to this scaling, at a higher density it is expected that the fraction of ejected electrons is decreased, whereas the simulations indicate an increase in ejection fraction: contradicting the quasi-static prediction.

Resonance in the FOM In the right figure of 4.5 the fraction of electrons ejected in various simulations (each point represents a separate simulation) is plot versus $\frac{1}{2}\xi$ in equation 4.3. The reason we plot η against $\frac{1}{2}\xi$ is that all electrons are displaced from the cluster according to FOM when $\frac{1}{2}\xi > 1$. For clarity, all points for which $\frac{1}{2}\xi > 1$ are translated to $\frac{1}{2}\xi = 1$. The blue line represents the FOM prediction. The inaccuracy of electron ejection fraction of the particle tracer simulations (by using the same input parameters) is 5-10 %. In the simulations, the density, amount of particles and electric field have been varied for each laser pulse case: $\rho = [10^{27}...10^{30}]$ m^{-3}, $N = [100...1200]$ and $E = [10^{10}...10^{11}]$ V/m. The high density simulations in the left figure (quasi-static prediction), at which resonance occurs correspond to the simulations surrounded by the red ellipse in the right figure (FOM). Therefore, particle tracer simulations show that these resonance effects are correctly predicted by the FOM.

Effect of the laser pulse frequency By the FOM it is predicted that η depends on ω_L. Hence, four different laser pulses with an extraordinary deviation in ω_L are used in the simulation to test this behaviour. In figure 4.5 it is confirmed that η depends on ω_L: when $\lambda = 8000$ nm, $\eta = 1$ for each simulation, for $\lambda = 800$ nm $\eta = [0.5...0.95]$ and for $\lambda = 80$ nm, $\eta = [0.1...0.25]$. However, $\lambda = 80$ nm and $\lambda = 8000$ nm violate the assumptions of the ADK theory of field ionisation in section 3. Nevertheless, for low-Z laser-cluster interaction, the electron ejection is insensitive to the ionisation dynamics as explained in chapter 3 (the same electron ejection fractions are obtained in the simulations when assuming a nano-plasma from the start and neglecting the ionisation process). The FOM predicts a low η in the case of low laser frequency, which is also indicated in the particle tracer results and agrees with simulations in [75]. However, the simulated η is in between $\eta = [0.1...0.3]$, whereas the FOM predicts a lower electron ejection fraction of $\eta = [0...0.1]$. This deviation was expected, because in the FOM it is assumed that the electron cloud is rigid, whereas in the case of low η thermionic emission is a dominant effect compared to field emission [14, 21].

The FOM compared to particle tracer simulations The standard pulse and long pulse simulations form a wide scatter of points, which corresponds with the forced oscillator model as upper limit reasonably well. As long as the laser envelope evolution is quasi-static compared to the laser oscillation, the FOM predicts the electron ejection does not depend on the laser pulse duration. This agrees with the particle tracer results, as there is no structural difference between the long and standard laser pulse. Although for some cases with the same cluster parameters (but varying electric field), η for long pulses is structurally higher. In addition, there is a vertical scatter in the simulation results of the long and standard laser pulse of up to 20 %. A part of this scatter is caused by the inaccuracy in the simulations, which is around 5 - 10 %. Another effect is that it is assumed that all electrons are expelled from the cluster, whereas some electrons can be re-absorbed by the cluster after they are expelled.

In order to illustrate this effect, η is compared with the FOM prediction as a function of time for three different simulations around $\frac{1}{2}\xi = 0.7 \pm 0.05$ (in which the electric field, amount of particles and pulse duration varies) in figure 4.6, where the FOM predicts a similar electron ejection fraction. In these time traces of the electron ejection fraction in the simulations, η rises until the maximum laser intensity at $t = 0$, after which η decreases - meaning that some electrons are re-absorbed by the cluster when the laser intensity decreases ($t > 0$). The scatter between maximum η of the three cases is larger than the scatter of η after the laser pulse. Therefore, a part of the scatter in figure 4.5 is caused by a difference in electron re-absorption by the cluster. This also explains why in certain cases the long laser pulse can lead to a larger electron ejection fraction (less electrons are reabsorbed). The amount of scatter might be reduced by predicting the amount of reabsorbed electrons, which is related to the delay between electron displacement from

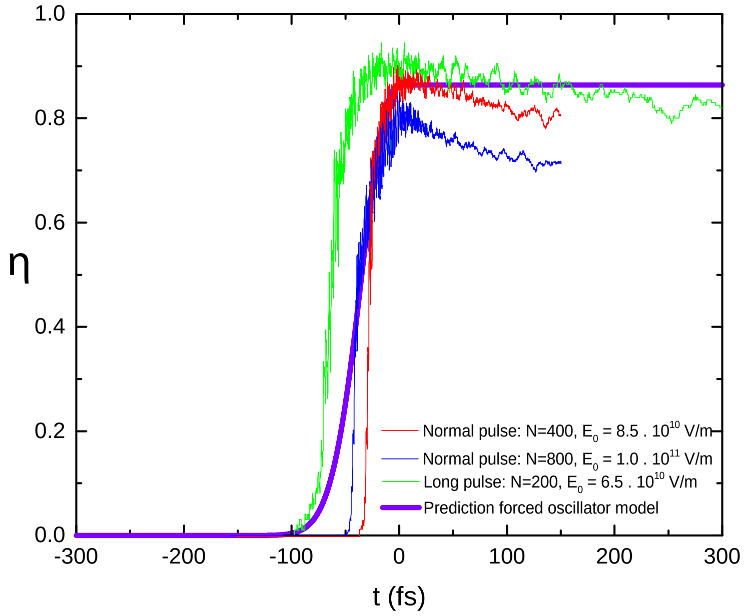

Figure 4.6: Time trace of the fraction of electrons removed of 3 different simulations for which $2\xi \approx 0.7$.

the cluster and electron ejection, discussed in section 4.2. This delay is not taken into account by the FOM (when this delay is shorter, we expect the FOM is more accurate).

In conclusion, the FOM corresponds to the particle tracer simulations well as an upper estimate. The particle tracer simulation results can be up to 15 % lower than the FOM prediction. This deviation is caused by electrons being reabsorbed after the maximum laser intensity. The FOM indicates that the electron ejection depends on the laser frequency, which is confirmed by the particle tracer simulations. Furthermore, the FOM takes resonance effects accurately into account.

4.2.5 Electron ejection in high-Z clusters

The aim of this section is to show how a high-Z model can be constructed using our process-based model. This picture is sufficient for understanding how high charge states can be obtained by clusters. However, the quantitative high-Z model requires the integration of the electron ejection model and the field ionisation model, which is beyond the scope of this thesis and remains as future work. As explained in the previous chapter, the high charge species obtained in laser-cluster interaction is a result of an avalanche effect between the field ionisation dynamics (for which the ADK tunnelling model is used) and the electron ejection model. In this chapter we provide a physical description of the integrated ADK - FOM model for high-Z clusters and its assumptions, in appendix C.2, more details about the calculation are provided.

In the electron ejection model for high-Z clusters, it is assumed that the amount of electrons inside the cluster $N_e(t)$ is distributed homogeneously across that part of the oscillating electron cloud, which overlaps with the ion cloud. The overlapping volume $V(d(t))$, is characterised by the distance between the electron and ion sphere $d(t)$ - which is provided by the solution of the FOM. Therefore, when the electric field of the laser is zero during the laser oscillation, the ion and electron cloud fully overlap ($d(t) = 0$) and the electrons spread throughout the cluster - leading to a lower electron density. At maximum displacement (peak in laser oscillation), a small part of the ion and electron cloud overlap and $N_e(t)$ is distributed over this small volume, leading to an increase in electron density. This oscillating electron cloud generates an electric field. The electric field of the electrons plus the electric field of the ions and the electric field of the laser make up the total electric field. In ADK theory, there is an ionisation probability, which depends

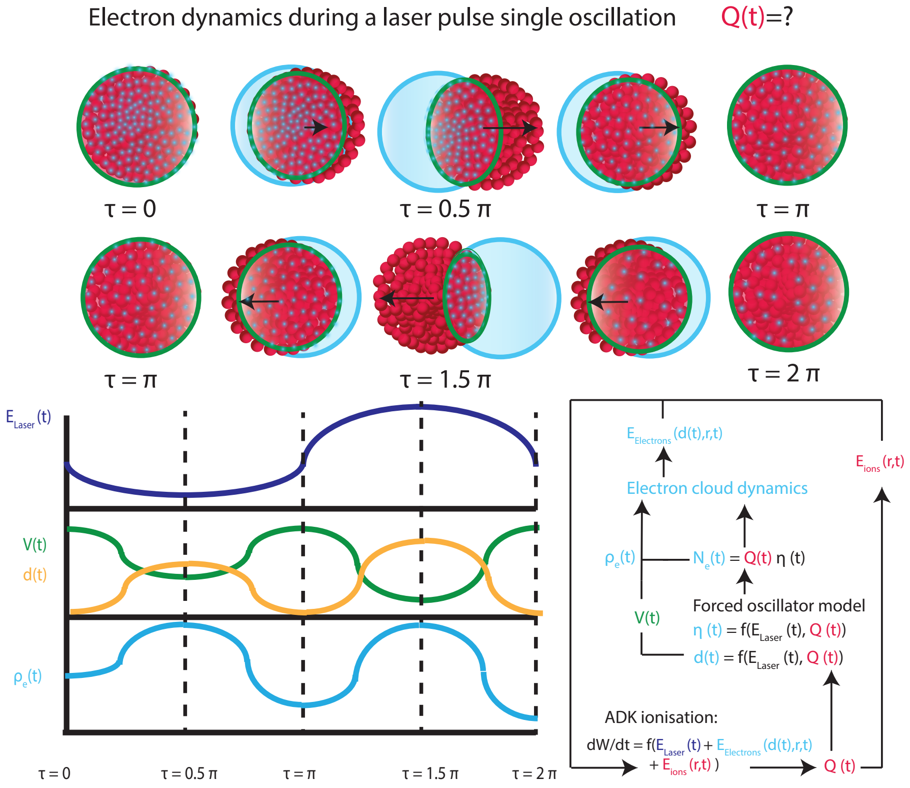

Figure 4.7: Schematic overview of the high-Z forced oscillator model.

on the electric field and atomic parameters. Hence the total electric field, which has a spatial and temporal dependence, results in additional ionisation of ions in the ion cloud. Using this spatial dependence, the ion cluster obtains a 3D charged density profile. However, in order to use the FOM for describing the electron oscillation - we have to assume the ion cluster density is homogeneous for calculating the electron cloud motion.

4.3 Conclusion

For laser-cluster interaction, the electron ejection process is of paramount importance, because it determines the subsequent ion cloud expansion, as will be shown in the next chapter. For high-Z clusters, the electron cloud dynamics during the electron ejection process becomes important for calculating the charge states of the high-Z ions, as well.

A charged particle can obtain a net displacement by a laser pulse at sufficiently high laser intensities due to magnetic field effects, which is one of the effects why an ejected electron generally stays ejected. Furthermore, a charged particle can obtain a drift when it suddenly ”appears” in a laser field, which can be used for performing attosecond measurements on the ionisation characteristics. It has been shown that an electron obtains such a drift when it is ejected from the cluster, which is one of the reason ejected electrons generally remain ejected.

By exploiting the fact that an electron is ejected from the cluster when it leaves the cluster, we derived a new analytical model for the electron ejection process, which is more generally applicable than literature models. Our simulations indicate that the model can be used as an upper limit of the amount of electrons ejected, which can deviate up to 15% with simulations.

Chapter 5

Ion cloud expansion model

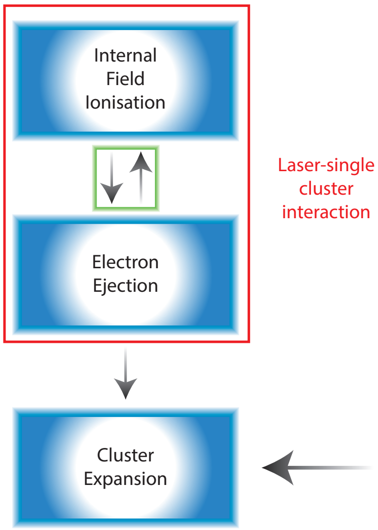

Figure 5.1: A schematic overview of the laser-cluster interaction model.

After the laser pulse irradiation, a portion of the electrons is removed from the cluster, leading to a build-up (ion charge excess) in the cluster. Therefore, the ions will repel each other, leading to the cluster's expansion. The cluster's expansion depends on the amount of electrons ejected and the cluster's parameters. Therefore, by understanding the expansion process, it is possible to control the ion density evolution and resulting ion energetics by controlling the electron ejection fraction and the cluster's parameters.

In this approach it is assumed that the ionisation process, electron ejection process and expansion process are separable, which implies that the electron ejection process should be fast compared to the ion cloud expansion process. A measure for the characteristic time of the cluster expansion is the Mie period, which is the inverse of the ion Mie frequency. According to literature and our own numerical inspection (see chapter 2), the acceleration of the ions is completed in 3-5 times the Mie period [32, 12, 14, 23]. Hence the laser pulse duration (which is a characteristic time for the electron ejection process) should be, at least, smaller than 3 times the Mie period for the processes to become separable (this approach is becomes more accurate for shorter laser pulse durations in comparison to the Mie period). When the two timescales overlap, our cluster expansion model and electron ejection model should be integrated, which we will explain in section 5.1.

Depending on the amount of electrons in the cluster, there are two entirely different limits of the ion expansion dynamics. When *all electrons are removed*, the charge-build up of the bare ion cluster is the largest, leading to a *Coulomb explosion (CE)*, resulting in *high energy ions* and a broad ion energy spectrum: the central ions obtain zero energy and the ions at the cluster radius obtain a maximum energy. Contrastingly, when *all electrons remain* inside the cluster, the light electrons (which are more mobile than the heavy ions) are thermalised (the electrostatic energy of the charge collection is transformed into kinetic energy of the electrons) and the electrons obtain a Boltzmann-like spatial distribution. Due to the kinetic energy of the electrons, a part of the electrons diffuse from the cluster, leading to a charge build-up in the cluster. The ions slowly adept to the electron distribution, also forming a thermal Boltzmann-like spatial distribution. In this case, physically the remaining electrons in the cluster remain primarily in the centre of the cluster, which leads to the expansion of the outer ions and the formation of a peaked density profile. Hence, this *ambipolar-like* expansion can be used to *control* the transformation of a homogeneous ion density profile into a central peaked ion density profile.

When calculating the ion expansion dynamics in both regimes, the main difference is that in the Coulomb case the electron dynamics can be ignored. Whereas in the ambipolar-like case the shape and dynamics of the electron distribution determine the cluster expansion and a *self-consistent model* incorporating the electron dynamics, ion dynamics and the effect of those two on each other, is required, which is presented in chapter 5.2. However, the problem of such a self-consistent model is that it only supports one ion specie with a very specific ion density profile [3, 2, 26, 53]. However, for the investigation of single-cluster fusion, the inner shells of the cluster have to collide into the outer shells of the cluster, for which either inhomogeneous density distributions or multiple specie clusters have to be used [26, 34, 3, 32, 82, 29, 27]. This requires a more general model, which we derive and present in section 5.1 for the Coulomb case.

In the analytical models, a continuous charge distribution is assumed and therefore the discrete nature of the charges is not taken into account, which can lead to deviations in cases where shock-shells occur. In order to test this approach, the predictions by the analytical models will be compared to particle tracer simulations in chapter 5.3.

5.1 Generalised Coulomb explosion model

The standard Coulomb model assumes a single specie cluster with a homogeneous density and a generalisation is necessary to support cases where single cluster fusion can occur, which also enables the study of heterogeneous clusters (multiple ion species). In addition, such a generalisation also enables the incorporation of an a priori electron dynamics model, which makes it possible to incorporate the electron ejection dynamics when the characteristic timescales of the ion expansion process and electron ejection process start overlapping.

The following part is based on literature work by [51, 55, 52, 32]

5.1.1 Standard Coulomb Model

The standard or "simple" Coulomb model is the evolution of a homogeneously charged sphere under action of its own potential in time. First the electric field of a homogeneously charged sphere is determined using the integral version of Gauss' law in equation 5.1, where r is the radial position, R is the cluster radius, ϵ_0 is the dielectric constant in vacuum and $eZ_i\rho$ is the homogeneous charge density.

$$\begin{aligned} \int\int \vec{E}\cdot\vec{dA} &= \frac{Q}{\epsilon_0} \\ \vec{E} &= \frac{eZ_i\rho r}{3\epsilon_0} \text{ for } r \leq R \\ \vec{E} &= \frac{eZ_i\rho R^3}{3r^2\epsilon_0} \text{ for } r \geq R \end{aligned} \tag{5.1}$$

For a test particle (ion) at r with charge number Z_i and mass m, the force working on that test particle is $\vec{F} = Z_i e\vec{E} \rightarrow \vec{F} = \frac{e^2Z_i^2\rho r}{3\epsilon_0} = \frac{eZ_iQ(r)}{4\pi\epsilon_0 r^2}$, in which $Q(r)$ is the enclosed charge at a position r. The motion of this particle is described by Newton's second law (assumed to be non-relativistic), which leads to equation 5.2: an equation of motion for the homogeneous ion cluster.

$$\frac{d^2r}{dt^2} = \frac{e^2Z_i^3\rho r}{3\epsilon_0 m_i} = \frac{eZ_iQ(r)}{4\pi\epsilon_0 m_i r^2} \tag{5.2}$$

The result of this equation is $r(t)$, which is the evolution of a certain begin position in time ($r_1(0) \rightarrow r_1(t)$). For a homogeneous, single specie cluster, the electric field increases radially.

An ion with a larger radius will hence obtain a larger acceleration and shock shells cannot occur ($r_1(0) > r_2(0) \rightarrow r_1(t) > r_2(t)$). Equation 5.2 leads to trajectories with a large acceleration around $t = 0$, when the charged particles are still close together. Due to the nature of the Coulomb force: $F_{\text{coulomb}} \propto r^{-2}$, this acceleration decreases rapidly when the particles are further apart, leading to a constant velocity. One important parameter for indicating how fast the expansion dynamics occur is the Mie time, which is obtained by transforming 5.2 into a dimensionless model. It takes approximately 3-5 times the Mie time for the acceleration to become effectively zero: therefore the velocity traces of the ions start with a high, linear rise, which flattens to effectively zero after approximately 5 times the Mie time, which was confirmed by our simulations in section 2.2.

Equation 5.2 implies that an ion in the middle of the cluster does not obtain any energy, because there is no enclosed space charge, whereas an ion at the edge of the cluster obtains a maximum energy. This results in a very broad ion energy spectrum, where the ion energy is determined by the radial position. This energy spectrum is indicated in equation 5.3 and is derived by converting the electrostatic energy of a charged sphere into kinetic energy - which leads to an energy distribution as function of the position. By taking into account the spherical distribution of the ions, this energy distribution as function of the radius can be transformed into an energy distribution for the ions.

$$\begin{aligned} f(\mathcal{E}_{\text{Ion}}) &= \begin{cases} \frac{3}{2}\frac{\sqrt{\mathcal{E}_{\text{Ion}}}}{(\mathcal{E}_{\text{Ion}}^{\text{Max}})^{3/2}}, & \mathcal{E}_{\text{Ion}} \leq \mathcal{E}_{\text{Ion}}^{\text{Max}} \\ 0, & \mathcal{E}_{\text{Ion}} > \mathcal{E}_{\text{Ion}}^{\text{Max}} \end{cases} \\ \mathcal{E}_{\text{Ion}}^{\text{Max}} &= \frac{4\pi e^2 Z_i^2 \rho R^2}{3\epsilon_0} = \frac{QZe}{4\pi\epsilon_0 R} \end{aligned} \tag{5.3}$$

General Coulomb Model For simplicity, equation 5.2 is rescaled into dimensionless units. The benefit of such an approach is that it provides us with a measure for the characteristic time of the expansion process: the Mie time. Furthermore, by using dimensionless units, it becomes apparent which parameters play a role in the Coulomb case cluster expansion [32, 82]. The mass is normalised to the ion mass, the length is normalised to the initial cluster radius $s = \frac{r}{R_0}$, the charge is normalised to the elementary charge ($Q \rightarrow \frac{Q}{e}$) and the time is normalised to the inverse of the ion Mie frequency, which is the ion plasma frequency in a sphere $t_0 = \frac{3M_i\epsilon_0}{\overline{\rho}Z^2e^2}$, $\tau = \frac{t}{t_0}$, in which $\overline{\rho} = \frac{\int_0^R \rho(r) r^2 dr}{\int_0^R r^2 dr}$ is the average charge density. This normalisation allows us to simplify equation 5.2 into equation 5.4 and replace ρ by $\rho(r)$, which is a radial ion density distribution, making this theory applicable to general charge density profiles. This results in the differential equation 5.4, in which $s = \frac{r}{R}$ ans $s_0 = \frac{r_0}{R}$.

$$\frac{d^2 s}{d\tau^2} = \frac{Q(s) - Q_{\text{electrons}}(s)}{s^2} \tag{5.4}$$

The previous part was based on literature work by [51, 55, 52, 32]. From this point onwards our generalisation of these models will follow.

Up until now it has been assumed that all electrons are removed from the cluster. However, this is not always the case, as we have seen in chapter 4. The forced oscillator model in chapter 4 can be used to determine the amount of electrons in the cluster and to determine the electron cloud dynamics during the cluster expansion.

In most cases, the electron ejection and Coulomb expansion process are separable. In that case, we correct the Coulomb model for the electrons shielding the ion cloud charge by correcting the cluster charge with the electron ejection fraction: $Q(s) \rightarrow \eta Q(s)$, where η is provided by the forced oscillator model of chapter 4. Here it has been assumed that the remaining electrons spread homogeneously in the cluster and that the electron dynamics can be neglected, which only holds when 30 % or less of the electrons remain in the cluster, as will be shown in section 5.3.

However, at high densities, the characteristic expansion time of the cluster is shorter and the electron dynamics might have to be taken into account. In order to take these effects into account, an a priori model for the electron cloud dynamics $Q_{\text{electrons}}(s,t)$ has to be included in equation 5.4, which can be provided by the forced oscillator model.

The Coulomb models (equations 5.4, 5.2, 5.5) are evaluated numerically by intersecting the cluster in spherical shells with radius r_i and by evaluating the evolution of these positions in time. When inner shells collide with outer shells in the general model ($r_i(t^{i,j}_{\text{col}}) = r_j(t^{i,j}_{\text{col}})$), the enclosed charge per shell changes (increased for the overtaking shell, decreased for the shell that is overtaken). Hence, $Q(r)$ should be evaluated at each time step. This numerical strategy in combination with the discretisation of the cluster in shells prevents the occurrence of singularities in the evolution of the density profile, which occur in [32], making it more straightforward to interpret the expansion dynamics results when shock shells occur.

We have generalised the model for multiple ion species in a similar way as the dimensionless approach of equation 5.4, which leads to a separate equation for each ion specie 5.4. In this equation the enclosed charge is the enclosed charge of all ion species in the cluster at a certain radius. Hence each ion specie has different expansion dynamics, which is characterised by a different Mie period per ion specie, which depends on the charge state per ion specie Z_n, the ion mass per ion specie $m_{i,n}$ and the total average cluster charge density $\rho_{av} = \frac{\sum_{i=1}^{N} \int 4\pi Z_i \rho_i(r) r^2 dr}{\int 4\pi r^2 dr}$.

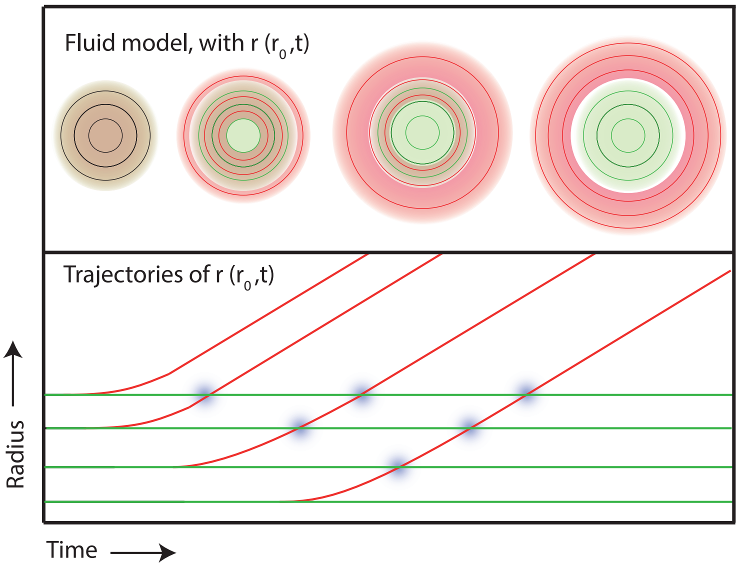

$$\frac{d^2 r_1}{d\tau_1^2} = \frac{\sum_{k=1}^{n} Q_k(r)}{r^2}$$
$$\frac{d^2 r_2}{d\tau_2^2} = \frac{\sum_{k=1}^{n} Q_k(r)}{r^2}$$
$$\frac{d^2 r_n}{d\tau_n^2} = \frac{\sum_{k=1}^{n} Q_k(r)}{r^2}$$

$$\tau_1 = t_{c,1} t = \sqrt{\frac{\rho_{av} Z_1 e^2}{3\epsilon_0 m_{i,1}}}\, t$$
$$\tau_2 = t_{c,2} t = \sqrt{\frac{\rho_{av} Z_2 e^2}{3\epsilon_0 m_{i,2}}}\, t$$
$$\tau_3 = t_{c,3} t = \sqrt{\frac{\rho_{av} Z_n e^2}{3\epsilon_0 m_{i,n}}}\, t$$

Figure 5.2: Schematic illustration of the cluster shell evolution of multiple ion species.

$$Q_{tot} = \int_0^{R_0} 4\pi r^2 dr \sum_{k=1}^{n} \rho_{i,k}^{t=0}(r) \tag{5.5}$$

Due to the differences in the characteristic expansion time of different ion species, the expansion dynamics of these different ion species are different with respect to each other, which is characterised by the ratio of their Mie periods. The ratio of the Mie periods of two ion species depends only on the mass/charge ratio of the ion species: $\alpha = \sqrt{\frac{Z}{m_i}}$, which is an important parameter quantifying the multi-species ion expansion dynamics, which corresponds to the relations presented in literature [19, 3, 34]. Because the dynamics of some ion species evolves faster than of other ion species, a homogeneous multi-specie cluster will eventually result in a layered cluster, as indicated in figure 5.2, in which each ion specie mainly constitutes a different part of the cluster. When a light (red section in figure 5.2) and heavy ion (green section in figure 5.2) specie with the same charge are mixed in a cluster and α is smaller for the light ion specie, the dynamics of the light ion specie is faster than of the heavy ion specie (its Mie period is smaller). Therefore, after some time, the light ion shells will overtake the heavy ion shells and shock shells are formed, represented by intersections of the trajectories in figure 5.2 (blue dots), which appears as separate events due to the discretisation of the shock shells. However, the cluster charge densities are modelled as continuous and hence shock shell formation is a continuous process spread over all trajectory intersections (spread over all blue dots). When the light ions overtake the heavy ions, the light ions form the outer shells of the exploding cluster, whereas the heavy ions will form the core, and the charge of the heavy ions will lead to an additional acceleration of the light ion specie (enclosed charge is increased), boosting the ion energies of the light ion specie, as indicated in figure 5.2. Therefore another important parameter quantifying multi-specie expansion is the relative amount of charge each specie contributes to the total cluster charge: $\frac{Q_i}{Q_1+Q_2+...+Q_n} = \frac{Q_i}{\sum_{k=1}^{n} Q_k(r)}$, which corresponds to literature work by [19, 3, 34]. This numerical approach makes equation 5.5 suitable for the investigation of shock-shells in multi-ion specie clusters, because there are no singularities in the density profile (in contrast to the approach of [32]) and the evolution of the shells in time can be studied (in contrast to the analytical approach of [34], which can only be used to determine the steady-state ion energy spectrum). Investing shock-shells in (multi-ion specie) clusters is a necessity for predicting the number of single cluster fusion reactions during the cluster expansion. Some practical applications of the general Coulomb expansion model (equation 5.5) will be shown in section 5.3.

Validation and verification The results of the generalised Coulomb model have been found to be in excellent agreement with the analytical "standard" Coulomb model, provided in literature [51, 55, 52, 32] in the case of homogeneous, single specie, clusters. In section 2.2 these results have been compared with particle tracer simulations and a good agreement between the two models (less than 15 % deviation) has been found. In section 5.3 we have compared the generalised Coulomb model with particle tracer simulations in the case of a heterogeneous cluster with a large difference in the α of the two ion species and a good agreement has been found. Additionally, we tested the generalised Coulomb model with peaked density profiles and a agreement of less than 20 % deviation has been found with particle tracer simulations.

5.2 Self-consistent plasma expansion model

One effect that is not taken into account in the Coulomb model is the electron density profile dynamics. When electrons remain in the cluster they eventually obtain a thermal distribution, which results in a Boltzmann-like spatial distribution. When the amount of electrons remaining in the cluster is relatively large (more than 30 % - as will be shown in section 5.3) this effect can be neglected. However, when more electrons remain inside the cluster, the electron dynamics will affect the ion expansion, which we refer to as *ambipolar-like* expansion. In this case, the ion and electron distributions affect each other, meaning that the electron and ion distributions have to be taken into account *self-consistently*, which cannot be performed by the Coulomb model, because the Coulomb model assumes an *a priori* model for the electrons. Therefore, we present a second model, which can take the ion and electron expansion dynamics into account self-consistently and can be used for all electron ejection fractions. The problem of this model is that it can only take one ion specie into account with a very specific ion density distribution. In order to overcome these limitations, the generalised Coulomb model is used in the case of high electron ejection fractions. Therefore, we use two different expansion models for the cluster expansion process in our process-based laser-cluster interaction model.

The following part is based on literature work by [3, 2, 26].

Essentially, a cluster can be approximated by a plasma sphere. Therefore, the expansion of a cluster with a portion of the electrons removed is essentially a plasma sphere with a net charge expanding to vacuum [2], which is "the first analytical solution which treats the effect of charge separation in a fully consistent way and allows a self-consistent determination of the position of the ion front and maximum energy of the accelerated ions".

It is assumed that at $t = 0$ the electron component of a finite spherical plasma is heated to a uniform temperature T_{e0}. Due to this temperature, the electrons expand from the cluster, which leads to a charge separation. The plasma expansion is than solved by using a model of two charged fluids coupled via a self-consistent electric field, in which the ions are assumed to remain cold. The dynamics of such a 3D spherical system is governed by five equations: the continuity equation for the electron and ion fluids, the momentum equation for the electron and ion fluid and the Poisson equation for determining the electrostatic potential, resulting in equations 5.6 in which $v_{e,i}$ is the velocity of the electron, ion fluid respectively and T_e is the electron temperature, which is assumed to be spatially uniform.

$$\begin{aligned}
\frac{\partial \rho_i}{\partial t} + \frac{1}{r^2}\frac{\partial}{\partial r}(r^2 v_i \rho_i) &= 0\\
\frac{\partial \rho_e}{\partial t} + \frac{1}{r^2}\frac{\partial}{\partial r}(r^2 v_e \rho_e) &= 0\\
\frac{\partial v_i}{\partial t} + v_i\frac{\partial v_i}{\partial r} + \frac{Ze}{m_i}\frac{\partial \vec{\Phi}}{\partial r} &= 0\\
\frac{\partial v_e}{\partial t} + v_e\frac{\partial v_e}{\partial r} + \frac{T_e}{m_e \rho_e}\frac{\partial \rho_e}{\partial r} - \frac{e}{m_e}\frac{\partial \vec{\Phi}}{\partial r} &= 0\\
\frac{1}{r^2}\frac{\partial}{\partial r}(r^2\frac{\partial \vec{\Phi}}{\partial r}) &= 4\pi e(\rho_e - Z\rho_i)
\end{aligned} \tag{5.6}$$

Using dimension analysis theory on this situation shows that the whole process depends on two parameters. One parameter is the relative ion mass, characterising the mobility of the ions: $\mu_e = \frac{m_e Z}{m_i}$. The other parameter is the ratio of the cluster radius and Debeye length, which both evolve coherently in time according to the Poisson equation $\Lambda = \frac{R(t)}{\lambda_D(t)} = \text{constant} = \frac{R_0}{\lambda_D(0)} = R_0\sqrt{\frac{4\pi e^2 \rho_e(0)}{T_e(0)}}$, which is proportional to the ratio between the electrostatic energy of the ion cluster (which retains the electrons from the cluster).and the electron temperature (which drives the "diffusion" of the electrons from the cluster). Because this parameter describes the balance between the driving force of the electrons and the retaining force of the electrons, this parameter can be directly related to the electron ejection fraction ($\eta \to \Lambda$) by comparing the overlap between the electron and ion density profiles of the solution of equation 5.6 [3, 26].

The evolution of the electron temperature is determined by using the polytropic law, which is a common technique in thermodynamics $T_e(t) = T_e(0)(\frac{n_e(t,r=0)}{n_e(0,r=0)})^{\gamma-1}$. When the polytropic law is combined with the rest of the equations for this problem, an analytic solution of equations 5.6 can be found when $\gamma = 4/3$, which is the adiabatic index of the electron gas and therefore represents the case of adiabatic expansion. This implies that the total energy of the heated electrons is conserved: therefore the ions obtain their energy during plasma expansion by drawing it from the electrons. This represents the case of laser-cluster interaction after the laser pulse irradiation. In contrast, when the ion cloud expands during the laser pulse irradiation (long laser pulse), the drained energy of the electrons is replenished by the laser interaction, representing the case of isothermal expansion, changing γ. Hence, this theory can only be used for short enough laser pulses.

In the adiabatic case, a self-similar solution of equations 5.6 can be found. The self-similar solution provides exponential ($\propto \exp(-r^2)$) Boltzmann-like profiles, which provide a static density profile as function of a normalised radius. Therefore, the evolution of the density only depends implicitly on time due to the dynamics of the cluster radius, which is determined by a single differential equation. The static density profiles are fully characterised by Λ (and hence the electron ejection fraction) and the ion mobility. Separating the dynamics from the system by introducing static profiles is the essence of the self-similarity ansatz. The ion density profiles behave in a similar way as the electron density profiles, but are cut off at a certain radius ξ_f, which is a fraction of the total (expanded) cluster radius: $\xi_f(\Lambda, \mu_e) = \frac{r_f}{R(t)}$. For more information, see appendix C.3.

Linking the self-similar solution to a cluster is complicated, because the ion density and electron density start uniform, whereas in the self-consistent model a thermal electron distribution - which implies a Boltzmann-like density profile for both the electrons and the ions - is assumed. Therefore, the time it takes for the electrons to obtain a thermal distribution after electron ejection, cannot be determined using the self similar solution - which leads to an unknown delay between the completion of the electron ejection process and the initialisation of the self similar model. This is also indicated in figure 5.3 (adopted from [3, 2]), where the homogeneous cluster density and the initialisation density profile profile by the self similar model are compared. Due to the difference between the self-similar initial density profile and the cluster initial density profile, the cluster parameters cannot be directly used in the self-similar solution. Using the work of [3] the nano-cluster parameters are parametrically related to the self-similar solution, by using the electron ejection fraction, which is verified with molecular dynamics simulations.

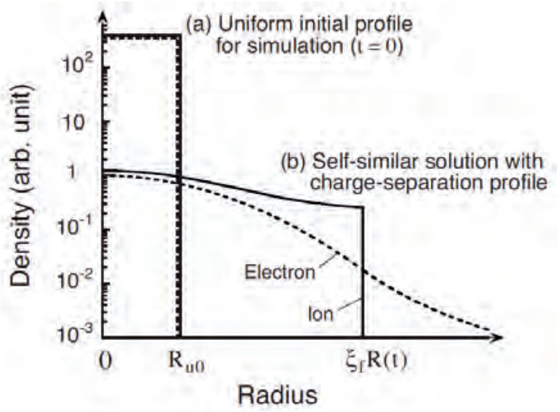

Figure 5.3: Comparison between cluster density profile and the corresponding density profile of the self-similar solution. This figure has been adopted from [2, 3].

The previous part is based on literature work by [3, 2, 26].

Validation and verification In section 5.3 we have compared the ion energy distribution for various electron ejection fractions, where it is confirmed that the self similar solution converges to the Coulomb explosion solution when all electrons are ejected from the cluster. A comparison between the solutions of the self similar model and molecular dynamics simulations / an ergodic expansion model [4] is provided in [3] and a further verification of the self similar solution is beyond the scope of this thesis.

5.3 Simulations and examples

In this section the generalised Coulomb expansion model and the self-consistent, self-similar solution (SSS) will be compared with particle tracer simulations.

5.3.1 Coulomb Explosion of heterogeneous clusters

In order to examine the dynamics of a heterogeneous cluster with a highly charged heavy core, a particle tracer simulation (PTS) is performed on a cluster with 1000 xenon 40+ ions (which is obtainable experimentally [12, 1]) and 1000 deuterium ions, which is compared with the prediction of the generalised Coulomb model (GCM). Both deuterium and xenon ions have a homogeneous density of 10^{27}m^{-3}, resulting in a cluster radius of 6.2 nm. Only the Coulomb explosion is modelled in the simulation: the laser interaction is neglected and it is assumed no electrons are present.

In figure 5.4 it is shown that the deuterium ions have a larger displacement than the xenon ions at 200 fs, which is to be expected, because α for deuterium is smaller than for xenon, indicating

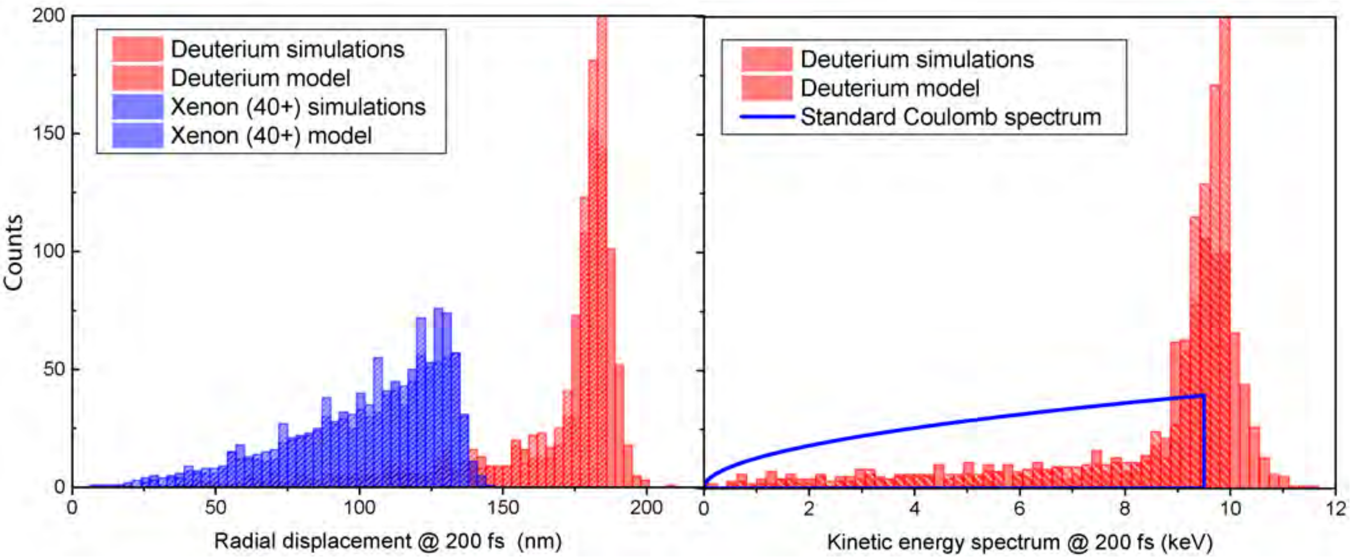

Figure 5.4: A histogram of the position of the ions at 200 fs and of the ion energy spectrum at 200 fs of a deuterium, xenon (40+) cluster expansion

a faster expansion dynamics for deuterium. The xenon ions obtain a broad spatial distribution, whereas the spatial distribution of the deuterium ions is more localised. Furthermore, it is evident that the xenon ions obtain a large spatial distribution, whereas the distribution of the deuterium ions is more localised, which implies that the spread of velocities of the deuterium ions (spread in ion energies) is much smaller, indicating a more mono-energetic ion energy spectrum as compared to the energy spectrum of a "standard" Coulomb explosion. The reason for this mono-energeticity is that most of the charge content is in the xenon ions and hence the deuterium ions obtain a large boost in ion acceleration when the deuterium ions overtake xenon ions, increasing the enclosed charge. In this case, a maximum ion energy of less than 1 keV would be obtained without the xenon ions, compared to 10 keV with the xenon ions. Additionally, when all deuterium shells overtake all xenon shells, the enclosed charge per deuterium shell is approximately the same, leading to a mono-energetic ion energy spectrum.

In figure 5.4 the result of the GCM corresponds well with the result of the PTS. At certain time steps, there is an excursion of the histogram provided by the GCM, which leads to a slight deviation between the PTS and the GCM (most easily noticeable in the radial displacement of the xenon 40+ ions). This excursion is a numerical artefact caused by the conversion of the model results to a histogram and is not an artefact of the model itself. A difference between the GCM and the PTS is that the GCM predicts a maximum count at the highest kinetic energy obtainable at 10 keV. In contrast, in the PTS the ion distribution does not go to zero abruptly after 10 keV but goes to zero gradually, leading to some overshoot between 10 and 11 keV. This is caused by the position of the particles in the PTS model, which are randomised across the sphere and can lead to gradual deviations in the electrostatic energy per particle. The good agreement between the PTS and GCM indicates that the model can account well for the differences in mass/charge ratios resulting in different Mie periods, even when these differences are fairly large. Additionally, the good agreement indicates that - even when shock shells occur - discrete effects can be neglected, which is to be expected, because momentum transfer from the light deuterium ions to the heavy xenon ions is very low in an elastic collision (all collisions in the particle tracer simulations are elastic, because radiation/retardation effects are not taken into account). We have performed a similar comparison between particle tracer simulations and the generalised Coulomb model for a deuterium cluster with a peaked density profile. In this case we found up to 15 % deviation between the PTS and the GCM, which indicates that even in this case (momentum transfer is expected to be more effective) momentum transfer from the overtaking inner shells to the outer

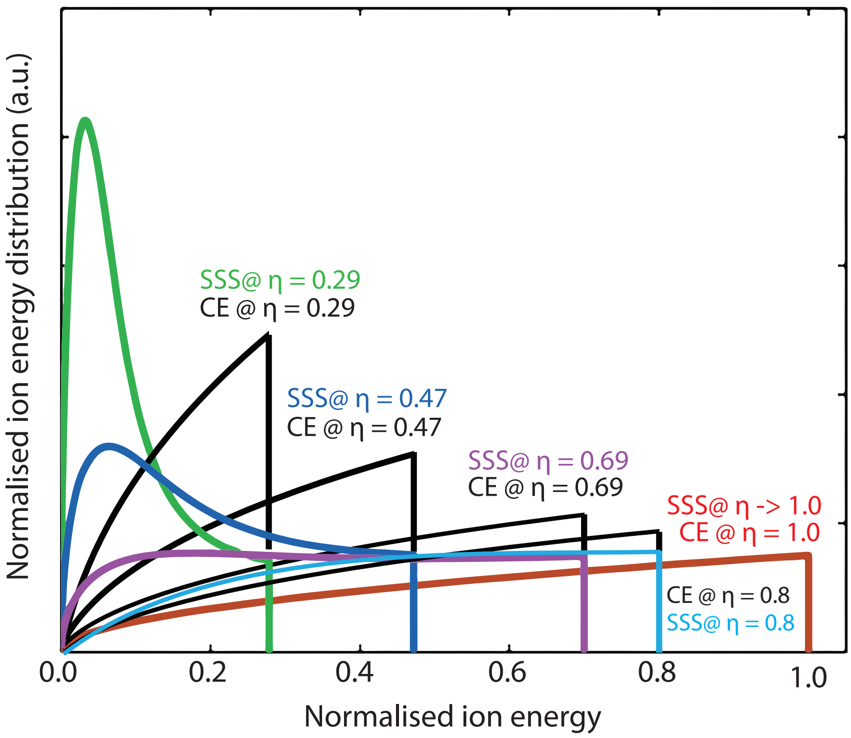

Figure 5.5: Comparison of the ion energy spectra of the SSS and GCM for various electron ejection fractions. Although this figure is based on our calculations, a similar figure is provided in [4, **?**].

shells can be neglected.

5.3.2 From Coulomb explosion to ambipolar-like expansion

In this section we have calculated the steady-state ion energy spectra provided by the general Coulomb explosion model and the self-consistent, self similar solution, cluster expansion model (SSS) for various electron ejection fraction, η of a homogeneous density cluster. A comparison between the GCM and the SSS for various electron ejection fractions provides the insight in the dynamics of the expansion in the Coulomb limit (all electrons ejected $\eta \to 1$), the ambipolar limit (no electrons ejected, $\eta \to 0$) and in between. Furthermore, it provides insight in the limitations of the Coulomb explosion model.

As explained previously, for the Coulomb expansion model it will be assumed that the electrons spread homogeneously across the cluster and the electron dynamics are neglected, hence $Q(r,t) - Q_{\text{electrons}}(r,t) \to \eta Q(r,t)$. In figure 5.5, the ion energy spectra have been normalised by the maximum ion energy obtainable in a pure Coulomb explosion (which is the energy obtained by the ions in the most outer shell of the cluster, see equation 5.3).

The Coulomb model energy distributions (GCM) are obtained by equation 5.3 and are indicated by the black lines in figure 5.5 for various η. The self similar solution (SSS), provided by the self-consistent model taking the electron distribution self consistently into account, is indicated by the coloured lines for various η, which we calculated analytically from the self-similar model.

When all electrons from the cluster are removed ($\eta = 1$), a pure CE follows leading to a very broad energy spectrum up to high energies, as indicated by both by the SSS and the GCM model (red line). When $\eta = 0.8$, the charge of the ions is partly shielded by the electrons, leading to a 20 % reduction in maximum ion energy. At this point, the SSS and the CE start deviating slightly (approximately 10 % deviation between the models) and the distribution by the SSS is somewhat flattened compared to the square-like CE distribution. This flattening increases until approximately $\eta = 0.7$, where the deviation between the SSS and the CE model is large at low energies and is up to 30 % at high energies. When $\eta < 0.7$ (green and dark blue spectra), the maximum in the SSS spectra shifts towards a lower energy than the maximum energy obtainable in the expansion, which is a different dynamics than the Coulomb explosion, indicating that ambipolar effects start playing an important role in the cluster expansion. Therefore, the resulting ion energy spectra are a combination of ambipolar effects (maximum at low ion energies) and Coulomb explosion effects, which form the tail of the ion energy distribution. When η decreases the ambipolar effects become relatively stronger. The CE model provides a fairly accurate physical picture for $\eta > 0.7$, otherwise the electrons should be taken into account self-consistently as in the self similar solution. Physically, in ambipolar-like expansion, the thermal electrons lead to a peaked electron density in the cluster. Hence, the charge excess of the ions is larger at the edge of the cluster than in the centre, which is illustrated in figure 5.3. Therefore, the ions at the edge of the cluster expand rapidly, forming the tail of the ion energy distribution (Coulomb effect), whereas ions in the centre are slowed down by the peaked electron density profile, leading to a maximum in the ion energy spectrum at lower ion energies. Effectively, this combination of ambipolar-like effects and Coulomb effects can be used to obtain a peaked density cluster, as illustrated in section 6.3.

5.4 Summary and conclusions

By controlling η, the ion expansion dynamics can be tailored within two limits: the Coulomb explosion limit, where all electrons are ejected and the highest ion energies are obtained and the ambipolar expansion limit, where no electrons are ejected.

Single cluster fusion requires collisions within the cluster at fusion relevant velocities. Such collisions form shock shells: parts where the inner shells of the cluster collide with the outer shells of the cluster. This requires energetic ions and therefore requires a Coulomb explosion. However, a Coulomb explosion of a single specie cluster with a homogeneous density distribution will not form shock shells, because the outer shell ions obtain the highest acceleration. Therefore, a Coulomb explosion has to be induced of either a multi-specie cluster (heterogeneous cluster) or a cluster with an inhomogeneous density. We derived a generalised Coulomb model, which supports heterogeneous clusters and clusters with arbitrary density profiles and we found a good agreement (within 15 %) between the generalised Coulomb model and particle tracer simulations.

The downside of such a model is that it does not take the electron dynamics into account self-consistently when electrons are present, although it is possible to use an a priori electron dynamics model. Therefore, it cannot model ambipolar expansion effects, which play an important role in the expansion dynamics when $\eta < 0.7$. For this purpose another model is used, which solves the problem self-consistently. However, this model sets stringent demands on the initial density profile, limiting the application of this model to homogeneous density distributions or Gaussian density distributions. When ambipolar expansion effects occurs, the charge excess of the ions is larger at the edge of the cluster, which can be used to obtain peaked density profiles.

Chapter 6

Single cluster fusion

In this work we have created a process-based model for the dynamics of a single cluster which takes all the fundamental laser-cluster interaction processes into account (chapters 2 to 5). In this chapter, we use this new model to investigate whether *single cluster fusion (SCF)* is possible and to estimate the resulting fusion yield/neutron flux from a single cluster fusion experiment. One potential benefit of single cluster fusion is that it exploits the high, solid-state density of the cluster, which might result in higher neutron yields as compared to multi-cluster fusion (MCF), where the average density is much lower. For SCF, the neutron pulses are expected to be much shorter (less than a picosecond) than for MCF ($\sim$ nanosecond [9]) because the ions do not have to travel a large distance for fusion to occur in SCF, as shown in figure 6.1. Short neutron pulses might be interesting for neutron detector calibration [17] and time-resolved radiation damage studies [9]. In multi-cluster fusion, the homogeneous clusters are usually fully stripped and the exploding clusters undergo a typical (broad) Coulomb ion energy spectrum (see chapter 5). The accelerated ions of each cluster interact with each other, altering the ion energy distribution of the ions into a thermal ion energy spectrum, which is less favourable for fusion [18]. Because single cluster fusion occurs too fast for a thermal equilibrium to establish, it might be possible to control the energies at which the collisions in a single cluster occur more accurately - possibly enhancing the fusion yield. In addition, SCF is not limited to deuterium-deuterium and deuterium-tritium fuel mixes and different (a-neutronic) fusion fuel mixes can be used to obtain ultrashort α and γ pulses, which might lead to future applications [27, 8, 28, 19].

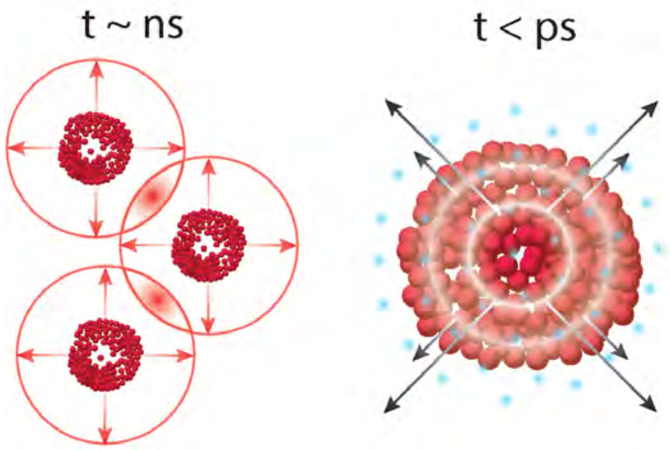

Figure 6.1: A schematic overview of the difference between single cluster and multiple cluster fusion.

SCF works by colliding the inside of the cluster against the outside of the cluster *during* the explosion of a *single* cluster, which can be achieved by controlling the expansion dynamics of a single, fully stripped cluster. The expansion of such a cluster can be controlled by using a cluster with a peaked density profile and/or by using multiple ion species in the cluster, which will be explained in section 6.2. Clusters with peaked density profiles can be obtained by ejecting a small number of electrons from the cluster, after which the edges of the cluster expand more rapidly than the centre of the cluster - leading to peaked density profiles as discussed in chapter 6.3. Using the methods of section 6.2, single cluster DD, DT and proton-boron fusion is optimised in section 6.6 and predictions of the fusion yield, Q-factor and pulse duration are provided. Additionally, with the strategy of section 6.2 it is possible to transform the very broad Coulomb energy spectrum of a single cluster into a mono-energetic ion energy spectrum, which can lead to significantly higher neutron yields and significantly higher Q-factors of current cluster fusion schemes, as shown in chapter 6.4.

6.1 Cluster fusion

Cluster fusion is a relatively inexpensive, table-top fusion device. Initial, multi-cluster based, experiments measured 10^4 - 10^6 neutrons per shot, with a repetition rate of up to 10 Hz [9]. The amount of energy used for the pulse is in the order of 0.1 - 10 J, leading to a Q-factor of $10^{-8} - 10^{-6}$ [8, 10, 7], which is far away from the break-even point. Because cluster fusion is a small neutron source (the focal volume of the laser is small), samples can be placed within 1 mm in current experiments [9, 20]. Hence its modest neutron yields can result in *averaged* neutron fluxes of 3×10^{10} n/s m^2 (1 mm from the source, 10 Hz laser repetition rate) [9]. The main limitation of cluster fusion at the moment is its limited flux and it is expected the current neutron yields should be enhanced by a factor 100-1000 for most neutron source purposes [20, 25, 83, 9].

When the laser pulse interacts with the cluster jet, a plasma filament is formed, which is only very short-lived - hence the energy confinement time (for laser-cluster interaction we assume the energy confinement time to be the life-time of the plasma filament) is insufficient to obtain net power from cluster fusion in these experiments. However, by using advanced schemes the confinement time can be improved significantly - resulting in Q-factors (the Q-factor is defined as power in divided by power out) of up to $Q = 10^{-2}$, which is comparable to current 'big science' fusion facilities such as the National Ignition Facility (NIF) [8]. One idea is to increase the confinement time by applying a strong magnetic field (200 T) (by exploding a coil), which is expected to increase the fusion yield by a factor 1000 or more [84, 85]. Other ideas focus on enhancing the confinement time by using source target cluster fusion [10, 7, 8], in which a cluster jet of deuterium clusters is injected in a lithium cylinder. Upon laser irradiation the deuterium clusters explode, and the deuterium ions are accelerated and stopped in the lithium cylinder, causing them to fuse - ultimately resulting in an a-neutronic fusion yield of 4.3×10^9 per joule laser energy and a Q-factor of 10^{-2} [8, 10, 7]. By tweaking the ion energy spectrum of the exploding deuterium clusters, it will be shown in section 6.4 that the fusion yield in this case can be enhanced by a factor 4.25 and the Q-factor can be enhanced by a factor 3.7.

Although cluster fusion is a very promising, relatively inexpensive, table-top neutron source with unique properties, the problem with cluster fusion is that a factor 100 higher neutron yield is required for most cluster fusion purposes. Therefore, in this chapter we investigate whether our single cluster model can be used to optimise the cluster fusion neutron yield by single cluster fusion and by using mono-energetic ion energy spectra. Additionally, we investigate the extraordinary short neutron pulses resulting from SCF.

6.2 Methods for controlling the Coulomb explosion dynamics

The Coulomb explosion dynamics can be controlled for single cluster fusion and for the generation of mono-energetic ion energy spectra by applying density gradients to the cluster (peaked density clusters) and by combining multiple ion species in a cluster (heterogeneous clusters).

6.2.1 Peaked density clusters

For convenience, we will model a peaked density cluster by equation 6.1, where the density profile consists of a high density homogeneous core with density A, which starts to decay after $r > fR$ (in which R is the cluster radius and f is the fraction of the cluster radius) with a decaying power α. We use this model because it can be directly related to the forced oscillator model, which is used to predict the electric field required for ejecting all electrons from the cluster, by only taking the high density core of the cluster into account - as discussed in section 4.2.2. In addition we choose for this model because understanding the expansion of the decaying edge is greatly simplified by describing the density in the decaying edge of the cluster by a power function: $\rho(r) \propto r^{-\alpha}$.

$$\rho(r) = \begin{cases} A & \text{if } r \leq fR \\ A(\frac{fR}{r})^{\alpha} & \text{if } fR > r \geq R \\ 0 & \text{if } r > R \end{cases} \tag{6.1}$$

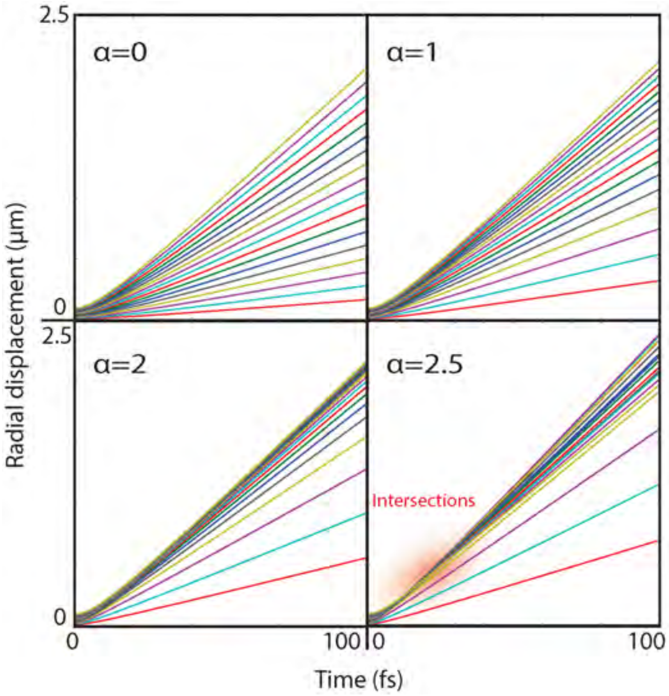

Figure 6.2: Trajectories of the ion cluster profile dynamics of equation 6.1 for various α.

The electric field inside the cluster is proportional to the integral over the cluster's density profile divided by the r^2 from the increase in flux surface (Gauss' law), which results in $E \propto r^{-\alpha+1}$ for $\rho = Ar^{-\alpha}$. Therefore, for a homogeneous cluster, the electric field rises linearly in the cluster, leading to a larger acceleration for outer cluster shells than inner cluster shells, which eventually results in a broad ion energy spectrum after the cluster's explosion. In order for single cluster fusion to occur, the electric field inside the cluster has to be larger than the electric field outside the cluster, which requires peaked density clusters ($\alpha > 1$). In this case, the shells of the cluster are "compressed" against each other. For the inner shells to overtake the outer shells (for inner ions to collide against outer ions of the cluster), a larger difference in electric field is required. From an algebraic (differential equation: $\ddot{r} \propto r^{-\alpha+1}$) and numerical inspection (generalised Coulomb model) we determined shock shells occur at $\alpha > 2$. When this occurs, the inner shells and outer shells overtake each other, leading to inner cluster collisions. When this occurs at sufficiently high relative velocities, single cluster fusion occurs. An illustration of the radial displacement of various cluster shells (each shell indicated by a different colour) is represented in figure 6.2 for a cluster with $f = 0.2$, $R = 100$ nm, 4.2×10^8 deuterium atoms (A is adjusted accordingly) and $\alpha = 0, 1, 2, 2.5$, with an equidistant discretisation mesh at $t = 0$. In this chapter, we limit peaked density clusters to single specie clusters for simplicity.

Single cluster fusion One remarkable feat in single cluster fusion for peaked density clusters is that the cluster shells only collide against each other for a relatively short amount of time, even when compared with the expansion timescale, which is shown in figure 6.3 where the shell trajectories of the case with $\alpha = 2.5$ studied in figure 6.2 are zoomed in. The relative position of four trajectories in the cluster are visualised, where it becomes evident that until approximately 35 fs most of the outer shells of the cluster are compressed and eventually the particle trajectories intersect each other in between 33 and 38 fs, after which the overtaking shells obtain an extra acceleration (their enclosed charge now includes the overtaken shell), leading to a divergence between the shell positions (from 3 to 4). Hence most of the fusion reactions in this case take place in less than 10 fs, whereas the characteristic expansion of this case is expected to be more than 40 fs (3+ times the Mie period, see chapter 5). The relative velocity of the shock shell collisions is always lower than the maximum expansion velocity of the cluster. When α becomes larger, the decay of the density profile becomes stronger, and the relative velocity of the shock shell collisions increases (although it stays under the maximum expansion velocity of the cluster). However, when α becomes larger, the amount of particles in the decaying part of the cluster is decreased and in order to keep the total number of particles in the cluster the same, A has to be increased accordingly (and a higher laser field strength is required for electron ejection). Hence there is a trade-off between the number of colliding particles, relative velocity of the collision shock shells and the laser field required for electron ejection.

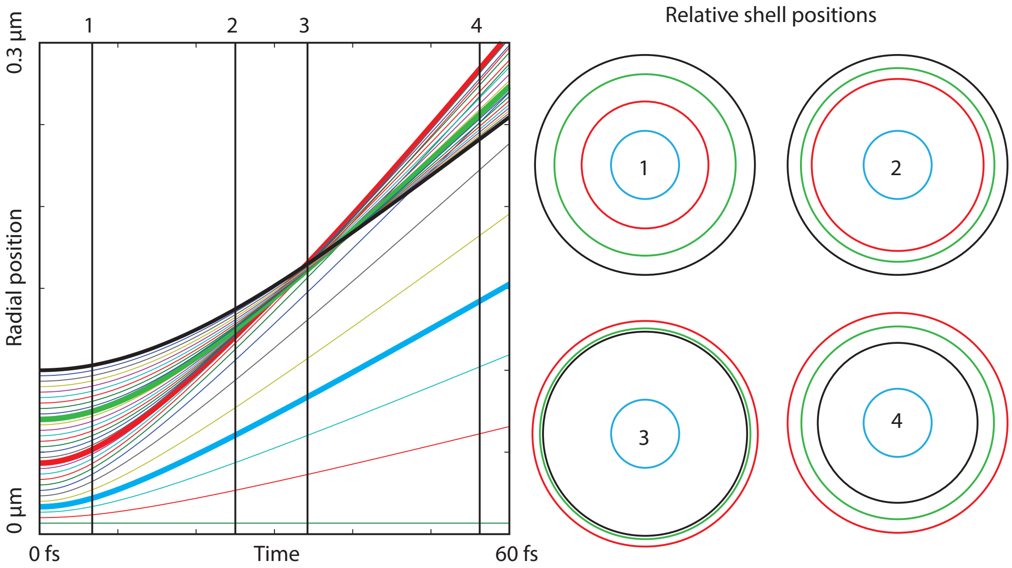

Figure 6.3: Intersecting trajectories where single cluster fusion occurs, with a schematic illustration.

Mono-energetic ion energy spectra From analytic inspection and the numerical inspection (such as figure 6.2), we determined that the compression effect is the strongest at $\alpha = 2$ (for larger α, the shells diverge after the intersection of the lower radius shells with the larger radius shells - as shown in figure 6.3). However, for $\alpha > 2$ higher ion energies are obtained than for $\alpha < 2$. When an inner shell takes over an outer shell, the enclosed charge of the inner shell is increased - leading to an additional boost of the inner shell. These boosts lead to an increase of maximum obtained ion energy. Hence by $\alpha > 2$ it is possible to create an energy band in the ion energy spectrum. When the shells are "compressed" against each other, the shells have a similar enclosed charge, similar position and hence a similar expansion velocity - resulting in mono-energetic ion energy spectra. Therefore, we expect that an optimal mono-energetic ion energy spectrum for a peaked density cluster is obtained for $\alpha = 2$, which agrees with the shell trajectories figure 6.2 and with the corresponding ion energy profiles in figure 6.4. The maximum ion energy obtained is the same for each α, because in each simulation the number of ions in the cluster is kept constant.

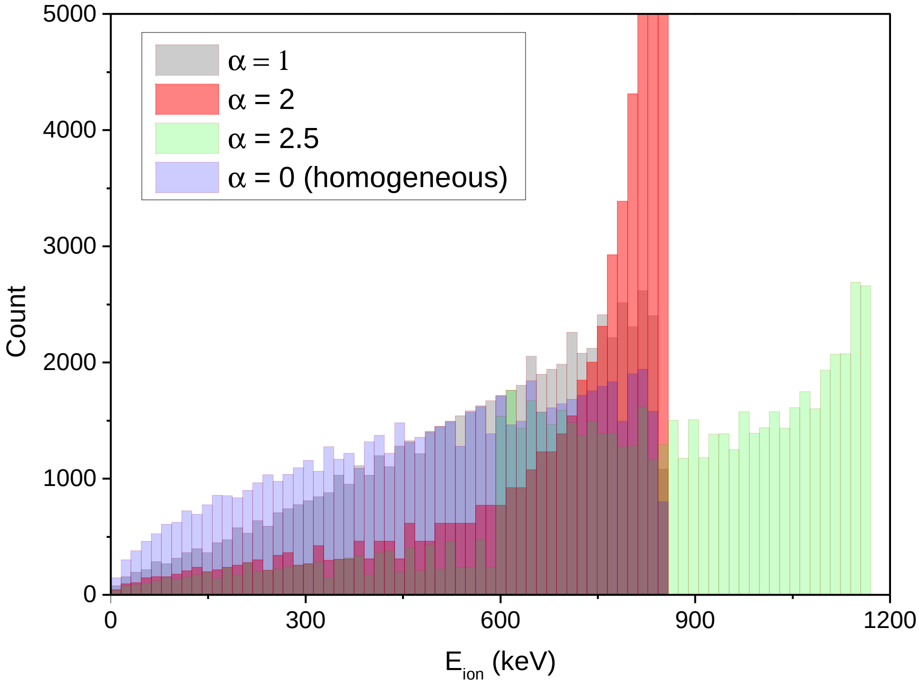

Figure 6.4: The ion energy spectrum in steady-state of the cluster density profile of equation 6.1 for various α.

However, by changing the cluster's density profile, also the electric field required for electron ejection changes. In the quasi-static approximation of electron ejection in section 4.2.3, the required electric field for electron ejection scales with $E_{\text{critical}} \propto \rho R \rightarrow E_{\text{critical}} \propto AfR$. Therefore, there is a trade-off between the mono-energeticity and required electric field: the smaller the f, the better the mono-energeticity at the cost of higher laser intensities, which has implications for the Q-factor. Taking this into account, the best trade-off for the Q-factor is found for $f = 0.35$, in which the ion energy spectrum is fairly mono-energetic and a 20 % higher laser electric field is needed for the electron ejection - resulting in a 44 % higher laser intensity.

6.2.2 Heterogeneous clusters

The characteristic time at which each ion specie expands in a heterogeneous cluster depends on the charge/mass ratio. Therefore, when combining a specie with a high charge/mass ratio (hydrogen for example) with a specie with a low charge/mass ratio (xenon 40+ for example), the hydrogen will expand faster than the xenon, causing the hydrogen shells to *overtake* the xenon shells, as discussed in chapter 5. This effect can be used for cluster fusion in heterogeneous clusters where the cluster consists out of two fusion fuel ion species with a different charge/mass ratio. When the hydrogen shells overtake the xenon shells, they obtain an extra acceleration due to the xenon charge. Hence using heterogeneous clusters can also boost the resulting ion energies for small

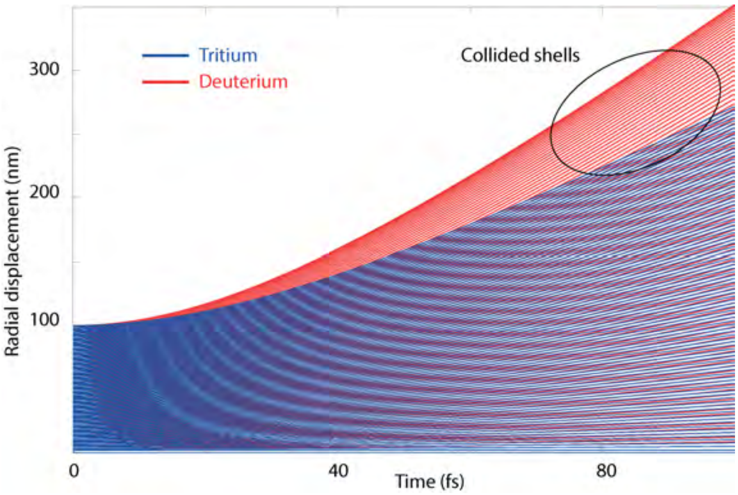

Figure 6.5: Trajectories of deuterium and tritium shells in a DT heterogeneous cluster

clusters and can be used to obtain mono-energetic ion energy spectra. Because xenon can obtain much higher charge states than hydrogen, the charge content of xenon of the cluster will probably be higher than the charge content of the hydrogen in the cluster. Therefore, not only the ion energy is boosted, but mono-energetic ion energy spectra are also obtained (for more information see section 5.3).

Single cluster fusion In figure 6.5, the trajectories of cluster shells of deuterium and tritium, determined by the generalised Coulomb model, with an equidistant discretisation mesh at $t = 0$ is plotted. The charge/mass ratio of deuterium is larger than tritium, hence deuterium expands faster, causing collisions between the deuterium and tritium shells. Depending on the difference on charge/mass ratio between the two species, the characteristic expansion time of each specie deviates. When this deviation is large, we expect the relative energies at which the two fusion species collide is larger, which can be beneficial for fusion (depends on the optimal collision energy for fusion). It should be noted in this work we only take heterogeneous clusters with homogeneous density profiles into account. However, heterogeneous clusters can also be layered (for example - a core of xenon ions with a layer of deuterium and a layer of tritium around the heavy xenon core) and the effect of a peaked density profile can be combined with the effect of using heterogeneous clusters for improved mono-energeticity [34] and for single cluster fusion. Although such cases can be analysed by our process-based model, presented in chapters 2 to 5, these investigations are beyond the scope of this work.

Mono-energetic ion energy spectra In current experiments the cluster radius and density are often much smaller than for optimal conditions, resulting in lower than optimal expansion energies. In this case, using heterogeneous clusters is an effective method for obtaining both a higher ion energies and for obtaining a mono-energetic ion energy spectrum [34, 3, 86, 87, 19]. However, using a combination of a light and heavy ion specie leads to pollution of the heavy ion specie in the cluster jet. The heavy ions will obtain a similar amount of energy than the light ions. Therefore, approximately half of the energy is lost to non-fusion ions. Additionally, the electrons resulting from the high Z specie will remain in the laser focal volume and increase the plasma frequency in the plasma filament - which might have a negative effect on the laser penetration in the cluster jet. Therefore, we conclude it is more beneficial to tune the cluster density profile for obtaining a mono-energetic ion energy spectrum, when the cluster can be made large and dense enough for this purpose.

6.3 Method for controlling cluster density profiles using ambipolar-like expansion

In the previous section we assumed that peaked density clusters can be used. The concept of using ambipolar-like expansion for controlling the cluster density profile has been shown in [26, 4, 31, 29] and has been recently experimentally achieved [33]. In this section we provide a proof of concept, by using our process-based laser-single cluster interaction model, of this cluster density shaping method. However, studying precisely how a certain cluster density profile is obtained is beyond the scope of this work.

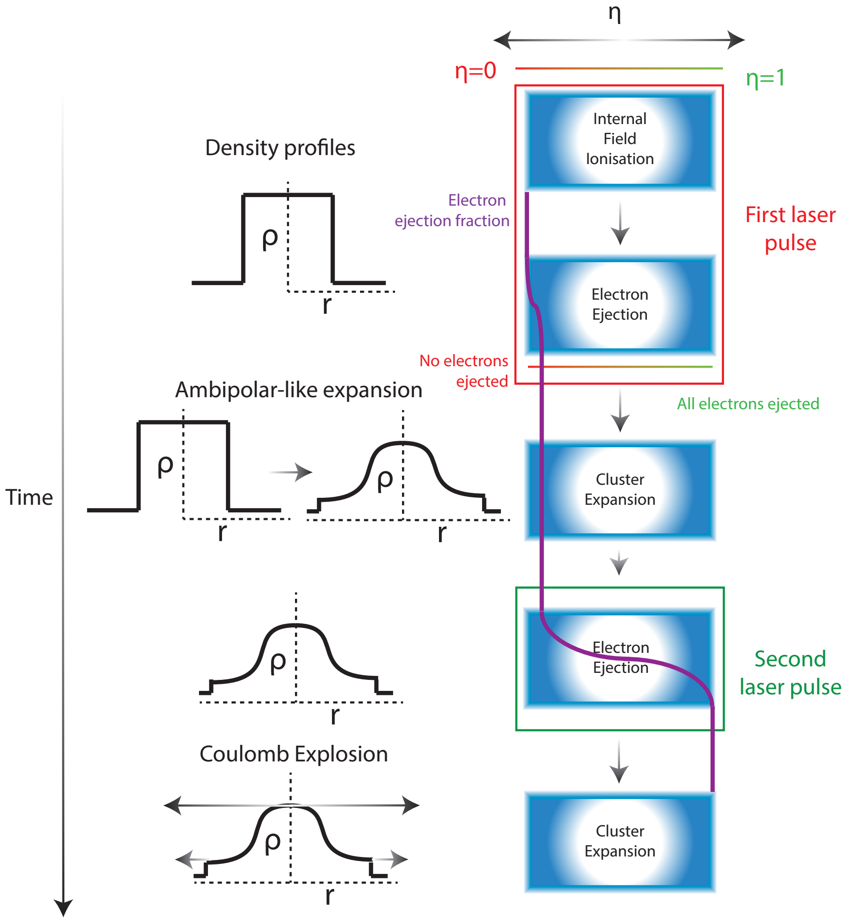

Figure 6.6: Schematic overview of density profile control with ambipolar-like expansion

By changing the amount of electrons in the cluster, the cluster expansion dynamics can be changed. When a laser pulse is intense enough to ionise the atoms in the cluster, but not to eject the electrons, the cluster expands ambipolar-like. During ambipolar-like expansion the edges of the cluster have more ion charge excess than the centre of the cluster, as described in chapter 5, resulting in a peaked ion density profile. Sequentially, a second, more intense, laser pulse can be used to induce a Coulomb explosion of this inhomogeneous profile. This double pulse scheme is presented schematically in figure 6.6. In a more sophisticated set-up the pulse-shaped laser intensity can gradually eject a small portion of electrons to tune the cluster's density temporal density evolution for more accurate density profile control, which is beyond the scope of this section.

In this example, we study the ion expansion dynamics of a cluster with 20 % of the electrons removed ($\eta = 0.2$), initial cluster density $n = 10^{30}$ m^{-3} and cluster radius 10 nm (indicated by the

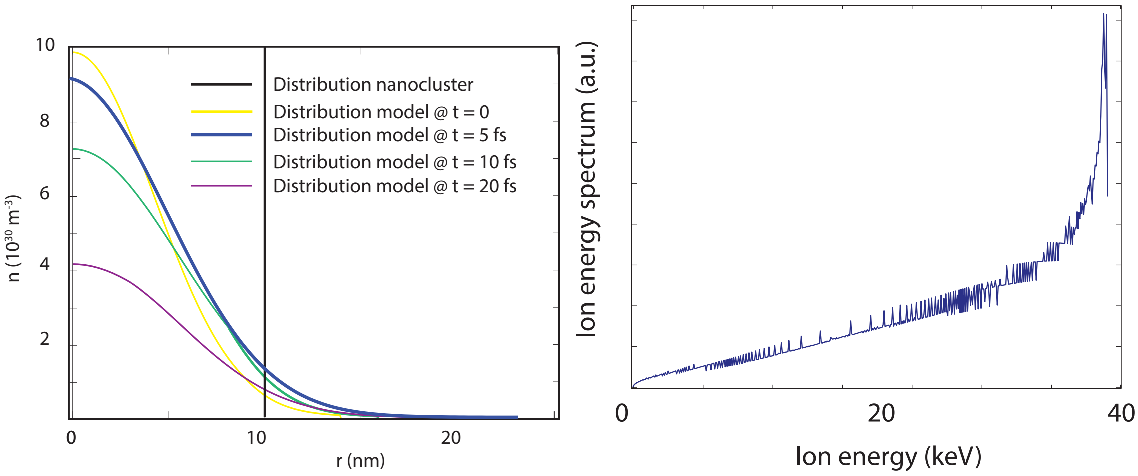

(a) Temporal evolution of the density profile in the self similar model

(b) Resulting ion energy spectrum from Coulomb explosion of self-similar solution at 5 fs.

Figure 6.7: Results of density profile control using ambipolar-like expansion

black line in figure 6.7a) by using the self-similar solution presented in chapter 5. One drawback of this scheme is that a relatively high initial cluster density is required, because the initial cluster density is lowered during the expansion, which can be problematic since most current experiments obtain cluster densities of up to 10^{28} m^{-3} [33] and most simulations are performed on clusters with densities up to 10^{29} m^{-3} [8, 27, 7]. As explained in chapter 5, there is an unknown time delay between the homogeneous cluster density profile (black line) and the initial self similar solution (yellow line). After this delay, the density profile stretches out in time, flattening the density profile in the centre and lowering the slope of the density profile (from yellow till purple). Hence, in order to obtain a Coulomb explosion of a certain peaked density profile, the second laser pulse has to be timed accurately, which is complicated by the unknown delay between the homogeneous density profile and the initial self similar solution density profile.

By using the resulting density profiles from the self similar solution, we calculated that this control scheme is insufficient for obtaining optimal density profiles for single cluster fusion, since these would require a steeper decay and a more accurate control strategy. However, this control strategy might be sufficient for obtaining mono-energetic ion energy spectra. In figure 6.7b we calculated the ion energy distribution of the Coulomb explosion of the self similar solution density profile at 5 fs (blue line - figure 6.7a), which is fairly mono-energetic. This shows that - as a proof of concept - ambipolar-like expansion can be used for density profile control. However, achieving this requires an additional investigation, due to the unknown time delay between the homogeneous density profile and the initial self similar solution density profile.

6.4 Cluster fusion with mono-energetic ion energy spectra

The following part is based on cluster fusion schemes by [8, 10, 7], which are improved by using our cluster expansion model for obtaining mono-energetic ion energy spectra.

After having discussed how mono-energetic ion energy spectra can be obtained by controlling the expansion characteristics of a single cluster, we will illustrate whether the fusion yield of the source target cluster fusion set-up of [8, 10], explained in section 6.1 can be enhanced by using mono-energetic ion energy spectra. In contrast to multi-cluster fusion, in this case the accelerated ions from the deuterium clusters act as a source of energetic ions interacting with the deuterium shell (source-target fusion). The ions do not thermalise until they reach the lithium shell and hence the ion energy spectrum of a single cluster is expected to remain relatively unaffected. Therefore, in the work by [8, 10], it is assumed that the deuterons obtain the energy spectrum of a homogeneous Coulomb explosion.

In [8, 7] it has been shown that the fusion yield per laser pulse, Y, can be calculated by multiplying the number of deuterons produced from the source, N, with the average reaction probability $< y >$: $Y = N < y >$. The average reaction probability is formed by the integral over the ion energy distribution $P(E)$ times the reaction probability per ion: $< y >= \int_0^{E_{\max}} P(E)y(E)dE$, in which $y(E)$ is provided by the ratio of the fusion cross-section and the stopping cross-section, which results in a power-like dependence [8, 7, 10] $y(E) = bE^{\xi}$, where b, ξ are parameters depending on the fusion reaction.

The previous part is based on cluster fusion schemes by [8, 10, 7]. From this point on, our improvement strategy of the source target cluster fusion scheme follows.

By using an ideal mono-energetic ion energy spectrum ($P(E)$), the fusion yield is increased by a factor 4.5 for deuterium lithium-6 fusion. However, the mono-energetic ion energy spectrum obtained from laser-cluster interaction is not ideal and by using the ion energy spectrum we calculated from the double pulse scheme (figure 6.7b), the fusion yield can be increased by up to a factor of 4. However, ejecting the electrons from the high density core requires more laser energy. When we take this effect into account by approximating the density profile by a homogeneous part and a decaying part (fitting the self similar solution density profile at t=5 fs of figure 6.7b with equation 6.1), the Q-factor of the source target cluster fusion scheme can be improved by a factor 3.6 (in the deuterium-lithium-7 scheme), resulting in a Q-factor of 3.6×10^{-2}. This shows that mono-energetic ion energy spectra, from single cluster expansion control, are a feasible method for significantly enhancing the fusion yield and Q-factor in certain cluster fusion scenarios.

6.5 Single cluster fusion calculations

Single cluster fusion calculations In order to obtain fusion from a single cluster - the ions have to be accelerated to high energies, which is performed by ejecting all electrons from the cluster. We determine the electric field required for the electron ejection from the forced oscillator model (chapter 4) (by taking only the high density core into account) and we use the generalised Coulomb model (chapter 5.1) to predict the cluster's expansion. Calculating the amount of fusion reactions from the generalised Coulomb model is relatively straightforward. In the generalised Coulomb model the cluster is discretised in spherical shells and each shell contains a number of ions. The evolution of the radial position of each shell is calculated as a function of time: $r_i(t)$, where the set $r_i(0)$ provides the mesh of the discretisation, which can be chosen arbitrarily - but we use an equidistant mesh at $r_i(0)$. A collision at $t = t_{\mathrm{col}}$ occurs when the radial trajectory of two shells intersect: $r_i(t_{\mathrm{col}}) = r_j(t_{\mathrm{col}})$ while $i \neq j$. The number of fusion reactions occurring from this collision, N is calculated by using the beam-target fusion cross-section σ_f: $N_{\mathrm{fusion}} = Vn_1n_2 < \sigma_f(v)v > \tau$, in which n_1, n_2 are the densities of the two shells and V is the volume of the shells (which is approximately the same for both shells). The collision velocity v is the relative velocity between the shells, which is used to determine $\sigma_f(v)$. The confinement time τ is the thickness of a shell divided by the relative velocity, which determines the duration of the collision between the two shells. Performing this routine for every intersection of the radial trajectories (t_{col} - ($r_i(t_{\mathrm{col}}) = r_j(t_{\mathrm{col}})$ while $i \neq j$), leads to the number of fusion reactions per cluster.

The single cluster Q-value can be approximated by assuming that the energy transition is ideal: which implies that all of the applied energy equals the electrostatic energy of the cluster. In practice, this cannot be achieved, because a portion of the energy is obtained by the electrons; in addition - only a small portion of the laser pulse energy can be absorbed, since this would decrease the laser electric field - after which the laser field can no longer eject the electrons from the cluster.

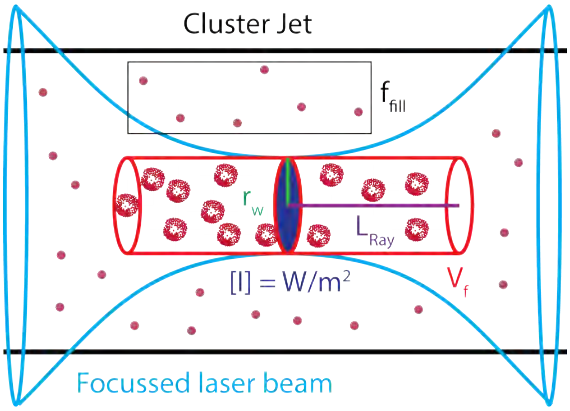

Figure 6.8: Schematic illustration of the cluster jet

Validation and verification This calculation provides us with the required field intensity for the electron ejection and the number of fusion reactions per cluster, for which the forced oscillator model (which we derived in chapter 4) and generalised Coulomb model (which we derived in chapter 5) are used. We have investigated special cases and provided a comparison with electron ejection models in literature in section 4.2.3. In section 4.2.4 we have compared the forced oscillator model with particle tracer simulations, from which it was concluded that the forced oscillator model provides an overestimation of η by up to 15 %. For the validation/verification of the generalised Coulomb model, the generalised Coulomb model predictions agree well with the result of special cases $\alpha = 0$ in sections 6.2, 5.1 and $\alpha = 2$ in section 6.2. In section 5.3 we have compared the generalised Coulomb model with particle tracer simulations in the case of a heterogeneous cluster and an agreement within 15 % between generalised Coulomb model and particle tracer simulations has been found. For single cluster fusion, the only addition to these models is a fusion calculation each time a shock shell occurs. Each numerical routine in this calculation has been tested thoroughly: the changes in density upon expansion are taken into account; the increase in volume of a shell upon expansion is taken into account and we tested that the sum of all collision times of a overtaking shell colliding into outer shells corresponds with the time interval between overtaking the first and last shell. In addition we tested that the model only predicts fusion reactions when shock shell collisions occur at sufficiently high α and sufficiently large clusters (otherwise the collision energy is not high enough for fusion (DD)). Moreover, the single cluster fusion results for DT presented later in this chapter correspond with results from molecular dynamics simulations from [27], which will be discussed in more detail in the discussion.

From single cluster to cluster jet Now we have calculated: the field intensity required, the fusion yield per cluster and the minimal required energy per cluster. In an experiment, a jet of clusters is irradiated, which is shown in figure 6.8. In order to translate the single cluster fusion yield to a cluster jet, we assume that each cluster in the cluster jet is identical and has the same fusion yield. Now we have to calculate how many can be irradiated by a single pulse.

We assume that the laser pulse energy is $E_j = 10$ J, with a laser pulse duration of $\tau_L = 20$ fs. The laser pulse energy and the field intensity are related by: $E_j = I_0 \pi r_w^2 \tau_L$, in which r_w is the laser beam waist. Hence, the required intensity (obtained from the forced oscillator model) sets the optimal laser beam waist, which determines the irradiated volume V_f and the Rayleigh length L_{Ray} (see figure 6.8). By using the Rayleigh length, the neutron pulse duration can be approximated, in the case of neutronic fusion. This can be a different particle, such as an α particle (proton-boron fusion), in the case of a-neutronic fusion.

In order to translate the single cluster results to a multi-cluster jet, laser beam attenuation effects have to be taken into account. In chapter 5 we concluded that the generalised Coulomb model is valid for $\eta > 0.7$. The required electric field for $\eta = 0.7$ is 49 % lower than for $\eta = 1$

(which can be determined using equation 4.3), which results in an approximately 30 % decrease in pulse intensity. Hence if the laser intensity equals the critical laser intensity for electron ejection and less than 30 % of the laser energy is absorbed by the cluster, we expect the Coulomb model to be valid. Hence we assume that up to 30 % of the laser energy can be absorbed by the clusters, which sets a condition on the maximum amount of clusters in the irradiated volume - which sets a maximum on the fraction of laser irradiated volume filled by clusters: f_{fill}. In this rudimentary model for the beam attenuation, we have not taken into account that the cluster charge shielding by the electrons. Another limitation of how many clusters can reside in the focal volume of the laser pulse is the available space required for the cluster's expansion - which has to be at least one cluster diameter. One cluster diameter free space between the clusters results in a theoretical maximum packing factor (regardless of energy absorption) of $\frac{1}{4}$ (required basis cubic lattice) times the sphere packing ratio in a cubic lattice: $\frac{\pi}{6}$, which corresponds to 0.13. When the number of irradiated clusters is limited by packing factor restrictions, the multi-cluster jet Q-factor would be less than 30 % of the theoretically ideal Q-factor, otherwise the multi-cluster jet Q-factor would be 30 % of the theoretically ideal Q-factor.

6.6 Single cluster fusion results

We have discussed that single cluster fusion can occur by using peaked density clusters ($\alpha > 2.5$, which we assume to be composed of one ion specie) and by using heterogeneous clusters (assumed homogeneous with two fusion ion species with a different mass/charge ratio). Using this understanding, we will study and optimise the single cluster neutron yield for three different fusion reactions: deuterium-deuterium - to illustrate cluster fusion in peaked density clusters; deuterium-tritium - to investigate neutronic single cluster fusion in heterogeneous clusters and proton-boron - to investigate a-neutronic single cluster fusion in heterogeneous clusters. For each case the fusion yield is optimised with a maximum cluster radius of 100 nm and a maximum (core) density of 10^{29} m^{-3} [1] to ensure laser attenuation effects do not play a role for a single cluster.

6.6.1 Deuterium - Deuterium - Fusion

In the DD fusion reaction two deuterons are fused together to obtain one neutron and one helium particle (in this approach the DD reaction resulting in tritium is neglected): ${}^2_1\text{D} + {}^2_1\text{D} \rightarrow {}^3_2\text{He} + {}^1_0\text{n}(2.45\text{MeV})$.

The single cluster DD fusion yield has been optimised for peaked density profiles described by equation 6.1, resulting in an optimised neutron yield of 0.1 neutrons per cluster with a density of 10^{29} m^{-3}, radius of 100 nm, $f = 0.42$ (relative radius of homogeneous density core - see equation 6.1) and $\alpha = 6.7$ (density decay power - see equation 6.1) and a single cluster neutron pulse duration of 4 fs. In this case, the single cluster fusion collision energies are limited to 180 keV, which is far below the optimal DD fusion cross-section of 1 MeV. Hence, in this case, the single cluster fusion yield might be enhanced by using heterogeneous clusters to enhance the collision energies. The single cluster neutron yield is too small to be detectable without a multi-cluster jet. To eject the electrons from the cluster a laser intensity of 2.9×10^{24} W/m^2 is required, which would be possible with very intense laser pulses (the most intense, short laser pulses at the moment can obtain intensities of $10^{25} - 10^{26}$ W/m^2 [88]). In this case a theoretically ideal Q-value of 1.2×10^{-8} would be obtained, which is lower than what is obtained experimentally [8] by multi-cluster fusion.

For a 10 J, 20 fs laser pulse, the required laser intensity would result in a laser-beam waist of 7.4μ m and a Rayleigh length of 250μ m. The number of irradiated clusters is limited by energy restrictions to 2×10^6 clusters, which leads to a neutron pulse of 2×10^5 neutrons within 840 fs, which is low compared to the multi-cluster fusion yield ($10^5 - 10^6$ neutrons / J) [83, 25, 5]. However, the neutron pulse duration of a single cluster fusion source is a factor 1000 shorter compared to a multi-cluster pulse duration: indicating that a very short neutron pulse can result from single cluster DD fusion. Additionally, the instantaneous neutron flux *during* the neutron pulse would be 2×10^{22} neutrons/s m^2, which is in the order of 100 times higher than for multi-cluster fusion and is significantly higher than the neutron flux predicted for the International Fusion Materials Irradiation Facility (IFMIF) (10^{18} neutrons/s m^2 - 14.1 MeV neutrons compared to 2.45 MeV neutrons obtained by DD fusion), which is designed to test fusion materials and is predicted to break the current hot neutron flux record [89]. Because the instantaneous neutron yield for single cluster fusion is higher than for multi-cluster fusion, the single cluster neutron pulse and multi-cluster neutron pulse from DD might be separable by time resolved neutron measurements.

6.6.2 Deuterium - Tritium - Fusion

In the DT fusion reaction one deuterium ion and one tritium ion are fused together to obtain one helium particle and one neutron ${}^3_1\mathrm{T} + {}^2_1\mathrm{D} \rightarrow {}^4_2\mathrm{He} + {}^1_0\mathrm{n}(14.1\mathrm{MeV})$. The advantage of this fusion reaction with respect to DD is that the likeliness for fusion (i.e. the fusion cross-section) is larger; the optimum of the fusion cross-section is at a lower collision energy than for DD and the resulting neutrons from the DT reaction are more energetic than from the DD reaction. Therefore, it is expected that the DT fusion yield is larger than the DD fusion yield. However, the disadvantage of this fusion reaction is that tritium is generally hard to obtain and is radioactive.

Single cluster DT fusion occurs due to the mass difference of deuterium and tritium (heterogeneous cluster with a homogeneous density). Optimising the single cluster DT fusion yield results in a yield of 170 fusion reactions per cluster, with a neutron pulse duration of 8 fs for a single cluster. This would require a cluster with a (deuterium, tritium combined) density of 2×10^{29} m^{-3} and a radius of 100 nm. In this case, the single cluster neutron yield might be measurable without using a multi-cluster jet. The ions collide against each others with energies ranging from 0 keV to 400 keV, which is sufficient for achieving the optimal DT fusion cross-section of 100 keV. The given density and radius would require an exceptionally intense laser field of 7×10^{25} W/m^2, which is just manageable by the world's most intense laser pulses. In this case, an ideal Q-factor of 4×10^{-7} would be obtained, which is comparable to current Q-values of DD multi-cluster fusion. The *fusion yield per cluster* has been optimised given the limitations, which does not mean that the Q-factor or single cluster fusion yield in a multi-cluster jet is optimised. In fact, by using smaller DT clusters the required laser intensity and the absorbed energy per cluster is reduced, whereas still a reasonably high neutron yield per cluster can be obtained. Therefore, by using smaller DT clusters than here, high Q-values and fusion yields in a multi-cluster jet can be obtained.

For a 10 J, 20 fs laser pulse, the required laser intensity results in a laser beam waist of 1.5 μ m and a Rayleigh length of $10 \mu m$. For those parameters, the number of irradiated clusters would be limited by packing factor restrictions, leading to a maximum of 4500 clusters in the laser focal volume, resulting in 8×10^5 neutron yield of single cluster DT reactions in a multi-cluster jet, which is comparable to experimental fusion yields obtained in current heterogeneous CD_4 experiments [87]. The packing factor restriction is caused by the small laser beam waist (and hence small laser focal volume), which is necessary for the high field required for electron ejection. However, the small size of the cluster irradiated volume also leads to a very short neutron pulse of 40 fs, resulting in an instantaneous neutron flux of 1.5×10^{24} neutrons/s m^2, which is a factor 100 higher than any currently known pulsed neutron flux [90, 91]. This single cluster neutron yield is sufficient to be detected in a single cluster experiment [27]. The single cluster neutron yield in a multi-cluster jet can be separated from the multi-cluster neutron yield by time-resolved measurements.

6.6.3 Proton - Boron - Fusion

The PB fusion mix might be particularly interesting for heterogeneous single cluster fusion because of the large difference in charge/mass ratio of protons and (fully ionised) boron, which leads to relatively high collision velocities. Proton - Boron fusion is a form of a-neutronic fusion which only releases α particles. The PB fusion reaction is: ${}^1_1\mathrm{H} + {}^{11}_5\mathrm{B} \rightarrow 3{}^4_2\mathrm{H}e(8.7\mathrm{MeV})$.

Optimising the proton boron single cluster fusion yield results in a yield of 2.5 fusion reactions per cluster with an α pulse duration of 4 fs, for a total charge density of 9×10^{28} m^{-3} and a radius of 100 nm (maximum radius of the optimisation is 100 nm; maximum total charge density is $\times 10^{29}$ m^{-3}). The reason this duration is shorter than for DT clusters is that the large difference in charge/mass ratio leads to a narrow time interval in which fusion takes place. In addition, due to this large difference, the energies of the collisions (up until 8 MeV) are much higher than the optimal energy for PB fusion, which is at 500 keV. Therefore, the large difference in charge/mass ratio leads to too energetic shock shell collisions and with further tuning of the single cluster expansion process, the collision energies can probably be lowered, leading up to a factor 10 improvement in fusion yield. A laser field intensity of 1.3×10^{25} would be required for stripping the PB cluster, which is a very intense - but practically achievable - laser pulse. In this case, an ideal Q-value of 1.8×10^{-8}, would be obtained - which is lower than for current DD based experiments.

For a 10 J, 20 fs laser pulse, such a laser intensity requires a laser beam waist of 3.5 μ m, resulting in a Rayleigh length of 55 μ m. The number of irradiated clusters is limited by energy restrictions, leading to a maximum of 30000 irradiated clusters, resulting in an α pulse of 3×10^5 α particles. The duration of the α pulse is 190 fs, resulting in an instantaneous α flux of $1.3\times10^{23}\alpha$/s m^2. This indicates that, by using PB fusion, ultrashort, intense α pulses can be created.

6.7 Summary and discussion

In summary we have shown that by using heterogeneous clusters and by using peaked density profiles (which can be obtained in a double pulse setup by exploiting ambipolar-like expansion) it is possible to create mono-energetic ion energy spectra, which can be used to enhance the yield/Q-factor of current cluster fusion schemes by up to a factor 4. Furthermore, we have shown that it is theoretically possible to achieve single cluster fusion by using deuterium, deuterium-tritium and proton-boron clusters, which does not significantly enhance the fusion yield/Q-factor of current multi-cluster fusion schemes, but which can be used to obtain extremely short neutron (DD, DT) and α pulses (PB). Such short neutron pulses result in very high instantaneous neutron fluxes (DT), higher than current instantaneous neutron fluxes for pulsed neutron sources.

Assumptions Obtaining single cluster fusion from peaked density clusters requires exceptionally accurate tuning of the density profile. In this work, we have assumed that the density profile can be tuned in the form of equation 6.1, which we have shown is plausible. Nevertheless, it is unlikely that the required accuracy can be obtained: from sensitivity analysis we have calculated that an inaccuracy of 20 % in the density profile results in a factor 100-150 decrease in the single cluster fusion yield (DD) in the case of a peaked density cluster. Additionally, we have assumed that all the clusters are identical in a cluster jet when translating our single cluster yields to yields obtained in a cluster yet due to single cluster fusion. Nevertheless, experiments indicate that there can be a large deviation of cluster parameters in s cluster jet, although there are methods to improve this [14, 54, 87, 6]. Considering the discussion of the forced oscillator model, the electric field for electron ejection predicted by the forced oscillator model is generally an under-estimation by up to 20 %. Hence, in order to ensure electron ejection, the laser field used for electron ejection for single cluster fusion should be increased by approximately 40 %. Additionally, we have assumed that 30 % of the laser pulse energy can be absorbed by the clusters. However, if $\eta > 0$ the cluster charge is damped by the remaining electrons, leading to less expansion energy. To account for these effects, the laser pulse intensity would have to be approximately 50 % larger than the calculated laser intensities. In the case of DT and PB clusters, this would result in laser intensities which are currently not achievable and the cluster density/radius would have to be decreased to make electron ejection with a lower required laser energy possible. Therefore, given our assumptions, the theoretical predictions for single cluster fusion presented here are optimistic and realistic fusion yields would be - generally - up to a factor 10 lower.

Comparison with literature Our relatively simple calculations correspond with previous theoretical single cluster fusion calculations of [27], where scaled molecular dynamics simulations have been performed to show that the DT fusion yield of a single cluster can be up to 200 (in our case 170), with single cluster fusion durations of 5-15 fs (in our case 3-8 fs). The difference between our process-based model and the scaled molecular dynamics simulation of [27] is that our model is simpler and incorporates the physics of the process - hence its results can be directly physically interpreted. In [29, 26] a single cluster neutron yield of $10^{-3} - 10^{-2}$ per DD cluster using a double pulse scheme is predicted, which is a factor 10 lower than our DD predictions. This can be explained by the fact that we use a peaked density cluster (equation 6.1) instead of a double pulse scheme. When we use our model to calculate the amount of fusion reactions in a double pulse scheme (by using the case of figure 6.7a) similar orders of magnitude are obtained. This shows that our simple model obtains similar solutions than large scale simulations performed in literature - both in the peaked density cluster case and in the heterogeneous cluster case.

Experiment schemes and practical applications Experiments on a single nano-plasma such as [33], where it was indicated that shock shells can be formed in a double pulse scheme, can be used to measure the ion cluster expansion dynamics for the verification of our process-based model. Laser-cluster interaction is generally a method to rapidly and efficiently generate a broad energy spectrum of high energy ions and in this work we have shown that this spectrum can be transformed in a mono-energetic ion energy spectrum, which is more widely applicable than cluster fusion and was found experimentally in [33]. Using mono-energetic ion energy spectra to enhance current cluster fusion schemes is theoretically feasible and can be used as one technique, in combination with other techniques, to enhance the neutron flux in cluster fusion experiments to neutron source application relevant levels. If this is achieved, it might be possible to use cluster fusion to perform time-resolved measurements of neutron damage in a pump-probe experiment [9, 20], which could be used to perform research on neutron material damage in fusion reactor components.

Although single cluster fusion is not viable for enhancing the total cluster fusion yield or enhancing the Q-factor of cluster fusion (when limiting the cluster radius to 100 nm), the results in this work clearly show that generating an ultra-short neutron / α pulse from single cluster fusion is possible - a prediction which should be put under experimental scrutiny. Since single cluster fusion generates ultra-short neutron/α pulses, the single cluster fusion yield in a multi-cluster jet can be verified experimentally by measuring the time-resolved bursts of neutrons (DD/DT) or αs (PB). In addition with an experiment such as [33] of a single DT cluster, it might be possible to measure the neutron yields originating from a single DT cluster. Although multi-cluster fusion is regarded as an ultrashort neutron source, single cluster fusion is much shorter and hence serves a different area of applications. Future applications which might be possible include: performing neutron radiation damage studies on an even shorter timescale [92, 90] (which can be used to visualise the neutron damage cascading), enhancing neutron radiography contrast (fast neutron resonance radiography) [90] and creating astrophysical conditions of heavy element synthesis in the laboratory [90]. The single cluster fusion study of proton-boron clusters shows as a proof-of-concept that single cluster is not only limited to DD or DT clusters. In a similar way, nucleosynthesis for astrophysical research, can also be achieved with single cluster fusion. When ultrashort particle sources (neutrons, alphas) become available, more possible applications of such sources will likely emerge.

6.8 Conclusion

From our work we can conclude that it is theoretically feasible to achieve single cluster fusion and to obtain mono-energetic ion energy spectra from peaked density clusters and heterogeneous clusters. By using a double pulse regime it is possible to obtain mono-energetic ion energy spectra, which can be used to enhance fusion yield in current cluster fusion schemes by up to a factor 4. It has been shown that single cluster fusion is not viable for enhancing the multi-cluster fusion yield. However, it is possible to use single cluster fusion to obtain a sub picosecond pulse of neutrons (DD and DT fusion) or αs (Proton-Boron fusion), which can be distinguished experimentally from the multi-cluster fusion yield by time-resolved measurements. Our predicted instantaneous neutron fluxes from single cluster fusion exceeds other (pulsed) neutron sources and might be applicable for neutron radiation damage studies.

Chapter 7

Summary and Discussion

In this work we derived a process-based model for laser-single cluster interaction, which we used to determine that mono-energetic ion energy spectra can be obtained from the explosion of a cluster with a density gradient and to show te theoretical feasibility of single cluster. First we will discuss the accuracy, reason of implementation and consequence of the main assumptions of the process-based model. Secondly we will discuss the validity of the results and their consequences. Thirdly, we will discuss the merit of our process-based model compared to previous literature. Finally, we will provide an outlook and suggest some experimental schemes to put our theoretical work under experimental scrutiny.

7.1 The process-based model

In chapter 2 we have assumed the field ionisation process, electron ejection process and expansion process can be separated for low-Z clusters, simplifying our process-based model considerably, which can only be done when the characteristic timescales at which these processes occur is different.

Separating the laser-cluster interaction process in three sequential processes However, for the clusters in chapter 6 the characteristic expansion timescale ranges from 20-40 fs. This implies that the electron ejection process has to be shorter than 20 fs, which can only be done by using short laser pulses of 10-20 fs, which is ,considering the required intensities for these laser pulses, touching the limits of what is currently possible. For longer laser pulse durations or smaller characteristic expansion timescales the electron ejection process can no longer be separated and both processes have to be integrated into each other.

This is similar to the high-Z model presented in chapter 4, where it is necessary to integrate the field ionisation and the electron ejection process because the field ionisation process takes place throughout the laser pulse irradiation. The field generated by the space charge locally amplifies the laser field in the cluster, leading to higher ionisation probabilities, which have to be investigated using tunnelling ionisation.

The main strength of our process-based model, compared to literature, is its relative simplicity, about which we will explain more later. When comparing the complexity of the high-Z model with the (equivalent for low-Z clusters) forced oscillator model (equation 4.3), it is evident that integrating the cluster interaction processes leads to a much more complicated model, eradicating some of the benefits of our process-based model compared to literature approaches. An additional problem of integrating the laser-cluster interaction processes is that each process requires different assumptions, which can lead to a violation of self-consistency. For example, in the high-Z model the ion cluster charge density has to be assumed homogeneous for the forced oscillator model, whereas the motion of the electron cloud leads to a boosted electric field in the cluster with a spatial dependence, eventually leading to a non-homogeneous ion charge density. In such cases, the impact of the violation of self-consistency has to be evaluated thoroughly.

An integrated electron ejection and cluster expansion model might be used to investigate more accurately how laser pulse shaping can be used to create a peaked density profile. Additionally, if the laser pulse duration is larger than the characteristic expansion time, the electron ejection process might be sufficiently slow for the cluster to form a peaked density profile directly without any additional requirement [31]. Related to this statement is that in our work it is assumed that clusters are spherical and often homogeneous, whereas it has been predicted might have a decaying edge density [32], which can result in single cluster fusion and/or mono-energetic ion energy spectra directly. Furthermore, integrating the cluster expansion with the electron ejection process might make the forced oscillator model more accurate in certain cases, because in that case it is possible to take the decline of the Mie frequency during the cluster's expansion into account.

Neglecting field ionisation in low-Z clusters For clusters whose atoms are fully ionised by the field (low-Z clusters), field ionisation does not have to be taken into account and it can be assumed the cluster is instantly ionised. The validity of this assumption has been confirmed by particle tracing simulations in chapter 3, where we showed that field ionisation can be neglected within the definition of low-Z clusters. This greatly simplifies our process-based model and bypasses the usage of field ionisation theories, which is still a highly debated subject [44, 62, 47]. Nevertheless, we have implemented field ionisation routines in particle tracer simulations. Ionisation routines determine when an atom/ion is ionised, whereas in instant ionisation schemes the atoms/ions are ionised at the beginning of the simulation. Hence, using ionisation routines effectively reduce the number of charged particles at the beginning of the simulation and because the ionisation probability calculation is numerically less intensive than the $\mathcal{O}(n^2)$ charged particle calculation, field ionisation routines should be used in extensive simulations, because it leads to a decrease in required computer cost.

Electron ejection model After the cluster is ionised a nano-plasma is formed. We assume electrons are displaced by the electric field outside the cluster, after which they are ejected and generally remain ejected from the cluster, which leads to our forced oscillator model (FOM) for the electron ejection process. The FOM converges to literature models in limiting cases, is generally more applicable than current models and is fully analytical.

The electron ejection model is a vital part of our process-based model and although it is more generally applicable than current analytical electron ejection models, its limitations set important limitations on the total laser-cluster interaction model. The forced oscillator model cannot be straightforwardly generalised to remove the need of using these assumptions and if the resulting limitations are too severe, extensive simulations might be required instead.

- The FOM can only take homogeneous densities into account, whereas we require modelling electron ejection in clusters with shaped density profiles. This requires making approximations which might harm the self-consistency of the laser-cluster interaction model.

- Furthermore, it is assumed the laser light can fully penetrate the cluster, which sets limits on the cluster density (10^{29} m^{-3}) and the cluster radius (100 nm) [35, 16]. In [27, 7] simulations have been performed on larger clusters, indicating that this limitation could be a limiting factor in the future.

- In the forced oscillator model, it is assumed the evolution of the laser pulse envelope is quasi-static compared to the oscillation period, which sets limitations on the envelope gradient - and hence the minimum laser pulse duration. This assumption might prove problematic when extrapolating current results to shorter, or pulse-shaped laser pulses. In addition, for certain cluster densities, separation of the laser-cluster interaction processes might require a very short laser pulse. Hence, the quasi-static approximation sets an indirect limit on the density, which we approximate to be around 10^{30} m^3.

- The forced oscillator model is designed to only take field emission of the electrons into account, hence it is unsuitable for determining low electron ejection fractions ($\eta < 0.2$). This limits the validity of our forced oscillator model to $\eta > 0.2$.

Our comparison between the particle tracer simulations and the FOM predictions showed that - as expected - the FOM prediction leads to an overestimation of η of up to 0.15. Hence the required electric field for electron ejection should be at least 20 % higher than predicted by the FOM, leading to an increase in laser pulse intensity of 44 %.

Cluster expansion After a portion of the electrons are ejected from the cluster, the cluster expands due to its self-generated field. By controlling the portion of electrons remaining in the cluster after laser irradiation, the ion expansion dynamics can be tailored within two limits: the Coulomb explosion limit and the ambipolar expansion limit. There are two ways the electrons can be taken into account: using an a priori model for the electrons or using a self-consistent model.

We derived the generalised Coulomb expansion model which requires an a priori electron dynamics model and can be used for analysing heterogeneous clusters and clusters with density gradients. When assuming the electrons are distributed homogeneously across the cluster, accurate results can be used for $\eta > 0.7$. Additionally, it might be possible to use the electron ejection model as an a priori electron dynamics model. Such an integration would allow the study of laser-cluster interaction for long pulses and could be used for studying density profile shaping, as discussed previously. The generalised Coulomb model results correspond within 15 % of particle tracer simulations in the case of heterogeneous clusters and peaked density clusters.

When $\eta < 0.7$ after the laser pulse irradiation, the electron expansion dynamics have to be taken into account self-consistently, which can only be done analytically for single specie clusters with very specific density profiles, resulting in the self-similar solution. This severely limits the application of our process-based model when $\eta < 0.7$. Additionally, there is an unknown delay between the initialisation of the self-similar solution and the electron ejection, which further reduces the applicability of our process-based model in the case of $\eta < 0.7$. Nevertheless, we have shown in a proof-of-principle we are able to crate a sufficiently peaked density cluster for obtaining a mono-energetic ion energy spectrum, by using the self similar solution. However, for obtaining the unknown delay and/or for supporting general density profiles, extensive simulations have to be performed, such as hydrodynamic simulations [33] or molecular dynamics [27] and our process-based model cannot be used.

7.2 Single cluster fusion results

We have used our process-based model to show it is theoretically feasible to obtain mono-energetic ion energy spectra and achieve single cluster fusion by using clusters with density gradients and by using heterogeneous clusters. We have shown that such mono-energetic ion energy spectra can be obtained in a laser double pulse scheme and can increase the fusion yield of current cluster fusion schemes by a factor 4. Recent experiments on laser single-cluster interaction [33] have confirmed that mono-energetic ion energy spectra can be obtained. Obtaining such a spectrum has more potential applications than just cluster fusion. Depending on the potential application, a multi-cluster jet may have to be used. In that case it is important the cluster parameters of each cluster in the cluster jet are the same, which is not experimentally achieved yet [12, 93, 87]. Another issue is laser-cluster interaction leads to a radial ion source, spreading the ion yield across 4 π steradians and lowering the number of ions impacting on the target.

We have shown single cluster fusion is theoretically feasible for deuterium-deuterium fusion using peaked density profiles and for deuterium-tritium/proton-boron fusion using heterogeneous clusters. These fusion schemes do not significantly enhance the fusion yield of current multi-cluster schemes, but can be used to obtain sub-picosecond neutron / α pulses with instantaneous neutron/α fluxes of up to $10^{22} - 10^{24} \frac{\mathrm{n},\alpha}{\mathrm{s\ m}^2}$, which is significantly higher than currently achieved by either continuous or pulsed neutron sources and can potentially lead to new applications.

Although the neutron flux is very high for a very short amount of time, the average neutron flux is lower than for multi-cluster fusion. Considering the neutron flux for multi-cluster fusion is too low for most neutron source applications [9, 20], possible applications for single cluster must be specifically designed for a large instantaneous neutron (or αs) flux and the total number of required neutrons (or αs) should be fairly low. Although it is theoretically possible to perform single cluster fusion by peaked density profiles, we expect this will be very difficult experimentally because single cluster fusion by peaked density profiles is extremely sensitive to the shape of the density profile. A deviation of 20 % in cluster density profile can lead to a factor 100 deviation in fusion yield. Additionally, a cluster jet will be required for obtaining a measurable neutron flux (DD). This implies that every cluster in the cluster jet will need to have a precisely tuned density profile with a maximum deviation of 20 %, which would result in a neutron flux a factor 10-100 lower than our ideal theoretical calculations. In contrast, single cluster fusion by heterogeneous clusters is much more robust and does not require density tuning.

Although single cluster fusion has not been achieved experimentally yet, we expect that our single cluster fusion calculations would correspond relatively fairly well with experimental results - provided the correct density profiles are used and all electrons are ejected from the cluster. The reason we expect a relatively accurate correspondence is that single cluster fusion is "cleaner" than multi-cluster fusion where the interaction of the various exploding clusters with each other leads to a transformation of the ion energy spectra. A good agreement has been found between our process-based model results and the elaborate single cluster fusion simulations of [27, 29, 26], although the cluster parameters used in these simulations deviate from our cluster parameters.

7.3 Merit of this work

In literature, laser - single cluster interaction is mostly studied by using extensive simulation schemes. It is often problematic to use such simulation schemes, because laser-cluster interaction often does not comply with the assumptions of these simulation techniques (see chapter 2.1). Such simulations are computationally expensive and do not provide an intuitive physical explanation of the process intrinsically. In contrast, in this work we have set up a methodology for studying laser-single cluster interaction by using an intrinsically physically intuitive process-based model. Furthermore, computational costs and scaling problems are not an issue of our process-based model. The output of this model is (for the low Z case) is a critical electric field for electron ejection (or an electron ejection fraction when the electric field is provided) and the resulting ion expansion dynamics (provided by radial trajectories of an initial mesh, such as the plots of figures 6.2), 6.5, 6.3). This implies that our process-based model can not only predict the cluster expansion dynamics from the input parameters, which enables controlling the cluster expansion dynamics. Such a prediction can not be provided by extensive simulations during one run, which can only relate input with output (although multiple simulations can be used to map input with output, which can be used to predict input parameters). However, for simplifying the laser-cluster interaction process for our process-based model additional assumptions are required, which were discussed previously. These assumptions can put severe limitations on our process-based model, which are not limiting extensive simulation schemes - such as particle tracer simulations (which have other limitations). Hence, it is recommendable to use our process-based model for an intuitive understanding of the laser-cluster interaction process and for a relatively quick indication of required cluster/laser parameters in combination with extensive simulation schemes for more accurate predictions.

Single cluster fusion calculations have been performed previously in literature and we illustrated our model by reproducing these results. Although calculations on single cluster fusion have been performed previously, the feasibility of single cluster proton-boron fusion has not been shown previously. In addition our methodological approach in section 6.2 provides us with a more intuitive understanding how mono-energetic ion energy spectra and how single cluster fusion can be obtained from applying density gradients to a cluster.

7.4 Outlook, experiments and possible applications

Our model for laser-single cluster interaction is not limited to cluster fusion and is generally applicable. One of the features of laser-cluster interaction is obtaining high ion energies and obtaining highly charged ions, which have been used previously for achieving higher harmonics generation [94]. Additionally, Coulomb explosion "is the most recent powerful probe for arresting reactive intermediates" [95], which can be used to study chemical reactions at a femtosecond timescale: femtochemistry. Laser-cluster interaction can be used to "reveal the secrets of reaction dynamics" [96], and hence is a hot topic in chemistry. This shows that laser-single cluster interaction is more widely applicable, and our general process-based model might be applicable in these fields for a more intuitive understanding of laser-cluster interaction.

However, there is a long way to go before laser-single cluster interaction can be used applications. First, it is important for the verification of laser-single cluster interaction models that the single cluster predictions are put under experimental scrutiny. It is experimentally very difficult to perform measurements on the dynamics of a single cluster, because a laser cluster experiment is usually performed on a multi cluster jet and the interaction of the various clusters with each other "pollutes" the single cluster effects. Ideally, experiments should be performed on a single nano-cluster, which has been achieved recently for the first time [33]. These results correspond with both our model and with simulations in literature. Additionally, it might be possible to measure the momentum spectrum of the ejected electrons of a single nano-cluster by using the technique described in chapter 4. By performing statistics on the momentum spectrum of the ejected electrons it might be possible to deduce the time (and hence laser field strength) at which electron ejection takes place, performing indirect experiments on the electron ejection process. Additionally, high ion charges are measurable and is a single cluster phenomenon. Therefore, after we integrated the electron ejection model and field ionisation models, we can directly relate our charge state predictions with current experiments.

After these model predictions are confirmed experimentally and it has been studied how the cluster parameters can be controlled, the predictions regarding single cluster fusion and obtaining mono-energetic ion energy spectra can be tested experimentally. In our work and in [35] it was calculated that the neutron yield of a single exploding DT cluster might be measurable, which can be used to experimentally verify single cluster fusion. In addition, by using the technique of [33], the ability to obtain mono-energetic ion energy spectra at various ion energies can be tested as an illustration of cluster parameter control.

After the confirmation of obtaining mono-energetic ion energy spectra from a single cluster, the applicability of obtaining mono-energetic ion energy spectra using a cluster jet can be studied experimentally. An ultra-short mono-energetic ion energy source might be used for several applications, including particle therapy [97, 98] and the development of new plasma diagnostics (proton imaging) [98, 99, 100] which can be used to investigate electromagnetic fields in (dense) plasmas "for the investigation of fundamental plasma physics problems which were impossible to explore until now" [100]. Obtaining mono-energetic ion energy spectra from a cluster jet experiment could serve as an illustration for how accurately the cluster parameters can be controlled throughout a cluster jet. If a high accuracy of cluster parameter control throughout the cluster jet can be achieved, single cluster fusion becomes experimentally feasible. We have calculated that the single cluster fusion neutron schemes might be experimentally verified by time resolved neutron flux measurements, since it is expected the single cluster fusion neutron pulse in a multi-cluster jet is up to a factor 100 higher (and a factor 1000 shorter) than that of multi-cluster fusion schemes. These very short, intense neutron pulses have not been achieved before and can possibly lead to a range of new applications, including time-resolved neutron radiation damage studies [92, 90] to perform measurements on the neutron damaging cascade in an irradiated material. This can prove to be a very valuable diagnostic for studying and developing new "first wall" materials for future fusion reactors [89].

Chapter 8

Conclusion

In this work a process-based model for the laser-single cluster interaction has been presented and compared with extensive particle tracer simulations. The process-based model provides an understanding of the fundamental physical characteristics of each laser-cluster interaction process intrinsically. Using the process-based model, the resulting cluster expansion dynamics can be predicted using the cluster parameters and the laser parameters. Additionally, the process-based model can be used to predict the required laser parameters and cluster parameters, given a preferred ion expansion energy/dynamics. Hence, the process-based model can be used to control the cluster expansion dynamics.

Using our process-based model, we have optimised mono-energetic ion energy spectra and single cluster fusion by using clusters with density gradients or with a combination of several ion species with a different mass/charge ratio. From this investigation we can conclude it is theoretically feasible to achieve mono-energetic ion energy spectra by using a double pulse scheme to control the cluster density gradient. Although we can conclude from our investigation that single cluster fusion is possible for various fusion mixes, leading to neutrons or α particles. However, the resulting fusion yield and the resulting Q-factor are lower than for multi-cluster fusion: hence single cluster fusion does not significantly enhance multi-cluster fusion. Nevertheless, single cluster fusion can theoretically lead to sub picosecond neutron pulses, with a very high instantaneous neutron flux.

Bibliography

[1] I. Last and J. Jortner, *Energetics at extremes in coulomb explosion of large finite systems*, Chemical Physics, 399 (2012), pp. 218–223. vii, 1, 2, 4, 7, 22, 43, 57

[2] M. Murakami and M. Basko, *Self-similar expansion of finite-size non-quasi-neutral plasmas into vacuum: Relation to the problem of ion acceleration*, Physics of plasmas, 13 (2006), p. 012105. vii, 5, 38, 41, 42, 43, 111

[3] M. Murakami and M. Tanaka, *Nanocluster explosions and quasimonoenergetic spectra by homogeneously distributed impurity ions*, Physics of Plasmas, 15 (2008), p. 082702. vii, 4, 5, 10, 38, 40, 41, 42, 43, 52, 79, 111

[4] F. Peano, G. Coppa, F. Peinetti, R. Mulas, and L. Silva, *Ergodic model for the expansion of spherical nanoplasmas*, Physical Review E, 75 (2007), p. 066403. vii, 4, 5, 43, 45, 53

[5] T. Ditmire, J. Zweiback, V. Yanovsky, T. Cowan, G. Hays, and K. Wharton, *Nuclear fusion from explosions of femtosecond laser-heated deuterium clusters*, Nature, 398 (1999), pp. 489–492. 1, 2, 3, 57

[6] J. Zweiback, T. Cowan, J. Hartley, R. Howell, K. Wharton, J. Crane, V. Yanovsky, G. Hays, R. Smith, and T. Ditmire, *Detailed study of nuclear fusion from femtosecond laser-driven explosions of deuterium clusters*, Physics of Plasmas, 9 (2002), p. 3108. 1, 3, 59

[7] A. Heidenreich, I. Last, S. Ron, and J. Jortner, *Conversion of laser energy to nuclear energy driven by coulomb explosion of nanostructures*, Molecular Physics, 111 (2013), pp. 2108–2117. 1, 4, 7, 48, 54, 55, 62

[8] I. Last, S. Ron, A. Heidenreich, and J. Jortner, *Coulomb explosion of nanodroplets drives the conversion of laser energy to nuclear energy*, High Power Laser Science and Engineering, 1 (2013), pp. 69–73. 1, 4, 7, 47, 48, 54, 55, 57

[9] J. Zweiback, T. Cowan, R. Smith, J. Hartley, R. Howell, C. Steinke, G. Hays, K. Wharton, J. Crane, and T. Ditmire, *Characterization of fusion burn time in exploding deuterium cluster plasmas*, Physical Review Letters, 85 (2000), p. 3640. 1, 3, 47, 48, 60, 64

[10] S. Ron, I. Last, and J. Jortner, *Nuclear fusion of deuterons with light nuclei driven by coulomb explosion of nanodroplets*, Physics of Plasmas (1994-present), 19 (2012), p. 112707. 1, 4, 48, 54, 55

[11] F. Baletto and R. Ferrando, *Structural properties of nanoclusters: energetic, thermodynamic, and kinetic effects*, Reviews of modern physics, 77 (2005), p. 371. 1

[12] T. Ditmire, E. Springate, J. Tisch, Y. Shao, M. Mason, N. Hay, J. Marangos, and M. Hutchinson, *Explosion of atomic clusters heated by high-intensity femtosecond laser pulses*, Physical Review A, 57 (1998), p. 369. 2, 14, 22, 33, 37, 43, 63

[13] J. Posthumus, *Molecules and clusters in intense laser fields*, Cambridge University Press, 2009. 2

[14] V. P. Krainov and M. Smirnov, *Cluster beams in the super-intense femtosecond laser pulse*, Physics reports, 370 (2002), pp. 237–331. 2, 3, 4, 5, 7, 14, 22, 23, 25, 26, 29, 30, 32, 34, 37, 59, 82

[15] V. Krainov and M. Smirnov, *Charge composition of a cluster plasma upon irradiation of large atomic clusters by the field of a superatomic femtosecond laser pulse*, Journal of Experimental and Theoretical Physics, 94 (2002), pp. 745–750. 2, 3, 22, 23, 25, 26, 29, 30, 82

[16] I. Last and J. Jortner, *Electron and nuclear dynamics of molecular clusters in ultraintense laser fields. i. extreme multielectron ionization*, The Journal of chemical physics, 120 (2004), p. 1336. 2, 4, 5, 22, 25, 26, 32, 62, 82

[17] R. Hartke, D. Symes, F. Buersgens, L. Ruggles, J. Porter, and T. Ditmire, *Fusion neutron detector calibration using a table-top laser generated plasma neutron source*, Nuclear Instruments and Methods in Physics Research Section A: Accelerators, Spectrometers, Detectors and Associated Equipment, 540 (2005), pp. 464–469. 2, 47

[18] J. Davis, G. Petrov, and A. Velikovich, *Fusion neutron yield from high intensity laser-cluster interaction*, Physics of plasmas, 13 (2006), p. 064501. 2, 47

[19] A. Heidenreich, J. Jortner, and I. Last, *Cluster dynamics transcending chemical dynamics toward nuclear fusion*, Proceedings of the National Academy of Sciences, 103 (2006), pp. 10589–10593. 2, 4, 40, 41, 47, 52

[20] P. Parks, T. Cowan, R. Stephens, and E. Campbell, *Model of neutron-production rates from femtosecond-laser–cluster interactions*, Physical Review A, 63 (2001), p. 063203. 3, 5, 25, 26, 30, 33, 48, 60, 64

[21] B. Shokri, A. Niknam, and M. Smirnov, *Ionization processes in the ultrashort, intense laser field interaction with large clusters*, Laser and Particle Beams, 22 (2004), pp. 45–50. 3, 29, 30, 34, 82

[22] I. S. Anderson, R. L. McGreevy, and H. Z. Bilheux, *Neutron imaging and applications*, vol. 200, Springer, 2009. 3

[23] T. Tajima, Y. Kishimoto, and T. Masaki, *Cluster fusion*, Physica Scripta, 2001 (2001), p. 45. 3, 4, 7, 10, 14, 37

[24] Y. Kishimoto, T. Masaki, and T. Tajima, *High energy ions and nuclear fusion in laser–cluster interaction*, Physics of Plasmas, 9 (2002), p. 589. 3, 7, 8

[25] K. W. Madison, P. K. Patel, M. Allen, D. Price, and T. Ditmire, *Investigation of fusion yield from exploding deuterium-cluster plasmas produced by 100-tw laser pulses*, JOSA B, 20 (2003), pp. 113–117. 3, 48, 57

[26] F. Peano, J. Martins, R. Fonseca, F. Peinetti, R. Mulas, G. Coppa, I. Last, J. Jortner, and L. Silva, *Expansion of nanoplasmas and laser-driven nuclear fusion in single exploding clusters*, Plasma Physics and Controlled Fusion, 50 (2008), p. 124049. 4, 10, 32, 38, 41, 42, 43, 53, 60, 64

[27] I. Last and J. Jortner, *Nucleosynthesis driven by coulomb explosion within a single nanodroplet*, Physical Review A, 77 (2008), p. 033201. 4, 38, 47, 54, 56, 58, 59, 62, 63, 64

[28] I. Last, S. Ron, and J. Jortner, *Aneutronic h+ b 11 nuclear fusion driven by coulomb explosion of hydrogen nanodroplets*, Physical Review A, 83 (2011), p. 043202. 4, 47

[29] I. Last, F. Peano, J. Jortner, and L. Silva, *Overrun effects in nuclear fusion within a single coulomb exploding nanodroplet*, The European Physical Journal D-Atomic, Molecular, Optical and Plasma Physics, 57 (2010), pp. 327–334. 4, 38, 53, 60, 64

[30] A. V. Andreev, V. M. Gordienko, and A. B. Savel'ev, *Nuclear processes in a high-temperature plasma produced by an ultrashort laser pulse*, Quantum electronics, 31 (2001), p. 941. 4

[31] F. Peano, R. Fonseca, J. Martins, and L. Silva, *Controlled shock shells and intracluster fusion reactions in the explosion of large clusters*, Physical Review A, 73 (2006), p. 053202. 4, 5, 10, 53, 62

[32] A. E. Kaplan, B. Y. Dubetsky, and P. Shkolnikov, *Shock shells in coulomb explosions of nanoclusters*, Physical review letters, 91 (2003), p. 143401. 4, 5, 14, 37, 38, 39, 40, 41, 62

[33] D. D. Hickstein, F. Dollar, J. A. Gaffney, M. E. Foord, G. M. Petrov, B. B. Palm, K. E. Keister, J. L. Ellis, C. Ding, S. B. Libby, et al., *Observation and control of shock waves in individual nanoplasmas*, Physical review letters, 112 (2014), p. 115004. 4, 33, 53, 54, 60, 63, 65

[34] M. Murakami and K. Mima, *Efficient generation of quasimonoenergetic ions by coulomb explosions of optimized nanostructured clusters*, Physics of Plasmas, 16 (2009), p. 103108. 4, 38, 40, 41, 52

[35] I. Last and J. Jortner, *Scaling procedure for simulations of extreme ionizations and coulomb explosion of large clusters*, Physical Review A, 75 (2007), p. 042507. 4, 5, 7, 10, 62, 65

[36] T. Ditmire, J. G. Tisch, E. Springate, M. Mason, N. Hay, R. Smith, J. Marangos, and M. Hutchinson, *High-energy ions produced in explosions of superheated atomic clusters*, Nature, (1997). 4, 22

[37] P. Mulser and D. Bauer, *High power laser-matter interaction*, vol. 238, Springer, 2010. 4, 87, 88

[38] D. Bauer, *Theory of intense laser-matter interaction*, URL: `http://www.physik.uni-rostock.de/fileadmin/Physik/Bauer/tilmi.pdf`, (2006). 4, 18, 20, 77, 92, 101

[39] F. Grossmann, *Theoretical Femtosecond Physics: Atoms and Molecules in Strong Laser Fields*, vol. 48, Springer, 2008. 4, 18, 20

[40] A. Landsman, *Laser-atom interactions.* Lecture notes ETH Zurich `http://www.ulp.ethz.ch/education/LaserAtomInteractions`. 4, 18, 20, 86, 87

[41] H. Reiss, *High-field laser physics.* Lecture notes ETH Zurich `http://www.ulp.ethz.ch/education/HighFieldPhysics`. 4, 18, 20, 87

[42] H. Reiss, *The tunneling model of laser-induced ionization and its failure at low frequencies*, arXiv preprint arXiv:1403.0568, (2014). 4, 18, 20, 86, 90, 91

[43] H. Reiss, *Limits on tunneling theories of strong-field ionization*, Physical review letters, 101 (2008), p. 043002. 4, 18, 20, 90, 91

[44] V. S. Popov, *Tunnel and multiphoton ionization of atoms and ions in a strong laser field (keldysh theory)*, Physics-Uspekhi, 47 (2004), p. 855. 4, 18, 19, 20, 62, 96, 100

[45] H. R. Reiss, *Theoretical methods in quantum optics: S-matrix and keldysh techniques for strong-field processes*, Progress in quantum electronics, 16 (1992), pp. 1–71. 4, 18, 20, 87, 90

[46] H. Reiss, *Limitations of gauge invariance*, arXiv preprint arXiv:1302.1212, (2013). 4, 20, 86, 90, 91, 97

[47] L. Gallmann, A. Landsman, M. Weger, J. Maurer, R. Boge, A. Ludwig, S. Heuser, C. Cirelli, and U. Keller, *Tunneling time in ultrafast science is real and probabilistic*, in Lasers and Electro-Optics Europe (CLEO EUROPE/IQEC), 2013 Conference on and International Quantum Electronics Conference, IEEE, 2013, pp. 1–1. 4, 18, 20, 25, 27, 29, 62, 86

[48] P. Eckle, A. Pfeiffer, C. Cirelli, A. Staudte, R. Dörner, H. Muller, M. Büttiker, and U. Keller, *Attosecond ionization and tunneling delay time measurements in helium*, science, 322 (2008), pp. 1525–1529. 4, 25, 27, 29

[49] A. Heidenreich, I. Last, and J. Jortner, *Extreme multielectron ionization of elemental clusters in ultraintense laser fields*, Israel Journal of Chemistry, 47 (2007), pp. 243–252. 5

[50] V. P. Krainov, H. R. Reiss, and B. M. Smirnov, *Appendix J: Properties of the Generalized Bessel Function*, Wiley-VCH Verlag GmbH & Co. KGaA, 2005, pp. 273–275. 5, 87

[51] R. Annou and V. Tripathi, *Femtosecond laser pulse induced coulomb explosion*, arXiv preprint physics/0510014, (2005). 5, 8, 14, 38, 39, 41

[52] R. P. Drake, *High-energy-density physics: fundamentals, inertial fusion, and experimental astrophysics*, Springer, 2006. 5, 14, 38, 39, 41

[53] F. Peano, F. Peinetti, R. Mulas, G. Coppa, and L. Silva, *Kinetics of the collisionless expansion of spherical nanoplasmas*, Physical review letters, 96 (2006), p. 175002. 5, 26, 38

[54] J. Zweiback, R. Smith, T. Cowan, G. Hays, K. Wharton, V. Yanovsky, and T. Ditmire, *Nuclear fusion driven by coulomb explosions of large deuterium clusters*, Physical review letters, 84 (2000), p. 2634. 8, 59

[55] M. R. Islam, U. Saalmann, and J. M. Rost, *Kinetic energy of ions after coulomb explosion of clusters induced by an intense laser pulse*, Physical Review A, 73 (2006), p. 041201. 8, 14, 38, 39, 41

[56] M. d. L. S.B. de Geer, *General Particle Tracer - User Manual*, vol. Version 3.10. 8, 9, 10

[57] S. de Geer and M. de Loos, *Pulsar physics - general particle tracer*. Webpage `http://www.pulsar.nl/`. 8

[58] R. A. Fonseca, L. O. Silva, F. Tsung, V. K. Decyk, W. Lu, C. Ren, W. B. Mori, S. Deng, S. Lee, T. Katsouleas, et al., *Osiris: A three-dimensional, fully relativistic particle in cell code for modeling plasma based accelerators*, in Computational ScienceICCS 2002, Springer, 2002, pp. 342–351. 9, 18, 19, 20, 82

[59] S. Martins, R. Fonseca, O. Silva, S. Deng, T. Katsouleas, F. Tsung, and W. Mori, *Tunneling ionisation in osiris*, in 31st EPS Conference on Plasma Physics, 2004. 9, 19, 20, 78, 82

[60] A. Pak, K. Marsh, S. Martins, W. Lu, W. Mori, and C. Joshi, *Injection and trapping of tunnel-ionized electrons into laser-produced wakes*, Physical review letters, 104 (2010), p. 025003. 9, 20, 78, 82

[61] S. Deng, C. Barnes, C. Clayton, C. O'Connell, F. Decker, P. Emma, O. Erdem, C. Huang, M. Hogan, R. Iverson, et al., *Modeling of beam-ionized sources for plasma accelerators*, in Particle Accelerator Conference, 2003. PAC 2003. Proceedings of the, vol. 3, IEEE, 2003, pp. 1933–1935. 9, 20, 78, 82

[62] P. Eckle, M. Smolarski, P. Schlup, J. Biegert, A. Staudte, M. Schöffler, H. G. Muller, R. Dörner, and U. Keller, *Attosecond angular streaking*, Nature Physics, 4 (2008), pp. 565–570. 18, 20, 25, 27, 29, 62

[63] M. V. Ammosov, N. B. Delone, and V. P. Krainov, *Tunnel ionization of complex atoms and atomic ions in electromagnetic field*, in 1986 Quebec Symposium, International Society for Optics and Photonics, 1986, pp. 138–141. 18, 19, 20, 89, 96, 100, 101

[64] L. D. Landau, E. Lifshitz, J. Sykes, J. Bell, and M. Rose, *Quantum mechanics, non-relativistic theory: Vol. 3 of course of theoretical physics*, Physics Today, 11 (2009), pp. 56–59. 18, 19, 20, 92

[65] A. Perelomov, V. Popov, and M. Terentev, *Ionization of atoms in an alternating electric field*, Sov. Phys. JETP, 23 (1966), pp. 924–934. 18, 19, 20, 88, 89, 96, 97, 100, 101

[66] R. Murray, *Tunnel Ionization in Strong Fields in atoms and molecules and its applications*, PhD thesis, University of Waterloo, 2011. 18, 20, 86, 90, 92, 97, 101

[67] S. Augst, D. Strickland, D. D. Meyerhofer, S.-L. Chin, and J. H. Eberly, *Tunneling ionization of noble gases in a high-intensity laser field*, Physical review letters, 63 (1989), p. 2212. 18

[68] D. J. Griffiths and E. G. Harris, *Introduction to quantum mechanics*, vol. 2, Prentice Hall New Jersey, 1995. 18, 92, 97

[69] J. J. Sakurai and S. F. Tuan, *Modern quantum mechanics*, vol. 104, Addison-Wesley Reading (Mass.), 1994. 18, 97

[70] A. A. Radzig and B. M. Smirnov, *Reference data on atoms, molecules, and ions (springer series in chemical physics)(volume 31)*, Springer, 2012. 19, 89, 100

[71] D. Bauer and P. Mulser, *Exact field ionization rates in the barrier-suppression regime from numerical time-dependent schrödinger-equation calculations*, Physical Review A, 59 (1999), p. 569. 19

[72] D. R. Hartree, *The wave mechanics of an atom with a non-coulomb central field. part i. theory and methods*, in Mathematical Proceedings of the Cambridge Philosophical Society, vol. 24, Cambridge Univ Press, 1928, pp. 89–110. 19, 89, 101

[73] N. Delone and V. P. Krainov, *Energy and angular electron spectra for the tunnel ionization of atoms by strong low-frequency radiation*, JOSA B, 8 (1991), pp. 1207–1211. 20, 81

[74] U. Saalmann, C. Siedschlag, and J. Rost, *Mechanisms of cluster ionization in strong laser pulses*, Journal of Physics B: Atomic, Molecular and Optical Physics, 39 (2006), p. R39. 25, 26, 29

[75] D. Bauer and A. Macchi, *Dynamical ionization ignition of clusters in intense short laser pulses*, Physical Review A, 68 (2003), p. 033201. 25, 26, 34

[76] J. Lawson, *Lasers and accelerators*, IEEE Transactions on Nuclear Science, 26 (1979), pp. 4217–4219. 26

[77] Y. I. Salamin, S. Hu, K. Z. Hatsagortsyan, and C. H. Keitel, *Relativistic high-power laser–matter interactions*, Physics Reports, 427 (2006), pp. 41–155. 26, 105

[78] P. Mulser and D. Bauer, *High power laser-matter interaction*, vol. 238, Springer, 2010. 26, 86

[79] A. Chao, *Lecture notes on topics in accelerator physics*, SLAC.-PUB, 9574 (2002). 26, 105

[80] A. N. Pfeiffer, C. Cirelli, M. Smolarski, and U. Keller, *Recent attoclock measurements of strong field ionization*, Chemical Physics, 414 (2013), pp. 84–91. 29

[81] S. H. Strogatz, *Nonlinear dynamics and chaos (with applications to physics, biology, chemistry a*, Perseus Publishing, 2006. 31, 32

[82] F. Peano, R. Fonseca, and L. Silva, *Dynamics and control of shock shells in the coulomb explosion of very large deuterium clusters*, Physical review letters, 94 (2005), p. 033401. 38, 39

[83] K. Madison, P. Patel, D. Price, A. Edens, M. Allen, T. Cowan, J. Zweiback, and T. Ditmire, *Fusion neutron and ion emission from deuterium and deuterated methane cluster plasmas*, Physics of Plasmas, 11 (2004), p. 270. 48, 57

[84] R. D. B. Kenneth W. Struve, Jeffrey W. Argo, *Ldrd final report on confinement of cluster fusion with magnetic fields*, tech. report, Sandia National Laboratories, 2011. 48

[85] B. B. Roger Bengston, *Cluster fusion in a high magnetic field.* `http://www.ph.utexas.edu/~iheds/2009talks/Bengtson_Breizman_IHEDS2009.pdf`, 2009. 48

[86] S. Li, Z. Zhou, Y. Tian, H. Lu, W. Wang, J. Ju, H. Li, Y. Xu, Y. Leng, G. Ni, et al., *Energetic proton generation from intense coulomb explosion of large-size ethane clusters*, Physics of Plasmas (1994-present), 20 (2013), p. 043109. 52

[87] H. Zhang, H. Lu, S. Li, Y. Xu, X. Guo, Y. Leng, J. Liu, B. Shen, R. Li, and Z. Xu, *Efficient generation of fusion neutrons from cryogenically cooled heteronuclear clusters irradiated by intense femtosecond lasers*, Applied Physics Express, 7 (2014), p. 026401. 52, 58, 59, 63

[88] T. Ditmire, E. W. Gaul, and M. D. Martinez, *Conceptual design report for the texas petawatt laser at the texas center for high intensity laser science*, TCHILS, Austin, (2004). 57

[89] M. Martone, *Ifmif: International fusion materials irradiation facility conceptual design activity: Final report*, tech. report, ENEA, Frascati (Italy). Dipt. Energia, 1997. 58, 65

[90] I. Pomerantz, E. McCary, A. R. Meadows, A. Arefiev, A. C. Bernstein, C. Chester, J. Cortez, M. Donovan, G. Dyer, E. Gaul, et al., *An ultra-short pulsed neutron source*, in High Intensity Lasers and High Field Phenomena, Optical Society of America, 2014, pp. HTh1B–1. 58, 60, 65

[91] J. M. Carpenter, *Neutron sources for materials research*, in National School on Neutron and X-ray Scattering, 2010. 58

[92] A. Calder, D. J. Bacon, A. V. Barashev, and Y. N. Osetsky, *On the origin of large interstitial clusters in displacement cascades*, Philosophical Magazine, 90 (2010), pp. 863–884. 60, 65

[93] H. Lu, J. Liu, C. Wang, W. Wang, Z. Zhou, A. Deng, C. Xia, Y. Xu, X. Lu, Y. Jiang, et al., *Efficient fusion neutron generation from heteronuclear clusters in intense femtosecond laser fields*, Physical Review A, 80 (2009), p. 051201. 63

[94] C. Deiss, N. Rohringer, J. Burgdörfer, E. Lamour, C. Prigent, J.-P. Rozet, and D. Vernhet, *Laser-cluster interaction: X-ray production by short laser pulses*, Physical review letters, 96 (2006), p. 013203. 65

[95] A. Zewail, *Femtochemistry. past, present and future*, Pure Applied Chemistry, (2000). 65

[96] L. Poth, E. S. Wisniewski, and A. W. Castleman Jr, *Cluster dynamics: fast reactions and coulomb explosion*, Am. Sci, 90 (2002), pp. 342–349. 65

[97] H. Schwoerer, S. Pfotenhauer, O. Jäckel, K.-U. Amthor, B. Liesfeld, W. Ziegler, R. Sauerbrey, K. Ledingham, and T. Esirkepov, *Laser-plasma acceleration of quasi-monoenergetic protons from microstructured targets*, Nature, 439 (2006), pp. 445–448. 65

[98] B. Hegelich, B. Albright, J. Cobble, K. Flippo, S. Letzring, M. Paffett, H. Ruhl, J. Schreiber, R. Schulze, and J. Fernandez, *Laser acceleration of quasi-monoenergetic mev ion beams*, Nature, 439 (2006), pp. 441–444. 65

[99] J. A. Cobble, R. P. Johnson, T. E. Cowan, N. Renard-Le Galloudec, and M. Allen, *High resolution laser-driven proton radiography*, Journal of Applied Physics, 92 (2002), pp. 1775–1779. 65

[100] M. Borghesi, A. Schiavi, D. Campbell, M. Haines, O. Willi, A. MacKinnon, L. Gizzi, M. Galimberti, R. Clarke, and H. Ruhl, *Proton imaging: a diagnostic for inertial confinement fusion/fast ignitor studies*, Plasma physics and controlled fusion, 43 (2001), p. A267. 65

[101] B. Quesnel and P. Mora, *Theory and simulation of the interaction of ultraintense laser pulses with electrons in vacuum*, Physical Review E, 58 (1998), p. 3719. 76

[102] C. Raju, *The electrodynamic 2-body problem and the origin of quantum mechanics*, Foundations of Physics, 34 (2004), pp. 937–962. 79

[103] D. J. Griffiths and R. College, *Introduction to electrodynamics*, vol. 3, Prentice hall Upper Saddle River, NJ, 1999. 79, 80

[104] W. Lotz, *Electron-impact ionization cross-sections for atoms up to z=108*, Zeitschrift fr Physik, 232 (1970), pp. 101–107. 82

[105] L. Keldysh, *Ionization in the field of a strong electromagnetic wave*, Sov. Phys. JETP, 20 (1965), pp. 1307–1314. 84

[106] V. Popov, *Tunneling and above-barrier ionization of atoms in a laser radiation field*, Journal of Experimental and Theoretical Physics, 91 (2000), pp. 48–66. 89, 101

[107] M. Göppert-Mayer, *Elementary processes with two quantum transitions*, Annalen der Physik, 18 (2009), pp. 466–479. 90, 97

[108] E. Sarachik and G. Schappert, *Classical theory of the scattering of intense laser radiation by free electrons*, Physical Review D, 1 (1970), p. 2738. 90, 103, 105

[109] Y. I. Salamin and F. H. Faisal, *Harmonic generation by superintense light scattering from relativistic electrons*, Physical Review A, 54 (1996), p. 4383. 90, 101, 103, 105, 106

[110] V. P. Krainov, *Ionization rates and energy and angular distributions at the barrier-suppression ionization of complex atoms and atomic ions*, JOSA B, 14 (1997), pp. 425–431. 96

[111] A. Loeb, L. Friedland, and S. Eliezer, *Autoresonance laser acceleration of guided quasineutralelectron-positron beams*, Physical Review A, 35 (1987), p. 1692. 105

[112] H. Goldstein, *Classical mechanics*, vol. 4, Pearson Education India, 1962. 105

Appendix A

Additional notes

A.1 Glossary

For the reader's convenience, a glossary of the most important terms used in this thesis is shown in table.

- α: Parameter indicating the steepness of the decline of the density profile.
- Ambipolar-like expansion: The expansion of a nano-plasma with no electrons removed, in which the thermal electron distribution leads to a thermal ion energy distribution.
- Ammosov Delone Krainov tunnelling model (ADK): Quantum mechanical model, based on tunnelling of the electron out of the Coulomb potential, for field ionisation, leading to a field ionisation probability.
- Atomic units: A unit system often used in field ionisation theory where $m_e = e = \hbar = \frac{1}{4\pi\epsilon_0} = 1$ (dimensionless) by definition. For more information see appendix A.4.
- Cluster: Spherical collection of atoms/molecules of solid state density with a radius of 1 to 100 nanometre.
- Barrier suppression ionisation (BSI): Classical model for field ionisation, which can be used to determine at which electric field strength ionisation occurs.
- Cluster expansion: The expansion of the cluster due to an excess of ion charge.
- (Multi-)Cluster jet: When gas is ejected from a nozzle, the gas particles condense as clusters - forming a spray of clusters: a cluster jet.
- Coulomb explosion: The rapid expansion of a cluster when all electrons removed and maximum ion energies are generated.
- Electron ejection: The process in which the light electrons are removed from the cluster by the laser field.
- Electron ejection fraction, η: The fraction of electrons ejected from the cluster. $\eta = 0$ means no electrons are ejected. $\eta = 1$ means all electrons are ejected.
- Electron dynamics: The motion of the electron cloud in the cluster during the laser pulse oscillation.
- Enclosed charge: Charge enclosed by a Gaussian flux surface.
- (Inner) Field ionisation: Perturbing the Coulomb potential by an applied electric field, causing field ionisation.

- Forced oscillator model, (FOM): model used for determining which electric field is required for ejecting the electrons from the cluster, which is based on describing the electron cloud motion using an harmonic forced oscillator. Additionally it can be used to determine the electron ejection fraction and it can be used to describe the electron dynamics.
- Fusion cross-section σ: Parameter indicating the likeliness of a fusion reaction occurring in barns 10^{-28} m^2, which depends on the collision energy.
- Generalised Coulomb Model (GCM): A Coulomb expansion model, which requires the input of an a priori electron dynamics model, which we have generalised to support clusters with arbitrary density profiles and clusters with multiple ion species.
- Heterogeneous cluster: A cluster with multiple ion species.
- ”Injection” phase effect: The effect that a charged particle can obtain a net momentum when it is injected (i.e. appears) in a laser field at a non-zero laser phase.
- International Fusion Materials Irradiation Facility, IFMIF: A facility expected to break current neutron flux records with a continuous neutron flux, which is being constructed to mimic the high neutron load subjected to materials in future fusion facilities.
- Laser beam attenuation: The loss of electric field of the laser pulse due to deposited energy to the clusters, which can cause the laser beam to not fully penetrate the cluster jet/cluster.
- Laser pulse envelope: Shape of the electric field amplitude of the laser as a function of time.
- Laser pulse model: The laser pulse model we use in this work is a monochromatic plane wave linearly polarized electromagnetic field convoluted by a laser pulse envelope. For more information see appendix A.3.
- Multi-cluster fusion, (MCF): Fusion reactions occurring due to the collisions of ions from various clusters colliding due to the explosion of multiple clusters.
- Nano-plasma: State of the cluster in which the cluster contains of a cloud of ions and a cloud of electrons.
- Particle tracer simulations, (PTS): Simulations performed by GPT, which can only take charge particles into account, and calculates the complete interaction between all the charged particles, as explained in section 2.1.
- Peaked density profiles: Ion density profiles which are peaked in the centre of the cluster.
- Process-based model: Our laser-cluster interaction model, which is based in dissecting the laser-cluster interaction in three sequential processes.
- Proton-boron, (PB): An a-neutronic fusion mix, releasing α particles instead of neutrons.
- Restoring force: Attracting force by the cluster space charge on the electron cloud in the electron ejection model - which tries to prevent the electrons from being ejected.
- Self-consistent expansion model: An expansion model, which takes the dynamics of the electrons self-consistently into account, such as the self-similar solution.
- Self-similar solution, (SSS): An algebraic model we use for determining the cluster's expansion with arbitrary electron ejection fraction, which is limited for very specific input density profiles, as discussed in section 5.2.
- Single cluster fusion, (SCF): Fusion reactions occurring during the expansion of a single cluster by colliding faster cluster shells against slower cluster shells.

- Stripping/Stripped: Full removal of the electrons from the cluster during electron ejection.
- Ultra-short: A process with a duration of less than a picosecond.
- (low/high)-Z cluster: If the electric field strength is sufficient for full (BSI) ionisation of the atoms in the cluster - the cluster is a low-Z cluster. If not, the cluster is a high-Z cluster.

A.2 Code

All code will be listed and updated on my GitHUB: `https://github.com/kevinverhaegh/Cluster-Fusion`.

A.3 Laser pulse

The laser pulse used in this work is usually restricted to equation A.1, which is a plane wave linearly polarized electromagnetic field convoluted by an envelope and uses a Gaussian lase pulse shape.

An excerpt of the laser pulse used in this work adopted from chapter 2: "The laser is modelled by a plane wave linearly polarized electromagnetic field convoluted by an envelope, which is provided by the equations A.1. Here the electric field is $\vec{E}$, the magnetic field is $\vec{B}$, the maximum value of the electric field in the laser pulse is E_0, the phase of the laser field is $\eta = \omega_L(t - \frac{z}{c})$, in which ω_L is the laser frequency, t is the time, c is the speed of light and x, y, z represents Carthesian coordinates. The parameter $f(\eta)$ represents the "envelope function", which describes the shape of the laser pulse - usually assumed to be Gaussian: $f(\eta) = \exp(-\frac{1}{2\tau^2}\eta^2)$. The parameter τ represents the width/time duration of the Gaussian laser pulse; e.q, which is related to the Full Width Half Maximum (FWHM) duration by $t_{\mathrm{FWHM}} = 2\sqrt{2\ln 2}\tau$. "

$$
\begin{aligned}
\vec{E} &= E_0 f(\eta)\sin\eta\vec{e}_x \\
\vec{B} &= \frac{E_0}{c} f(\eta)\sin\eta\vec{e}_y \\
\eta &= \omega_L(t - \frac{z}{c})
\end{aligned}
\tag{A.1}
$$

The monochromatic plane wave model for a laser field is a basic mathematical description of a laser beam. Line-width effects (the laser does not have one frequency, but a band of frequencies) have been neglected, which are particularly large for short pulsed (femtosecond) lasers (the monochromatic approximation only holds for continuous wave lasers). Additionally, the laser has a spatial dependence - forming a Gaussian beam. The plane wave description is most accurate in the centre of the laser beam. Hence we assume that laser-single cluster interaction occurs in the centre of the beam. However, when investigating single cluster effects in a multi-cluster jet (in chapter 6), a rudimentary model of the spatial dependence of the laser is required. In that case we assume that within a cylinder, describing the laser focal volume (determined by the Rayleigh length and the waist size), the laser beam can be approximated by a monochromatic plane wave model.

For simplicity, this laser pulse model has also been used in particle tracer simulations. However, in future work, investigating laser-cluster interaction with circular polarization and/or elliptical polarization is possible. This might provide more insight in the laser-cluster interaction process. Additionally it can be used as an extra verification for the laser-atom interaction process, as described in section 4.1.1. It would also be instructive to check the electron ejection of a cluster when it is irradiated by a non-monochromatic laser (a range of laser frequencies might trigger resonance in a range of cluster densities). Although it is possible to use a more accurate laser model in particle tracer simulations, such as the laser model used in [101], taking the spatial dependence of the laser into account will probably not lead to additional information, because particle tracer simulations are limited to one cluster (which is placed in the centre of the laser beam).

A.4 Atomic units and SI units conversion

Atomic units are often used in atomic physics calculations and have been used in this work for the field ionisation calculations. More specifically, we assume Hartree atomic units, which set $m_e = e = \hbar = \frac{1}{4\pi\epsilon_0} = 1$ by definition [38]. Care should be taken when performing dimensional analysis on atomic units. Because the electron mass, charge, Planck's reduced constant and Coulomb constant are set to 1 and *dimensionless* by definition. Hence, other units, such as time, length and electric field become dimensionless as well. In table A we provide a list of important physical quantities, with their units and their value on SI units.

Dimension	Atomic units	Value in SI units
energy	$\frac{m_e e^4}{\hbar^2(4\pi\epsilon_0)^2}$	4.36×10^{-19} J = 27.2 eV
time	$\frac{\hbar^3(4\pi\epsilon_0)^2}{m_e e^4}$	2.42×10^{-17} s
velocity	$\frac{e^2}{4\pi\epsilon_0\hbar}$	2.2×10^{6} m/s
electric field	$\frac{m_e^2 e^5}{\hbar^4(4\pi\epsilon_0)^3}$	5.1×10^{11} V/m
length	$\frac{\hbar^2 4\pi\epsilon_0}{e^2 m_e}$	0.53×10^{-10} m
mass	m_e	9.11×10^{-31} kg
charge	e	1.602×10^{-19} C
action	$\hbar$	1.05×10^{-34} J s

Appendix B

Particle Tracer simulations

First we will discuss how clusters are implemented in GPT and which important considerations should be taken when performing particle tracer simulations in GPT for laser-cluster interactions. Afterwards we will provide more background on three important assumptions in GPT. At last we will conclude with a description of our implementation of field ionisation routines in GPT. The combination of field ionisation routines with a check on retardation and radiation effects are two general, important routines - which might make (with further development) GPT applicable to high field physics research. Examples of such research are: [60, 61, 59], where a relativistic particle-in-cell code has been used for studying high field physics processes.

B.1 Particle tracer simulations and laser-cluster interaction

As explained in chapter 2.1, particle tracer simulations are a viable simulation method for laser-cluster interaction. However, there are some complications which can arise when performing particle tracer simulations on laser-cluster interaction. The aim of this section is to provide an overview of these complications and how to deal with them, for people who use the GPT particle tracer simulation package for laser-cluster interaction in the future.

Computational costs, scaling and integration accuracy First, it should be noted that - although particle tracer simulations scale $\mathcal{O}(N^2)$, for laser-cluster interactions the scaling is more unfavourable. When increasing the amount of particles in a cluster, the electron ejection fraction (for the same laser pulse intensity) decreases. When an electron is not ejected, it will collide frequently against the ions in the cluster. The electron trajectory during these collisions has to be calculated accurately, else numerical inaccuracies can lead to wrong simulation results (for example, the numerical inaccuracy can affect the electron ejection fraction - changing the cluster's expansion dynamics). The accuracy parameter of the Runge Kutta integrator solving the system of equations of motions can be tuned in GPT. This should be small enough, such that the resulting simulation results are no longer affected by increasing the accuracy parameter. The numerical Runge Kutta algorithm changes the required time step to meet the accuracy conditions. When there are many collisions (when an electron is not ejected from the cluster), it becomes more difficult to determine the electron's trajectory with the required accuracy - and the required time step is very small, which leads to much more calculations and a large increase in required computational time. Hence, for laser-cluster interaction the particle tracer simulation scaling is effectively more unfavourable than for standard simulations. This effect becomes large when the electrons remain in the cluster. Hence, it is particularly difficult to perform simulations in GPT with $\eta < 0.5$ using the particle tracer algorithm.

However, when the electron ejection fraction is smaller, particle in cell codes - which have difficulties taking Coulomb explosions into account, start to become more applicable. Hence for future work, it might be worthwhile to dissect a laser-cluster interaction simulation in two parts.

One part with η relatively low, where particle in cell code routine can be applied. And another part when more electrons are ejected from the cluster (larger η)), where a particle tracer simulation strategy is applied.

Discrete effects Particle tracer simulations initialise the cluster by quasi-randomly placing atoms in a sphere (which can be subjective to a certain cluster density distribution). Therefore, by comparing GPT with fluid based models (such as the generalised Coulomb model), the effect of having discrete particles instead of a continuous mass can be investigated. However, this is only correct when the GPT simulation has a sufficient amount of particles. For this approximation to be correct, the continuous distribution should be a good approximation of the discrete particle distribution, which can only be performed for a sufficient amount of particles. In addition, when clusters with a certain density distribution are simulated using particle tracer routines, this issue becomes more critical and a larger number of atoms is required in order for the density of discrete particles to correspond with the intended density profile [3].

B.2 Assumptions

In this section we will discuss two important intrinsic assumptions in GPT, which are not only limitations in the case of laser-cluster interaction, but which are general limitations of GPT.

B.2.1 Retardation and radiation effects

The GPT particle tracer package assumes that the electric emitted by every charged particle is a Coulomb electric field, which are relativistically transformed using a Lorentz transformation. However, the Coulomb electric field is only valid when the particles are relatively static with respect to each other. Considering laser-cluster interaction, this is incorrect.

When charged particles travel relativistically with respect to each other - or when charged particles accelerate/decelerate - deviations on the Coulomb electric field occur, because the Coulomb interaction assumes the interaction between charged particles is instantaneous. However, this is not true: electromagnetic information is carried by a photon, which travels at the speed of light. In order to take this effect into account, the Lienard-Wiechert potentials have to be used instead of the Coulomb potentials. The equations of motion with the Lienard-Wiechert potentials result in a differential equations with derivatives evaluated at a retarded time. This poses a problem, because this no longer leads to an ordinary differential equations - but it leads to a functional differential equation. The behaviour of such an equation is mathematically different than an ordinary differential equation [102]. GPT is not designed to solve functional differential equations and hence retardation and radiation effects cannot be currently implemented in GPT.

Therefore, we have created a model which can be used to check whether the GPT calculations are correct - or not. First, we complete the GPT calculation, which gives us the particle trajectories of all the charged particles in the simulations. Afterwards, we choose a random charged particle and check the Lorentz force on this particle using the Lienard-Wiechert potentials ((10.67 of [103]) and the Lorentz force due to the Coulomb field, where the magnetic arising from a charge particle in motion is included as well. Because the particle trajectories have already been calculated, the retarded force can be relatively easily calculated. If the force from the Lienard Wiechert potentials corresponds with the force provided by the Coulomb field, then it can be said that radiation and retardation effects do not play an important role. When these two forces deviate, it might imply that radiation and retardation effects do play an important role. However, this cannot be said with certainty, while the trajectories have been calculated using the Coulomb force. If the Coulomb force deviates from the retarded force, it means the particle would have obtained a different trajectory. However, when the trajectory is changed, the difference between the Coulomb force and the retarded force also changes. Hence, this model can only be used to give an indication of whether it might be possible that retardation and radiation effects play a role. It should be noted that with radiation effects the interaction of the radiation of one particle on the other particle is implied. Energy losses due to radiation effects have not been checked.

As can be seen from inspecting equation 10.67 in [103], the equation for the retarded force is fairly complicated. In addition, the retarded time has to be accurately predicted. Therefore, numerical errors can be easily obtained. Hence the testing scheme suggested here, has been tested extensively with textbook examples, where the trajectory of two charged particles is determined from which the retarded force can be calculated analytically.

Retardation and radiation effects in clusters After these extensive tests, this model has been used to check when radiation and retardation effects might occur in laser-cluster interaction. From first principles, retardation and radiation effects might occur during a Coulomb explosion. Hence the Coulomb explosion has been tested for dense clusters, but radiation and retardation effects only play a role here when the density is extremely high (higher than 10^{32} m^3), which is a factor 100-1000 higher than the densities generally used in this thesis. The reason for this is that most of the acceleration in a Coulomb explosion occurs in the initial stages of the explosion, where the velocities are relatively low. Radiation effects might play a role when electrons move in anti-phase on the laser field during electric field strengths of more than 10^{12} V/m. This is not realistic for clusters, since a single cluster is lower than the wavelength of the laser. Hence the various electrons of a cluster do not move in anti-phase with respect to each other. Additionally, it has been checked whether an oscillating electron cloud can have an effect on the ions. The answer is that this is possible when electrons are swept through the cluster by a laser field of more than 10^{12} V/m. However, the resulting force (and the duration of this force) is negligible compared to the Coulomb forces between the ions of a cluster. Therefore, conclusively, retardation and radiation effects (not taking the radiation energy losses into account) are not expected to have a significant effect on laser-cluster interaction under the parameters we use.

B.2.2 Cut-off parameter

The cut-off distance of the ions is chosen of the order of the Van der Waals radius, which is an approximation for the size of an atom. The effect of introducing a cut-off parameter is visualised in figure B.1. The cut-off distance of the ions is chosen of the order of the Van der Waals radius, which is one of the earliest approximations for the size of an atom. The reason the cut-off distance is chosen at the Van der Waals distance is that atomic effects are not taken into account: therefore effects that take place at a scale smaller than the Van der Waals distance are not taken into account, which makes it plausible to take the cut-off distance at the Van der Waals radius. However, it should be noted that changing this parameter - especially choosing a smaller cut-off distance - can have a large impact on the simulation - especially on the field ionisation module. When the cut-off distance is small, the Coulomb forces become relatively large when charged particles are close together. This implies that when an "ionisable element" is close to an electron, the electric field of the electron on the "ionisable element" becomes so large that the "ionisable element" is sequentially ionised to a high ion charge.

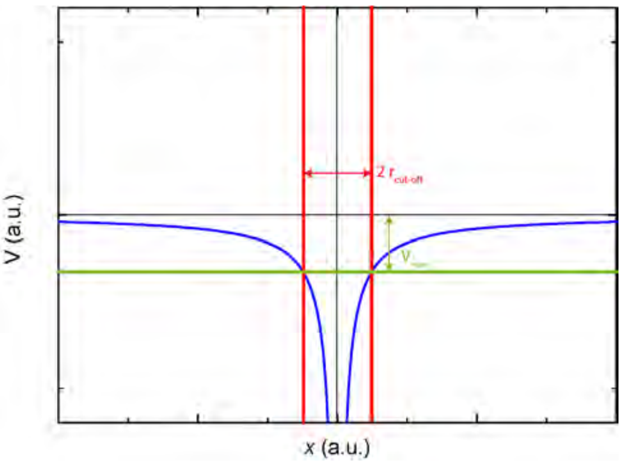

Figure B.1: Illustration of the cut-off parameter.

B.3 Field ionisation in GPT

The implementation of the ionisation process in the analytical model is coupled with the electron ejection process and will be discussed in chapter 4.

The implementation of the ionisation process in the numerical particle tracer model GPT is briefly described in section 2. The ADK tunnelling rate provided by equation C.6 is investigated with Monte-Carlo methods for each "ionisable element" (atom or not-fully ionised ion). This provides the time when the ionisation takes place. At this time, the atom/ion charge is increased by one and an electron is generated in the numerical model. However, in order to initialise an electron in the numerical model, not only the time at which ionisation occurs should be known, but also the electron's position and velocity.

As explained previously, the Coulomb interaction provides a mathematical singularity when the distance goes to zero. In order to counter this singularity in the particle tracing model, a cut-off parameter is introduced in chapter 2.1. The initialisation of the electron's position should be accurate within a single cut-off parameter. The cut-off parameter is taken to be the Van-der-Waals radius of the atom. In a crude approximation, the electron is initialised at the exit point of the perturbed Coulomb potential, as described by equation B.1, where the position of the exit point is calculated. This parameter is usually of the order of the Bohr radius. The Van der Waals radius is of a similar order, implying that the crude approach of initialising the electron at the exit point position is sufficiently accurate.

$$E_z = -\frac{Z}{r} + Er \rightarrow Er^2 - E_z r - Z = 0 \rightarrow r = \frac{E_z + \sqrt{4EZ}}{2E} \tag{B.1}$$

The velocity of the tunnelling electron is provided by the velocity distribution adopted from [73]. The momentum distribution is separated in the momentum in the polarization direction of the laser $p_{\|}$ and the momentum in the perpendicular direction of the laser $p_{\perp}$, as indicated in equation B.2. The equation provided for the momentum distribution in the perpendicular direction of the laser is consistent with the alternative derivation of the PPT model provided in appendix C.1.6. The distribution for the momentum in the perpendicular and parallel direction are not coupled and can be expressed as two separate Gaussians, with width $\sigma_{\|} = \frac{\sqrt{3}E}{\omega\kappa}\sqrt{\frac{E}{2\kappa}}$ for the parallel momentum and $\sigma_{\perp} = \sqrt{\frac{E}{2\kappa}}$ for the perpendicular momentum.

$$\frac{dW}{dt}(p_{\|}, p_{\perp}) = \frac{dW}{dt}(0,0)\exp(-p_{\perp}^2\frac{\kappa}{E} - p_{\|}^2\frac{\gamma^3}{3\omega}) \tag{B.2}$$

As expected and explained in appendix C.1, the width of the momentum distribution is larger in the polarization direction of the electric field of the laser than in the perpendicular direction, because the perpendicular velocity effectively makes it more difficult for tunnelling to occur (the potential well is not perturbed in this direction). In the case of ionisation at the critical BSI field for a hydrogen atom with a $\lambda = 800$ nm laser, the resulting energy distribution of the ionisation ($E = \frac{1}{2}p^2$) is 1.54 eV in the parallel direction, 0.43 eV in the perpendicular direction. In this case, the ponderomotive energy of an electron at this laser intensity is 4.1 eV. Therefore, the energy of the freed electron obtained during ionisation can be of the same order as the ponderomotive energy. When ionisation occurs in the leading edge of the laser pulse, the laser intensity increases significantly in time, increasing the ponderomotive energy of the electron such that the energy of the freed electron obtained during ionisation is negligible. However, when ionisation occurs near the maximum of the laser pulse, the energy obtained by the freed electron during ionisation is comparable to the maximum ponderomotive energy. Therefore, the energy of the electrons obtained during ionisation can have an important effect on the laser-cluster dynamics when the ionisation occurs close to the maximum laser intensity.

It should be noted that the field ionisation theory implemented in GPT can be used generally. The following discussion is about the possibilities of such an implementation and is irrelevant for the rest of this thesis.

Field ionisation is at the basis of most high field physics processes. Supplementing GPT with field ionisation models - in addition to a supplemented routine which can check whether the electrostatic assumption (which is assumed in GPT) is correct (see section 2.1) is one of the steps in order to make GPT a handy tool for high field physics calculations. OSIRIS [58] is a particle-in-cell code often used for high field physics - which is also equipped with ADK field ionisation modules [59]. A clear difference between our work and the work by [59] is that the limits on the validity of tunnelling theories are clearly mentioned. In [59] the tunnelling ionisation routine has been illustrated by performing laser wakefield simulations with an intensity of $I = 2.1 \times 10^2 2$ W/m^2, which is nearly at relativistic intensity. For a wavelength of 800 nm, from $I = 7.1 \times 10^{19}$ W/m^2 magnetic effects are expected to violate the dipole approximation and from $I = 4.3 \times 10^{22}$ W/m^2 relativistic effects are expected to violate the dipole approximation. Nevertheless it should be mentioned that the intensity at which ionisation takes place is not mentioned in [59] and - depending on the pulse shape - this can be significantly lower than $I = 2.1 \times 10^{22}$ W/m^2. Also the observation that tunnelling ionisation reduces calculation time in [59] because the ionisation probability is less computationally costly than the electromagnetic interaction calculations, has been reproduced in GPT.

The field ionisation module in [59] has been used in various papers [60, 61]. In paper [60] it can be seen that ionisation occurs at $a_0 = 2$, which corresponds to $I = 8.7 \times 10^2 2$ W/m^2, violating both the relativistic limit and magnetic limit of tunnelling theories. This illustration illustrates that a thorough analysis on the validity of tunnelling theories is needed before it can be implemented in numerical codes for the analysis of high field physics phenomena.

B.3.1 Collisional ionisation

When an electron oscillates through the cluster, it can collide against an ion and cause ionisation: electron impact ionisation. The effect of collisional ionisation can be estimated by using the semi-empirical Lotz formula in equation B.3 [14, 15, 104, 21]. In here σ is the cross-section of the collision ionisation in atomic units, f_i is the number of electrons in the valence shell of the, E_z is the ionisation energy in atomic units and E_e is the incident electron's energy.

$$\sigma = 2.17 f_i \frac{\ln(E_e/E_z)}{E_e E_z} \tag{B.3}$$

In our approach this ionisation scheme has been neglected. Our initial calculations show that collisional ionisation can play a role in high-Z laser-cluster interaction. However, due to f_i this only occurs at certain ionisation shells. In addition we have shown that taking ADK ionisation into account is much more important for obtaining the predicted synergistic effect of field ionisation and electron ejection than collisional ionisation. The reason for this is that collisional ionisation depends on the incident electron energy, which should be at least the ionisation energy. At high charge states, the ionisation energy is relatively high and the electron impact energy is relatively low. High charge states lead to a higher restoring force, which leads to less less amplitude of the electron cloud, which leads to a lower electron energy. In contrast, at high cluster charges, the enhanced electric field by the cluster space charge is relatively high - and a relatively large portion of the total electric field is dominated by the cluster space charge. Hence it is likely that ADK ionisation is much more effective than collisional ionisation for the ionisation of high-Z clusters, which is confirmed in [14]. However, this disagrees with the predictions of [16], where ADK ionisation is not taken into account (only BSI and collisional ionisation). The problem is that in high-Z clusters ionisation mechanisms can work synergistically. Therefore, although our initial calculations indicate that collisional ionisation is not a dominating effect, the actual effect is hard to predict. Although it is possible in future work to implement collisional ionisation in particle tracer simulations, this would lead to a severe increase in required computational time because the Lotz formula works by using a cross-section and hence the electrons going through this cross-section should be taken into account for every ion.

Appendix C

Additional information

In this chapter we will present additional information, including derivations, on the field ionisation; electron ejection and cluster expansion chapters of this work.

C.1 Field ionisation

First, some background theory of field ionisation in literature will be discussed. Afterwards, the derivation of the Landau, Perelomov, Popov, T'erentev (PPT) and Ammosov, Delone, Krainov (ADK) tunnelling model will follow.

Please note that in this section atomic units are used. In atomic units the electron mass m_e, electron charge e, reduced plank's constant $\hbar$ and the Coulomb constant $\frac{1}{4\pi\epsilon_0}$ are defined as 1 (dimensionless): $m_e = e = \hbar = \frac{1}{4\pi\epsilon_0} = 1$. Making the units of the atomic constant dimensionless, has a large impact on the meaning of a certain unit. Using atomic units in atomic physics is common practice and a conversion table to SI units is provided in appendix A.4.

C.1.1 Regimes of field ionisation

Which mechanism is dominant is determined by the ratio of the laser period and the electron movement period inside the atom, defined as the Keldysh parameter γ [105]. By using some simple approximations, this movement period can be calculated. The "electron movement period" is - when tunnelling occurs - the time it takes for the electron to tunnel: and it is therefore in literature referred to as the tunnelling time T_t.

In figure C.1b, a 1D representation of the potential perturbation is shown. The electric field of the laser perturbs the Coulomb potential in an atom, which causes the effective potential barrier to bend, forming a local maximum. In a single electron atom approach, the Coulomb potential experienced by the single electron is $V_c = -\frac{Z}{r}$, in which Z is the ion charge of the to be ionised ion. The electric field is assumed to be static: $\vec{E} = E\vec{e}_x$, which leads to the perturbed potential in equation C.1. At large distances, the potential can be assumed to be purely dictated by the additional electric field ($r \to \infty, V \to Ex$), which is visualised in figure C.1b.

$$V = -\frac{Z}{r} + Ex \tag{C.1}$$

In this approximation, a triangle is formed between the potential of the applied electric field (Ex), the ionisation potential (depicted by the height of the cyan line in figure C.1b) and the tunnelling distance, here called x can be easily calculated using the small angle approximation $x = \frac{E_z}{E}$. Using the virial theorem, the average kinetic energy of an electron can be calculated

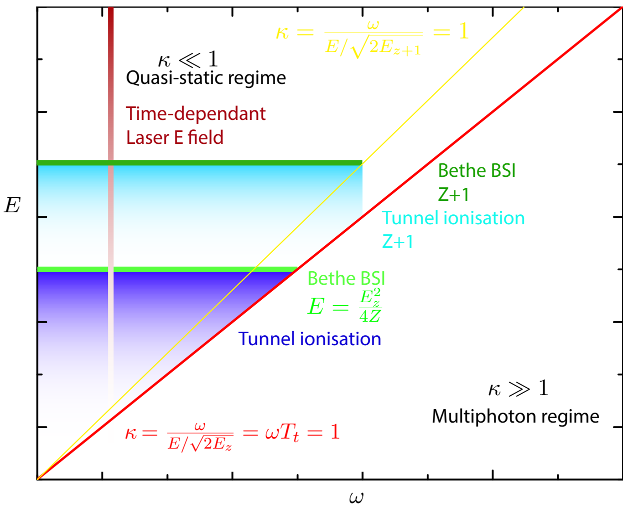

(a) The Keldysh parameter is indicated in an intensity/-frequency plot to indicate the different regimes of field ionisation.

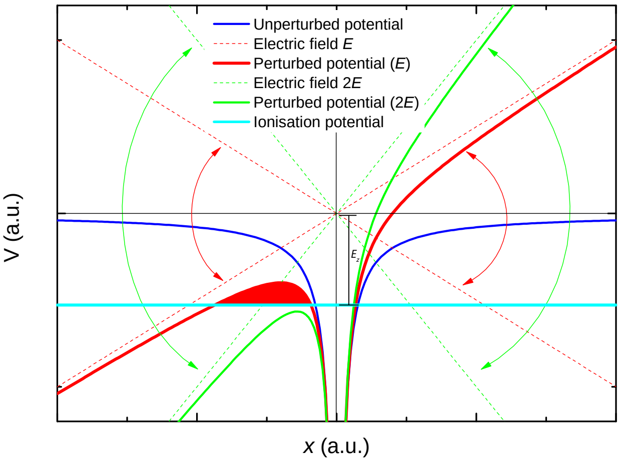

(b) Visualisation of the perturbation of the potential in the quasi-static domain.

from the ionisation potential E_z: $v_g = \sqrt{2E_z}$. In this case, the time it takes for the electron to tunnel is the time it takes for the electron to pass this width is: $T_t = \frac{\sqrt{E_z}}{\sqrt{2E}}$. Tunnelling occurs if the tunnelling time is less than half the period of the laser (a half period of the laser is the effective time the perturbation lasts on one side) which is the Keldysh tunnelling time. However, the Keldysh parameter is usually defined as the Keldysh tunnelling time times the laser frequency and hence this effect is incorporated in the Keldysh tunnelling time $T_t \rightarrow 2T_t \dashrightarrow T_t = \frac{\sqrt{2E_z}}{E}$, leading to the Keldysh parameter shown in equation C.2.

$$\gamma = \frac{\omega}{E/\sqrt{2E_z}} = \omega T_t \tag{C.2}$$

A small Keldysh parameter ($\gamma \ll 1 \rightarrow \omega \ll T_t$) implies that the electron tunnelling time is much smaller than the period of the field and hence it can be assumed that the field is quasi-static (if the tunnelling time is much smaller than the period of the field, the oscillating field has approximately the same field strength during the tunnelling of the electron). In this regime, ionisation is caused by the field nature of the laser irradiation and requires many photons. When the Keldysh parameter is large ($\gamma \gg 1 \rightarrow \omega \gg T_t$), the tunnelling time is much larger than the period of the field. Hence, the perturbation of the Coulomb potential due to the applied field does not cause the electron to leave the potential well (the perturbation moves from one side to the other before the electron has the chance to escape). In order for the electron to escape, it has to ”jump” out of the potential barrier. In order for this to occur, the electron has to absorb the photon energies: so in the multiphoton regime, ionisation takes place because of the photon nature of the laser field and requires less, but more energetic photons. For laser-cluster interaction relevant laser parameters, the probability of this occurring is far smaller than of tunnelling in the quasi-static regime. In figure C.1a the quasi-static regime and multiphoton regime are indicated.

Do note that there is, however, no hard boundary between these two regimes: in reality both processes occur simultaneously and these two regimes are limit cases of the Keldysh parameter. Therefore, there is also some debate about at which Keldysh parameter these regimes should be separated; most sources discuss a boundary between $\gamma = 0.5 - 1$. Moreover, there is some debate on whether the Keldysh parameter is correct for separating these regimes, or whether the Keldysh parameter is a correct indicator for the usability of a certain field ionisation theories, as explained in chapter 3.

C.1.2 Tunnelling and the Strong Field Approximation

There are many different theoretical approaches that result in a field ionisation model which include the probabilistic nature of field ionisation. The reason there are so many different theoretical models is that it is hard to measure atomic processes on attosecond timescales, resulting in heavy debates by theoretical scientists on the nature of laser-atom interaction. Furthermore, it should be noted that the field of laser-atom interaction and field ionisation is vast and that fundamental science on these aspects is still performed today [42, 47, 46, 66, 40, 78]. In order to incorporate the field ionisation process in our numerical and analytical model, analytical ionisation probability functions are required: $\frac{dW}{dt} = f(E, p)$, as it is computationally far too expensive to evaluate the Schrödinger equation numerically in each ionisation event for the numerical model.

A popular method for providing such approximations which allow the problem to be solved analytically is perturbation theory. However, the applied electromagnetic field is so strong, that the region of convergence of perturbation theory is surpassed. Nevertheless, exploiting the fact that the field is so strong, makes it possible to make other approximations, which allow the numerical Time Dependant Schrödinger Equation (TDSE) problem to be solved analytically, resulting in analytical ionisation probability functions. There are two main approaches for providing such functions for intense fields: tunnelling ionisation theories and theories based on the Strong Field Approximation (SFA).

With tunnel ionisation, the quasi-static perturbation problem is investigated quantum mechanically. Instead of the electron escaping the potential barrier classically (BSI model), which is a deterministic process (when the electric field is high enough, ionisation occurs). A quantum-mechanical treatment of the perturbed potential calculates the possibility of the electron tunnelling through the perturbed potential barrier. When the barrier is perturbed (see figure C.1b), there is a finite distance the electron has to pass through the potential in order to escape the potential barrier (which is etched red in the case of the electric field strength E). This finite distance leads to a certain tunnelling probability per unit of time dW/dt. When the perturbation is larger, the distance that is required to tunnel through the barrier is decreased, which enhances the tunnelling probability. Therefore the tunnelling probability is related to the electric field strength $dW/dt = f(E)$.

The problem of tunnel ionisation can be solved by approximating the perturbed wavefunction in an atom. Such wave functions can often be solved semi-classically by using the Wentzel - Kramers - Brillouin (WKB) approximation, which is often used in tunnelling problems and expands the exponential wavefunction by assuming that either the amplitude or phase of the wavefunction is slowly changing. Using the wavefunctions, it is possible to calculate the probability current, which would lead to the tunnelling probability per unit of time: dW/dt.

By applying this general recipe on a static field and the hydrogen atom, the Landau tunnelling ionisation model is obtained (C.3). The full derivation of the Landau tunnelling rate can be found in appendix C.1.5. In the Landau tunnelling ionisation model, the electric field works in one dimension, whereas the hydrogen wavefunction is three dimensional. This problem can be separated in parabolic coordinates and the wavefunction can be approximated by using the Wentzel - Kramers - Brillouin (WKB) approximation. This yields a tunnelling probability function of a constant times an exponential depending on the ratio of the electric field and the ionisation potential.

$$\frac{dW}{dt} = \frac{4}{E} \exp\left(-\frac{2(2E_z)^{3/2}}{3E}\right) \tag{C.3}$$

A large limitation to using the tunnelling theories is the fact that only a quasi-static electric field is taken into account. This results in two problems: when the laser intensity is relatively weak, or the laser frequency is relatively high, the quasi-static approximation no longer holds and tunnelling ionisation theory becomes invalid. Furthermore tunnelling theories take a quasi-static electric field into account, whereas a laser pulse contains both an electric and magnetic field. Therefore, if the magnetic field component becomes too large (more information about this in C.1.4), tunnelling methods start to fail. These limitations lead to a limited regime in laser intensity, frequency space where tunnelling theories are valid, as discussed in section C.1.4.

In contrast, the Strong Field Approximation (SFA) uses a S-matrix approach. This approach is commonly used in scattering theory, where the input and output asymptotes of an interaction are observed - and the dynamics of the interaction itself does not need to be tracked. Although scattering is strictly free-free interaction, whereas ionisation is a bound-free interaction - nevertheless the S-matrix approach is still valid. Before the ionisation, the electron wavefunction is assumed to be a bound wavefunction where the Coulomb interaction is assumed to be so much stronger than the laser interaction, so the laser interaction can be assumed to be non-existent. After ionisation, it is assumed that the laser interaction is much stronger than the Coulomb interaction, therefore the Coulomb interaction is neglected and the wavefunction is that of a free electron in a strong plane wave field: the Volkov wavefunction. Here it is assumed that the ponderomotive energy of the electron (energy of an electron quivering in a laser field) is much stronger than the ionisation energy $U_p > E_z$. Furthermore, it is assumed that the dipole approximation is valid (the laser field is assumed to be constant over the atom: $\omega t - \vec{k} \cdot \vec{r} \approx \omega t$). For more information about the SFA, see [37, 45, 40, 41]. For a linearly polarized field, the SFA ultimately leads to the tunnelling probability provided in equation C.4. The SFA does not only give the ionisation per time, but also per solid angle. The momentum of the electron is p_n, in which n is the amount of absorbed photons and can be calculated by using the conservation condition, which states that the kinetic energy of the photoelectron equals the energy supplied by n photons minus the energy required to overcome the binding energy minus the ponderomotive energy. The kinetic energy of the photoelectron should be positive, implying that $n\omega_L - E_z - U_p > 0$. The first n for which this is possible is n_0, meaning that n_0 photons are required to overcome the binding energy and to supply the interaction energy of the free electron in the field. Furthermore, equation C.4 is a summation over all possible photon absorptions ($n = [n_0, \infty]$). A different number of photons absorbed leads to a different photoelectron energy. Essentially, this summation can be regarded as an integral over the photoelectron energy spectra, which converges. Taking the summation out of the equation would provide a tunnelling probability per solid angle per photonelectron energy (which is quantised by the photon energy of the field). The parameter $\phi_i(\vec{p}_n)$ is the initial momentum space wave function of the electron in the atom before the laser interaction, which can be determined by using Hartree-Fock methods. The function J_n is the generalised Bessel function, which is defined as $J_n(u,v) = \frac{1}{2\pi}\int_{-\pi]}^{\pi} d\theta \exp(i(u\sin\theta + v\sin 2\theta - n\theta))$, where $J_n(u) = J_n(u,0)$ [50]. As will be shown in section C.2, studying the trajectories of an electron in an intense laser field is important for understanding how the electron ejection process occurs. Furthermore, this has important implications for the field ionisation physics. In section C.2 it is shown that an electron in a plane wave laser field, in the rest frame of the electron, travels in a figure-8 motion due to a combined action of electric and magnetic fields. The figure-8 motion has an amplitude in the electric field direction, α_0 and an amplitude along the direction of propagation β_0, generated by the Lorentz force (see figure C.7 and chapter C.2). These dynamics describe the interaction of the laser pulse with a free electron and yield implications for the Volkov wavefunction. Therefore they appear in the generalised Bessel function in the SFA. A close investigation of the validity of tunnelling approximations in section C.1.4 also makes use of this figure-8 motion (because the figure-8 motion contains information about the effect of the magnetic field of a free electron).

$$
\begin{aligned}
\frac{dW}{dtd\Omega} &= \frac{1}{(2\pi)^2}\sum_{n_0}^{\infty} p_n\left(\frac{p_n^2}{2} + E_z\right)^2 |\phi_i(\vec{p}_n)|^2 (J_n(\alpha_0 p_n \cos\theta - \beta_0 c)^2) \\
\frac{p_n^2}{2} &= n\omega_L - E_z - U_p \\
n_0 &= \lceil \frac{E_z + U_p}{\omega_L} \rceil
\end{aligned}
\tag{C.4}
$$

By comparing tunnelling methods (Landau model, equation C.3) and the Strong Field Approximation (Landau model, equation C.3), it is notable that the SFA depends heavily on the precise laser-interaction - and not just the electric field as in tunnelling models. This has the advantage that the magnetic field of the laser pulse is taken into account, making the SFA applicable for a larger domain in the intensity, frequency space of the laser pulse. Consequentially, it also implies that the SFA is only valid for plane wave laser fields, whereas tunnelling equations are applicable for quasi-static alternating/static electric fields which, considering the discussion on field ionisation in high-Z clusters, can be a disadvantage of the SFA. In first instance, the atoms/ions interact with a plane wave laser field and are ionised. However, as mentioned before, laser-cluster interaction leads to extremely high charge states because the laser field is effectively amplified by the electric field of the space charges - which is not a plane wave. Nevertheless, it remains to be a quasi-static field (since the additional space charge field changes slower than the laser dynamics). Nevertheless, the assumption that the plane wave laser pulse can be modelled as an alternating electric field leads to limits to the applicability of tunnelling theories, as explained in section C.1.4. Although the resulting electromagnetic field is not necessarily well defined by neither a plane wave field or alternating electric field, an advantage of tunnel theories is that all tunnelling theories (either static or alternating electric field) have a similar exponential function, leading to a similar exponential accuracy. Therefore, whether the electric field is an oscillating field or a static field does not critically affect the result in tunnelling theories. Contrastingly to the exponential accuracy, the SFA has a summation over generalised Bessel functions, whose behaviour is much more complicated, depends on the precise laser electron interaction (which is heavily affected in laser-cluster interaction by the space charge of the ions and electrons) and does not necessarily show this exponential accuracy. Furthermore, the result provided by the SFA depends heavily on the electron momentum wavefunction $\phi_i(\vec{p}_n)$ and from the derivation of the SFA it is assumed that this is accurately known. This means that in order to adopt the SFA, another routine has to be available to accurately determine the electron momentum wavefunction. Furthermore, calculating the SFA equations C.4 is obviously more computationally intensive than calculating the tunnelling equations C.3: especially evaluating the generalised Bessel function and the summation over all photon numbers is numerically demanding and prone to numerical instabilities than the relatively simple relations provided by tunnelling theories. Therefore at the present the SFA is too computationally demanding to be used in the simulations. Nevertheless, a few points should be made in favour of the SFA. The SFA is able to give more accurate predictions of the photoelectron spectra than tunnelling theories. Furthermore, the SFA can be used to take recombination into account enabling the possibility to model higher harmonic generation by using the SFA. Furthermore, the SFA has been used to accurately predict atom stabilization (the effect that at high intensities the ionisation probability lowers due to stabilization in the atom) [37].

Taking this comparison in consideration, although the SFA has the advantage that it is less restrictive for plane wave fields, tunnelling theories will be used in this thesis as a field ionisation model. Furthermore, it should be noted that in cluster-laser interaction relevant parameters, tunnelling theories are not necessarily more restrictive than the SFA as will be explained in section C.1.4, because femtosecond lasers operate around $\lambda = 800$ nm, where the applicability of tunnelling theories and the SFA is similar.

C.1.3 Tunnelling theories of field ionisation

Having made the choice for using tunnelling theories for treating the field ionisation in laser-cluster interaction, various models of tunnelling ionisation are explained and derived, eventually leading to the model used in this thesis - the Ammosov Delone Krainov (ADK) tunnelling model.

The Landau tunnelling rate is for a static electric field of a hydrogen atom, which has been generalised by Perelomov, Popov and Terent'ev (PPT) [65] who developed a method for calculating the probability of ionization of a bound state under the action of an alternating field. Compared to Landau, there are two changes in GPT. First, the wavefunction of an electron in a general atom is taken into account, instead of the hydrogen wavefunction. This also implies taking the quantum numbers of the electrons in orbit into account. Secondly, the wavefunction of the electron in the perturbed potential changes when the perturbation is alternating. In order to counter this problem, the WKB approximation in the Landau derivation (equation C.16 till C.24 in appendix C.1.5) is generalised in order to support time-varying fields. In order to do so, the following assumptions have been made (please note that the PPT model can be derived in multiple ways, the assumptions shown below are adopted from the original PPT derivation by [65]):

- The derivation is restricted to cases of relatively low field strengths and frequencies ($\omega_L << \omega_0$, in which ω_0 corresponds with the oscillation time of an electron in an atom, which corresponds with the ionization energy of the electron in an atom ($\omega_0 = E_z$ in atomic units); $F_L << F_0$ in which F_0 is a typical interatomic field (more information about this will follow in section C.1.4)). This implies that the ionisation occurs slowly in atomic times.
- The electric field of the laser across an atom is uniform; this implies that the wavelength of the laser light is much smaller than the radius of the atom. This is essentially the dipole approximation, however in the original paper it is not mentioned that there are limits on the dipole approximation by magnetic and relativistic effects.
- The original assumption in the PPT model is that "The electron speed inside an atom is assumed to relatively small, such that the effect of the magnetic field of the laser field does not have to be taken into account.", however this assumption is erronous, because magnetic field effects can also occur at small(er) velocities (onset of magnetic effects is v/c, whereas the onset of relativistic effects is $(v/c)^2$).
- Implicitly it has been assumed that no relativistic effects occur, although thi has not been explicitly assumed in the original PPT papers [65].

Please note that in more recent field ionisation papers, a part of these assumptions is under scrutiny (the assumption $F_L << F_0$ is believed to be erronous). The full derivation of the PPT ionisation rates in the quasi-static regime are provided in appendix C.1.6 and the result is shown in equation C.5. Please note that the derivation provided in appendix C.1.6 is different from the original derivation in [65].

$$\Gamma_{lm} = \frac{\kappa^2}{2}|C_{\kappa l}|^2 \frac{2l+1}{2^m m!}\frac{(l+m)!}{(l-m)!}(\frac{2\kappa^3}{E})^{2Z/\kappa-m-1}\exp(-2\kappa^3/3E(1-\frac{1}{10}\gamma^2)) \tag{C.5}$$

In the PPT model, the ionisation probability depends on the quantum numbers n, l, m of the ionisable element. The parameter $\kappa = \sqrt{2E_z}$ is the characteristic momentum of the bound electron, the parameter Z is the ion charge of the core ion in the single active electron approximation, the parameter E is the electric field strength, the parameter γ is the Keldysh parameter and the parameter $C_{\kappa l}$ is the asymptotic coefficient, which is a remnant of the electron wavefunction in the bound atom.

One problem of the PPT model, which limits its practical, general usage, is the coefficient $C_{\kappa l}$, which has to be determined beforehand or adopted from tables such as [70]. Furthermore, it is also not known beforehand which quantum numbers an atom will have in a practical application.

The most popular tunnelling theory is the Ammosove-Delone-Krainov (ADK) tunnelling theory [63], which is a variety of the PPT theory aimed at practical applications. In the ADK theory, the quantum number l is assumed to be zero (therefore $m = 0$ as well). In order to determine the coefficient $C_{\kappa l}$, the equation of Hartree is used [72], ultimately resulting in the ADK tunnelling theory in equation C.6. A full derivation of the ADK tunnelling theory is presented in appendix C.1.7. Furthermore it has been assumed that the Keldysh parameter is so small that its effect in the exponent is negligible. It should be noted that using the equation of Hartree for determining the $C_{\kappa l}$ coefficient can lead to a deviation of up to 20 % in $C_{\kappa l}$ as compared to extensive numerical schemes for determining $C_{\kappa l}$, as provided in tables such as [70, 106] In equation C.6 the parameter $n^\star$ is the effective principal quantum number, which is defined as $n^\star = \frac{Z}{\kappa}$.

$$\frac{dW}{dt} = \frac{\kappa^2}{\sqrt{36\pi n^\star}}(\frac{2e}{n^\star})^{n^\star}(\frac{2\kappa^3}{E})^{2Q/\kappa-1}\exp(-2\kappa^3/3E) \tag{C.6}$$

Please note that all tunnelling theories in this section are derived for alternating electric fields with linear polarization. Derivations for elliptical or circular polarization are available as well and lead to different results. Furthermore, the instantaneous version of the tunnelling probability is used, whereas most tunnelling equations presented in papers provide a period averaged tunnelling rate.

C.1.4 Complications and limitations of tunnelling theories

It has been discussed that tunnelling ionisation is an approximation which is only valid in the quasi-static domain, which leads to certain limitations. Furthermore, additional limitations arise from the fact that tunnelling theories assume an alternating electric field, whereas a laser pulse is modelled by a plane wave, which also has a magnetic field component. These limitations complicating the application of tunnelling theories are discussed in this section.

Please note that the following part is based on [43, 46, 42].

Originally it was theorised that the limit $\gamma \to 0$ leads to the tunnelling limit, because in this limit the alternating electric field changes into a static electric field, which is the limit of the quasi-static approximation. However there are some fundamental issues with this limit. The Keldysh parameter is defined as $\gamma = \frac{\omega}{E/\sqrt{2E_z}}$. This implies that either $E \to \infty$ or $\omega \to 0$ when $\gamma \to 0$. In both cases, the electron will be accelerated to relativistic velocities and both magnetic and relativistic effects will become important, hence there are is a limit associated with low frequencies and a limit associated with high energies. When the electron velocity in the laser field is increased, first magnetic field effects will start to occur (v/c) and at higher velocities, true relativistic effects start to occur $(v/c)^2$. These magnetic field effects will be investigated.

An alternating electric field and a plane wave laser field are fundamentally different fields. However, as mentioned in the alternative derivation by [66] in appendix C.1.6, alternating electric fields are gauge equivalent to plane wave fields by using the Göppert-Mayer gauge transformation [107], which is only valid in the dipole approximation. This implies that implicitly the dipole approximation is essential for tunnelling theories, although this is not mentioned explicitly in the derivation of tunnelling theories. In the dipole approximation it is assumed that the phase of the pulse is constant across the size of the atom, because the atom is much smaller than the wavelength of the laser: $\omega t - \vec{k} \cdot \vec{r} \approx \omega t$. However, due to gauge equivalence and Göppert-Mayer gauge transformation, the dipole approximation is violated when the magnetic field effects of a plane wave field affect the result of the interaction.

In a frame of reference moving with the electron centre of displacement, a free electron in a strong plane-wave field produces a figure 8 pattern, as will be explained in section C.2 in the $\vec{E}, \vec{k}$ direction of the laser pulse ($\vec{k}$ is the propagation vector of the laser pulse). The amplitude of the figure 8 motion in the $\vec{E}$ and $\vec{k}$ axis can be calculated using equation C.7 [108, 109, 43]. The amplitude of the figure 8 pattern in the $\vec{E}$ direction is α_0 and the amplitude of the figure 8 patter in the $\vec{k}$ direction is β_0. Note that these are the non-relativistic expressions for the figure-8 motion, which can be used for investigating magnetic field effects, which have an earlier onset than relativistic effects. In a naive model, the bound electron is assumed to quiver in a figure-8 motion in the binding potential. The electron drift is assumed to be countered by the attracting Coulomb force of the ion [45, 43].

$$\begin{aligned} \alpha_0 &= \frac{E_0}{\omega^2} \\ \beta_0 &= \frac{E_0}{8c\omega}\alpha_0 \end{aligned} \tag{C.7}$$

When the displacement of the electron in the propagation direction becomes larger than the Bohr radius it effectively means that the magnetic field can have an impact on the ionisation of the electron, violating the dipole approximation. Therefore $\beta_0 = 1$ is a lower frequency (or upper intensity/field) limit of the dipole approximation (in atomic units, the Bohr radius is one) [45, 43], as shown in equation C.8. This limit applies to all dipole-approximation theories, including the strong-field approximation.

$$\begin{aligned} &\beta_0 < 1 \\ &\rightarrow E_0 < \sqrt{8c\omega^3} \end{aligned} \tag{C.8}$$

Previously it was discussed that the Keldysh parameter should be low, such that the Coulomb well is deformed sufficiently for tunnel ionisation to occur. Furthermore it was discussed that ionisation in this regime takes place due to the field nature of the laser pulse. In order for the field nature of the laser pulse to dictate the ionisation, the photon energy has to be small compared to the ionisation potential ($\omega < E_z$), which was already assumed in the original derivation of the PPT tunnelling model, setting an upper limit on the frequency. This is a limitation of tunnelling theories, which is not limiting other dipole based approximations such as the SFA.

Therefore there is an upper limit and lower limit on the validity of tunnelling theories, which does not correspond with the traditional picture of using the Keldysh parameter to seperate the multi-photon and tunnelling regime, as indicated in equation C.9. Therefore, the Keldysh parameter does not provide the correct limits for the applicability of tunnelling theories.

$$\begin{aligned} &\omega > (\frac{E_0^2}{8c})^{1/3} \\ &\omega < E_z \end{aligned} \tag{C.9}$$

Please note that the previous part was based on [43, 46, 42].

It should be noted that typical laser parameters in laser-cluster interaction studies are around the same laser wavelength ($\lambda = 800$ nm). Therefore, in the case of interaction with such a laser pulse the situation can be simplified: the upper frequency limit sets a minimum restriction on the ionisation energy and the lower frequency limit sets a limit on the maximum field intensity. In the case of $\lambda = 800$ nm, the minimum ionisation energy in which tunnel ionisation theory can be applied is $E_z = 1.55$ eV and the maximum field intensity in which dipole approximation based methods can be applied (such as tunnelling ionisation) is $E = 0.23$ TV/m, which corresponds with intensities of $I = 7.1 \times 10^{19}$ W/m^2. Please note that these restrictions only apply during ionisation. Therefore, this will not pose a problem for the investigation of low Z clusters (ionisation takes place before the upper field limit is reached). However, it can pose a problem in laser-cluster studies for high Z atoms. The derivation of these restrictions is based on the figure-8 motion of an electron in a plane-wave field. As explained previously, during laser-cluster interaction for a general (high Z) atom, the electric field at the position of an ion in the cluster consists out of the field generated by the laser and the field generated by the space charges. The field generated by the space charges is dominantly an electric field (it is assumed that the magnetic field generated by the relativistic motion of the electrons can be neglected), whereas the laser field is a plane-wave field with a magnetic field component. The additional field generated by the space charges hence does not violate the dipole approximation - implying that only that the intensity limit only applies on the laser field intensity. Furthermore, it should be noted that the derivation for the limit on the dipole approximation due to onset of magnetic effects is a rather crude model. From a qualitative point of view, it is evident that there should be a lower frequency limit on the application of the dipole approximation, due to the onset of relativistic and magnetic effects. However, it is uncertain whether this is precisely at $\beta_0 = 1$. It should be noted that for the laser frequency used mostly in laser-cluster experiments, the high frequency limit of tunnelling ionisation theories is not a problem, but the low frequency limit of the dipole approximation can pose a problem. Although it should be mentioned that the total electric field does count towards the relativistic limit, which occurs when the ponderomotive energy equals the rest energy of the electrons: $U_p = \frac{1}{2}c^2 \rightarrow E < c\omega\sqrt{2}$. The relativistic limit at $\lambda = 800$ nm is $E = 5.7$ TV/m, which corresponds to an intensity of $I = 4.3 \times 10^{22}$ W/m^2. Furthermore, to our knowledge, all methods for field ionisation use the dipole-approximation (strong field approximation, tunnelling theories, numerical solutions of the Schrödinger equation, etc.). This implies that in the case of ionisation at high intensities (such as in high-Z clusters), all theoretical methods for determining the ionisation probability may be inadequate and there is no reason why tunnelling theories in this regime are more inadequate than other theories.

C.1.5 Derivation - Landau tunnelling model

The Landau tunnelling rate described in section 3.1 is derived in this section. First the solution of Schrödinger's equation of the hydrogen atom under action of a static electromagnetic field is transformed to parabolic coordinates. Secondly, the Wentzel - Kramer's - Brillouin (WKB) approximation, which is a standard technique in quantum mechanics for solving the wave function semi-analytically, is introduced. Thirdly, the WKB approximation is used to solve Schrödinger's equation of the hydrogen atom under action of a static electromagnetic field and calculate the tunnelling probabilities from this wavefunction.

Please note that the derivation of the Landau model is adopted from [64], [38], [66] and [68].

Schrödinger's equation in parabolic coordinates of the hydrogen atom The Hamiltonian of an electron moving in a perturbed Coulomb potential (V_{pert}, given by equation C.1) is shown in equation C.10 ($\hat{A}$ means that A is an operator).

$$\hat{H} = \frac{1}{2}\hat{\vec{p}}^2 + V_{pert} = \frac{1}{2}\hat{\vec{p}}^2 - \frac{Z}{x} + Ex \tag{C.10}$$

The Schrödinger equation with this Hamiltonian will be transformed from cylindrical coordinates ($r,\ x, \phi$) to parabolic coordinates (ξ, η, ϕ), as indicated in equation C.11.

$$\begin{aligned} \xi &= r + x \\ \eta &= r - x \\ \phi &= \phi \end{aligned} \tag{C.11}$$

With this transformation, the Schrödinger equation (being the eigenenergy$\mathcal{E}\Psi = \hat{H}\Psi$, $\mathcal{E}$) can be seperated in parabolic coordinates with the ansatz $\Psi = f_1(\xi)f_2(\eta)\exp(im\phi)$, m being the magnetic spin number, which results in equation C.12. This is the Schrödinger equation seperated in parabolic coordinates (in the form of an eigenequation: $\hat{A}f = Bf$).

$$\begin{aligned} [-\frac{1}{2}(\frac{d^2}{d\xi^2} + \frac{1}{\xi}\frac{d}{d\xi} - \frac{m^2}{4\xi^2}) - \frac{Z_1}{2\xi} + \frac{E}{8}\xi]f_1(\xi) &= \frac{\mathcal{E}}{4}f_1(\xi) \\ [-\frac{1}{2}(\frac{d^2}{d\eta^2} + \frac{1}{\eta}\frac{d}{d\eta} - \frac{m^2}{4\eta^2}) - \frac{Z_2}{2\eta} - \frac{E}{8}\eta]f_2(\eta) &= \frac{\mathcal{E}}{4}f_2(\eta) \end{aligned} \tag{C.12}$$

In equation C.12 the seperation constants Z_1, Z_2 add up to the ion charge $Z_1 + Z_2 = Z$. In the case of no field ($E = 0$) the two equations are the same if $Z_1 = Z_2$, so the nuclear charged has to be split equally over both Z_1 and Z_2: $Z_1 = Z_2 = \frac{Z}{2}$. Furthermore, equation C.12 has the same structure as two Schrödinger equations in cylindrical coordinates with potentials shown in equation C.13 and visualized in figure C.1b. It can be seen that the V_η is the downhill potential, which is the potential through which tunnelling can take place. Hence solving the eigenequation for $f_2(\eta)$ yields the wavefunction through which tunnelling ionization can take place.

$$\begin{aligned} V_\xi &= -\frac{Z_1}{2\xi} + \frac{E}{8}\xi \\ V_\eta &= -\frac{Z_2}{2\eta} - \frac{E}{8}\eta \end{aligned} \tag{C.13}$$

If the electron is in the ground state of the hydrogen atom, the magnetic spin number is zero, the nuclear charge is 1, so $Z = 1 \rightarrow Z_2 = \frac{1}{2}$ and the eigenenergy is $\mathcal{E} = -\frac{1}{2}$. This transforms the downhill potential equation in equation C.12 into C.14.

$$[-\frac{1}{2}(\frac{d^2}{d\eta^2} + \frac{1}{\eta}\frac{d}{d\eta} - \frac{1}{4\eta} - \frac{E}{8}\eta]f_2(\eta) = -\frac{1}{8}f_2(\eta) \tag{C.14}$$

By substituting the eigenvalue equation C.14 with $\chi(\eta) = \sqrt{\eta}f_2(\eta)$, this transforms into the one-dimensional motion of an electron in a potential $V(\eta)$ and total energy ϵ in equation C.15.

$$\begin{aligned} -\frac{1}{2}\frac{d^2\chi}{d\eta^2} + V(\eta)\chi = \mathcal{E}\chi \\ V(\eta) = -\frac{1}{2}(\frac{1}{2\eta} + \frac{1}{4\eta^2} + \frac{1}{4}E\eta) \\ \mathcal{E} = -\frac{1}{8} \end{aligned} \tag{C.15}$$

Solving the wavefunction with the WKB approximation One method for solving the 1D wavefunction of this system is by using the Wentzel-Kramers-Brillouin (WKB) approximation, which is a common method for approximating tunnelling rates in complex systems. In the theory an exponential is assumed as the solution to the time independent Schrödinger equation (equation C.16).

$$\Psi(x) = \exp(-iS(x)) \tag{C.16}$$

Inserting this equation in the time independent Schrödinger equation yields a differential equation for $S(x)$ (equation C.17):

$$\frac{1}{2}(\frac{dS}{dx})^2 - \frac{i}{2}\frac{d^2S}{dx^2} = E - V(x) \tag{C.17}$$

When it is assumed that the second derivative of $S(x)$ is negligible, the differential equation above can be solved analytically easily (equation C.18):

$$\frac{1}{2}(\frac{dS}{dx})^2 = E - V(x) \rightarrow S = \pm\int\sqrt{2(E - V(x))}dx = \pm\int p(x)dx \tag{C.18}$$

Naturally, this approximation is only valid when the first term in equation C.17 is much larger than the second term, implying equation C.19.

$$|(\frac{dS}{dx})^2| >> |\frac{d^2S}{dx^2}| \rightarrow |\frac{1}{(\frac{dS}{dx})}dx| << 1 \tag{C.19}$$

As shown, in this approximation, $\frac{dS}{dx} = \pm p(x)$. The momentum is related to the De Broglie wavelength: $\lambda = \frac{2\pi}{p}$. Therefore, it is possible to write the requirement for the approximation in terms of the De Broglie wavelength C.20.

$$|\frac{1}{pdx}| << 1 \rightarrow \frac{1}{2\pi}|\frac{\lambda}{dx}| << 1 \tag{C.20}$$

So therefore this approximation is valid if the spatial variation of the De Broglie wavelength is small enough. Since only the potential can vary the De Broglie wavelength, this implies that the spatial variation of the potential has to be small enough. Furthermore, the momentum has to be large enough (since $\lambda \propto p^{-1}$, meaning that $E >> V(x)$ (classical regime) or $E << V(x)$ (classical forbidden regime (e.q. imaginary momentum)). The WKB approximation is not valid in the turning point ($E \approx V(x)$ at $x = a$) where the particle changes direction, because the momentum will become zero, which means the de Broglie wavelength will become infinite.

Equation C.18 is a zero-order solution of equation C.17. This approximation can be improved by adding a term to S, with a negligible small second order derivative: $S = \int p(x)dx + S_1(x)$. Plugging this S into equation C.17 yields equation C.21.

$$(\frac{dS}{dx})^2 - i\frac{d^2S}{dx^2} = p(x)^2 \to (p + S_1')^2 - ip'' = p^2 \to S_1'p = \frac{1}{2}ip'' \to S_1 = -\frac{1}{2}\log p(x) \tag{C.21}$$

This gives $S = \int p(x)dx - \frac{1}{2}\log p(x)$. This can be combined with the plane wave in equation C.16 to yield two sets of solutions shown in equation C.22. One in the classical regime $E >> V(x)$ (classical regime) and one in the classical forbidden regime $E << V(x)$ (e.q. imaginary momentum).

$$\begin{aligned} \Psi &= \frac{A}{\sqrt{p(x)}}\exp(i\int p(x)dx) + \frac{B}{\sqrt{p(x)}}\exp(-i\int p(x)dx) \qquad E >> V(x) \\ \Psi &= \frac{C}{\sqrt{p(x)}}\exp(\int p(x)dx) + \frac{D}{\sqrt{p(x)}}\exp(-\int p(x)dx) \qquad E << V(x) \end{aligned} \tag{C.22}$$

These two equations are valid far from the turning point, but as explained earlier, the WKB approximation is invalid at the turning point. One method to combine the two regimes is to create formulas that connect the two regions. This can be done by linearising the potential at the turning point and solving Schrödinger's equation analytically for a linearised potential. The resulting wavefunction is an Airy function. The WKB approximation is valid far from the turning point, whereas linearised potential is valid near the turning point. This creates two overlap regions in which both the WKB approximation and the linearised potential are valid. By using this overlap

$$D = B\exp(i\frac{\pi}{4}) = A\exp(-i\frac{\pi}{4}) \tag{C.23}$$

The reconnecting procedure yields a full WKB wave function C.24

$$\begin{aligned} \Psi &= \frac{A}{\sqrt{p(x)}}\exp(\int_x^a p(x')dx' + \frac{\pi}{4}i) \qquad x < a \\ \Psi &= \frac{A}{\sqrt{|p(x)|}}\exp(-|\int_a^x |p(x')|dx') \qquad x > a \end{aligned} \tag{C.24}$$

Using the WKB approximation to derive the Landau-tunnel rate Now we continue with deriving the Landau tunnel theory (equation C.15), which is repeated for clarity:

$$\begin{aligned} -\frac{1}{2}\frac{d^2\chi}{d\eta^2} + V(\eta)\chi &= \mathcal{E}\chi \\ V(\eta) &= -\frac{1}{2}(\frac{1}{2\eta} + \frac{1}{4\eta^2} + \frac{1}{4}E\eta) \\ \mathcal{E} &= -\frac{1}{8} \end{aligned} \tag{C.25}$$

The wavefunction χ will be calculated with the full WKB wave function. Ionization corresponds with the electron moving in one direction (η). In this case, the value of η in the perturbed regime is larger than 1 and the electric field strength is much smaller than one (note that if $E \approx 1$, this theory is incorrect), hence the turning point is shown to be at $\eta_1 = \frac{1}{E}$ in equation C.26.

$$\begin{aligned} p(\eta) &= \sqrt{2(\mathcal{E} - V)} = \sqrt{-\frac{1}{4} + \frac{1}{2\eta} + \frac{1}{4\eta 2} + \frac{1}{4}E\eta} \\ p(\eta_1) &= 0 \to V(\eta_1) = \mathcal{E} \to \eta_1 \approx \frac{1}{E} \end{aligned} \tag{C.26}$$

The turning point is at $V = \mathcal{E} \rightarrow \eta = \frac{1}{E}$. It is assumed that $E < 1$, (ionization will probably occur before $E < 1$), so $\eta > 1$ in the region $V < \mathcal{E} \rightarrow \eta < \frac{1}{E}$. In this region tunnelling will occur, so the wavefunction of this region has to be calculated. In order to calculate the constant A of the WKB approximation (equation C.24), the WKB wave function is matched with the unperturbed wavefunction of the 1s hydrogen state at a position η_0.

The unperturbed wavefunction of the 1s hydrogen state in parabolic coordinates is given in equation C.27.

$$\Psi = \frac{1}{\sqrt{\pi}} \exp(-\frac{\xi + \eta}{2}) \tag{C.27}$$

This is matched with the WKB wave function far from the turning point ($\eta_0 << \frac{1}{E}$). The WKB solution is then propagated to the end point at the turning point.

Matching the WKB solution to the hydrogen wave function leads to the constant A, which is calculated in equation C.28.

$$\frac{A}{\sqrt{p(\eta_0)}} = \frac{1}{\sqrt{\pi}} \exp(-\frac{\xi + \eta_0}{2}) \rightarrow A = \frac{p(\eta_0)}{\sqrt{\pi}} \exp(-\frac{\xi + \eta_0}{2}) \tag{C.28}$$

Using this constant to calculate the WKB wave function from η_0 to the turning point $\frac{1}{E}$ leads to the WKB wave function shown in equation C.29. In order to determine the tunnelling probability, the wavefunction needs to be squared, which is also done in equation C.29.

$$\begin{aligned} \chi &= \sqrt{\frac{p(\eta_0)}{\pi p(\eta)}} \exp(-\frac{\xi + \eta_0}{2} + \int_{\eta_0}^{1/E} p(\eta) d\eta + i\frac{\pi}{4}) \\ |\xi|^2 &= \frac{|p(\eta_0)|}{p\pi} \exp(-xi - \eta_0 + 2\int_{\eta_0}^{1/E}) \end{aligned} \tag{C.29}$$

In the beginning the assumption that $\eta >> 1$ (e.q. the electron is far away from the core in the η direction) was made. With this assumption, the momentum is expanded in equation C.30.

$$p = \sqrt{-\frac{1}{4} + \frac{1}{2\eta} + \frac{1}{4\eta 2} + \frac{1}{4} E\eta} = \frac{1}{2}\sqrt{E\eta - 1} - \frac{1}{2\eta\sqrt{E\eta - 1}} + ... \tag{C.30}$$

Since $E\eta_0 << 1 \rightarrow p(\eta_0) \approx \frac{1}{2}$. The dependence of the wave function on the momentum is stronger in the exponent than in the denominator, therefore a first order approximation is used in the denominator and a second order approximation is used in the exponent, leading to the result shown in equation C.31. This expression is solved by solving the integrals and using the approximation that $\eta_0 E << 1$, which leads to the second wavefunction in equation C.31.

$$\begin{aligned} |\xi|^2 &= \frac{1}{\pi\sqrt{E\eta - 1}} e^{-(\xi - \eta_0)} \exp(-\int_{\eta_0}^{1/E} (\sqrt{E\eta - 1} - \frac{1}{\eta\sqrt{E\eta - 1}}) d\eta) \\ |\xi|^2 &= \frac{4e^{-\xi}}{\pi E\sqrt{E\eta - 1}} e^{-\frac{2}{3E}} \end{aligned} \tag{C.31}$$

Now the squared wave function of the problem is calculated. This wavefunction determines the solutions of the original wave functions $f_1(\xi)$ and $f_2(\eta)$ defined in equation C.12. Using equation $\chi(\eta) = \sqrt{\eta} f_2(\eta)$ the function $f_2(\eta)$ can be calculated. Furthermore, the wave function we have constructed is $|\chi(\eta, \xi)|^2$, which is ξ dependent. The ξ dependent part $|f_1|^2$ is included in $|\chi|^2$, so that $|f_1(\xi) f_2(\eta)|^2 = \frac{|\chi(\eta, \xi)|^2}{\eta}$.

With the original wave functions, it is possible to calculate the total probability current through a plane perpendicular to the z-axis, which is shown in equation C.32, where v_z is the velocity in the z direction (through the plane perpendicular to the z-axis) and ρ is the radial coordinate (so integrating over $2\pi\rho d\rho$ is integrating over an infinite cylinder).

$$\begin{aligned}\Gamma &= \int_0^\infty |f_1(\xi)f_2(\eta)|^2 v_z 2\pi\rho d\rho \\ \Gamma &= \int_0^\infty |\frac{|\chi(\eta,\xi)|^2}{\eta} v_z 2\pi\rho d\rho\end{aligned} \tag{C.32}$$

This equation can be solved if v_z can be calculated and if $d\rho$ is converted to a function of $d\eta$, $d\xi$. Equation C.11 contains the transformation between the parabolic coordinates and the cylindrical coordinates, and the unit element $d\rho$ can be transformed by assuming that $\eta >> \xi$.

$$\rho = \sqrt{\xi\eta} \rightarrow d\rho = \frac{1}{2}\frac{\eta}{\sqrt{\xi\eta}}d\xi + \frac{1}{2}\frac{\xi}{\sqrt{\xi\eta}}d\eta \approx \frac{1}{2}\sqrt{\eta}\xi d\xi \tag{C.33}$$

With the same assumption, z can be transformed in η: $z = (\xi - \eta)/2 \approx -\eta/2$. The eigenenergy of the hydrogen atom $E_{eig} = -\frac{1}{2}$ equals the kinetic energy $E_{kin} = \frac{1}{2}v_z^2$ plus the potential energy $E_pot = Ez$ (assuming that the velocity in other directions is negligible (the tunnelling takes place through this plane, since the electric field is directed in the z direction). This results in a value for the velocity in the z direction shown in equation C.34, while assuming that xi is small and eta is large.

$$-\frac{1}{2} = \frac{1}{2}v_z^2 + Ez \approx \frac{1}{2}v_z^2 - \frac{1}{2}E\eta \rightarrow v_z \approx \sqrt{E\eta - 1} \tag{C.34}$$

With v_x and $d\rho$ t is possible to solve equation C.32 and calculate the tunnelling probability current, which leads to the Landau ionization rate in equation C.3.

$$\begin{aligned}\Gamma &= \int_0^\infty |\frac{|\chi(\eta,\xi)|^2}{\eta} v_z 2\pi\rho d\rho \rightarrow \Gamma = \int_0 \infty \frac{4}{E}\exp -\frac{2}{3E}\exp -\xi d\xi \\ \Gamma &= \frac{4}{E}\exp -\frac{2}{3E}\end{aligned} \tag{C.35}$$

C.1.6 Perelomov Popov, Terent'ev (PPT) tunnelling rate

Please note that in this section atomic units are used. In atomic units the electron mass m_e, electron charge e, reduced plank's constant $\hbar$ and the Coulomb constant $\frac{1}{4\pi\epsilon_0}$ are defined as 1 (dimensionless): $m_e = e = \hbar = \frac{1}{4\pi\epsilon_0} = 1$. Making the units of the atomic constant dimensionless, has a large impact on the meaning of a certain unit. Using atomic units in atomic physics is common practice and a conversion table to SI units is provided in appendix A.4.

When the tunnelling time is much shorter than the laser period ($\gamma << 1$), the change of the field during the ionisation of the electron through the barrier can be neglected. This regime quasi-static regime is often referred to as the adiabatic approximation, since the Keldysh parameter also characterizes the degree of adiabaticity of the electron motion through the barrier (e.q. if the adiabaticity is high, the field accelerates the electron to its maximal position e.q. adiabatic motion, if the adiabaticity is low, the frequency of the field limits the motion of the electron (before the electron can escape the barrier, it has to go back again due to the laser oscillation)). Although the PPT ionisation rates are valid for a larger regime than the tunnelling ionisation regime (since they sum the tunnelling and many-photon processes, which depict ionisation in the $\kappa >> 1$ regime), these general PPT ionisation rates lead to complicated equations which often cannot be solved generally [63, 110, 44, 65], which can be simplified in the quasi-static regime using the adiabaticity approximation.

Please note that the derivation of the PPT model is not the initial derivation by PPT [65], but is a more insightful derivation by [66] based on partial Fourier transforms. The derivation below has been adopted from [66].

In the length-gauge (the Göppert-Mayer gauge transformation [46, 107] transforms the vector potential of an applied plane wave laser field to a scalar potential of a quasi-static electric field in the dipole approximation) the Hamiltonian of an electron in an atom in the single active electron approximation is shown in equation C.36.

$$H = \frac{1}{2}\hat{p}^2 + V(r) - \vec{r}\cdot\vec{E}(t) \tag{C.36}$$

For an electron in a static field in the z direction: $\vec{E}(t) \to E\vec{e}_z$, and neglecting the contribution of the ionic core $V(r) \to 0$, this leads to the Hamiltonian shown in equation C.37 - also called the zero-range potential Hamiltonian. The time independent Schrödinger equation of the bound state yields $-E_z\Psi(x,y,z) = \hat{H}\Psi(x,y,z)$, in which E_z is the ionisation potential.

$$\begin{aligned} \hat{H} &= \frac{1}{2}\hat{p}^2 - Ez \\ -E_z\Psi(x,y,z) &= \hat{H}\Psi(x,y,z) \end{aligned} \tag{C.37}$$

The idea is to match the wavefunction for an electron in a static field with the bound wavefunction at some z_0: $\Psi(z_0) = \Psi_0(z_0)$, using WKB methods. Using the mixed representation wave-function [68, 69], the bound spatial wavefunction and the bound wavefunction in the momentum space representation can be Fourier transformed into one another, as indicated in equation C.38. This representation makes it more insightful to derive the WKB solution.

$$\begin{aligned} \Psi(x,y,z) &= \frac{1}{2\pi}\int dp_x \int dp_y \exp(ixp_x + iyp_y)\Phi(p_x,p_y,z) \\ \Phi(p_x,p_y,z) &= \frac{1}{2\pi}\int dx \int dy \exp(-ixp_x - iyp_y)\Psi(x,y,z) \end{aligned} \tag{C.38}$$

Combining the momentum space representation in equation C.38 and the time independent Schrödinger equation C.37 leads to equation C.39.

$$-\frac{\partial^2\Phi(p_x,p_y,z)}{\partial z^2} = (2E_z + p_x^2 + p_y^2 + 2Ez)\Phi(p_x,p_y,z) \tag{C.39}$$

The three dimensional Schrödinger differential equation is therefore reduced to one dimension, resulting in the momentum space wavefunction. From equation C.39 it can be deduced that the terms $p_x^2 + p_y^2$ effectively enhances the ionisation potential. This implies that when the electric field is in the z direction, most likely the electrons will escape the atom in the z direction, since movement in the perpendicular direction leads to an effectively larger ionization potential.

The WKB approximation solution is given in equation C.24 and repeated in equation C.40 (first equation). The WKB solution now has to be matched to the bound wavefunction at z_0. The momentum space wavefunction can then be rewritten as indicated in equation C.40 (second equation). Matching the bound wavefunction at z_0 provides us with the constant C. $S(p_x,p_y,z)$ is the classical action, which is related to the kinetic momentum

$$\begin{aligned} \Phi(p_x,p_y,z) &= \frac{C}{\sqrt{|p_z(z)|}}\exp(iS(p_x,p_y,z)) \\ \Phi(p_x,p_y,z) &= \Phi(p_x,p_y,z_0)\sqrt{\frac{p_z(z_0)}{p_z(z)}}\exp(i(S(p_x,p_y,z) - S(p_x,p_y,z_0))) \end{aligned} \tag{C.40}$$

Combining equation C.40 and C.39, yields a differential equation for the classical action. This equation has a similar form as the Hamilton-Jacobi equation can be solved by direct integration, as indicated in equation C.41:

$$\begin{aligned}&\frac{1}{2}(\frac{\partial S(p_x,p_y,z)}{\partial z})^2 - Ez = E_z + \frac{1}{2}p_x^2 + \frac{1}{2}p_y^2\\&S(p_x,p_y,z) - S(p_x,p_y,z_0) = \frac{1}{3E}(2E_z + p_x^2 + p_y^2 + 2Ez)^{3/2} - \frac{1}{3E}(2E_z + p_x^2 + p_y^2 + 2Ez_0)^{3/2}\end{aligned} \tag{C.41}$$

The result of equation C.41 is expanded in terms of z_0. One issue of this WKB solution is that it includes the field throughout the entire range of z, whereas for $z < z_0$ (the bound wavefunction) the solution should be free of the field interaction (it has been assumed that for the bound wavefunction, there is no field - similar to the strong field approximation approach).By dropping all orders of $O(z_0^2)$ or higher, this problem is solved and the wavefunction can be matched.

We define the exit point of the barrier as z_e. According to the derivation of the BSI in section 3.1, $z_e = \frac{E_z}{E}$. The classical action at the exit point can then be calculated using equation C.41 resulting in equation C.42.

$$S(p_x,p_y,z_e) = S(p_x,p_y,z_0) + i(\frac{\kappa^3}{3E} + \frac{\kappa p_\perp^2}{2E} - \kappa z_0) \tag{C.42}$$

In equation C.42 the parameter κ is defined as the characteristic momentum of the bound state $\kappa = \sqrt{2E_z}$ and $p_\perp^2 = p_x^2 + p_y^2$. The expression for the action in equation C.42 can be combined with equation C.40 in order to obtain the momentum space wavefunction, as is shown in equation C.43.

$$\Phi(E,p_\perp) = \Phi(p_\perp,z_0)\sqrt{\frac{\kappa}{p_z(z)}}\exp(-\frac{\kappa^3}{3E} - \frac{\kappa p_\perp^2}{2E} + \kappa z_0) \tag{C.43}$$

Equation C.43 gives the momentum space function in the case of short range potentials. From this equation, the exponential result common in tunnelling theories is already there. The idea is to extend this short range potentials to long range potentials. Originally this has been done by perturbation theory on the action S, where the short-range potential is used as the zero-order approximation for the Hamilton-Jacobi equation. Corrections on this action are found in the first order in the core potential $V(z) = Q/z$. The correction on the action results in equation C.44. The integral only has to be performed over the z direction, because of the strong decrease in tunnelling probability in the perpendicular direction, due to the exponential behaviour. When the Coulomb potential is used: $V(z) = \frac{Q}{z}$, the result of the integral is the second equation in equation C.44. The square roots in equation C.44 can be expanded in a similar fashion as above (dropping $O(z_0^2)$ or higher), resulting in a simple expression for the correction in action.

$$\begin{aligned}\Delta S &= \int_{z_0}^{z} dz' \frac{V(z')}{p_z(z')} = \int_{z_0}^{z} dz' \frac{V(z')}{\sqrt{\kappa^2 - 2Ez}}\\\Delta S &= \frac{Q}{\kappa}\ln(\frac{1+\sqrt{1-2Ez_0/\kappa^2}}{1-\sqrt{1-2Ez_0/\kappa^2}})\\\Delta S &= \frac{Q}{\kappa}\ln(\frac{2\kappa^2}{Ez_0})\end{aligned} \tag{C.44}$$

Combining equation C.44 and equation C.43, leads to a long range momentum space wavefunction shown in equation C.45.

$$\Phi(E,p_\perp) = \Phi(p_\perp,z_0)\sqrt{\frac{\kappa}{p_z(z)}}(\frac{2\kappa^2}{Ez_0})^{Q/\kappa}\exp(-\frac{\kappa^3}{3E} - \frac{\kappa p_\perp^2}{2E} + \kappa z_0) \tag{C.45}$$

The recipe above is general and can be used for any atomic wavefunction and for the starting point of an eikonal like treatment of any arbitrary core potential.

Now we will incorporate the atomic wavefunctions in the long range momentum space wavefunction in equation C.45, by using the partial Fourier transform. The hydrogen-like atomic wavefunction with quantum numbers l, m in cylindrical coordinates (ρ, ϕ, z) is listed in equation C.46.

$$\Psi(x, y, z) = \frac{1}{\sqrt{2\pi}} \exp(im\phi)\Psi_m(\rho, z) \tag{C.46}$$

Using the Fourier transformation on equation C.46, by combining equation C.46 with equation C.38, leads to a relation for the atomic momentum space wave function in equation C.47. Since the atomic wave function is in cylindrical coordinates, the momentum space wavefunction has to be calculated in cylindrical coordinates, leading to the second equation C.47. In this equation it is convenient to group the perpendicular momentum together $p_\perp = \sqrt{p_x^2 + p_y^2}$. The angle ϕ_0 is a term from that arises from the coordinate transformation and is the angle between the momentum and the z-axis.

$$\begin{aligned}
\Phi(p_x, p_y, z_0) &= \frac{1}{(2\pi)^{3/2}} \int dxdy \exp(-ip_x x - ip_y y + im\phi)\Psi_m(\rho, z) \\
\Phi(p_x, p_y, z_0) &= \frac{\exp(im\phi_0)}{(2\pi)^{3/2}} \int_0^\infty \rho d\rho \Psi_m(\rho, z_0) \int_0^{2\pi} d\phi \exp(-ip_\perp \rho \cos\phi + im\phi)
\end{aligned} \tag{C.47}$$

By using Bessel functions, the result of equation C.47 can be determined (the result of the integral over ϕ is determined). The Bessel function is defined in equation C.48.

$$J_m(x) = \frac{1}{2\pi} \int_0^{2\pi} \cos(m\phi - xsin\phi)d\phi \tag{C.48}$$

Implementing the Bessel function in equation C.47 leads to equation C.49. Because the tunnelling is suppressed in the perpendicular direction, the term $\rho p_\perp$ will be less than unity and the Bessel function can be approximated as $J_m(\rho p_\perp) = \frac{1}{m!}(\frac{\rho p_\perp}{2})^m$, as indicated in equation C.49.

$$\begin{aligned}
\Phi(p_x, p_y, z_0) &= \frac{\exp im\phi_0}{(2\pi)^{3/2}} (-i)^m \int_0^\infty \rho d\rho \Psi_m(\rho, z_0) J_m(\rho p_\perp) \\
\Psi(p_x, p_y, z_0) &= \frac{\exp(im\phi_0)}{(2\pi)^{3/2}} \frac{(-i)^m}{m!} \int_0^\infty \rho d\rho \Psi_m(\rho, z_0) (\frac{\rho p_\perp}{2})^m
\end{aligned} \tag{C.49}$$

For $\Psi_m(\rho, z_0)$ a hydrogen-like wavefunction is implemented, which has the form given in equation C.50. This hydrogen wavefunction is in its asymptotic region.

$$\begin{aligned}
\Psi_m(\rho, z_0) &= \frac{\kappa^{3/2} \exp(im\phi)}{\sqrt{2\pi}} C_{\kappa l} N_{lm} (\kappa r)^{Q/\kappa - 1} \exp(-\kappa r) P_l^m(cos\theta) \\
C_{\kappa l} &= \frac{(-1)^{n-l-1} 2^n}{\sqrt{n(n+l)!(n-l-1)!}} \\
N_{lm} &= \sqrt{\frac{(2l+1)(l+m)!}{2(l-m)!}} \frac{1}{2^m m!}
\end{aligned} \tag{C.50}$$

The last equation of C.49 can then be calculated to determine the momentum space wavefunction. $P_l^m(x)$ is the Legendre polynomial, which can be approximated as $P_l^m(\cos\theta) \approx \sin(\theta)^m$ for small angles. Because the momentum in the perpendicular direction is limited, the motion in the perpendicular direction is limited as well. Therefore the angle can be approximated by $\sin\theta \approx \frac{\rho}{z_0}$. The radius can be approximated by $r^2 = z^2 + \rho^2 \rightarrow r = z\sqrt{1 + \frac{\rho^2}{z^2}} \rightarrow r \approx z + \frac{\rho^2}{2z}$. Using equation C.50, the momentum space wavefunction in C.49 can be calculated, resulting in equation C.51.

$$\Phi(p_x, p_y, z_0) = \frac{(-i)^m \exp(im\phi_0)}{\sqrt{2\pi}} C_{\kappa l} N_{lm} \exp(-\kappa z_0)(\frac{p_\perp}{\kappa})^m \kappa^{Q/\kappa-1/2} z_0^{Q/\kappa} \tag{C.51}$$

The momentum space wavefunction C.51 represents the bound wavefunction. This bound wavefunction can be incorporated in the WKB solution in equation C.40, which eventually resulted in equation C.45. Combining the bound wavefunction of C.51 and the tunnelling part of the wavefunction in equation C.45, leads to a mixed representation wavefunction valid at any z. The matching point of the WKB approximation z_0 drops out of the equation that way (like it should - otherwise the wavefunction would depend on the matching point and the WKB approximation would be invalid). This leads to the equation C.52.

$$\Phi(p_\perp, z \to z_e, E) = \frac{1}{\sqrt{2\pi p_z(z)}}(-i)^m \exp(im\phi_0) C_{\kappa l} N_{lm} (\frac{2\kappa^3}{E})^{Q/\kappa} (\frac{p_\perp}{\kappa})^m \exp(-\kappa^3/3E - \kappa p_\perp^2/2E) \tag{C.52}$$

The problem of this WKB wavefunction is that the wavefunction diverges near the exit point $p_z(z) \to 0$. However, the tunnelling probability Γ_{lm} is calculated by integrating this wavefunction, as can be seen in equation C.53.

$$\Gamma_{lm} = \int dp_x dp_y p_z(z) |\Phi(p_x, p_y, z)|^2 \tag{C.53}$$

By using complex analysis integration theory, this integral can be calculated and converges to the static tunnelling rate calculated by PPT in equation C.54, valid in the adiabatic approximation, for hydrogen like atoms.

$$\Gamma_{lm} = \frac{\kappa^2}{2} |C_{\kappa l}|^2 \frac{2l+1}{2^m m!} \frac{(l+m)!}{(l-m)!} (\frac{2\kappa^3}{E})^{2Q/\kappa-m-1} \exp(-2\kappa^3/3E) \tag{C.54}$$

The original PPT paper [65] also provides results in an oscillating electric field. This generates (for the instantaneous tunnelling amplitude which is not averaged over a laser pulse) a correction term in the exponent as shown in equation C.55.

$$\Gamma_{lm} = \frac{\kappa^2}{2} |C_{\kappa l}|^2 \frac{2l+1}{2^m m!} \frac{(l+m)!}{(l-m)!} (\frac{2\kappa^3}{E})^{2Q/\kappa-m-1} \exp(-2\kappa^3/3E(1 - \frac{1}{10}\gamma^2)) \tag{C.55}$$

C.1.7 Derivation - Ammosov, Delone, Krainov (ADK) tunnelling rate

Please note that in this section atomic units are used. In atomic units the electron mass m_e, electron charge e, reduced plank's constant $\hbar$ and the Coulomb constant $\frac{1}{4\pi\epsilon_0}$ are defined as 1 (dimensionless): $m_e = e = \hbar = \frac{1}{4\pi\epsilon_0} = 1$. Making the units of the atomic constant dimensionless, has a large impact on the meaning of a certain unit. Using atomic units in atomic physics is common practice and a conversion table to SI units is provided in appendix A.4.

Please note that this derivation is adopted from [44]. The original ADK paper is [63].

One problem of applying the PPT tunnelling equation in practical cases - for general atoms - is the determination of the constant $C_{\kappa l}$ - which has been given for hydrogen, but depends on the quantum number l. It is possible to convert this to an effective parameter C_κ, which is called the asymptotic coefficient, which can be adopted from tables like [70]. The issue of these parameters is that they are not available for all atoms, which limits the practical applicability of PPT. However, Hartree developed a method for the general calculation of the asymptotic coefficients in atoms.

The asymptotic coefficient $C_{\kappa l}$ can be determined using Hartree-Fock methods and are often encountered in atomic physics. The asymptotic coefficient is present in the hydrogen wavefunction. By solving the Schrödinger equation for the hydrogen atom, the asymptotic coefficient for the wavefunction in hydrogen can be determined. This method has been generalised by Hartree [72] resulting in the coefficient provided in equation C.56, in which $n^\star$ is the effective principal quantum number of the level, Z is the ion core charge in an single electron approximation (for example: in the case of an atom, in the single electron approximation an atom consists out of an electron and a single charged ion, so $Z = 1$, in the case of an ion of charge Q, in the single electron approximation, the ion of charge Q consists out of an electron and an ion with charge $Q + 1$, so $Z = Q + 1$).

$$\begin{aligned} C^2_{\kappa l} &= \frac{2^{2n^\star-2}}{n^\star(n^\star+l)!(n^\star-l-1)!} \\ n^\star &= \frac{Z}{\kappa} \end{aligned} \tag{C.56}$$

It is assumed that $l = 0$, which simplifies equation C.56 into equation C.57 ($C_{\kappa l} \to C_\kappa$). This immediately also implies that $m = 0$. It should be noted that there are also more general forms of the ADK theory, which do not assume $l = 0$. Also note that $n^\star$ is not necessarily an integer, therefore in order to calculate the provided factorials, the Gamma function definition has to be introduced: $x! = \Gamma(x + 1)$. The Gamma function in equation C.57 can be approximated by using the Stirling approximation: $x! = \Gamma(x + 1) \approx \sqrt{2\pi x}(\frac{x}{\mathrm{e}})^x$, in which $\mathrm{e} = \exp(1)$, resulting in a final expression for C_κ.

$$\begin{aligned} C^2_\kappa &= \frac{2^{2n^\star-2}}{n^\star(n^\star)!(n^\star-l)!} \\ C^2_\kappa &= (\frac{2^{n^\star-1}}{\Gamma(n^\star+1)})^2 \\ C_\kappa &= \frac{2^{n^\star-1}}{\Gamma(n^\star+1)} \\ C_\kappa &= \frac{1}{\sqrt{8\pi n^\star}}(\frac{2e}{n^\star})^{n^\star} \end{aligned} \tag{C.57}$$

Combining the asymptotic coefficient derived in C.57 with the PPT ionisation rate C.55 and neglecting the contribution of the Keldysh parameter in the exponent (which is there to correct for the time-varying nature of the field and is negligible for low Keldysh parameters) leads to the ADK model in equation C.58

$$\frac{dW}{dt} = \frac{\kappa^2}{\sqrt{36\pi n^\star}}(\frac{2e}{n^\star})^{n^\star}(\frac{2\kappa^3}{E})^{2Q/\kappa-1}\exp(-2\kappa^3/3E) \tag{C.58}$$

There are many debates in field ionisation literature about the ADK theory. Although ADK theory is the most used tunnelling theory, due to its practical applicability, there is much discussion whether the authors of the ADK theory in paper [63] should be accredited for this theory. It is debated in literature whether the authors of [65] should not be accredited for the ADK theory, because the transformation from the original PPT theory to the ADK theory is a rather "trivial one" [106, 38, 66].

C.2 Electron Ejection

First the laser-charged particle interaction will be studied in more detail (providing the equations of our self-derived laser-charged particle interaction model) and providing examples of our model result. In the last sections our laser-charged particle interaction model, which is a generalised version of the work by [109], is provided.

C.2.1 Laser-charged particle interaction

The laser pulse can be modelled by an electromagnetic wave with frequency ω and propagation vector $\vec{k}$. The phase of the laser pulse is $\eta = \omega t - \vec{k} \cdot \vec{r}$. A valid approximation for a laser pulse in the waist of a laser beam is a plane wave electric field multiplied by an envelope function $f(\eta)$ describing the laser pulse shape. Such a laser pulse can be modelled by a vector potential $\vec{A}(\eta) = f(\eta)\vec{a}(\eta)$, in which $\vec{a}$ is a periodic function of η. The vector potential of a linearly polarized laser pulse with Gaussian envelope is $\vec{A}(\eta) = A_0 \exp(-(\frac{t}{2\tau})^2)\sin(\eta)\vec{e}_x$, which corresponds with a laser pulse with electric field $\vec{E}(\eta)$, magnetic field $\vec{B}(\eta)$ and propagation direction $\vec{k}$. Furthermore, it is assumed that the laser pulse is a transverse electromagnetic wave: $\vec{k}\cdot\vec{A} = 0$. Using Hamiltonian and Lagrangian mechanics, this problem can be solved by finding the Hamilton principal function, which can be found by solving the Hamilton-Jacobi equation for charged particle - vector-field interaction. The gradient of the principal function is related with the canonical momentum, from which the momentum of a charged particle in a laser-field can be derived. More details about the derivation can be found in appendix C.2.3, where the full derivation is shown and explained.

The propagation vector is in the z direction: $\vec{k} = k\vec{e}_z = \frac{\omega}{c}\vec{e}_z$ and wave is polarized in the x, y direction: $\vec{a}(\eta) = a_x(\eta)\vec{e}_x + a_y(\eta)\vec{e}_y$ (no $\vec{e}_z$ direction, since $\vec{a} \cdot \vec{k} = 0$). This splits the vector potential in two parts: $\vec{A}(\eta) = f(\eta)(a_x(\eta)\vec{e}_x + a_y(\eta)\vec{e}_y)$. When the charged particle is "injected" in the laser field, it is injected at phase $\eta_0 = \omega t_0 - \frac{\omega}{c} z_0$, in which t_0 is the time injected and z_0 is the position where the particle is injected. Such an "injection" is defined as: the particle is not affected by the laser field at $\eta < \eta_0$, and from $\eta = \eta_0$ onwards it is affected by the laser field. The particle is injected at a velocity $\vec{v}_0 = v_{x0}\vec{e}_x + v_{y0}\vec{e}_y + v_{z0}\vec{e}_z$, with Lorentz factor $\gamma_0 = \frac{1}{\sqrt{1-\frac{\vec{v}_0\cdot\vec{v}_0}{c^2}}}$. The result of the derivation in appendix C.2.3 is the momentum ($\vec{p} = P_x\vec{e}_x + P_y\vec{e}_y + P_z\vec{e}_z$) as function of the laser phase η, which is shown in equation C.59.

$$
\begin{aligned}
P_x(\eta) &= \gamma_0 m v_{x0} + \frac{e}{c}(f(\eta)a_x(\eta) - f(\eta_0)a_x(\eta_0)) \\
P_y(\eta) &= \gamma_0 m v_{y0} + \frac{e}{c}(f(\eta)a_y(\eta) - f(\eta_0)a_y(\eta_0)) \\
P_z(\eta) &= \gamma_0 m v_{z0} + \frac{1}{2\gamma_0 m(c - v_{z0})}[(\frac{e}{c})^2[f(\eta)^2(a_x(\eta)^2 + a_y(\eta)^2) - 2f(\eta)f(\eta_0)(a_x(\eta)a_x(\eta_0) + a_y(\eta)a_y(\eta_0)) \\
&\quad - f(\eta_0)^2(a_x(\eta_0)^2 + a_y(\eta_0)^2)] + 2\frac{e}{c}\gamma_0 m[v_{x0}(f(\eta)a_x(\eta) - f(\eta_0)a_x(\eta_0)) + v_{y0}(f(\eta)a_y(\eta) - f(\eta_0)a_y(\eta_0))]
\end{aligned}
\tag{C.59}
$$

Equations C.60 and C.59 give a relation between the momentum and the phase of the laser:$\eta = \omega t - \frac{\omega}{c} z(t)$. Essentially this is a differential equation, because the displacement in the propagation direction determines the phase, which is determined by the momentum in the propagation direction, which depends on the phase. However, when the particle interaction is non-relativistic, there is a direct relation between the phase and the time $\omega t >> \frac{\omega}{c} z(t) \rightarrow \eta \approx \omega t$, reducing the differential equation into a direct equation. However, when the particle is accelerated relativistically in the propagation direction of the laser, the momentum of the charged particle in the z-direction changes the position $z(t)$ such that $\frac{\omega}{c} z(t)$ can become comparable to ωt and the differential equation has to be solved numerically, such that $\vec{P}(\eta) \rightarrow \vec{P}(t)$. Physically, this implies that the charged particle follows the laser pulse in the propagation direction relativistically, therefore, it experiences a slower oscillation of the laser pulse, which effectively increases the period of the particle's oscillation (essentially this is a Doppler shift effect). An example of this effect is shown in section C.2.2 in figure C.3a, where the differential equations C.59 and C.60 are solved numerically using the Euler method.

Equation C.59 predicts that the charged particle quivers in the direction of the electric field of the laser pulse (x, y direction). Because the charged particle quivers up and down the electric field, it is not displaced by the laser field in the polarization direction. However, the charged particle obtains a velocity and the Lorentz force displaces the particle in the propagation (z) direction. This is not a quivering motion, but $P_z(\eta) > 0$, indicating that the charged particle is net displaced by the laser field in the propagation direction.

In order to obtain a better understanding of the particle's behaviour during the laser irradiation, the *net momentum* is calculated, which is defined as the momentum of the particle, as function of time, averaged over a single oscillation. This eliminates the oscillatory behaviour of the periodic vector $\vec{a}$. The net momentum of a charged particle $< \vec{P}(\eta) >$ should not be confused with the particle's drift $< \vec{P}^d(\eta_0) >$, which is the particle's momentum obtained due to its injection phase, which remains after the laser pulse irradiation. For simplicity, it is assumed that the laser field is linearly polarized in the x direction ($\vec{a} = \sin\eta\vec{e}_x$), although it should be noted that C.59 is generally applicable. The net momentum can be obtained by discretising the continuous equation C.59 with a spacing of one phase (2π) and averaging the momentum across the spaces of the discretised points, which is shown in appendix C.2.3. The result of this approach is shown in equation C.60. Furthermore, the envelope function $f(\eta)$ has been normalised, such that $f(\eta)\vec{a} \rightarrow A_0 f(\eta)\sin\eta\vec{e}_x$ and $\max(f(\eta)) = 1$.

$$\begin{aligned}
< P_x(\eta) > &= \gamma_0 m v_{x0} - \frac{eA_0}{c}(f'(\eta) + f(\eta_0)\sin\eta_0) \\
< P_y(\eta) > &= \gamma_0 m v_{y0} \\
< P_z(\eta) > &= \gamma_0 m v_{z0} + \frac{1}{2\gamma_0 m(c - v_{z0})}[(\frac{eA_0}{c})^2(\frac{1}{2}f(\eta)^2 - 2f'(\eta)\sin(\eta_0)f(\eta_0) - f(\eta_0)^2\sin(\eta_0)^2) \\
&\quad - 2m\gamma_0 v_{x0}(\frac{eA_0}{c})[f'(\eta) + f(\eta_0)\sin(\eta_0)]]
\end{aligned} \tag{C.60}$$

One important parameter in equation C.60 is $\frac{eA_0}{c}$, which is linearly related to the dimensionless laser-strength parameter in equation C.61. If this parameter is larger than one, the laser field is superintense [108, 109]. The implications of this parameter will be shown and discussed in C.2.2.

$$a = \frac{eA}{m_e c^2} \tag{C.61}$$

In equation C.60 it is evident that the net momentum in the polarization direction is an effect of the gradient of the envelope of the laser pulse in combination with phase injection effects, whereas the net momentum in the transverse direction is mainly an effect of the field strength in combination with phase injection effects. Studying the net momentum of the charged particle is important, because a nonzero net momentum leads to the charged particle's displacement. Therefore, there are three effects which can lead to a charged particle's displacement in a laser field: a large gradient in the laser envelope leading to a displacement in the polarization direction; a high laser intensity leading to a Lorentz force displacement in the propagation direction (magnetic field effect) and phase injection effects, leading to a net momentum in both the propagation and polarization direction.

Phase injection effects not only lead to a net momentum *during* the laser interaction, but this net momentum also remains *after* the laser pulse irradiation. This will be referred to as the *particle's drift* $< \vec{P}^d(\eta_0) >$. At the end of the laser pulse, the laser pulse intensity goes to zero and the phase of the laser goes to infinity: $\eta \rightarrow \infty, f(\eta) \rightarrow 0, f'(\eta) \rightarrow 0$. Combining this information with equation C.59 leads to the charged particle's drift, shown in equation C.62. In order to ease the interpretation of this equation, it is assumed that the charged particle has a zero velocity before the laser particle interaction. From equation C.62 it is apparent that the moment of the injection of the particle $\eta_0 = \omega t_0 - \frac{\omega}{c}z_0$ leads to a net momentum both during and after the laser pulse interaction, which depends on the phase of the laser field and the amplitude of the laser field at the moment of injection.

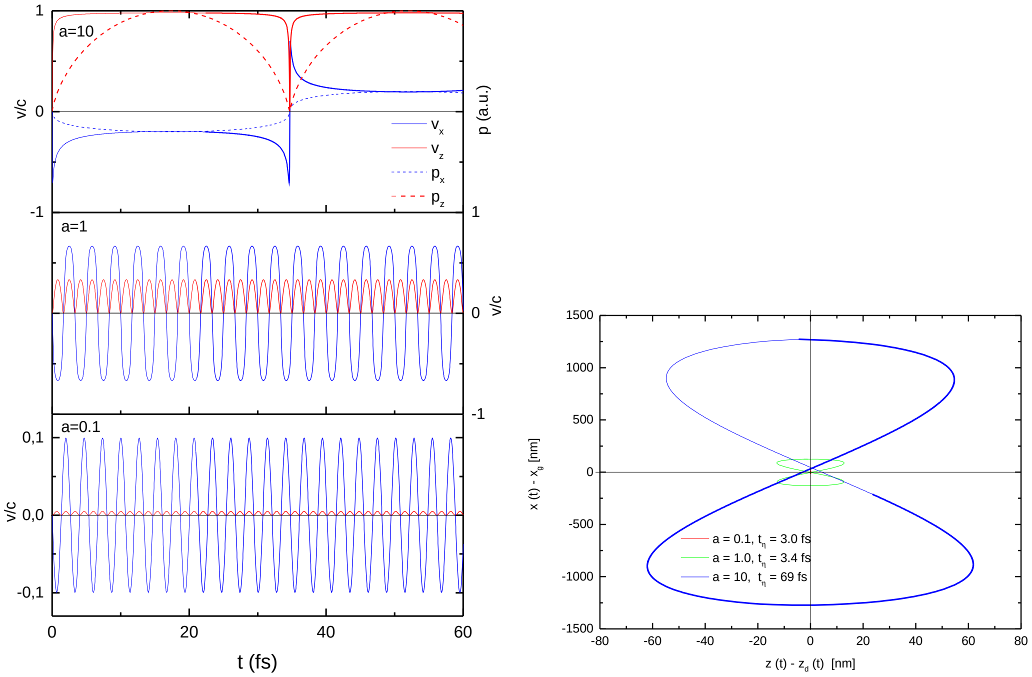

(a) The velocity of an electron in a plane wave field in the propagation direction and in the polarization direction.

(b) The trajectory of an electron being accelerated in a plane wave field in the electron's rest frame, showing a figure-8 motion.

Figure C.2: The velocity and trajectories of an electron in a plane wave field with various laser intensities, indicating different interaction regimes. $a = 0.1$ corresponds to sub-relativistic interaction, $a = 1.0$ corresponds to mild relativistic interaction and $a = 10$ corresponds to superintense relativistic interaction.

$$\begin{aligned}
&< P_x^d(\eta_0) > = -\frac{eA_0}{c} f(\eta_0) \sin \eta_0 \\
&< P_y^d(\eta_0) > = 0 \rightarrow v_y = 0 \\
&< P_z^d(\eta_0) > = -\frac{1}{4mc} (\frac{eA_0}{c} f(\eta_0) \sin(\eta_0))^2
\end{aligned} \tag{C.62}$$

C.2.2 Implications and applications

The dimensionless laser-strength parameter expresses the laser energy in terms of the rest energy of an electron. The effect of the dimensionless laser-strength is shown in figure C.2a, where the envelope effects of the laser pulse are neglected (the laser-amplitude is assumed to be constant). When $a << 1$, the laser-electron interaction is sub-relativistic: the electron experiences only the effect of the electric field and quivers in the polarization direction. Because the particle's quiver is sub-relativistic, the effect of the B field is negligible and the charged particle is not net displaced. When $a \approx 1$, the laser-electron interaction is mildly relativistic $\gamma = 2$ and the electron starts to experience the effect of the B field as well: resulting in a net displacement in the propagation direction of the laser. When $a >> 1$, the laser field is superintense and the electron is accelerated relativistically in the propagation direction of the laser $\eta = \omega t - \frac{\omega z}{c}, v_z \approx bt \rightarrow \eta \approx \omega t(1 - \frac{b}{c})$. When the electron is accelerated relativistically in the propagation direction of the laser, the parameter b becomes of the order of c, effectively prolonging the time an electron experiences the laser field at a certain phase (essentially this is a Doppler shift). In this superintense regime, the momentum in the propagation direction becomes relatively larger than in the polarization direction. Due to relativistic effects, this leads to a heavier electron mass, which leads to a decrease in electron velocity in the polarization direction. This effect is often called auto-resonance acceleration, because $\eta \to 0$ implies that the particle's oscillation is in resonance with the electromagnetic field [79, 111, 77].

Relativistically accelerated electrons gyrate in a figure-8 motion in the rest frame. This implies that the frame moves with the electron drift speed. While the electron gyrates in a figure-8 motion, the electron radiates due to acceleration effects, which leads to higher harmonic generation [108, 109]: a form of non-linear Thomson scattering. The figure-8 motions is shown in figure C.2b for different laser intensities. The figure-8 trajectories calculated using this model have been compared with literature (equation C.7 in the previous chapter) and a good agreement (within 1 %) has been found.

C.2.3 Derivation - Laser-charged particle interaction trajectories

Please note that this work is a repeat of a part of the work of Salamin [109].

We start with the Hamilton-Jacobi equation, which relates the derivative of the action and the Hamiltonian in classical mechanics [112], following the same fashion as the work by Salamin [109]. The Hamiltonian of a charged particle in a laser field is in which $S(\vec{r}, t)$ is the Hamilton principal function, c is the speed of light, e is the electron charge, m is the mass of the charged particle, and $\vec{A}$ is the vector potential of the plane wave: equation C.63.

$$(\frac{S}{t})^2 = H^2 \to (\frac{S}{t})^2 = c^2(\nabla S + \frac{e}{c}\vec{A})^2 + (mc^2)^2 \tag{C.63}$$

The solution of the Hamilton is usually of the following form of equation C.64 in which $\vec{\alpha}$ and β are constants to be determined from the initial conditions of the problem. Furthermore, transversality is assumed $\vec{k} \cdot \vec{A} = 0$.

$$S(\vec{r}, t) = \vec{\alpha} \cdot \vec{r} + \beta ct + F(\eta) \tag{C.64}$$

This leads to a first-order differential equation for F. A single integration with respect to η then gives equation C.65.

$$F(\eta) = \frac{1}{2}(\vec{\alpha} \cdot \vec{k} + \beta k)^{-1} \int_{\eta_0}^{\eta} [\alpha^2 - \beta^2 + (mc)^2 + 2(e/c)\vec{\alpha} \cdot \vec{A} + (e/c)^2 A^2] d\eta \tag{C.65}$$

By using equations C.65 and C.64, the gradient of the principal function ∇S can be calculated. This equals the canonical moment of motion: $\nabla S = \vec{p}_{can} = \vec{p} - \frac{e}{c}\vec{A}$. This leads to an equation for the momentum of the electron, equation C.66.

$$\vec{p} = \frac{e}{c}\vec{A} + \vec{\alpha} - \frac{\vec{k}}{2} \frac{\alpha^2 - \beta^2 + (mc)^2 + 2(e/c)\vec{\alpha} \cdot \vec{A} + (e/c)^2 \alpha^2}{\vec{\alpha} \cdot \vec{k} + \beta k} \tag{C.66}$$

By using the principal function, the energy of the electron can also be derived: $E = -\frac{\partial S}{\partial t}$, which leads to equation C.67:

$$E = -c(\beta + \frac{\vec{k}}{k} \cdot (\vec{\alpha} - \vec{P}_{can})) \tag{C.67}$$

Derivation - Generalisation of Salamin's theory with injection phase effects

From this point on, our work - the generalisation of [109] begins to include phase injection effects.

By setting the starting conditions of the electron, a relation for the arbitrary constants of $\vec{\alpha}$ and β can be derived. This derivation combined with equation C.66 leads to equation C.59 for the momenta of a charged particle in a plane-wave laser field.

For the initial conditions of the electron, it is assumed that the initial velocity of the electron is $\vec{v}_0 = v_{x0}\vec{e}_x + v_{y0}\vec{e}_y + v_{z0}\vec{e}_z$ with Lorentz factor $\gamma_0 = \frac{1}{\sqrt{1-\vec{v}_0\cdot\vec{v}_0/c^2}}$. The canonical momentum at the start is therefore $\vec{P}_{can} = \gamma_0 m\vec{v}_0 = \gamma_0 m v_{x0}\vec{e}_x + \gamma_0 m v_{y0}\vec{e}_y + \gamma_0 m v_{z0}\vec{e}_z$. The electron enters the region of interaction of the field with this start velocity at phase $\eta_0 = \omega(t_0 - \frac{z_0}{c})$. The laser-field has a vector potential of $\vec{A} = f(\eta_0)(\vec{a}_x(\eta_0) + \vec{a}_y(\eta_0))$ at $\eta = \eta_0$. Here, it is assumed that z is the propagation direction of the laser beam: $\vec{A}\cdot veck = 0$. Combining the start conditions of the electron with equations C.66 and C.67 leads to equation for $\vec{\alpha} = \alpha_x\vec{e}_x + \alpha_y\vec{e}_y + \alpha_z\vec{e}_z$ and β. This leads to equations C.68.

$$
\begin{aligned}
E_0 = \gamma_0 mc^2 &\rightarrow \gamma_0 mc^2 = -c(\beta + \alpha_z - \gamma_0 m v_{z0}) \\
p_{x0} = \gamma_0 m v_{x0} &\rightarrow \gamma_0 m v_{x0} = \frac{e}{c} f(\eta_0) a_x(\eta_0) + \alpha_x \\
p_{y0} = \gamma_0 m v_{y0} &\rightarrow \gamma_0 m v_{y0} = \frac{e}{c} f(\eta_0) a_y(\eta_0) + \alpha_y \\
p_{z0} = \gamma_0 m v_{z0} &\rightarrow \gamma_0 m v_{z0} = \alpha_z - \frac{1}{2(\alpha_z+\beta)}(\alpha_x^2 + \alpha_y^2 + \alpha_z^2 - \beta^2 + (mc)^2 + 2\frac{e}{c} f(\eta_0)(a_y(\eta_0)\alpha_y + a_x(\eta_0)\alpha_x) \\
&\qquad + (\frac{e}{c})^2 f(\eta_0)^2 (a_x(\eta_0)^2 + a_y(\eta_0)^2))
\end{aligned}
$$

Equation C.68 can be simplified into equation C.68

$$
\begin{aligned}
\alpha_x &= \gamma_0 m v_{x0} - \frac{e}{c} f(\eta_0) a_x(\eta_0) \\
\alpha_y &= \gamma_0 m v_{y0} - \frac{e}{c} f(\eta_0) a_y(\eta_0) \\
\alpha_z + \beta &= \gamma_0 m (v_{z0} - c) \\
\alpha_z &= \gamma_0 m v_{z0} + \frac{1}{2(\alpha_z+\beta)}(\alpha_x^2 + \alpha_y^2 + \alpha_z^2 - \beta^2 + (mc)^2 + 2\frac{e}{c} f(\eta_0)(a_y(\eta_0)\alpha_y + a_x(\eta_0)\alpha_x) \\
&\quad + (\frac{e}{c})^2 f(\eta_0)^2 (a_x(\eta_0)^2 + a_y(\eta_0)^2))
\end{aligned}
$$

By using the first two equations of the equation set C.68 for α_x and α_y, the third and fourth equations of the equation set C.68 can be used to simplify the relation between α_z and β. The plan is to group all terms α_z and β together in the third equation of set C.68, such that only terms of $\alpha_z + \beta$ appear in the equation, which is shown in equation C.68. Furthermore, $\alpha_z^2 - \beta^2 = (\alpha_z + \beta)(\alpha_z - \beta)$ is used.

$$\begin{aligned}
\alpha_z &= \gamma_0 m v_{z0} + \frac{1}{2(\alpha_z+\beta)}()\gamma_0^2 m^2 v_{x0}^2 + (\frac{e}{c})^2 f(\eta_0)^2 a_x(\eta_0)^2 - 2\gamma_0 m v_{x0}\frac{e}{c} f(\eta_0) a_x(\eta_0) + \gamma_0^2 m^2 v_{y0}^2 + \\
&(\frac{e}{c})^2 f(\eta_0)^2 a_y(\eta_0)^2 - 2\gamma_0 m v_{y0}\frac{e}{c} f(\eta_0) a_y(\eta_0) + (\alpha_z+\beta)(\alpha_z-\beta) + (mc)^2 + 2\frac{e}{c} f(\eta_0)(\gamma_0 m v_{y0} a_y(\eta_0) \\
&-\frac{e}{c} f(\eta_0) a_y(\eta_0)^2 + \gamma_0 m v_{x0} a_x(\eta_0) - \frac{e}{c} f(\eta_0) a_x(\eta_0)^2) + (\frac{e}{c})^2 f(\eta_0)^2 (a_x(\eta_0)^2 + a_y(\eta_0)^2)) \\
\rightarrow \alpha_z &= \gamma_0 m v_{z0} + \frac{1}{2(\alpha_z+\beta)}(\gamma_0^2 m (v_{x0}^2 + v_{y0}^2) + (mc)^2) + \frac{1}{2}(\alpha_z+\beta) \\
\rightarrow \alpha_z + \beta &= \gamma_0 m v_{z0} + \frac{1}{2(\alpha_z+\beta)}(\gamma_0^2 m^2 v_{x0}^2 + \gamma_0^2 m^2 v_{y0}^2 + (mc)^2) + \frac{1}{2}(\alpha_z+\beta)
\end{aligned} \tag{C.68}$$

This implies that equation C.68can be simplified with the help of equation C.68 into C.69, which shows that the problem does only depend on the terms α_x, α_y and $\alpha_z + \beta$.

$$\begin{aligned}
\alpha_x &= \gamma_0 m v_{x0} - \frac{e}{c} f(\eta_0) a_x(\eta_0) \\
\alpha_y &= \gamma_0 m v_{y0} - \frac{e}{c} f(\eta_0) a_y(\eta_0) \\
\alpha_z + \beta &= \gamma_0 m (v_{z0} - c) \\
\alpha_z + \beta &= 2\gamma_0 m v_{z0} + \frac{1}{\alpha_z+\beta}(\gamma_0^2 m^2 v_{x0}^2 + \gamma_0^2 m^2 v_{y0}^2 + (mc)^2)
\end{aligned} \tag{C.69}$$

The last two equations of C.69 both depend on one parameter $\alpha_z + \beta$, this implies that either the third or fourth equation in C.69 are either wrong, or both equations actually represent the same (because the system of equations is overdetermined). Therefore we need to check whether the last two equations correspond with each other. For simplicity $\alpha_z + \beta = \xi$. Both equations are actually the same, which is shown in equations C.70.

$$\begin{aligned}
&\xi = \gamma_0 m (v_{z0} - c) \\
&\xi = 2\gamma_0 m v_{z0} + \frac{1}{\xi}(\gamma_0^2 m^2 v_{x0}^2 + \gamma_0^2 m^2 v_{y0}^2 + (mc)^2) \\
\Rightarrow \quad &\xi^2 - 2\gamma_0 m v_{z0}\xi - \gamma_0^2 m^2 v_{x0}^2 - \gamma_0^2 m^2 v_{y0}^2 - m^2 c^2 = 0 \\
\xrightarrow[\xi]{\text{test input}} \quad &\gamma_0^2 m^2 (v_z 0 - c)^2 - 2\gamma_0^2 m^2 v_{z0}(v_{z0} - c) - \gamma_0^2 m^2 (v_{x0}^2 + v_{y0}^2) - (mc)^2 = 0 \\
&v_{z0}^2 - 2v_{z0}c + c^2 - 2v_{z0}^2 + 2v_{z0}c - v_{x0}^2 - v_{y0}^2 - c^2\frac{1}{\gamma_0^2} = 0 \\
&-v_{z0}^2 + c^2 - v_{x0}^2 - v_{y0}^2 - c^2(1 - \frac{v_{x0}^2 + v_{y0}^2 + v_{z0}^2}{c^2}) = 0 \qquad \checkmark
\end{aligned} \tag{C.70}$$

This implies that any terms for α_z and β can be chosen such that $\alpha_z + \beta = \gamma_0 m(v_{z0} - c)$. Analogous to α_x and α_y, which can be written as $\alpha_{x,y} = \gamma_0 m v_{x0,y0} - \frac{e}{c} f(\eta_0) a_{x,y}(\eta_0)$, α_z is chosen such that $\alpha_z = \gamma_0 m v_{z0}$. Therefore the term $\vec{\alpha}$ can be written as $\vec{\alpha} = \gamma_0 m \vec{v}_0 - \frac{e}{c}\vec{a}(\eta_0)$ (because $\vec{A} \cdot \vec{k} = 0 \rightarrow a_z = 0$). Since $\alpha_z + \beta = \gamma_0 m(v_{z0} - c)$, this implies that β has to be chosen such that this equation holds, which results in $\beta = -\gamma_0 mc$. Therefore, the equations for $\vec{\alpha}$ and β have been derived, which are shown in equation set C.71.

$$\begin{aligned}
\vec{\alpha} &= \gamma_0 m \vec{v}_0 - \frac{e}{c} f(\eta_0)\vec{a}(\eta_0) \\
\beta &= -\gamma_0 mc
\end{aligned} \tag{C.71}$$

By combining equations C.71 with equations C.66the momentum of a charged particle in a plane wave laser field can be derived. Eventually this leads to equation C.59. The momenta in the polarization direction of the laser are easily obtained and are shown in equation C.72.

$$\begin{aligned} p_x &= \gamma_0 m v_{x0} + \frac{e}{c}(f(\eta)a_x(\eta) - f(\eta_0)a_x(\eta_0)) \\ p_y &= \gamma_0 m v_{y0} + \frac{e}{c}(f(\eta)a_y(\eta) - f(\eta_0)a_y(\eta_0)) \end{aligned} \tag{C.72}$$

The momenta in the propagation direction of the laser involves more mathematics and a derivation is shown in equation C.73

$$\begin{aligned} p_z &= \alpha_z - \frac{1}{2(\alpha_z+\beta)}(\vec{\alpha}\cdot\vec{\alpha} - \beta^2 + m^2c^2 + 2\frac{e}{c}(f(\eta)(\alpha_x a_x(\eta) + \alpha_y a_y(\eta))) + (\frac{e}{c})^2(f(\eta)^2(a_x(\eta)^2 + a_y(\eta)^2))) \\ \Rightarrow p_z &= \gamma_0 m v_{z0} + \frac{1}{2\gamma_0 m(c - v_{z0})}(\underline{\gamma_0^2 m^2 v_0^2} + (\frac{e}{c})^2 f(\eta_0)^2(a_x(\eta_0)^2 + a_y(\eta_0)^2) - 2\frac{e}{c}f(\eta_0)\gamma_0 m(v_{0x}a_x(\eta_0) + v_{0y}a_y(\eta_0)) \\ &\quad \underline{-\gamma_0^2 m^2 c^2 + m^2c^2} + 2\frac{e}{c}f(\eta)\gamma_0 m(v_{0x}a_x(\eta) + v_{0y}a_y(\eta)) - 2(\frac{e}{c})^2 f(\eta_0)f(\eta)(a_x(\eta_0)a_x(\eta) + a_y(\eta_0)a_y(\eta)) + \\ &\quad (\frac{e}{c})^2 f(\eta)^2(a_x(\eta)^2 + a_y(\eta)^2)) \\ \Rightarrow p_z &= \gamma_0 m v_{z0} + \frac{1}{2\gamma_0 m(c - v_{z0})}((\frac{e}{c})^2(f(\eta)^2(a_x(\eta)^2 + a_y(\eta)^2) - 2f(\eta)f(\eta_0)(a_x(\eta)a_x(\eta_0) + a_y(\eta)a_y(\eta_0)) \\ &\quad + f(\eta_0)^2(a_x(\eta_0)^2 + a_y(\eta_0)^2)) + 2\frac{e}{c}\gamma_0 m(v_{x0}[f(\eta)a_x(\eta) - f(\eta_0)a_x(\eta_0)] + v_{y0}[f(\eta)a_y(\eta) - f(\eta_0)a_y(\eta_0)])) \end{aligned} \tag{C.73}$$

Combining the equations C.72 and C.73 leads to a set of equations - equation C.74 for the momentum of a charged particle in a plane wave field with an envelope (a model for a laser beam in the waist of a laser). This equation is the same as equation C.59 in section C.2.2.

$$\begin{aligned} p_x &= \gamma_0 m v_{x0} + \frac{e}{c}(f(\eta)a_x(\eta) - f(\eta_0)a_x(\eta_0)) \\ p_y &= \gamma_0 m v_{y0} + \frac{e}{c}(f(\eta)a_y(\eta) - f(\eta_0)a_y(\eta_0)) \\ p_z &= \gamma_0 m v_{z0} + \frac{1}{2\gamma_0 m(c - v_{z0})}((\frac{e}{c})^2(f(\eta)^2(a_x(\eta)^2 + a_y(\eta)^2) - 2f(\eta)f(\eta_0)(a_x(\eta)a_x(\eta_0) + a_y(\eta)a_y(\eta_0)) \\ &\quad + f(\eta_0)^2(a_x(\eta_0)^2 + a_y(\eta_0)^2)) + 2\frac{e}{c}\gamma_0 m(v_{x0}[f(\eta)a_x(\eta) - f(\eta_0)a_x(\eta_0)] + v_{y0}[f(\eta)a_y(\eta) - f(\eta_0)a_y(\eta_0)])) \end{aligned} \tag{C.74}$$

Net momentum

In order to simplify equation C.74 (which is equation C.59 in section C.2.2) the oscillatory behaviour of $a_x(\eta)$ and $a_y(\eta)$ can be eliminated by determining the net momentum. A net momentum can be defined by discretising the continuous equation C.59 with a spacing of one phase (2π) and averaging the momentum across the spaces of the discretised points .For example $< \vec{P}(\eta = \pi) >= \frac{1}{2\pi}\int_0^{2\pi}\vec{P}(\eta)d\eta, < \vec{P}(\eta = 3\pi) >= \frac{1}{2\pi}\int_{2\pi}^{4\pi}\vec{P}(\eta)d\eta, ..., < \vec{P}(\eta = (2N+1)\pi) >= \frac{1}{2\pi}\int_{2N\pi}^{2(N+1)\pi}\vec{P}(\eta)d\eta \rightarrow < \vec{P}(\eta) >= \frac{1}{2\pi}\int_{\eta-\pi}^{\eta+\pi}\vec{P}(\eta)d\eta$ for $N = 0, 1, 2, ...$. An illustration of this is shown in figure C.3a, where the momentum and net momentum of an electron in an example laser pulse is shown.

Note though that equation C.59 is general and can be used for all kinds of polarizations, as long as the laser beam is transverse. In order to simplify the equations, which enhances clarity and physical insight, a linear polarization is assumed: $\vec{a} = \sin\eta\vec{e}_x$ while calculating the drift momenta in equation C.75.

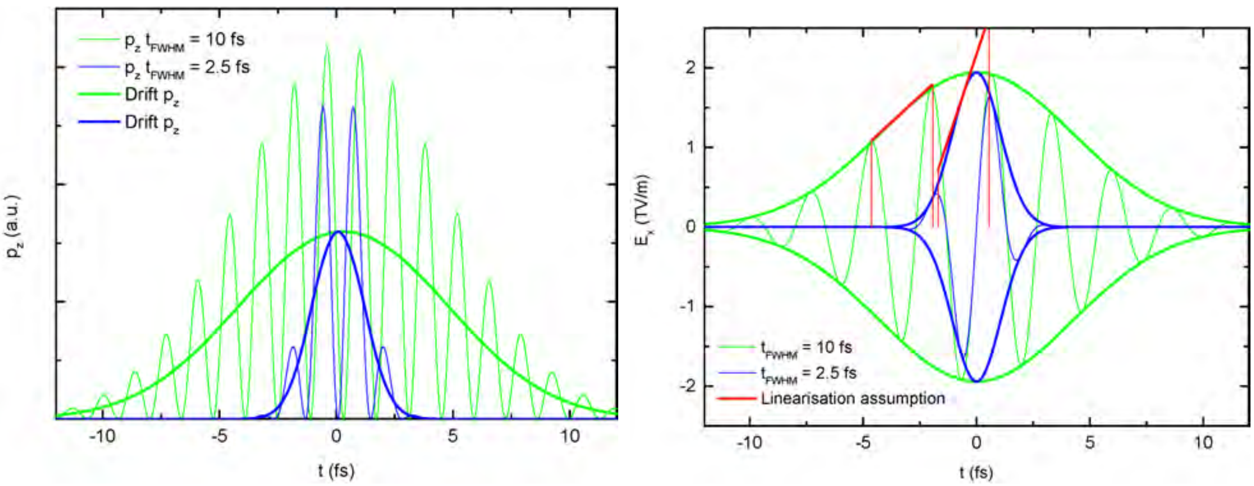

(a) The momentum and net momentum of an electron as function of time in the z direction for two different laser pulse durations.

(b) A plot of the electric field and the electric field envelope of the laser parameters used. The linearisation assumption is indicated in red

Figure C.3: The laser pulse has a linear polarisation: $\vec{E} = E_x\vec{e}_x$, $\vec{B} = B_y\vec{e}_y$. The laser envelope is a Gaussian function $f(\eta) = \exp(-(t/\tau)^2)$ with the full-width half maximum (FWHM) of the laser pulse at $t_{\text{FWHM}} = 10$ fs and $t_{\text{FWHM}} = 2.5$ fs. The laser frequency is $\omega = 2.35 \times 10^{15}$ rad/s.

$$
\begin{aligned}
&< P_x(\eta) > = \gamma_0 m v_{x0} + \frac{e}{c}(\frac{1}{2\pi}\int_{\eta-\pi}^{\eta+\pi} f(\eta')\sin(\eta')d\eta' - f(\eta_0)\sin\eta_0) \\
&< P_y(\eta) > = \gamma_0 m v_{y0} \\
&< P_z(\eta) > = \gamma_0 m v_{z0} + \frac{1}{2\gamma_0 m(c - v_{z0})}[(\frac{e}{c})^2(\frac{1}{2\pi}\int_{\eta-\pi}^{\eta+\pi} f(\eta')^2\sin(\eta')^2 d\eta' - \frac{1}{\pi}\sin(\eta_0)f(\eta_0)\int_{\eta-\pi}^{\eta+\pi} f(\eta')\sin(\eta')d\eta' \\
&\qquad + f(\eta_0)^2\sin(\eta_0)^2) + 2m\gamma_0 v_{x0}[\frac{1}{2\pi}\int_{\eta-\pi}^{\eta+\pi} f(\eta')\sin(\eta')d\eta' - f(\eta_0)\sin(\eta_0)]]
\end{aligned}
\tag{C.75}
$$

A last assumption made is that the change in the laser envelope during a single oscillation is small enough such that a linear approximation can be used to model the envelope during one oscillation. In practice, this assumption is valid when the laser pulse contains many oscillations, which is illustrated in figure C.3b. The reason this assumption is made is that it makes it possible to create a general solution for the integrals in equation C.75. These integrals are evaluated in equation C.76

Furthermore, here it is assumed that there are enough oscillations in one laser pulse in order to approximate the evolution of the envelope as a function of time from oscillation to oscillation with a linear Taylor expansion.

$$
\begin{aligned}
\frac{1}{2\pi}\int_{\eta-\pi}^{\eta+\pi} f(\eta')\sin(\eta')d\eta' &= \frac{1}{2\pi}\int_{\eta-\pi}^{\eta+\pi} (f(\eta) + f'(\eta)(\eta - \eta'))\sin(\eta')d\eta' = -f'(\eta) \\
\frac{1}{2\pi}\int_{\eta-\pi}^{\eta+\pi} f(\eta')^2\sin(\eta')^2 d\eta' &= \frac{1}{2\pi}\int_{\eta-\pi}^{\eta+\pi} (f(\eta)^2 + 2f(\eta)f'(\eta)(\eta - \eta'))\sin(\eta')^2 d\eta' \approx \frac{1}{2}f(\eta)^2
\end{aligned}
\tag{C.76}
$$

In equation C.76 it is assumed that the derivative of the envelope has a much smaller value than the envelope itself ($f(\eta) >> f'(\eta)$). Combining equations C.76 and C.75 leads to simplified net momentum equations, equation C.77. Furthermore, the envelope function $f\eta$ has been normalised, such that $f(\eta) \rightarrow A_0 f(\eta)$ and $\max f(\eta) = 1$.

$$\begin{aligned}
< P_x(\eta) > &= \gamma_0 m v_{x0} - \frac{eA_0}{c}(f'(\eta) + f(\eta_0)\sin\eta_0) \\
< P_y(\eta) > &= \gamma_0 m v_{y0} \\
< P_z(\eta) > &= \gamma_0 m v_{z0} + \frac{1}{2\gamma_0 m(c - v_{z0})}[(\frac{eA_0}{c})^2(\frac{1}{2}f(\eta)^2 - 2f'(\eta)\sin(\eta_0)f(\eta_0) - f(\eta_0)^2\sin(\eta_0)^2) \\
&\quad - 2m\gamma_0 v_{x0}(\frac{eA_0}{c})[f'(\eta) + f(\eta_0)\sin(\eta_0)]]
\end{aligned} \tag{C.77}$$

Equation C.77 is the same as equation C.60 in section C.2.2. The importance and implications of this equation are discussed in section C.2.2.

C.2.4 High-Z model

The portion of electrons inside the cluster as a function of time is $\eta(t)$, which is provided by the FOM presented previously. The motion of the electrons through the cluster (e.q. the electron dynamics) is described by an forced oscillating electron sphere with a homogeneous density, of which only the overlapping part with the immobile ion cluster is taken into account. The amount of electrons is: $N_e = Q(t)\eta(t)$, in which $Q(t)$ is the cluster charge. The amount of electrons $N_e(t)$ is assumed to be homogeneously distributed over the part of the electron cloud that overlaps with the ion cluster. Hence the charge density of the overlapping part of the electron cloud is $\rho_E(t) = \frac{N_e(t)e}{V(d(t))}$, in which $V(d(t))$ is the volume of the overlap between the electron and the ion cloud. The displacement of the electron sphere is provided by the solution of the forced oscillator: $x(t) = A\cos(\omega_L t)$. The cluster charge $Q(t)$ is determined by the ion charge states of the atoms in the cluster, which is determined by ADK theory. ADK theory provides an ionisation probability as a function of electric field E and atomic parameters $\vec{a}$: $\frac{dW}{dt} = f(E, \vec{a})$. The electric field is a combination of the electric field generated by the laser pulse: $\vec{E}_{\text{Laser}} = E_0 f(\omega t)\cos(\omega t)\vec{e}_x$ (spatial dependence is neglected), the electric field generated by the ion cloud, $\vec{E}_{\text{ions}}$ and the electric field generated by the dynamic electron cloud $\vec{E}_{\text{electrons}}$.

For the forced oscillator model it is necessary to assume that the ion charges are distributed homogeneously across the ion cloud, hence it is assumed that the ion charge distribution $\rho_I(t)$ is homogeneous for the determination of the electric field generated by the ion cloud: $\vec{E}_{\text{ion}} = \frac{\rho_I r}{3\epsilon_0}\vec{e}_r$. This is an approximation, because the ion charge distribution might not be homogeneous, because of the spatial dependence of the fields of the electron and ion clouds. the field generated by the ion cloud and because of the spatial and temporal dependence of the field generated by the electron cloud dynamics. In order to approximate the inhomogeneity of the ion charge distribution, the ion sphere is discretised (by the amount of atoms in the cluster). At each position, ADK theory is used in order to predict the charge state of the ion at that position with a Monte Carlo routine (similar to the GPT implementation of the ADK theory). the charge species in the discretised ion sphere are summed and averaged over the cluster sphere in order to determine $rho_I(t)$.

The electric field generated by the electron sphere overlapping the ion cluster is determined numerically, resulting in $\vec{E}_{\text{electrons}}$. This is done by discretising the electron sphere and investigating the electric field of each volume element at each ion position numerically by using Coulomb's law: $\vec{dE} = \frac{\rho dV}{4\pi\epsilon_0}\frac{\vec{r}}{r^3}$ and summing over each volume element of the electron sphere. Only the part of the sphere that overlaps with the ion cloud is taken into account.

This creates a closed set of equations which has to be solved dynamically. The start condition is a cluster whose ions are singly charged (as in the low-Z model) and whose electron sphere overlaps the ion sphere exactly. This process and its close set of equations is visualised schematically in figure 4.7.

C.3 Expansion models

Here some more details on the self-consistent expansion model, created by [2, 3] is provided.

C.3.1 Self-consistent expansion model

The set of equations 5.6 can be solved by using a similarity ansatz in equation C.78. The similarity ansatz states that the electron and ion density profiles, relative to the cluster radius, do not change in time. The temporal dynamics of the density are governed by a linear velocity profile, which is linear because the radius of the cluster will expand linearly in time when the initial acceleration phase has taken place.

$$\begin{aligned}
v_i(t,r) &= \dot{R}\xi \\
v_e(t,r) &= \dot{R}\xi \\
\dot{R} &= \frac{dR}{dt} \\
\xi &= \frac{r}{R(t)} \\
\rho_e(t,r) &= \rho_e(0,r)(\frac{R_0}{R(t)})^3 N_e(\xi) \\
N_e(\xi) &= 0 \\
\rho_i(t,r) &= \rho_e(0,r)(\frac{R_0}{R(t)})^3 N_i(\xi) \\
N_i(\xi) &\neq 0
\end{aligned} \tag{C.78}$$

The radius in these equations can be solved implicitly by using the result of the polytropic law, which leads to a single differential equation C.79, in which $c_{s0} = \sqrt{\frac{ZT_{e0}}{m_i}}$ is the sound speed of the expansion.

$$\dot{R}(t) = 2c_{s0}\sqrt{1 - \frac{R(0)}{R(t)}} \tag{C.79}$$

In order to calculate the position of the ion front (ξ_f), which denotes the boundary of the ion distribution, and the self-consistent profile of the potential ϕ a second order equation is derived by combining the Poisson equation with the self-similarity ansatz, which results in equation C.80, in which $\phi = \frac{e\Phi}{T_e}$. Effectively, the eigenvalue equation is a second-order equation requiring three boundary conditions for the unique determination of the function $\phi(\epsilon)$ and ξ_f.

$$\begin{aligned}
\frac{1}{\xi^2}\frac{d}{d\xi}(\xi^2\frac{d\phi}{d\xi}) &= \begin{cases} \Lambda^2(N_e(\xi) - N_i(\xi)), & \xi \leq \xi_f \\ \Lambda^2 \exp(\phi - \mu_e\xi^2), & \xi > \xi_f \end{cases} \\
\phi(\xi_f) &= -\xi_f^2 \\
\frac{d\phi(\xi_f)}{d\xi} &= -2\xi_f \\
\lim_{\xi\to\infty} \xi^2\frac{d\phi}{d\xi} &= 0
\end{aligned} \tag{C.80}$$

When equation C.80 and equation C.79, the self-consistent and self-similar profile of the potential can be calculated and the time dynamics of the system can be calculated. The solution of C.80 depends on Λ and μ_e, therefore $\xi_f = f(\Lambda, \mu_e)$ and in order to determine this, the $\xi > \xi_f$ relation has to be used. From this point onward, we will assume that the general solution of ξ_f is known (which is impossible to calculate algebraically and has to be calculated numerically for a large range of ξ_f, μ_e), such that $\xi_f = f(\Lambda, \mu_e)$. When these are combined with the static profiles of the result of the self-similar ansatz in equation C.81, the evolution of the electron and ion density can be determined in time and is characterised by the two dimensionless parameters Λ (directly related to the ratio of the temperature and the electrostatic Coulomb energy (or the relation between the radius and the Debeye length of the cluster plasma)) and μ_e, denoting the relative electron mobility (as compared to the ions), which are valid in the case of $\xi < \xi_f$. When these equations are combined with the self-similarity ansatz (equation C.78), the evolution of the electron and ion density in time can be calculated.

$$\begin{aligned} \phi &= -\xi^2 \\ N_e(\xi) &= \exp(-(1+\mu_e)\xi^2) \\ N_i(\xi) &= N_e + \frac{6}{\Lambda^2} \end{aligned} \tag{C.81}$$

Appendix D

Simulation results

D.1 Simulation overview

A table of all the simulations visualised with a trajectory plot in section D.1.1

	Laser parameters					Cluster parameters				Results				
Tag	Env	E	λ	$t_{1/2}$	t_m	Typ	n	R	N	t_i	t_e	η	$E_{\text{kin}}^{\text{max}}$	Description
COUL1	Gaus	2×10^{12}	800	60	150	D	H: 10^{27}	3	100	66	90	100	1000	Coulomb explosion
COUL2	Gaus	2×10^{12}	800	60	150	D	H: 10^{27}	3	100	66	90	100	1000	Coulomb explosion
COUL3	Gaus	2×10^{12}	800	60	150	D	H: 10^{27}	3	100	66	90	100	1000	Coulomb explosion
COUL4	Gaus	2×10^{12}	800	60	150	D	H: 10^{27}	3	100	66	90	100	1000	Coulomb explosion
COUL5	Gaus	2×10^{12}	800	60	150	D	H: 10^{27}	3	100	66	90	100	1000	Coulomb explosion

D.1.1 Trajectory trace plots

This section contains the electron and ion trajectories and velocity traces of several simulations in this thesis. Concerning the results, the following should be noted (quoted from chapter 2):

”In order to give a full picture of the laser-single cluster dynamics, for the first case the x, y, z trajectories of the electrons and ions are plot and the v_x, v_y, v_z velocity traces of the electrons and ions are plot in figure 2.3. Each line represents the trajectory/velocity trace of an electron/ion in the simulation. The lines are coloured in order to distinguish the lines from each other. Please note that the electron data is plot in a different time axis than the ion data. The reason for this is that the electron dynamics take place during the laser interaction $\sim$ fs, whereas the ion dynamics take place on a slower timescale. Since the displacement is the integral of the velocity, practically most of the physics is governed by the velocity traces. However, for understanding the broader picture the electron and ion trajectories are provided as well. Imagine tracking a single atom in the deuterium cluster, this atom, or ”ionisable element” remains an atom until it is at some time ionised (t_{ion}), creating a single charged ion and an electron. In the simulation this implies that the electron and ion start appearing in $t > t_{\text{ion}}$ and before 5_{ion} the electron and ion did not exist yet in the simulation: because the atom was not ionised yet. In the simulation results, for numerical convenience, we denote that a particle does not exist yet (or does not exist any more: at $t > t_{\text{ion}}$ the atom does not exist any more, because it is transformed into an electron and an ion), with $(v_x, v_y, v_z, x, y, z) = (0, 0, 0, 0, 0, 0)$.”

Trajectory plots

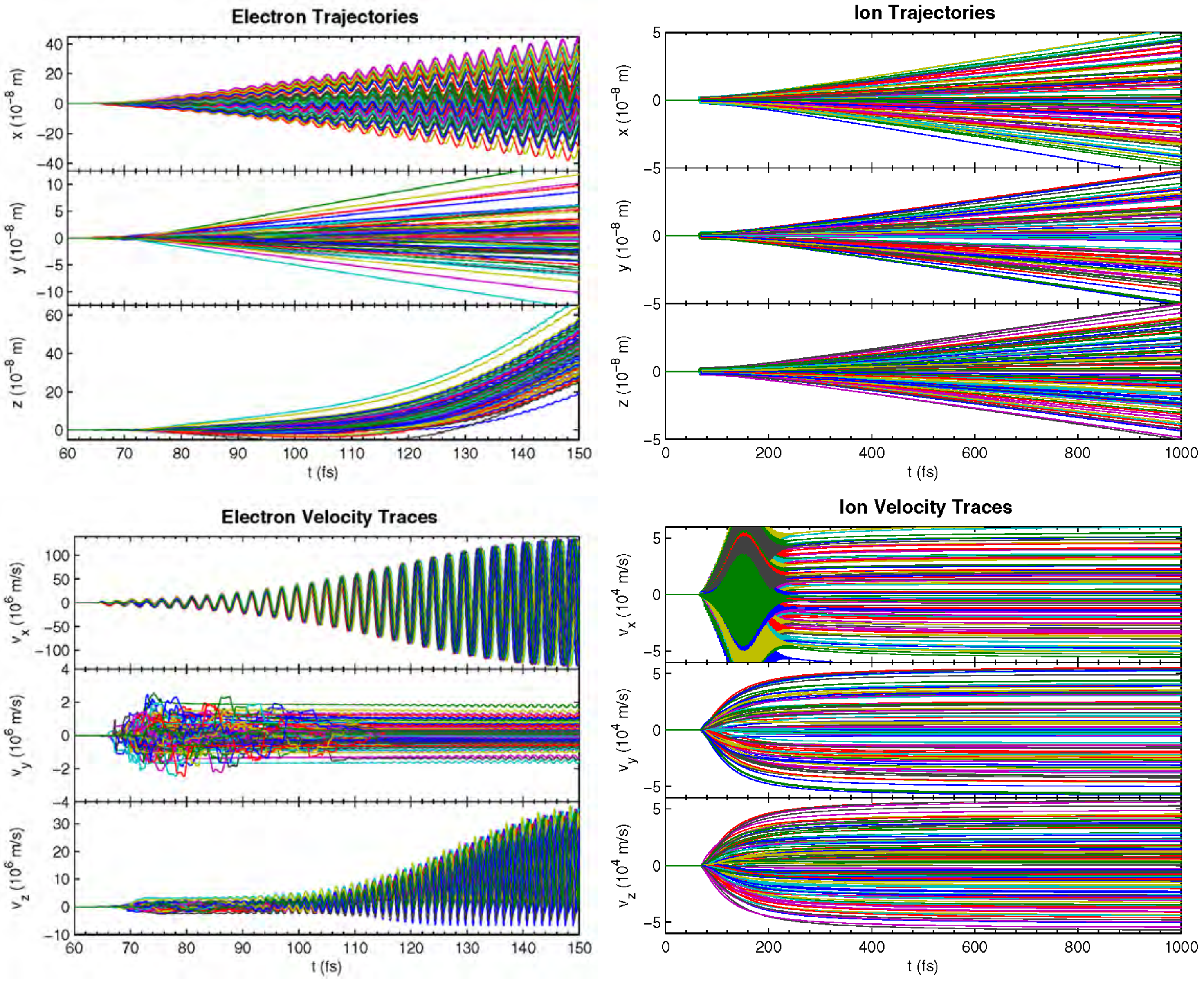

Figure D.1: [COUL1TRAJ]

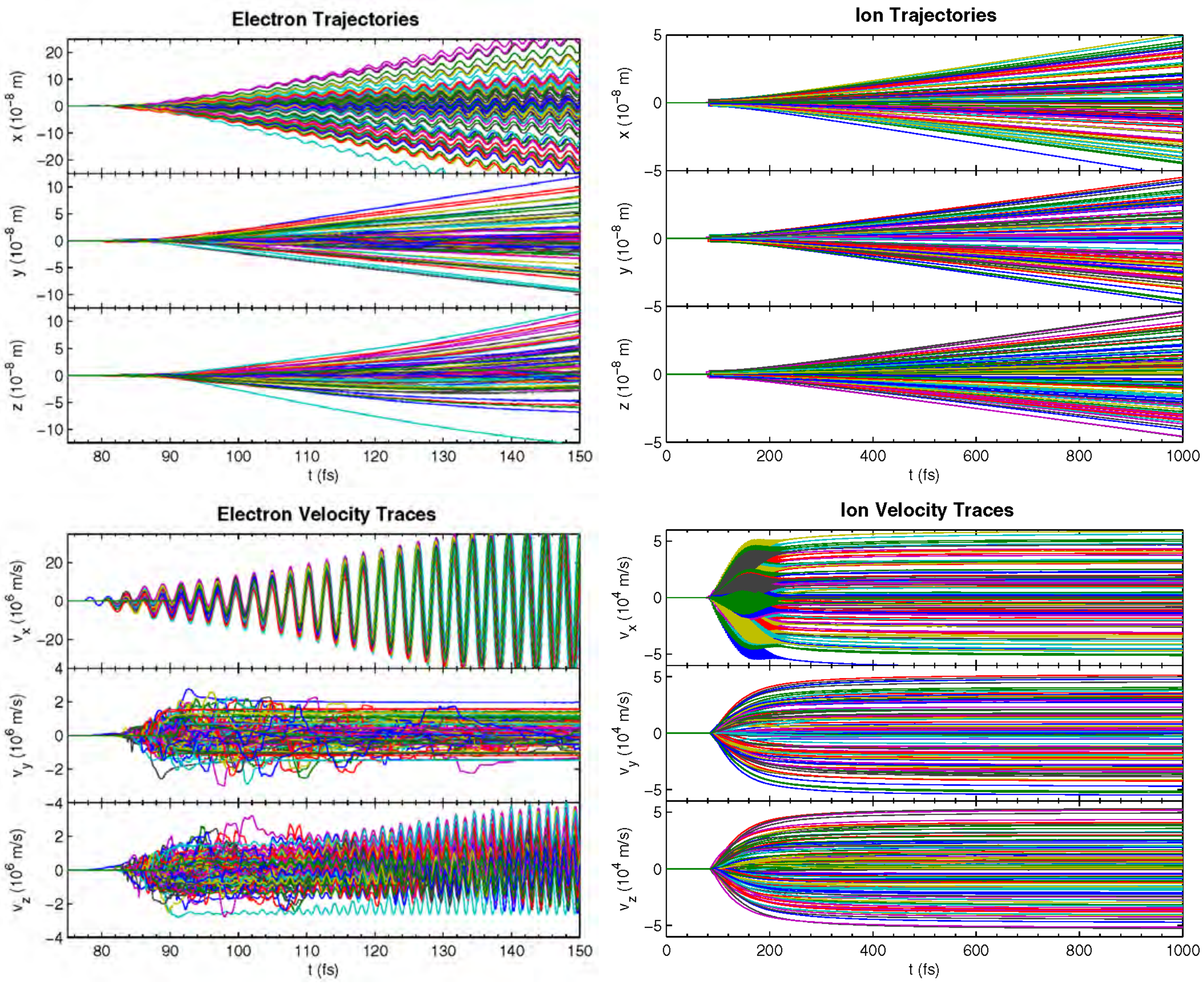

Figure D.2: [COUL2TRAJ]

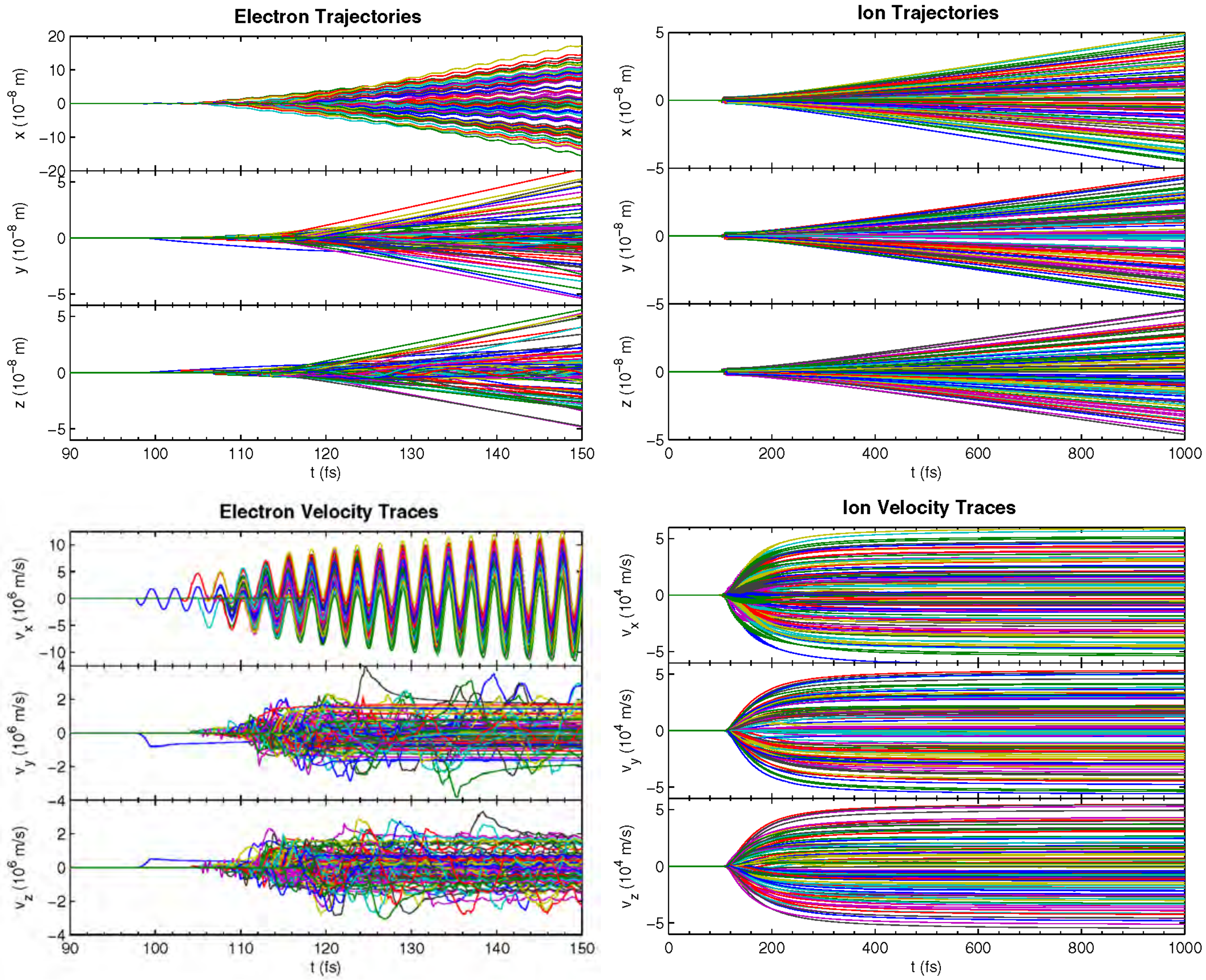

Figure D.3: [COUL3TRAJ]

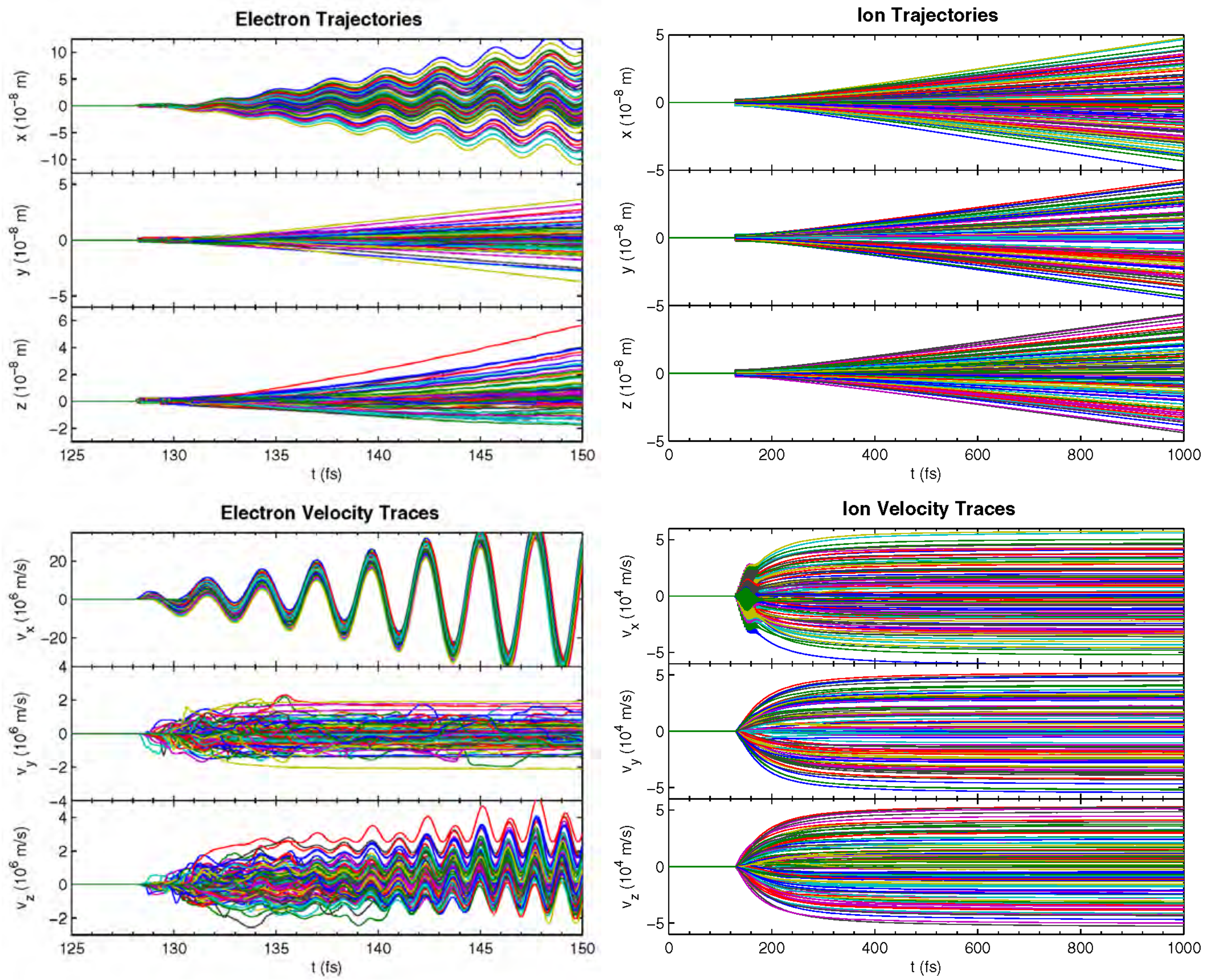

Electron Trajectories

Ion Trajectories

Electron Velocity Traces

Ion Velocity Traces

Figure D.4: [COUL4TRAJ]

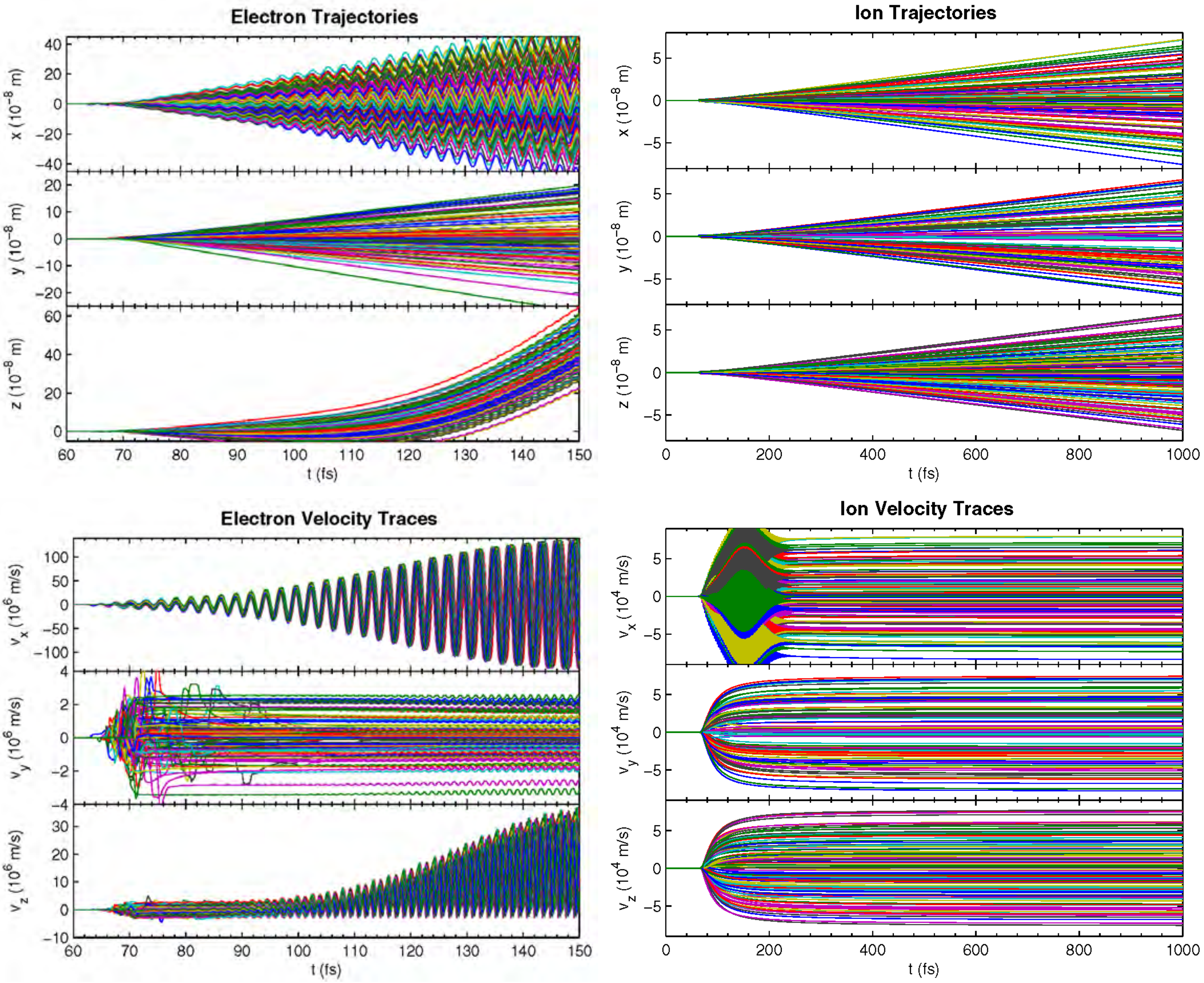

Figure D.5: [COUL5TRAJ]